

EXPLORING POTENTIAL THERAPEUTIC BENEFITS OF SPATIALLY FRACTIONATED RADIATION THERAPY

Judith Noemi Rivera

A dissertation submitted to the faculty at the University of North Carolina at Chapel Hill
in partial fulfillment of the requirements for the degree of Doctor of Philosophy in the
Department of Biomedical Engineering.

Chapel Hill
2020

Approved by:

Sha X. Chang

Paul A. Dayton

David S. Lalush

Michael W. Nolan

Gregory M. Palmer

© 2020
Judith Noemi Rivera
ALL RIGHTS RESERVED

ABSTRACT

Judith Noemi Rivera: Exploring Potential Therapeutic Benefits of Spatially Fractionated Radiation Therapy
(Under the direction of Sha X. Chang, PhD)

The work presented in this dissertation focuses on investigating new and safe ways to use radiation for enhancing cancer treatment via preclinical studies of Spatially Fractionated Radiation Therapy (SFRT). SFRT is a very promising, yet poorly understood, cancer radiotherapy approach that has recently gained traction due to its remarkable tissue selectivity, eradicating tumors effectively with little treatment toxicity, as well as its easy implementation on a wide range of clinical radiotherapy machines. Decades of clinical and preclinical research have demonstrated that SFRT may be used as a safe and effective way to shrink very large, bulky tumors in patients for whom other modern treatment approaches have been ineffective. Despite its very high therapeutic ratio and potential to satisfy several unmet needs in cancer treatment, SFRT remains largely an experimental approach, and a lack of preclinical SFRT research leaves many important questions unanswered.

This body of work investigates the development of a novel SFRT-delivery system and its implementation in a variety of preclinical SFRT research scenarios in the hopes of shedding light on some of the unanswered questions that hinder clinical translation of this promising treatment technology. In this work, systemic studies investigate key unique SFRT dosimetric parameters and their correlations with treatment response, as well as SFRT's specific advantages over conventional radiotherapy, particularly those enhancing multi-modality cancer therapy approaches such as anti-cancer immunotherapy and nanoparticle chemotherapy drug-delivery to tumors. SFRT is a low-toxicity and low-cost radiation therapy treatment that offers hope for many cancer patients, especially

those failed by current cancer treatment technologies. The work presented here aims to improve the understanding of this treatment approach and contribute to the effective and accessible treatment of cancer.

Dedicado

A mi hija, Noemi, porque simplemente te amo. Tu me enseñas cada día mucho más de lo que yo te pueda enseñar a ti.

A mis padres, Lorena y Jose Daniel, por haber sido como lo fueron conmigo, por haberme dado todo sin esperar nada a cambio, y que por su gran apoyo y amor he podido alcanzar una meta más en mi carrera.

A mis hermanos, mis amigos, y demás familia en general por estar siempre a mi lado y quererme tanto.

Amo estar con ustedes, viviendo cada anécdota, emoción, y experiencia que cada día nos acerca más.

ACKNOWLEDGEMENTS

I am indebted to many people for their contributions to the work described in this dissertation:

To my mentor, Dr. Sha Chang, for your constant support throughout every stage of the PhD process and especially for believing in me and demanding excellence, always. Thank you for setting the very high expectations you did and for knowing that if you pushed me hard enough I would succeed. I could not have asked for a better mentor- you always had the right words to say when I stumbled and have helped shape me into the researcher I am today.

To my committee co-chair and academic advisor Dr. David Lalush, for always being a strong ally and supporter of my research and academic endeavors.

To the members of my committee, Dr. Gregory Palmer, Dr. Michael Nolan, Dr. David Lalush, and Dr. Paul Dayton for their invaluable critiques and guidance of this work.

To my many wonderful collaborators across three different institutions and the many research labs that have helped make this work possible including: current and former members of the Palmer Lab (including Kenneth Young, Keith Laemont, Stefan Stryker, Dr. Artak Tovmasyan, and Dr. Hansford Hendargo), Dr. William Zamboni and former members of the Zamboni Lab (including Dr. Lauren Price, Dr. Andy Madden, Dr. Leah Herity, and Dr. Sophie Mageau), Dr. Jenny Ting and members of the Ting Lab (including Dr. June Brickey and Dr. Hao Guo), former and current members of the Dayton Lab (including Dr. Sunny Kasoji, Thomas Kierski, Dr. Brooks Lindsay, Dr. Gloria Nyankima, Dr. James Tsuruta, Dr. Virginie Papadopoulou, Dr. Kennita Johnson, Dr. Samantha Fix, and Dr. Ryan Gessner), members of the UNC Division of Laboratory Medicine and

Animal Studies Core (including Charlene Santos, David Darr, and Mark Ross), Dr. Hong Yuan, Dr. Shen Collette, and Mr. Jonathan Frank, members of the Duke Departments of Medical Physics, Chemistry, and Environmental Health & Safety (including Dr. Terry Yoshizumi, Dr. Brian Langloss, Dr. Matthew Belley, Dr. Michael Therien, Dr. Ian Stanton, and Ms. Giao Nguyen), members of the Department of College of Veterinary Medicine at North Carolina State University (including Dr. Michael Nolan, Dr. Tracy Gieger, and Dr. Donald Roback), members of the Chang Lab and current and former members of the Department of Radiation Oncology at UNC (including Mr. John Dooley for his computational expertise and excellent handiwork that is next to none, Dr. Elaine Zeman for sharing some of your vast knowledge and radiobiology expertise and wisdom, as well as Dr. Panayiotis Mavroidis, Dr. Ross McGurk, Mr. Leith Rankine, Dr. Tong Zhu, Dr. Lu Lan, Ms. Zeynep Karakas, Mr. Donald Roback, and Mr. Alex Price for all of their assistance in various aspects of this work and your words of encouragement).

To my best friend and amazing editor, Alpin Geist, for graciously reading the entirety of my dissertation, helping me fine-tune the text, for talking me off the ledge on occasion, for being a backup babysitter when I really needed it, and for being an all-around standup and generous person. Everyone needs an Alpin in their life.

To my friends and colleagues Sunny Kasoji, Gloria Nyankima, Devin Hubbard, and Lei Zhang for leading the way and for your many words of advice and support.

To my friends Alpin Geist, Anthony Abrantes, Michael Brown, Sugandha Singh, Deveshwar Hariharan, Nikhail Patel, and Flor Lara for very patiently sitting through all of my long practice presentations, asking me the tough practice questions, and celebrating all of my achievements with me.

To my husband, Anthony Abrantes, for his constant support and willingness to take care more than his share of the household and childcare duties so that I can have extra time and space to write and work.

To my mother, Lorena Rivera, my father, Jose Daniel Rivera, my brothers Daniel

Rivera and Miguel Angel Rivera, and all the rest of my family for their unfailing love and support throughout the PhD and my whole life. Ya'll are too many to list, but know that I love and appreciate you dearly.

To my greatest love, Noemi Christine Abrantes, for continuing to be all that I could ever ask for in a daughter.

TABLE OF CONTENTS

LIST OF FIGURES	xv
LIST OF SYMBOLS AND ABBREVIATIONS	xviii
CHAPTER 1: CANCER AND RADIATION THERAPY	1
1.1 Cancer- What Is It?	1
1.2 Radiobiology- The Hallmarks of Cancer	2
1.3 Background and History of Radiotherapy	5
1.4 Overview of Modern Radiotherapy Treatments	6
1.4.1 Multi-fractionated RT	6
1.4.2 3D Conformal RT, Intensity Modulated RT, and Image-Guided RT	7
1.4.3 Stereotactic Body RT	8
1.4.4 Proton RT	9
1.4.5 Combination Therapies	10
1.5 The Case for Additional Treatment Technologies	10
1.6 The Scope of This Work	12
CHAPTER 2: SPATIALLY FRACTIONATED RADIATION	15
2.1 Introduction	15
2.2 Unique Dosimetric Characteristics of SFRT	16
2.2.1 Peak dose, valley dose, and peak-to-valley dose ratio	16
2.2.2 Peak width, valley width, and peak-to-peak distance	17
2.2.3 Collimator (or GRID) output factor	18

2.3	The Evolution of SFRT	19
2.3.1	A brief history of SFRT	19
2.3.2	The modern resurgence of SFRT	20
2.4	Clinical SFRT	20
2.4.1	GRID Therapy	20
2.4.2	Advanced clinical SFRT techniques	23
2.5	Preclinical SFRT	25
2.5.1	Microbeam Radiation Therapy	25
2.5.2	Radiobiological studies in MRT	26
2.6	Potential Working Mechanisms of SFRT	28
2.6.1	Bystander effect	28
2.6.2	Reoxygenation effect	30
2.6.3	Differential microvasculature and microenvironmental effects	30
2.6.4	Dose-volume effect	31
2.7	Challenges to Clinical Translation	32
CHAPTER 3: DEVELOPMENT OF PRECLINICAL SFRT		35
3.1	Introduction and Motivation	35
3.1.1	Synchrotron-based MRT	35
3.1.2	Non-Synchrotron-based MRT using compact irradiators	36
3.2	SFRT Treatment Delivery System and Design	38
3.2.1	Overview	38
3.2.2	Physics considerations- energy and filtration	39
3.2.3	Physics considerations- radiation shielding	42
3.2.4	Geometric considerations	44

3.2.5	Animal considerations	48
3.3	Machine Specific Dosimetry	52
3.3.1	Equipment for measurements of exposure	52
3.3.2	Dose calculation	54
3.3.3	Beam quality	55
3.3.4	Irradiator linearity of current output	57
3.3.5	Irradiator energy response and kVp check	58
3.3.6	Radiation field uniformity- flatness and symmetry	59
3.4	Relative Dosimetry	61
3.4.1	Relative dosimetry using film	61
3.4.2	EBT-3 film calibration	62
3.4.3	Film limitations	66
3.4.4	Film dosimetry for SFRT	67
3.4.5	Relative dosimetry using the NanoFOD	68
3.4.6	NanoFOD calibration	70
3.4.7	NanoFOD dosimetry for SFRT	71
3.4.8	NanoFOD limitations	72
3.5	SFRT Dosimetry for Small Animal Studies	73
3.5.1	SFRT beam profiles	73
3.5.2	SFRT percentage depth dose	76
3.5.3	Integral dose calculation	78
3.6	SFRT Delivery System	79
3.7	SFRT Delivery System Limitations	81

CHAPTER 4: CONVENTIONAL DOSE RATE SPATIALLY FRACTIONATED RADIATION THERAPY TREATMENT RESPONSE AND ITS ASSOCIATION WITH DOSIMETRIC PARAMETERS – A PRECLINICAL STUDY IN A FISHER 344 RAT MODEL	85
4.1 Overview	85
4.2 Introduction	86
4.3 Materials and Methods	88
4.3.1 Study design	88
4.3.2 Animal tumor model	90
4.3.3 Animal radiation dosimetry	92
4.3.4 Animal radiation delivery and verification	97
4.3.5 Tumor volume imaging and body weight monitoring	97
4.3.6 Association between SFRT dosimetry and treatment response	99
4.3.7 Statistical methods	100
4.4 Results	100
4.4.1 Overall treatment response	100
4.4.2 Association between tumor response and SFRT dosimetry	103
4.4.3 Association between body weight change and SFRT dosimetry	106
4.5 Discussion	111
4.5.1 Study limitations	111
4.5.2 SFRT dosimetric association with treatment tumor response	113
4.5.3 SFRT dosimetric association with normal tissue toxicity	116
4.6 Summary	119
4.7 Acknowledgments	120

CHAPTER 5: MINIBEAM RADIATION IS SUPERIOR TO UNIFORM RADIATION FOR ABSCOPAL EFFECT WITH COMBINED PD-L1 CHECKPOINT INHIBITOR IMMUNOTHERAPY	121
5.1 Overview	121
5.2 Introduction	122
5.3 Methods	124
5.3.1 Study design	124
5.4 Animal Model Description and Cell Culture	125
5.4.1 Animal monitoring and husbandry	127
5.4.2 Radiotherapy dosimetry and treatments	128
5.4.3 Flow cytometry studies and analysis methods	131
5.5 Results	132
5.5.1 Irradiated tumor response	132
5.5.2 Unirradiated tumor response	133
5.5.3 Spleen lymphocyte profile	133
5.5.4 Tumor lymphocyte profiles	134
5.6 Discussion and Conclusions	136
5.7 Conflicts	138
5.8 Acknowledgements	138
CHAPTER 6: MICROBEAM RADIATION THERAPY ENHANCED TUMOR DELIVERY OF PEGYLATED LIPOSOMAL DOXORUBICIN IN A TRIPLE NEGATIVE BREAST CANCER MOUSE MODEL	139
6.1 Overview	139
6.2 Introduction	141
6.3 Methods	144

6.3.1	Treatments	144
6.3.2	Pharmacokinetic studies	144
6.3.3	PLD quantification	145
6.3.4	Pharmacokinetics analysis	146
6.3.5	Tumor Staining and Immunohistochemistry	146
6.4	Results and Discussion	147
6.4.1	Single dose pharmacokinetics	147
6.4.2	Multiple dose pharmacokinetics	151
6.4.3	Tumor microenviroment profiling	154
6.5	Acknowledgements	157
6.6	Funding	157
CHAPTER 7: DISCUSSION AND FINAL CONCLUSIONS		158
7.1	The Potential Global Impact of SFRT	158
7.2	New Horizons in SFRT	160
7.3	Conclusions	162
REFERENCES		165

LIST OF FIGURES

	Page
Figure 1 Unique Dosimetric Characteristics of SFRT	16
Figure 2 GRID Output Factor	18
Figure 3 Dose Profiles for GRID-compensator SFRT	21
Figure 4 2Dimensional SFRT Dose Distribution	24
Figure 5 MRT Beams	26
Figure 6 RT Energy and Filtration	41
Figure 7 Specifications for Different RT Shielding Materials	43
Figure 8 Specifications for Different RT Shielding Materials	46
Figure 9 Schematic of a SFRT-Minibeam Collimator	48
Figure 10 Animal Irradiation Setup and Shielding	49
Figure 11 Animal Anesthesia and Body Temperature Maintenance	52
Figure 12 Ion Chamber Specifications and Dark Current Measurements	54
Figure 13 Dose Calculation Coefficients	56
Figure 14 Dose Calculation Coefficients	57
Figure 15 Linearity of Output for the XRAD-320 Irradiator	58
Figure 16 Energy Response and kVp check	59
Figure 17 Field Uniformity Measurements of Flatness and Symmetry	60
Figure 18 Film cross-calibration setup with ion chamber	64
Figure 19 EBT-3 Film Calibration Curves	66
Figure 20 EBT-3 Film Calibration Setup for SFRT Dosimetry	68
Figure 21 NanoFOD Detector General Setup	69
Figure 22 NanoFOD Calibration Results	71

Figure 23	NanoFOD for SFRT Beam Profile Measurements	72
Figure 24	SFRT Dosimetry Using NanoFOD and Film	74
Figure 25	Dose Profile Results for a variety of SFRT Collimators	75
Figure 26	Dose Profile Results for a variety of SFRT Collimators	76
Figure 27	Percentage Depth Dose measurements for Variety of SFRT Collimators	77
Figure 28	Integral Dose Calculation	79
Figure 29	The SFRT Delivery System Setup	80
Figure 30	Example Treatment Challenges and Remedies	82
Figure 31	Illustration of the SFRT spatial fractionation study design	89
Figure 32	Summary of nine SFRT dosimetric parameter specifications in the six-arm study.	89
Figure 33	Animal irradiation setup and treatment alignment and verification.	93
Figure 34	Phantom dosimetry measurement.	94
Figure 35	Measured dose beam profiles and percentage depth doses for all treatment arms. .	95
Figure 36	Tumor and Normal Tissue EUD Calculations	96
Figure 37	3D ultrasound imaging-based tumor volume measurement.	98
Figure 38	Animal survival, tumor volume change, and body weight change	102
Figure 39	Tumor volume changes for all six study arms	103
Figure 40	Associations between Percentage Survival and dosimetric parameters.	104
Figure 41	Univariate linear regression analysis of Survival on Day 17.	105
Figure 42	Coefficients table for univariate Cox Proportional Hazards survival analysis . . .	106
Figure 43	Associations between Body Weight and dosimetric parameters.	108
Figure 44	Table of coefficients for univariate linear regression analysis of Body Weight (Day 17)	109
Figure 45	Multivariate hierarchical regression analysis of predictors of Body Weight (Day 17)	110

Figure 46	Hierarchical multivariate CoxPH analysis of predictors of Survival	111
Figure 47	Illustration of treatment delivery verification analysis by film.	112
Figure 48	Pearson Correlation coefficient matrix for the eight SFRT dosimetric parameters relevant for tumor treatment response.	119
Figure 49	Experimental design of seamless (UniformRT) vs spatially fractionated (MinibeamRT) radiation therapy study of the systemic immune response of mice.	125
Figure 50	Experimental Timeline for the Immunotherapy Study	127
Figure 51	Radiotherapy Dosimetry and Treatment Setup	129
Figure 52	Dosimetric parameters for both radiotherapy treatment types used in the study .	130
Figure 53	Tumor volumes changes observed post-radiation	132
Figure 54	Results from flow cytometry immunophenotypic analysis of spleen cells	134
Figure 55	Results from flow cytometry immunophenotypic analysis of tumor cells	135
Figure 56	Doxorubicin Concentrations in Plasma and Tumor Over Time	148
Figure 57	Summary of PLD Pharmacokinetics After a Single Dose of PLD Alone, BRT + PLD, or MRT + PLD	149
Figure 58	Comparison of MRT-Induced Delivery Enhancement at Low and High Plasma Exposures After Single Dose MRT28Gy + PLD	151
Figure 59	Encapsulated Doxorubicin concentrations Following Single Dose Versus Multi Dose MRT.	152
Figure 60	Summary of PLD Pharmacokinetics After a Single Dose of PLD Alone or One or Two Treatments of MRT 28Gy + PLD Weekly.	153
Figure 61	Tumor Microenvironment profiles 24 hours post-Treatment.	155

LIST OF SYMBOLS AND ABBREVIATIONS

μm	micrometer, micron
ρ	Density
c	Speed of Light
D_{max}	Maximum dose
Gy	Gray
J	Joules
J/s	Joules per second
m	milli-
$m/s, \frac{m}{s}, ms^{-1}$	meters per second
P	Pressure
R	Roentgen
s	seconds
A	Ampere
BRT	Broadbeam radiation therapy
cm	centimeter
D	Dose
IGRT	Image guided radiation therapy
IMRT	Intensity modulated radiation therapy
m	meter
MRT	Microbeam radiation therapy
PDD	Percentage depth dose
Pk	Pharmacokinetics
RT	Radiation therapy, radiotherapy
SBRT	Stereotactic body radiation therapy
SFRT	Spatially fractionated radiation therapy

SRS	Stereotactic radiosurgery
T	Temperature
TBI	Total body irradiation
W	watt
WBI	Whole brain irradiation

CHAPTER 1: CANCER AND THE ROLE OF RADIATION THERAPY

1.1 Cancer- What Is It?

Loosely defined, cancer refers to a group of cells that have lost their inherent ability to perform normal functions or form normal tissues, and these cells even gain new functions including the ability to grow uncontrollably, invade, and metastasize. These cells often create a small body of cells, a tumor, but though a tumor is made from cancerous cells, the environment is far from homogenous. A distinct microenvironment exists within a tumor, including different cell types and vasculature, and this microenvironment is still not fully understood. Because each instance of cancer is unique and highly dependent on the environment, mutation, and other factors, the most effectual treatment methods for cancer still remain mysterious.

New discoveries are made every year that help shed light on some of these mysteries and the very definition of “cancer” and what are considered to be its distinguishing features are still evolving [1]. A vast amount of molecular cancer research has embraced the notion that the key to curing cancer lies in finding and decoding the common cancer genes responsible for the majority of cancers [1]. The gene mutation theory of cancer indicates that the genetic differences between cancer types determine how aggressively any individual type of cancer grows and affects its host environment. Numerous studies have created molecular and genetic profiles of cancer and their different subtypes. With huge amounts of emerging genetic molecular data of cancer. In 2000 Hannan and Weinberg classified these large number of diverse gene mutations into simplified molecular principles, known as the Hallmarks of Cancer [2].

1.2 Radiobiology- The Hallmarks of Cancer

Hannan and Weinberg organized the framework for the Hallmarks of Cancer into 6 major pathways which cancer alters to develop: insensitivity to anti-growth signals, self-sufficient oncogenes, evasion of apoptosis, sustained angiogenesis, metastasis, and limitless replicative potential[2]. Each leg of this framework offers a method through which cancer develops, grows, and develops a distinct microenvironment and are briefly summarized, below.

1. Cancers cells are insensitive to anti-growth signals, circumventing the cell's natural tumor suppressor genes through mutations that prevent anti-growth signals from binding to a receptor, or alternatively, phosphorylation, etc.
2. Cancer cells develop self-sufficiency in growth signals, locking a cell's oncogenes into an ON state so normal sources for growth signals are not needed.
3. Cancers evade cell death, apoptosis, through mutations in tumor suppressor signals, such as the p-53 tumor suppressor protein, which allow tumor cells to survive where they otherwise would not, potentially bypassing replicative senescence, a natural stop to cell division after appropriate population doublings.
4. Cancers have sustained angiogenesis, development of new vasculature. This present a unique challenge as tumors may become resistant to angiogenesis inhibitor drugs, such as VEGF-pathway inhibitors, by seeking alternative signaling pathways for recruiting vasculature into the tumor [3].
5. Cancers have an increased ability to both invade surrounding normal tissues and also metastasize, wherein tumor cells breach the tumor basement membrane and move after proliferation and angiogenesis of the primary tumor. In addition, metastatic cells may detach themselves from the primary tumor and invade the circulatory

system, adhere to a vessel wall, extravasate, establish a microenvironment in a micrometastases and then further proliferate. However, this metastatic cascade is extremely inefficient and very few cells manage to generate macroscopic metastases.

6. Cancers have limitless replicative potential, where disruption of the pathway that limits cell replication allows tumor cells to become immortalized. Benign tumor cells that have undergone the first five major pathway mutations discussed so far cannot yet divide with infinite replicative potential. However, these cells finally become immortalized due to the overexpression of telomerase, an enzyme cells use to synthesize DNA, after the erosion of the cell's telomeres.

The gene mutation theory of cancer underlying the hallmarks that Hannahan and Weinberg organized into a blueprint for understanding carcinogenesis have served as a driver of cancer biology research. By organizing the cellular properties of carcinogenesis into a framework of six pathways they provided a guideline for cancer treatments. The majority of modern cancer treatments attempt to target and disrupt at least one of these major pathways to halt cancer progression [4], [5]. Cancer therapies with drugs that target one or more of these pathways are an area of very active investigation; thousands of drugs are in development [6].

Notably, a decade after their initial publication, Hannahan and Weinberg updated Hallmarks of Cancer framework to include four additional pathways: reprogramming energy metabolism, evading the immune response, and the enabling traits of genome instability/mutation, and tumor promoting inflammation [7]. “Hallmarks II” also mentions the emerging importance of the Tumor Microenvironment and its numerous modifiers.

Many investigators have noted that the majority of research on cancer to date has focused on the parenchyma of the tumor and the associated normal tissues [5], where the parenchyma is the part (s) of the tissue that performs biological functions and in a tumor refers to the tumor cells themselves. However, in the last decade there has been emerging

evidence of the importance of the tumor microenvironment, including the tumor stroma, tissues that support the function of the parenchymal cells such as the basement membrane, extracellular matrix, immune cells, and vasculature etc. [8], [9]. The seed and soil theory, in which cells will only grow in microenvironments that are correct for them [10], [11], invites cancer therapies to target the tumor microenvironment and many treatments have been developed to do so [3], [8], [12]. One such treatment includes altering the tumor microvasculature, a component that plays a key role in the tumor's ability to grow [5], [13]. These and other modifiers within the tumor microenvironment play a role in the health and persistence of the tumor, and along with targeting the pathways described in the Hallmarks of Cancer, research can be guided toward effective and appropriate treatment [1].

One common treatment for cancer, Radiation Therapy (RT), is used in about half of all cases of cancer within the U.S. [14], [15]. The primary target of Radiation Therapy is to cause ionization events within the tissue, resulting in damage to DNA base-pairs, single strand breaks (SSBs), and double-strand breaks (DSBs) [16], [17]. In each of these, a pathway to tumor growth is potentially disrupted and researchers have linked these pathways to the original Hallmarks [4], [5]. In principle, highly energetic, ionizing radiation penetrates tissues and deposits energy to the cells that it passes through, destroying them or inducing genetic changes that result in eventual cell death [17]. Radiation does not distinguish between normal cells and cancer cells and is equally damaging to both; however, all cells do not respond to radiation in the same way. Normal cells generally have vastly improved repair mechanisms compared to cancer cells and can recover from radiation damage more quickly [16], [18]. Radiation therapy may be used to exploit these differences in cellular repair mechanisms to kill cancer cells, while minimizing exposure to normal cells [16].

1.3 Background and History of Radiotherapy

The start of Radiation Therapy can be traced to the discovery of x-rays by Wilhelm Rontgen in 1895, natural radioactivity by Henry Becquerel in 1896, and radium by Pierre and Marie Curie in 1898. The biological and physiological effects of x-ray radiation immediately caught the interest of researchers and physicians around the world, and only two months later, Austrian radiologists Freund and Schiff proposed their potential therapeutic use [19], [20]. This discovery was quickly followed by the first experimental, but ultimately fatal, treatment with x-rays. French physician Victor Despeignes attempted to use x-rays to treat a case of stomach cancer in 1896, and though ultimately fatal, a year later Radiation Therapy resulted in the successful treatment of lupus by Schiff in 1897 [19], [20]. The recognized therapeutic benefits of ionizing radiation for the use in treatments of cancers and other malignancies quickly ushered in an era of rapid technology development and a radical change in how cancer treatment was approached. Since the turn of the 20th century, radiation therapy treatments have undergone several massive changes, which have greatly enhanced therapeutic indices for patients as well as improved survival and quality of life [16].

Among these changes is the development of the modern linear accelerator (LINAC) machine, which has the ability to precisely deliver highly energetic x-ray radiation to target patient tumors in any site of the body and destroy them. These machines use advanced technology to shape the x-rays as they exit the machine to conform to the specific shape of a tumor, while avoiding some of the surrounding critical organs. This modern linear accelerator has revolutionized the way cancer is treated and over a century after the initial discover of radiation, radiation therapy is still routinely used around the world as a means for treating cancer and a multitude of other ailments. Today, radiation therapy is used in approximately 50% of cancer treatments in the U S. [14].

1.4 Overview of Modern Radiotherapy Treatments

The benefits of Radiation Therapy have advanced with technology and research, though the ultimate goal has long remained: to eradicate the malignancy while minimizing the effects on normal tissue, especially those tissues that are critical to patient survival and quality of life. Modern radiation therapy technologies and techniques have been specifically developed to enhance the Therapeutic Index (TI) of cancer treatment, that is, the ability to eradicate tumors, while maximally sparing surrounding critical structures and normal tissues in the body. In the last two decades, highly sophisticated and complex radiation therapy and imaging technologies have been developed that result in high precision and conformal radiation targeting of tumors. When combined with advanced radiobiological understanding of tissue responses, these developments have led to significant improvements in patient outcomes [21]. These developments include radiation therapy techniques used both separately and in tandem to allow clinicians to strive toward eradication of malignancy but preservation of normal tissue. Some of these techniques include Multi-fractionated Therapy, Image-Guided Radiation Therapy (IGRT), Intensity Modulated Radiation Therapy (IMRT), Stereotactic Radiosurgery (SRS) and Stereotactic Body Radiation Therapy (SBRT), Proton Therapy, among others.

1.4.1 Multi-fractionated RT

The dose required to kill a tumor is often very high, and when delivered as a single treatment may result in severe normal tissue toxicities [22]. These toxicities may cause undue pain and stress to the patient and result in decreased quality of life. One technique for limiting the damage to normal tissues involves dividing the tumor killing dose into a number of smaller dose fractions, delivered over time, known as multi-fractionated radiation therapy (MFRT). This technique effectively exploits differences between tumor and normal tissue radiobiological repair mechanisms to guide treatment, effectively sparing

normal tissues while increasing damage to the tumor [16].

1.4.2 3D Conformal RT, Intensity Modulated RT, and Image-Guided RT

Further sparing of normal tissue is achieved by conforming the 2-dimensional radiation beam to fit the shape of the tumor volume and deliver a customized, irregular radiation field shape to fit the tumor for each treatment angle used. Individually controlled miniature radiation shields, called multi-leaf collimators (MLCs), create beamlets that when combined with advances in CT imaging technology allow for this 3-dimensional conformal radiation field shaping, called 3-dimensional Conformal Radiation Therapy (3DCRT) [23]. By optimizing beam placement and shielding, 3DCRT has an enhanced ability to localize treatment to the target volume and avoid nearby critical structures, known as organs at risk (OAR), compared to conventional 2D radiotherapy that used rectangular-shaped fields [24]. Intensity modulated radiation therapy (IMRT) improves on the 3DCRT technique via advancements in treatment planning software [25]. The software user delineates the treatment targets and OARs, defines the minimum and maximum dose limits and number of beam angles to use, then the inverse planning software algorithm calculates the optimal intensity for each individual beamlet. Computer-controlled MLCs are then used to modulate each beamlet intensity for each angle which enables enhanced OAR sparing, even for complex concave radiation field shapes [26].

As these advanced highly conformal 3D IMRT techniques allow users to create much narrower treatment margins and higher dose gradients than ever before, there is also enhanced risk of setup error and inadvertent radiation to nearby OARs [25]. The development of advanced image-guided radiotherapy (IGRT), such as cone-beam CT scans acquired before each treatment, allow for more accurate positioning to avoid nearby misses. IGRT's anatomical tracking allows for changes in daily treatment repositioning, as well as computing the total volumetric dose from the entire treatment course [25]. These advances in modern image-guidance procedures, as well as highly advanced treatment

planning techniques and computer-controlled MLC technology, have helped make IMRT possible.

The primary patient and physician concern is to control or eradicate cancers in the immediate future; however, the biggest drawback of advanced radiotherapy techniques like 3DCRT, IMRT, and IGRT is the increased total dose delivered to the patient's body, which is correlated with secondary malignancies later in life [27]. While the dose to critical organs is minimized, the use of smaller beamlets of radiation through more angles in the body leads to longer treatment times and, hence, increased radiation leakage through the collimator leaves. The increased leakage is especially enhanced in patients with larger tumor sizes or patients with recurring or more aggressive tumors types that require higher total dose to eradicate. However, this radiation leakage contributes only a few percent of the total dose to the body, where the total dose is largely determined by the prescription dose and treatment tumor volume. In addition to being time-consuming and complex, these advanced radiotherapy techniques require very expensive, sophisticated equipment and well-trained staff to implement [26]. IMRT in particular remains very sensitive to setup error and treatment misses near the setup margins [25].

1.4.3 Stereotactic Body RT

Advances in both IGRT, IMRT, as well as specialized treatment planning methods have helped resulted in high targeting accuracy and steep dose gradients beyond the target volume [28], [29]. In conjunction with anatomy tracking, they have additionally enabled the development of stereotactic body radiation therapy (SBRT), which precisely delivers high, tumor-killing doses of radiation as a single treatment session, or a limited number of time-fractionated session to cranial or extracranial targets anywhere within the body [30]. These treatments have shown remarkable success in the treatment of extracranial oligometastases less than 3cm [30] and limited success for all solid tumors less than 5cm [31]; however, it is not recommended for tumors 5cm or larger due to high risk of fatal

normal tissue toxicity complications [32].

1.4.4 Proton RT

Radiation therapy may also be carried out with energetic charged particles such as protons. In x-ray radiotherapy, as well as electron radiotherapy, the x-rays deposit their maximum energy at or near the tissue entrance and then continue depositing dose along their entire trajectory until they come out the other side of the patient, killing cancer as well as damaging normal cells in the process. However, protons in radiotherapy have a very low dose at the tissue entrance which then increases with increasing depth until they reach a sudden peak, maximum dose at the tumor and then falls off very rapidly, with no exit dose [33]. In principle, protons are much less damaging to normal tissue cells compared to modern x-ray radiotherapy for similar rates of tumor killing [34], [35]; however it is also more sensitive to organ motion as well as anatomy changes within the path of the beam than x-ray radiotherapy [34]. The distinct radiobiological advantages inherent to proton therapy make a very promising treatment approach that has been used on thousands of patients already, but it comes at a very steep cost and is considered a highly controversial treatment. A single treatment room may be up to an order of magnitude higher than for even the most high-end photon radiotherapy unit, requiring costly cyclotrons or synchrotron facilities to produce and uses the most advanced beam shaping collimators, image-guidance, and treatment planning techniques [33], [36]. In addition, several physicians and researchers have raised concerns over its lack of cost-effectiveness as there is little convincing evidence that proton therapy is superior to x-ray radiotherapy in terms of clinical outcomes [35], [37]. Proton therapy is still considered a largely experimental, evolving approach and needs further investigation to demonstrate its cost-utility balance on the world-wide stage [38].

1.4.5 Combination Therapies

Combination therapies are designed to exploit complementary cancer treatment strategies to disrupt the pathways for malignancies. Though radiation therapy is the most successful treatment type, the addition of other therapies may dramatically enhance the effects of radiation therapy [39], [40]. Research shows a relationship between radiation therapy and the immune response, complementary to immunotherapy [21], [41] as well as chemotherapy [42]. Hannan and Weinberg’s Hallmarks of Cancer have been hugely influential in driving the new molecular cancer and genetic research, which has identified several new targets for anti-cancer drug development and revolutionized the field of immunotherapy research citeahmadClinicalDevelopmentNovel2019. Currently, cancer research that targets specific parts of the tumor’s genetic pathways to disrupt progression is being explored [43]–[45]. There is evidence, albeit limited, that combining radiation with immunotherapy may help augment the biological effects of treatment and induce a greater tumor response and several immunomodulatory agents in development for this purpose [46]–[49]. In 2016, the CTRad working group within the UK National Cancer Research Institute (NCRI), published a consensus statement that called for identifying barriers and solutions to increase the number of clinical trials in drug-radiotherapy combinations as well as a list of recommendation and guidelines for future work in this area [21]. In this call to action, the UK NCRI acknowledged many challenges to widespread clinical implementation, and has shifted focus away from exclusive use of Radiation Therapy alone.

1.5 The Case for Additional Treatment Technologies

Modern day radiotherapy treatments have undoubtedly benefited millions of patients across the US and the world. These advancements include geometric precision and targeting abilities and allow for some differentiation between the treatment target (tumor) and other

sensitive tissues to control cancers and improve clinical outcomes [28], [29], [50]. However, the benefit of these advanced technologies come with a high price tag. Several researchers have argued that the development of these state-of-the-art technologies have significantly contributed to the high rise in treatment costs [29], [50], [51], general healthcare costs [52], [53], and places additional financial barriers to quality cancer care on medically underserved communities [38], [49]. In addition, many of these treatment technologies are still largely inaccessible for developing countries, where the majority of the world’s cancer population resides [54], [55].

Beyond the need for cost-effective treatments, leaps made in this technological revolution have not led to improvements in clinical outcome near the same order of magnitude. Today, many experts believe that further geometric and dosimetric improvements have had a diminishing return in clinical utility of radiation therapy. There remain a host of patients with cancers that do not respond to conventional treatment approaches or for whom these approaches are extremely dangerous. These patient populations include pediatric and geriatric patients [29], [55], [56], patients whose critical organs have already received the maximum tolerance dose [57], [58], patients with chemoresistant and radioresistant cancers [59]–[62], and patients with recurring or metastatic disease [62]. Further, by 2040, the global number of newly diagnosed cancers is expected to increase drastically to nearly 28 million, an increase of almost 40% from 2018 as a result of population growth and an aging population [63], [64].

Therefore, there is a need to look beyond the physics and engineering approaches for cancer therapy advancement and towards very different and innovative, radiobiologically-driven, approaches that have the potential to significantly increase the treatment therapeutic ratio compared to the current conventional standards, especially for those patients for whom modern treatment approaches remain ineffective or are not an option [65]. In addition, a closer look at alternative, cost-effective approaches may make effective cancer treatment more widely accessible to all radiation therapy clinics [66]–[68].

A treatment approach that may meet some of these clinical needs and has gained traction in recent years is spatially fractionated radiation therapy (SFRT). Spatially fractionated radiation therapy is an experimental treatment approach that may offer new hope for these cancer patients. Modern radiotherapy treatment approaches generally fall under the umbrella of classical radiobiology, wherein the entire tumor volume, including margins, must receive a high curative radiation dose to achieve tumor control and any unirradiated volume may eventually lead to local treatment failure in the form of disease progression or recurrence. However, recent SFRT research has shown that local tumor control may still be achieved even with multiple “cold”, unirradiated spots present within the tumor [69]–[71]. In fact, numerous preclinical and limited clinical studies have supported the hypothesis that this unique treatment is more effective in tumor control with less treatment toxicity [72]. Additionally, compared to conventional radiotherapy, this spatially inhomogeneous dose distribution may induce vastly different microenvironmental effects in tumors and may even play an important role in multimodal treatment approaches such as chemotherapy and immunotherapy [73]. Despite the potential for SFRT to satisfy several unmet needs in cancer treatment, this approach has historically been difficult to accept by most clinicians and researchers. Further, a general lack of preclinical SFRT research leaves many important questions unanswered and the underlying working mechanism of this treatment is still poorly understood, hindering the broad clinical translation of this promising cancer treatment technology.

1.6 The Scope of This Work

This body of research discusses the development of a novel SFRT-delivery system and its implementation in a variety of SFRT preclinical research scenarios in the hopes of shedding light on some of the unanswered questions that hinder clinical translation of SFRT treatment technology. Systemic studies demonstrating SFRT’s ability to control tumors while sparing normal tissue as well as on potential methods to optimize treatment

are performed. However, no research is completed in isolation and the work described in this dissertation is no exception. The development, validation, and implementation of this novel SFRT-delivery system for use in a variety of preclinical studies has required extensive multi-disciplinary collaborations with a variety of researchers at three major universities and may be broken down into three major parts:

1. Development of a novel pre-clinical SFRT-delivery system for cancer treatment in Chapter 3, including all relevant design, construction, testing, methodologies, and results. This work was dosimetrically validated with the help of the Duke University Dosimetry Laboratory and Department of Medical Physics.
2. Application of the SFRT-delivery system for use in an investigation of unique SFRT dosimetric parameters and their correlations with treatment outcomes in Chapter 4. This work was completed in collaboration with Dr. Paul Dayton and the Dayton Lab in the department of Biomedical Engineering at UNC-Chapel Hill and NC State University.
3. Investigations of the specific advantages of SFRT over conventional radiation therapy in multi-modality cancer therapy approaches, including
 - An investigation of potential methods for immunotherapy enhancement using spatially fractionated radiation therapy in Chapter 5. This work was completed in collaboration with Dr. Palmer and the Palmer Lab at the Duke University Dept. of Radiation Oncology.
 - An investigation of potential methods for anti-cancer drug delivery enhancement via SFRT-induced changes to the tumor microenvironment in Chapter 6. This work was completed in collaboration with Dr. Zamboni, the Zamboni Lab, and the UNC Animal Studies Core at UNC-Chapel Hill.

In addition, Chapter 2 provides a literature review of the current state of SFRT, including its historical background and modern-day clinical treatment outcomes, preclinical SFRT research, as well as the current major challenges facing its broad-clinical translation. Lastly, Chapter 7 offers a more global perspective on the potential impacts of SFRT treatment technology and its promising future prospects.

SFRT is a new low toxicity and low-cost radiation therapy treatment that offers hope for many cancer patients, especially those failed by the current cancer treatment technologies. The work presented hopes to improve our understanding of this treatment approach and in small part, contribute to the effective and accessible treatment of cancer.

CHAPTER 2: SPATIALLY FRACTIONATED RADIATION THERAPY BACKGROUND

2.1 Introduction

Spatially fractionated radiation therapy (SFRT) is a very promising experimental cancer treatment approach that has recently gain traction due in part to its high therapeutic ratio and relatively easy implementation on a wide range of clinical machines. SFRT has remarkable tissue selectivity, eradicating tumors effectively with little treatment toxicity. Decades of clinical studies have demonstrated that SFRT may be used as a safe and effective way to shrink very large, bulky tumors in patients for whom other modern treatment approaches have been ineffective. In direct contrast to conventional radiotherapy, which demands treating the entire tumor volume with a high, uniform dose, SFRT directly irradiates only small sub-regions within the treatment volume with very high doses of radiation, and so the broad clinical translation of this promising cancer treatment technology has both been historically difficult to accept and achieve. A general lack of preclinical SFRT research has left many important questions unanswered, notably including optimal spatial fractionation pattern and dose. Furthermore, the working mechanisms behind this technique are not yet understood, but some theories include systemic immune stimulation effects, radiation-induced bystander (abscopal) effects, altered cell signaling that induces indirect cell death, and even changes to the tumor micro-vasculature or micro- environment. This chapter provides a general overview of SFRT, a review of some prominent clinical and preclinical studies, brief explanation of some of SFRT's potential working mechanisms, and a discussion of some of the critical barriers to widespread clinical translation of the approach.

2.2 Unique Dosimetric Characteristics of SFRT

Both clinical and preclinical SFRT share the same characteristic trait with very few exceptions; a single, high dose, spatially inhomogeneous radiotherapy treatment is delivered to the target. While the specific dose distributions and dosimetric parameters in preclinical and clinical SFRT are vastly different, they may be described using largely the same nomenclature. Common terms include the peak dose, valley dose, peak-to-valley dose ratio (PVDR), peak width, valley width, peak-to-peak distance, as well as the percentage % of target directly irradiated (also known as the ratio of open-to-shielded area). Figure 1 visually describes some of the characteristic properties that are common to all SFRT treatments.

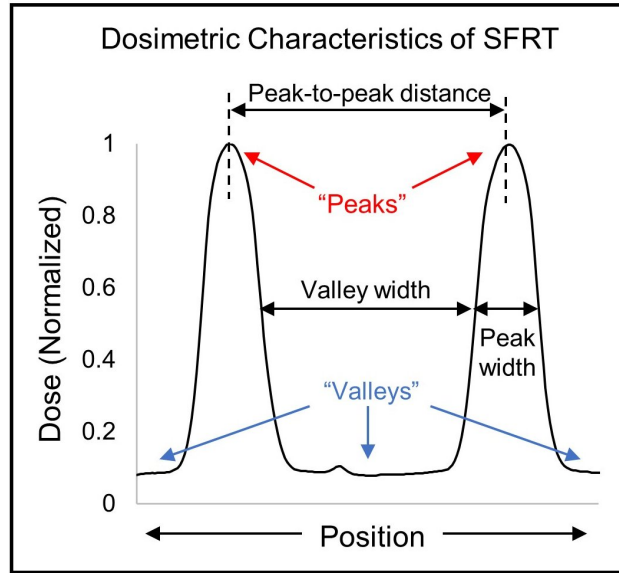


Figure 1: The unique beam profiles of SFRT may be dosimetrically characterized, in part, by the high dose in the "peak" region, the low dose in the "valley" region between consecutive peaks, the ratio of the peak to the valley dose, the peak widths and the distance between them, as well as the valley widths.

2.2.1 Peak dose, valley dose, and peak-to-valley dose ratio

The peak dose is the maximum dose measured in the unshielded "peak" region of the collimator opening located along the central axis of the SFRT field and at a depth at

which dose for specific-energy photons are at maximum, D_{max} . Ideally, the peak dose is the same for each of the SFRT beams in the field. Peak dose is critically important to the effectiveness of SFRT treatments and must be carefully considered in the selection or design of a collimator and GRID pattern. Another critical factor in SFRT treatments is the valley dose, defined as the minimum dose measured in the shielded “valley” region, located between two adjacent collimator openings, at the same depth, D_{max} . The peak-to-valley dose ratio (PVDR) is a numerical description of the difference in dose intensity between the dose delivered to an unshielded area, the peak dose, and the dose delivered under a shielded area, the valley dose, at D_{max} [74]. Ideally, the valley dose would be zero; however, in practice the PVDR is maximized for a given peak dose, in order to deliver the lowest possible dose to the shielded areas of the GRID pattern. High PVDR is presumed to maximally spare the negative effects of radiation on skin cells below the shielded regions and enable the repopulation of skin cells in the unshielded regions of the GRID collimator and decrease the severity of possible skin reactions to the treatment and normal tissue toxicities [74]. Decreased time to heal and reduced severity of reactions is a distinct benefit of SFRT therapy, therefore peak dose, valley dose, and PVDR must be designed, measured, and calibrated for effective treatment.

2.2.2 Peak width, valley width, and peak-to-peak distance

Peak width, valley width, and peak-to-peak distance are factors that rely heavily on the design of a collimator/GRID pattern. The peak width is the measured full-width-at-half-maximum (FWHM) of the central SFRT peak located along the central axis of the SFRT field. The peak-to-peak distance is the measured distance between the central SFRT peak and the next nearest peak. In practice, the measured peak-to-peak distance may vary along different axes of the SFRT field depending on the specific geometry of the collimator. For example, in an ideal hexagonally-shaped, or honeycomb-shaped, lattice GRID collimator [75], the peak-to-peak distance between the

central peak and its nearest neighbor along one axis is geometrically calculated to be exactly $\sqrt{3}$ times larger than the peak-to-peak distance between the central peak and its nearest neighbor along the other, orthogonal axis. The valley width describes the overall width of the valley regions of the SFRT collimator and may be calculated as the peak-to-peak distance measurement minus the peak width measurement.

2.2.3 Collimator (or GRID) output factor

The collimator output factor (alternatively known as the GRID output factor) may be described as the ratio of the dose with the SFRT/GRID collimator to the dose absent the collimator at the linear accelerator calibration condition, measured at a given field size. The collimator output factor is a function of field size and photon energy and is an important tool for determining the treatment exposure time for a specific dose prescription. An example output factor calculation for a clinical-type SFRT (GRID) collimator is shown in Figure 2 [74].

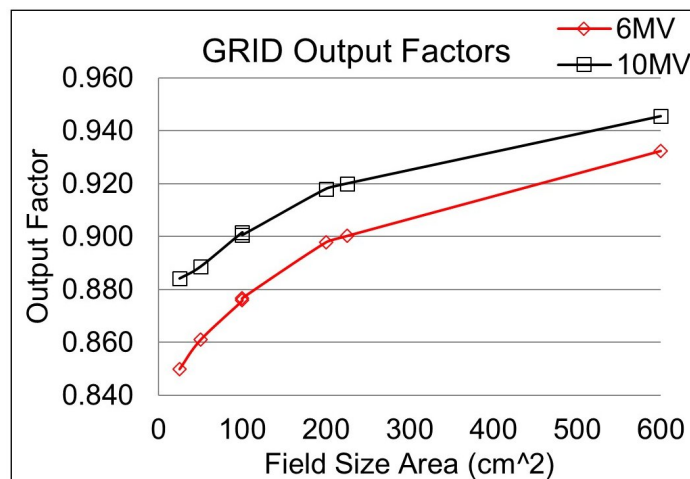


Figure 2: The measured GRID factor as a function of field size, in cm², at isocenter, d=Dmax, for 6MV and 10MV photons on Novalis Varian accelerator using a brass GRID collimator. For a given field size, the GRID treatment dose is calculated using the GRID output factor curve [76].

2.3 The Evolution of SFRT

2.3.1 A brief history of SFRT

Spatially Fractionated Radiation Therapy is an old radiotherapy treatment modality that has been around for over a century, with varying degrees of use throughout that time. Soon after x-rays were introduced for the treatment of malignancies, a growing number of patients began experiencing severe radiation-induced normal tissue toxicities such as skin ulcerations. The low, orthovoltage energy x-rays were heavily irradiating and subsequently damaging the radiosensitive, superficial skin tissues on their path to the tumor [77]–[79]. In addition, the risk for developing a refractory, un-healing skin ulcer was increased when delivering the tumoricidal doses needed to treat very large and very deeply seated tumors. In 1909 Alban Kohler invented a sieve-like iron mesh to partially shield patient skin from the radiation with remarkable success [77], [80]. The skin cells lying directly beneath the iron “sieve” were protected from the high doses of radiation, and this protection promoted skin healing in the unprotected regions [77]–[79], [81]. By the 1930s, this early form of SFRT, known at the time as “sieve therapy” or “GRID therapy”, became a commonly used method for limiting skin tissue toxicities while delivering a high dose of radiation to tumors, and a variety of different types of collimator shapes and materials such as steel, lead, and lead-rubber were utilized [69]. The technique remained in use through the 1950s until the advent of the megavoltage, clinical linear accelerator (LINAC). The LINAC completely revolutionized the way that radiation is delivered, allowing for greater tissue penetration with improved surface skin sparing capabilities than ever before. By the late 1960s, GRID therapy as a treatment modality became largely phased out, and eventually abandoned until a group of physicians and researchers at Thomas Jefferson University Hospital revived the technique in the late 1980s [69], [82].

2.3.2 The modern resurgence of SFRT

The development of clinical linear accelerators undoubtedly benefited hundreds of thousands of patients across the US and the world; however, there remain a host of patients with cancers that do not respond to conventional treatment approaches or for whom these approaches are extremely dangerous. The search for innovative cancer treatment approaches with the potential to significantly increase the treatment therapeutic ratio has sparked renewed interest in SFRT. Physicians and researchers have asked how precise delivery and exact dosimetry in SFRT affect survival, as well as what is needed to significantly improve patient outcomes. Significant resources have been dedicated to these questions, and while specific answers may vary, it is becoming increasingly clear that an improved understanding of radiobiology is necessary to understand the impact of physics on clinical outcomes. Though it has century-old roots, SFRT is a radically different, very promising, and unique treatment approach, which makes studying the radiobiological mechanism behind it very attractive.

2.4 Clinical SFRT

2.4.1 GRID Therapy

In late 1980s, Mohiuddin et al. at Jefferson University Hospital were the first group to revive orthovoltage-style “sieve” therapy and adapt it for megavoltage accelerators for the treatment of very large, deeply seated tumors [82], [83]. They accomplished this by creating a large, square array grid of cylindrical apertures with a 1:1 open-to-closed area made from a combination of stainless-steel tubing and lead alloy [74], [83]. The new “GRID compensator” collimator was then mounted onto a fixed tray in the blocking tray-holder of a LINAC head, and single fields of approximately 10-20Gy dose to Dmax were delivered to patient tumors. Figure 3 shows an example of SFRT dose profiles created using a similar type of GRID-compensator fitted onto a LINAC.

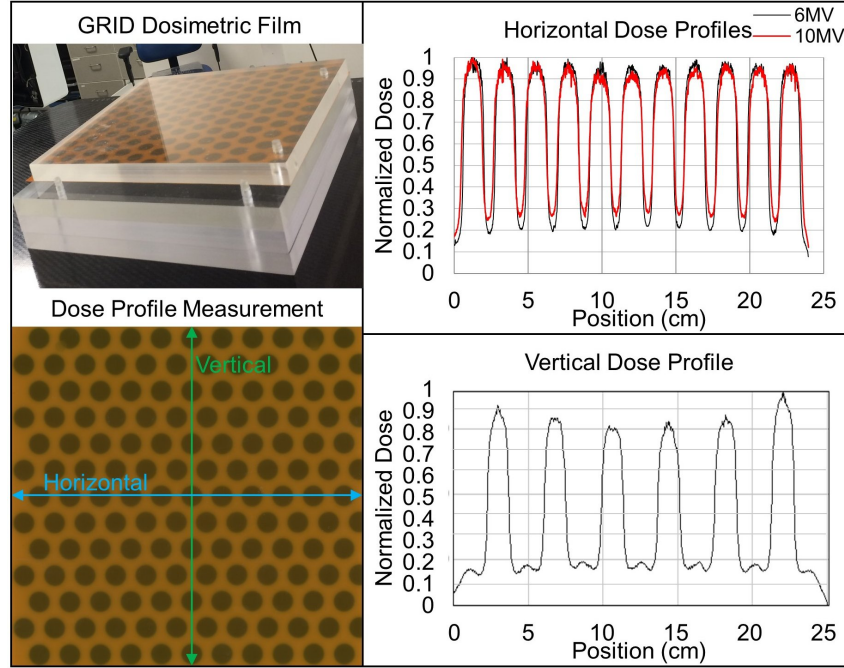


Figure 3: On the left, Gafchromic RTQA-2 film is irradiated, top, and then, bottom. The film density is converted to dose using a film density calibration curve based on ion chamber data. Blue, horizontal, and Green, vertical, lines on film to indicate the location of beam profiles measured. On the right, the GRID horizontal, top, and vertical, bottom, dose profiles are measured at Dmax for 6MV and/or 10MV beams using 25x24cm field size, 100cm SSD and either 1.5cm or 2cm buildup.

Despite these very high single doses of radiation, results using this GRID-compensator type of megavoltage SFRT, now named “GRID radiotherapy”, have demonstrated high rates of pain relief (in up to 91% of patients) with few to no associated normal tissue morbidities [73], [82], [84]–[88], as well as reductions in bleeding [73], [82], and partially-controlled shortness of breath [82]. In addition, reductions in tumor volume were observed in both palliative and definitive treatment settings. In fact, complete tumor control responses were observed when GRID radiotherapy was used as neoadjuvant to conventional radiotherapy, chemotherapy, surgery, or immunotherapy [49], [73], [82], [86]. This improved tumor control is not limited to SFRT; several non-SFRT studies have suggested that high “induction” doses of uniform radiation prior to a conventional course of radiotherapy may result in even better tumor suppression outcomes, though not without significant side effects [89].

This GRID therapy technique has been used for treatment in a variety of sites and specifically for bulky disease, larger than 8cm. Some treatment sites include (but are not limited to) tumors in the extremities [73], [82], [84], the abdomen and pelvis in the case of gynecological, gastrointestinal, and liver cancers [73], [82], [84], the thorax in the case of breast and lung cancers [73], [85]–[87], and notably, in the rapidly proliferating tumor cells common in head and neck cancers [49], [52], [73], [84], [90], [91]. These treatments have all reported good oncological outcomes and few to none reported complications in the short or long term, including to the CNS [73]. Importantly, the GRID therapy treatments targeted advanced, very large disease that has historically been very difficult to treat, especially for patients with recurring tumors, or patients that had already reached the maximum chemotherapy or radiotherapy tolerance dose [82]. Massive, recurring tumors not only have unfavorable tumor histology with limited chemotherapy options, but are also highly vascularized, precluding treatment with surgery due to the risk of uncontrolled blood loss during excision. In addition, traditional radiotherapy has limited impact on radio-resistant tumors and tumoricidal doses do little to spare normal tissues with unacceptably high risks for tissue morbidity [92]. The large size of bulky tumors also makes them unsuitable candidates for treatment with specialized stereotactic radiosurgery [93], [94].

The amazing treatment outcomes reported by Mohiuddin et al in the 1990s sparked a renewed interest in this radically different radiotherapy treatment modality, especially for its potential as an additional tool in the radiation oncologist’s toolbox for treating patients that have exhausted all other treatment options. The overall design principles used in creating the compensator-based GRID therapy have not changed significantly over the last 3 decades. GRID compensators may now be purchased commercially and are customizable to fit a variety of LINAC models for use in clinical SFRT [76], [95].

2.4.2 Advanced clinical SFRT techniques

Beyond customizable commercial collimators, in the last decade researchers have developed additional methods for delivering spatially fractionated radiation patterns to targets. MLC-based GRID therapy uses the multi-leaf collimators (MLCs) that come pre-installed in modern LINAC treatment heads to create spatially modulated beam patterns. This technique was developed in response to the impracticalities of repeatedly installing and removing the heavy (up to 50lbs) GRID-compensator for treatment as well as the fact that SFRT treatments are not optimized, employing a wide range of SFRT pattern geometries [96]–[98]. MLCs allow for greater flexibility in creating different geometric GRID patterns and ease in treatment planning since the dosimetry can more readily be determined within the treatment planning system. However, major drawbacks to MLCs include the limited ability for the large collimator leaves to generate small beam sizes comparable to the pencil-beams generated with GRID-compensators [96]. In addition, MLC-based GRID therapy produces up to 2 rows of spatial modulation at a time, requiring a longer treatment time, which results in a higher surface dose as result of leakage through the MLCs [99].

Both GRID-compensator and MLC-GRID-based SFRT share many of the same dosimetric features, particularly that each delivers a single, high-dose fractionated pattern to tumors, as well as normal tissues, using one (and sometimes two) field(s). To minimize the dose delivered to normal tissues, especially for deeply seated tumors, Helical Tomotherapy or Volumetric Arc Therapy techniques may be applied to simulate a virtual GRID collimator and deliver SFRT to tumors with the advantage of sharp dose fall-offs just outside the tumor treatment volume, avoiding critical structures [100].

The “traditional” GRID-compensator-based radiation dose distribution is fractionated only in the plane perpendicular to the radiation pencil beams (x- and y- axes) and is not fractionated in the direction parallel to the beams (z-axis), where the dose distributions

for each beamlet may be approximated as 2-dimensional gaussians at any given depth in (z), (an example of a 2-D gaussian model shown in Figure 4) [101]. Three-dimensional Lattice Radiotherapy (3DLRT) is a novel spatial fractionation technique which expands the 2-dimensional traditional dose distribution and applies it in 3-dimensions, spatially fractionating the dose distribution throughout the entire 3-dimensional target volume. This technique results in multiple spherical “hot spots” of high doses within the tumor [102]. To date this technique has safely been used in treating large, bulky tumors without observed normal tissue toxicities at doses of up to 18Gy [86]–[88]. The advanced SFRT treatment techniques described above offer additional, potentially life-saving treatments for patients, achieving more normal tissue sparing than ever before with high rates of tumor eradication. However, these advancements would not have been possible without the vast number of preclinical SFRT studies that helped elucidate some of the working mechanisms of the promising treatment approach.

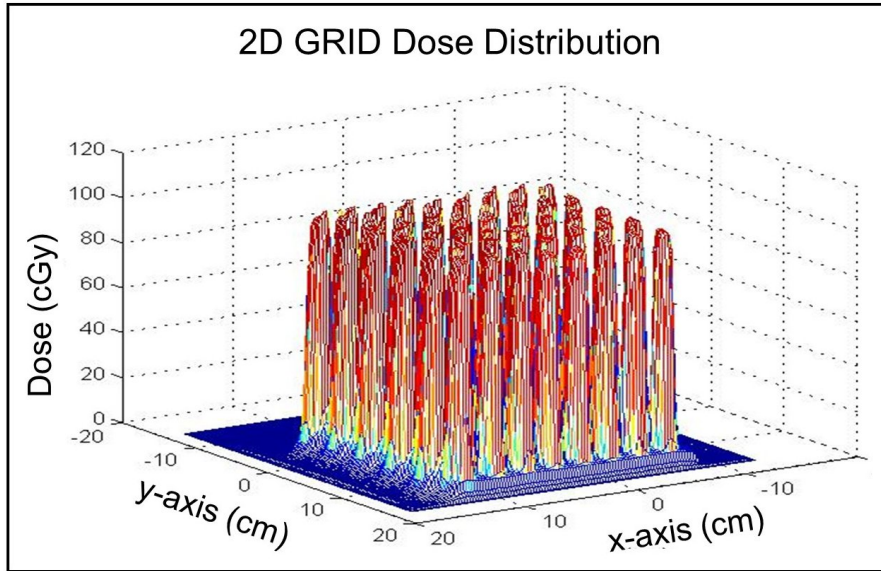


Figure 4: The dose distribution from a GRID-compensator with a “square lattice” pencil beam geometry may be modeled as an array matrix of 2-dimensional gaussians at any given depth in tissue. Image modeled in Matlab [103].

2.5 Preclinical SFRT

2.5.1 Microbeam Radiation Therapy

Spatially micro-fractionated radiation therapy (MRT) is an experimental, preclinical form of SFRT consisting of very high (peak) and very low (valley) doses that are alternated at a high spatial frequency over the treatment volume. Like SFRT, these spatially modulated doses are usually, though not always, delivered as a single field to the treatment volume. However, MRT is distinctly different from SFRT in several ways. MRT typically consists of very narrow, highly collimated planes of radiation, each approximately 20-700 microns wide (FWHM) and between 100 to 4000 microns apart (peak-to-peak distance) [104], [105]. The unique geometry of these micro-planar arrays allows for the delivery of well-tolerated peak doses up to 2000Gy (or higher) for the smallest beam widths [105]–[107]. One example of a multi-slit MRT collimator is shown in Figure 3.

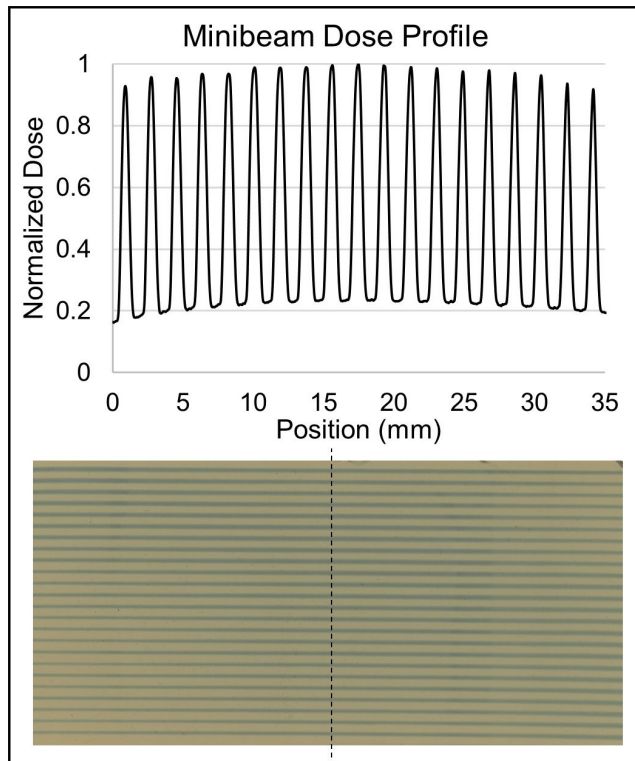


Figure 5: The SFRT Minibeam dose profile measurement, top, is calculated along the direction perpendicular to the beams. For this specific collimator, the minibeam PVDR was 5.11 with peak width = 0.69mm and peak-to-peak distance = 1.87mm. At the bottom, an irradiated EBT-3 film is shown with the dotted line on the film indicate location of Beam Profile. Measurement specifications include 160kVp, 25mA, 0.254mmCu added filtration, 37cm SSD, at 1cm depth.

To achieve these astounding dosimetric values, MRT is typically conducted at synchrotron light source facilities, which are capable of producing brilliant, nearly parallel x-rays, 50-600 keV, with minimal beam divergence and at ultra-high dose rates, 8-16 kGy/second [105]. Placing a multi-slit collimator in the path of the beam results in highly collimated planes of light with very high dose gradients, peak-to-valley dose ratios of up to 56 [104], [106], [107], and that are well-preserved even at depths of 15cm [108].

2.5.2 Radiobiological studies in MRT

Decades of preclinical research have demonstrated that SFRT has the ability to eradicate tumors while simultaneously sparing normal tissues and functions, even when these are

exposed to the same tumor-killing radiation. Preclinical MRT research from the last three decades has demonstrated that these incredibly high doses are very well tolerated for the given beam geometries. Early dose escalation studies investigated heavy cosmic radiation exposure delivered by 25um-wide MRT beams with peak skin entrance doses of up to 10,000Gy to live rodent cerebellums and reported maximum tissue tolerance doses of 5000Gy at the skin entrance, with no apparent histological brain damage reported for doses ≥ 5000 Gy [109]–[111]. In addition, this tolerance dose is several orders of magnitude higher than conventional uniform or even millimeters-wide beams [109], [112] and the tissue-sparing effect increases with increasing distance between beams [109].

These very promising early studies have sparked significant interest in advancing understanding of SFRT through preclinical research. Since then, other preclinical studies have validated the remarkably high tissue sparing effect of SFRT. Studies of CNS tissues irradiated with MRT, between 50-600Gy, have demonstrated extremely high dose tolerances with no long-term observable effects to tissue function or developmental behavior, including in immature embryonic duck brain tissues [113], brains of suckling rat pups [114], weaning piglet brains [115], and rat spinal cords observed without paralysis for over a year [116]. Most recently, highly sensitive testes organ germ cells were irradiated with MRT and showed preserved spermatogenesis [117], [118].

MRT also preferentially kills tumors over normal tissues when exposed to the same radiation doses and with high efficacy. This tumoricidal effect has been demonstrated in a vast number of preclinical small animal studies, with nearly all demonstrating either effective growth suppression or complete tumor eradication in several tumor models [119]; examples include tumoricidal results in very advanced stage rat 9L gliosarcomas [120]–[125], in mouse EMT-6.5 mammary carcinomas [126], in human glioma xenografts in nude mice [127], in mouse 4T1 mammary carcinomas [128], among others. In addition, these studies have been repeated for highly radioresistant tumors such as squamous cell carcinoma VII [129] and radioresistant B16-F10 melanomas in mice [130]. This preferential tissue

sparing effect combined with the high tumor killing efficacy has led to much longer-term survival outcomes compared to conventional, uniform radiation fields at significantly lower doses [121], [122], [131], [132] . Additionally, similar studies examined the effects of interlacing MRT beams for tumor killing and added tissue sparing [133], and then applied this interlacing pattern to suppress seizures [134] as a potential treatment for epilepsy [135].

2.6 Potential Working Mechanisms of SFRT

Radiation does more than just kill cells; it can affect biological processes throughout the body. The radiobiological mechanisms behind the SFRT preferential normal tissue sparing and tumor ablative effects, especially in relation to conventional radiation therapy, are not well understood. Several theories and studies have been developed to help explain some of these mysteries, such as the bystander and system immune effects, the tumor reoxygenation effect, and differential microvascular tissue responses. However, these effects are very complex and are likely inter-related, so studies have had difficulty isolating and determining cause.

2.6.1 Bystander effect

The most interesting mystery in SFRT radiobiology is that although a large portion of the tumor lies within the spared tumor fraction, which is not directly irradiated, tumor growth suppression or outright eradication still occurs in the low dose non-cytotoxic “valley” region, which means cells in the spared tumor fraction are being indirectly killed. This indirect cell killing has been observed in numerous SFRT preclinical and clinical studies and may be attributed to the Bystander Effect, the indirect killing of cells as a result of radiation damage to other, adjacent cells [91], [136]–[138]. In theory, the high amount of direct cell killing within the tumor causes this indirect cell killing response, which may trigger other radiobiological observations, including the induction of cell signaling

pathways and systemic immune (abscopal) effects [139], [140]. Many of these effects may fall under the category of radiation bystander effects and these extended effects are theorized to stimulate physical changes to tumor vasculature, which have been directly observed [141]–[143]. Subsequently, some combination of these effects are likely responsible for changes in tumor volume and eventual eradication.

Some of the potentially important cell signaling pathways that have been induced after SFRT treatment include bystander factors such as TNF-alpha (protein), TRAIL (protein), and Ceramide (lipid). TNF-alpha, TRAIL and Ceramide have all been identified as potential mediators of or participants in the cell killing response (cellular apoptosis) after exposure to high doses of radiation [144]–[146], including high-dose SBRT [147]. In studies of serum samples taken from patients before and after SFRT treatment, TNF-alpha [144], [145], TRAIL [144], and Ceramide [146] induction in the high-dose, unshielded areas of the radiation beam was strongly correlated with increased incidences of partial or complete tumor therapeutic response to the SFRT treatment, and induced pathways may even have played a part in the improved 2-year survival of these patients [145]. Conversely, activity levels for these bystander factors were not elevated in patients whose tumors were unresponsive to the treatment [145], [146]. These observed bystander-type effects have not been limited to the localized, primary tumor treatment. Distant, or “abscopal” systemic, bystander effects have been reported as well, wherein completely unirradiated tumors, distant from the irradiated volume, partially or completely respond to the radiotherapy treatment [49], [91], [136], even in the case of advanced metastatic disease [49], [91]. Further, Tubin et al. reported progression-free disease at least 9 months post treatment with SFRT in 87% of patients [136]. The role of SFRT in tumor oxygenation and, relatedly, the bystander/abscopal effect is under active investigation; however, some of the effects observed include increased oxygenation levels in radioresistant, hypoxic tumors within 2 weeks following treatment with SFRT [128]. This re-oxygenation effect may not be directly involved in tumor-cell killing; however, it may still have therapeutic benefits.

2.6.2 Reoxygenation effect

The interactions between high dose radiotherapy and tumor oxygenation are not well understood. Although tumor oxygenation effects may not directly be involved in tumor cell killing, some clinical outcomes show tumor reoxygenation following SFRT [89] may be exploited as a radio-sensitizing agent, where the addition of oxygen to hypoxic tumors increases the effectiveness of radiation therapy. In addition, targeting only the radioresistant, hypoxic regions of tumors with high doses of radiation similar to SFRT may successfully induce bystander and abscopal immune responses in clinical patients with advanced metastatic disease [136]. In theory, these enhanced bystander/abscopal responses may be due to the combined effect of the very high dose of radiation used [148] and the observed significant increases in bystander and abscopal responses in cases when radiation is targeted to hypoxic tumor cells [149]. However, these effects may depend in part on the initial hypoxic fraction, the % of tumor volume directly irradiated, as well as dose [89].

2.6.3 Differential microvasculature and microenvironmental effects

SFRT also modifies the tumor microenvironment differently than uniform radiation by preferentially damaging or reorganizing the tumor and tumor rim vascular architecture [128], [150], [151], a theory which is supported by increased endothelial apoptosis in tumors [146], [152]; however, these effects may depend on the state of vascular maturation [151], differences in HIF-1 expression, a pro-angiogenic factor and participant in the bystander effect, and which specific tumor model is studied [153]. For example, SFRT has also shown increased tumoral angiogenesis [150], increased tumoral vascular density in radioresistant tumors [150], and upregulated expression of HIF-1 and VEGF, a pro-angiogenic factor [154], [155]. Generally, HIF-1 and VEGF are both associated with tumor progression, tumor angiogenesis [156], [157], and promoting oxygen delivery to tumors [158], [159],

though over-expression of HIF-1 may correlate with treatment failure and increased patient mortality [153]. In MRT, hypoxia is associated with increased HIF-1 and VEGF expression, and may lead to tumor cell protection from apoptosis and tumor radio-resistance [155]. Conversely, VEGF inhibition may decrease tumor blood vessel density and increase tumor hypoxia following high-dose radiation [160].

2.6.4 Dose-volume effect

An additional potential working mechanism that may help to explain the tissue sparing effect of SFRT is the dose-volume effect. The dose-volume effect in tissues is where the tolerance dose of a given tissue is strongly correlated with the irradiated volume of that tissue. In SFRT this may play a role to partially explain the treatment effects. For example, in an MRT study researchers varied the spacing between radiation beams, from 50 to 100 μ m, delivered to intracranial rodent tumors to determine peak-to-peak distance impact on survival. The resulting median survival for all rodents in the larger beam spacing was more than double that of the smaller width used [113]. This indicates that increasing the distance between beams not only allows for improved animal survival, but also allows for higher tumor peak doses while minimizing the skin dose and improving the skin sparing effect. This dose-volume effect may help partially explain the normal tissue sparing effects seen in SFRT treatments; however, the overall working mechanisms behind the radiobiological outcomes of SFRT largely remain unclear.

This discussion presented several examples of some of the potential working mechanisms behind SFRT and demonstrated their complex interconnectedness. Although each of these individual radiobiological effects may potentially impact the tumor response, it is unlikely that they act independently. In fact, these radiobiological effects are not unique to SFRT. However, SFRT uniquely combines multiple radiobiological mechanisms, and it is the complimentary nature of these effects, each working in unison to induce the observed tumor control and tissue sparing, that makes SFRT exceptional.

2.7 Challenges to Clinical Translation

There are many challenges impeding the widespread clinical translation of SFRT. Although SFRT treatment technology has been around for decades, it remains relatively poorly understood, and a lack of preclinical SFRT research on varied animal models and cancer types remains a serious obstacle. A review of MRT preclinical research showed that while nearly a hundred experimental animal studies have been completed, nearly 60% are in a single rat model of 9L gliosarcoma and about 33% are in other murine models of only a handful other types of cancer [119]. The use of so few severely limits our ability to characterize the effects of SFRT treatment, so more and different types of animal and cancer models desperately need be studied in preclinical SFRT. In addition, the pace of research output, as measured by the number of MRT-specific papers published, is exceedingly slow, peaking at 11 publications at one year, but usually only about 5 per year [119]. Furthermore, the working mechanisms behind this technique need further investigation, including SFRT's systemic immune stimulation effects, radiation-induced bystander (abscopal) effects, altered cell signaling that induces indirect cell death, and changes to the tumor micro-vasculature or micro- environment. In addition, some SFRT studies have shown synergy or success with other treatments, such as anti-cancer immunotherapy and chemotherapy, which both deserve further investigation with neoadjuvant SFRT.

Solving some of the dosimetric challenges faced in SFRT may improve the pace of preclinical research. MRT dosimetry in particular is challenging due to due to the high dose gradients, sub-millimeter sized widths of the microbeams, and a lack of dosimeters available with the spatial resolution necessary to measure them [161]–[164]. A number of dosimeters have been developed or tested for application in MRT with these specific dosimetry needs in mind, including novel Ge-doped silica fibers for thermoluminescence measurements of dose [165], MOSFETs [108], [166], thermoluminescent dosimeters [164], radiochromic film [167], [168], and related advancements in Monte Carlo dose simulations

[108], though their success has varied. Beyond dosimetry, accurately positioning tumors and organs under the MRT beams is often challenging and has led to developments in image guidance [169] techniques and optical CT [170], [171], as well as the use of g-H2AX as a marker for dose deposition in rodent brains for post-vivo analysis of treatment and positioning accuracy [172].

One of the potential keys to unlocking our understanding of SFRT may involve large-scale studies examining clinical treatment outcomes as a function of specific SFRT parameters, fractionation patterns, dose prescriptions, etc... SFRT is not a well-characterized and all researchers and clinicians apply it differently. Very few studies have looked at SFRT pattern optimization, which can vary based on desired outcome (destroy tumor, induce inflammatory response, etc) [98]. However, even if such a study was attempted, understanding how to interpret the impacts would be a difficult undertaking as human patients are highly variable; different ethnic and socioeconomic backgrounds, ages, gender, and other relevant factors in human patients may play a role in treatment outcome and should be considered in data collection methods. As with any new or not well-understood treatment, there is a fear of potentially inducing negative short- or long-term effects in patients. This fear is rightly justified. More conventional radiotherapy temporally fractionates high doses, delivering only very small doses daily over several weeks and at multiple entrance sites, while SFRT is characteristically delivered as a single, very high dose to the treatment volume, intentionally irradiating normal tissues lying directly in the beam path along the way. Any miscalculation or setup error could lead to unintended, potentially disastrous effects to the patient such as accidentally delivering a very high single dose to an at-risk organ or other critical structure. However, with the advent of the novel 3D Lattice therapy that delivers a high, spatially fractionated dose within the tumor only and at multiple angles around the patient's body, hesitation to use SFRT may soon change as recent studies using these techniques have resulted in very positive patient outcomes [86]–[88], [173] [xxx].

With a century-old history of treating tumors, and a resurgence of interest from modern research, Spatially Fractionated Radiation Therapy (SFRT) has potential cost-reducing benefits as well as the potential to serve patients who are not eligible for conventional cancer treatments. SFRT also has several unique benefits from multiple complementary radiobiological effects, including a network of bystander factors, distinct vasculature response, and re-oxygenation of hypoxic tumors. Though SFRT researchers face many technical and general challenges, including a lack of preclinical research on varied models in the literature, the next chapter will address the specific difficulties faced in this research through applied engineering, physics, and unavoidable trial-and-error.

CHAPTER 3: DEVELOPMENT OF PRECLINICAL SFRT DELIVERY SYSTEM

3.1 Introduction and Motivation

Decades-long research in SFRT has demonstrated the ability to eradicate tumors while sparing normal organs exposed to the same radiation. However, SFRT remains relatively poorly understood and many challenges impede its widespread clinical translation. One of the potential keys to unlocking a better understanding of SFRT technology may lie in the small-scale, preclinical research designed to examine the new radiobiology observed in SFRT. However, there is currently no commercially available microbeam radiation therapy (MRT) treatment system and, as such, the pace of preclinical research progress is slow. Hence, there is a need to develop SFRT-tech using existing small animal RT irradiators.

3.1.1 Synchrotron-based MRT

To this end, Microbeam Radiation Therapy (MRT) technology is a novel form of SFRT consisting of very narrow, highly collimated microplanar arrays of radiation, approximately 20 – 700 μm wide, delivering alternating high and low radiation doses at a high spatial frequency over the treatment volume [104], [174]. The majority of MRT research is conducted in synchrotron facilities, particle accelerators that use very high-energy electrons travelling at or nearly the speed of light in a large closed-loop that is approximately a kilometer in circumference [105], [175]. The unique physics intrinsic to a synchrotron light source results in a very intense and highly brilliant biomedical radiation beamline capable of ultra-high dose-rates on the order of hundreds of Gray per second [105]. These ultra-high dose-rates result in radiotherapy treatment times of fractions of seconds [105]. Furthermore,

synchrotron-MRT involves a unique geometry where the synchrotron light source is a very large relative distance (approximately 40 meters) from the MRT collimator, thus closely mimicking an ideal point source. This results in highly collimated, nearly perfectly parallel set of micro-planar arrays of radiation with very sharp edges [174][xxx] that may be adjusted to be anywhere between just a few microns in width up to several-hundred microns width [107].

This highly specialized treatment technology has opened new doors to understanding SFRT; however, these magnificent, extremely small and non-divergent beamlets of radiation delivered at ultra-high dose rates come with several inherent limitations and achieving a successful MRT treatment at any of these facilities is no small feat. The unique physics and geometry of synchrotron-based MRT require complex dosimetric techniques and unique technologies to achieve that are not readily available to a majority of researchers [176]. Investigations involving synchrotron-MRT are extremely expensive[177]; each of these facilities may cost many millions of dollars to build and significant manpower to operate [178]. In addition, since there are only a handful of synchrotron facilities around the world equipped to perform MRT research, synchrotron-MRT investigations are also geographically inaccessible to a majority of investigators.

3.1.2 Non-Synchrotron-based MRT using compact irradiators

To help combat the technological and monetary barrier to preclinical MRT research, there has been a recent move to develop low-cost MRT-treatment machines that are much more compact and therefore, more easily accessible for preclinical studies and patients [176], [179]–[181]. There is currently no commercially available microbeam radiation therapy (MRT) treatment system. To help increase the pace of this exciting research, a handful of investigators, including ourselves, have taken to developing our own non-synchrotron-based, low-cost MRT-treatment technologies.

One such research group at UNC-Chapel Hill has developed the first MRT-system

made up of miniature x-ray tubes using a unique carbon nanotube (CNT) design. Researchers Zhou and Chang at UNC-Chapel Hill developed and patented a novel compact MRT-treatment delivery system with built-in CT imaging that used this CNT field emission technology to produce highly collimated micro-beamlets of radiation[179], [182]. This system utilizes an array of CNTs as the “cold” cathode to emit electrons under a bias electrical field at room temperature [179]. This technology has successfully been used to image and then treat hundreds of small animals with remarkable tissue sparing and imaging results [176], [183], [184]. A handful of other researchers have developed desktop SFRT research irradiators by modifying existing small animal research irradiators and demonstrated their feasibility for conducting preclinical MRT research [180], [181], [185], [186]. By placing a multi-slit collimator in the beam path between the source and the animal, then aligning the target (tumor or other animal part) very close to the collimator exit, they have been able to produce beam arrays with peak and valley beam widths sufficiently collimated for MRT research and have achieved geometries on the order of hundreds of microns, known as Minibeam radiotherapy (MBRT).

Several major limitations are associated with non-synchrotron-based MBRT research including inherently low dose-rates and long treatment exposure times compared to synchrotron-based MRT [179]. When combined with the animal anesthesia exposure time limitations, the low dose-rate of non-synchrotron MBRT place an upper limit to the achievable peak dose that may be delivered. Further, the long exposure times may result in radiation off-target effects, where peak “broadening” (or blurring) occurs due to respiratory and cardiac motion [104]. While the beams used in MBRT are slightly larger than for synchrotron-MRT, dosimetry remains a challenge. While none of these research irradiators can reproduce the distinct geometry and dosimetry possible using synchrotron technology, these alternative methods for producing SFRT-beams provide additional, unique, low-cost opportunities for furthering SFRT preclinical research [186]. The widespread availability and far-reduced cost of small animal irradiators makes them

a very attractive resource. Using a conventional research irradiator and modifying it to produce preclinical SFRT-treatment capable beams, we create a low-cost, accessible alternative to investigating SFRT in a variety of radiobiological applications and scenarios.

In this chapter, I will focus largely on SFRT technology development using a commercial research irradiator as well as on resolving some of the dosimetric challenges that require novel approaches for measuring dose. Further, I will address some of the unique considerations and challenges in designing spatially fractionated radiation fields and will validate their experimental treatment accuracy and uncertainty. In this dissertation work, I do not intend to replicate the superior synchrotron-specific dosimetry, but rather, show that the SFRT beams generated using commercial research irradiators may achieve similar radiobiological responses in tumor and normal tissues as their synchrotron-generated counterparts. Therefore, by developing our own SFRT-treatment system, we take a crucial first step towards investigating the effects of spatial fractionation in living systems and, hopefully, advance preclinical research in the process.

3.2 SFRT Treatment Delivery System and Design

3.2.1 Overview

The primary goal in this chapter is to develop a novel small animal treatment system capable of delivering a variety of unique spatial dose distribution profiles from sub-millimeter-sized beamlets of radiation to seamless conventional radiotherapy patterns, intended for delivery to solid tumors in small animals. These fractionation patterns are carefully designed such that a specific peak/integral dose, valley dose, peak and valley width, dose-rate, dose-profile, and percentage of tumor coverage are achieved for the intended radiobiological outcome studied. I solve the unique physics and dosimetric challenges for measuring dose in each of my SFRT collimators using novel approaches. Finally, I will address the unique considerations and challenges to designing spatially

fractionated radiation fields, and then will validate the experimental treatment accuracy and uncertainty for these challenges.

I will modify a commercially available XRad-320 research irradiator [Precision XRay, Inc., North Branford, CT] to accommodate the specialized the SFRT-treatment system for small animals. This involves many unique inter-related design considerations, including physics, geometry, and animal design-related issues, each of which present a unique set of challenges. For example, beam spreading is one of the major challenges in SFRT-treatment design with three major causes: geometry, radiation physics, and animal motion. Throughout this chapter I will address each challenge or limitation as I come across them and describe solutions developed to overcome them.

3.2.2 Physics considerations- energy and filtration

Physics considerations are an important component of the SFRT-delivery system design. For example, the tube potential, the electrical potential difference, or voltage, applied between the anode and cathode components of the x-ray tube, used during treatment has a downstream effect on resulting beam dosimetric profiles and on the patient normal tissues and organs at risk, such as the skin. In any x-ray tube, electrons are accelerated from the cathode through a vacuum up to a high energy, then strike a target material, the anode, wherein the production of x-ray photons occurs [187]. The tube potential essentially defines the energy of the x-rays produced. Inherently, this process produces photons in a range of energies and types, rather than photons with uniform parameters. Bremsstrahlung photons, for example, are emitted from the x-ray tube and consist of a broad, continuous energy spectrum, up to the maximum accelerated electron energy used. Furthermore, a unique set of target material-dependent characteristic x-rays with specifically defined energies are produced. Any material placed in the path of the photons between source and detector will attenuate photons to a degree, which is dependent on the material composition and thickness. However, lower energy photons are preferentially

attenuated due to their higher interaction probabilities with in-path materials. On the other hand, higher energy photons have significantly lower interaction probabilities for these same materials. In practice, skin is a nearly unavoidable in-path material, which can lead to skin toxicity damage.

To enhance skin sparing during treatment, physics photon attenuation principles may be exploited by preferentially filtering lower energy photons that would otherwise deposit their energy at the immediate skin surface, or at 0cm depth. Known as beam hardening, specific materials and thickness, such as those shown in Figure 6, are chosen to filter these lower energy photons to maximize the photons that are directly contributing to the dose delivered to the target, while simultaneously minimizing the energy deposited at the skin surface. These factors must be taken into careful consideration during the treatment design.

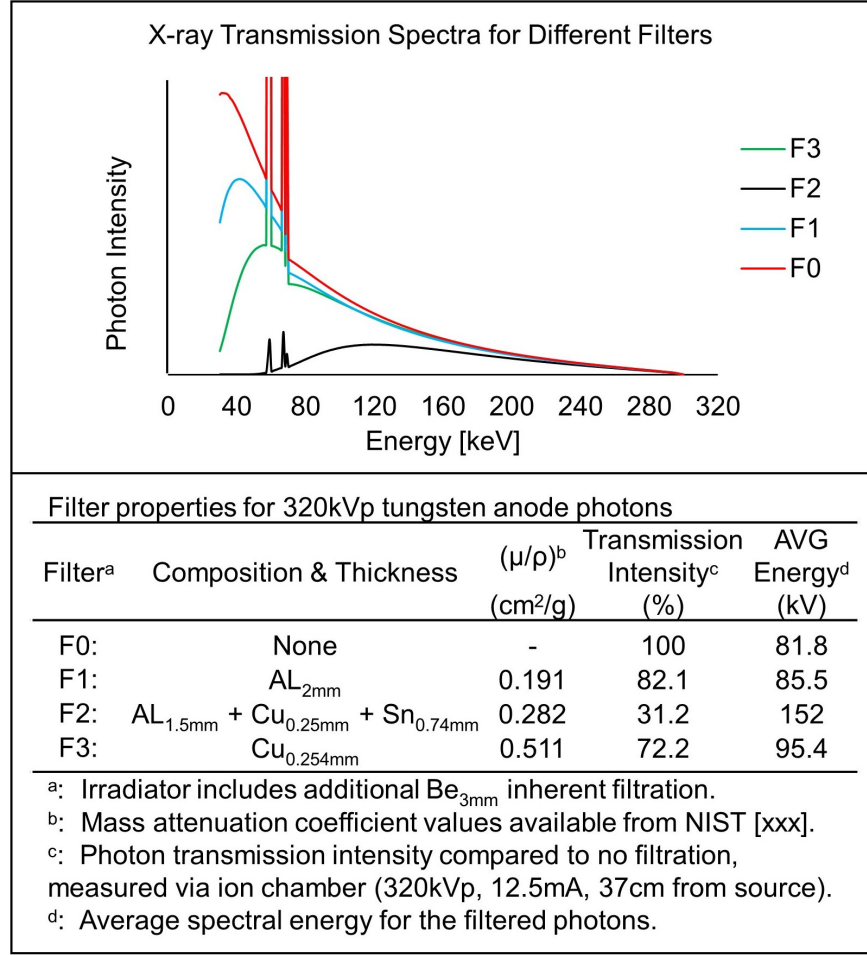


Figure 6: The x-ray transmission spectra through different filtration materials is shown, above. The table, below, show the specific properties for 3 different types of filters used with the X-Rad 320 Irradiator . Each filter attenuates x-rays differently, allowing for varying degrees of photon transmission through the filtration material. These unique, material-specific properties may be exploited to maximize tissue sparing in small animal studies and are taken into consideration in the SFRT system design. Mass attenuation coefficients from NIST Database [188].

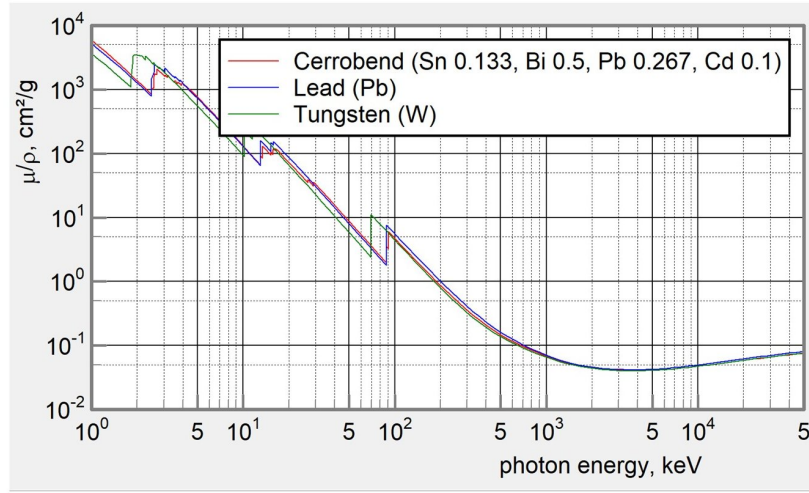
Figure 6 shows a few properties of different filters that are useful for the range of energy photons produced by the x-ray tube and that may be used in the SFRT-delivery system. Among these properties are the type of filter material used, the filter thickness, the mass attenuation coefficients (a measure of the ability for the material to attenuate radiation) of each filter, the specific fraction of the incident x-ray beam intensity that is attenuated for each filter, as well as the approximate average photon energy of the resulting transmitted

x-rays. Compared to the filter-free measurement, each of the different filters produce vastly different degrees of photon attenuation. The right-shifted spectra following the addition of the different filters shows the preferential attenuation of the lower energy photons, photons that would otherwise play no role in the overall dose deposited to the treatment target. In addition, these resulting average spectral energies have an important role in approximating the amount of dose that is absorbed by the target tissue and is discussed in detail in the Dosimetry Section 3.3.

3.2.3 Physics considerations- radiation shielding

From a radiation safety design perspective, we want to shield everything that is not the intended target of treatment, such as the animal's healthy tissues or sensitive electronics, to minimize unnecessary exposure to the electromagnetic radiation. All materials placed between the source and detector attenuate radiation differently. Less attenuative materials require additional thickness, often several orders of magnitude thicker than others, to achieve the same total attenuation. Since the probability that a photon travelling a set distance will undergo any scattering or absorption interaction in a medium is directly correlated to its initial energy, more energetic photons require additional shielding (or denser radiation absorbers) to achieve the same overall exposure underneath the shield.

In our studies we largely attenuate radiation with Cerrobend (Bolton Metal Products Co., Inc, PA, USA) (Tin 13.3%, Bismuth 50%, Lead 26.7%, Cadmium 10%) due to its high attenuation coefficient and ease of use (see Figure 7). Comparable to lead, Cerrobend attenuates photons well and is convenient in radiotherapy treatment applications as it can be used to make custom-shaped apertures and blocks. A eutectic alloy, Cerrobend has a low melting point, below that of water, and is firmer than lead at standard temperature and pressure. However, even in solid form it is easily prone to damage.



Specifications for Different Shielding Materials

Shielding Material	Melting Point (°C)	Density (g/cm³)	$\mu/\rho _{320\text{kV}}^b$ (cm²/g)	$\mu/\rho _{95\text{kV}}^b$ (cm²/g)	Yield Strength (MPa)
Lead (Pb)	327.5	11.34	0.36	6.37	19
Tungsten (W)	3422	19.35	0.29	5.1	750
Cerrobend® ^a	70	9.4	0.31	5.42	26.2

^a: Cerrobend®, also known as Bolton 158 or Wood's Metal, is an alloy with % composition (Sn 13.3%, Bi 50%, Pb 26.7%, Cd 10%)

^b: Total material attenuation coefficients calculated for 320kV (peak keV energy of photons produced by x-ray tube) and 95kV (mean of their bremsstrahlung energy spectra).

Figure 7: At the top, a table of several specifications are shown for the three different shielding materials used to block the 320kVp photons in our SFRT delivery system. Each material is weighted against the other in terms of its ability to attenuate photons effectively, its ease of use for creating custom shapes, and its ability to withstand repeated use without deformation. The figure below shows the mass attenuation coefficients for each of the shields across a wide range of energies, calculated using XMuDat Photon Attenuation software [189].

In terms of collimator aperture design, we use shielding materials that maximize photon attenuation while allowing the flexibility to create specific collimator shapes. In most cases our collimator apertures are made of either Cerrobend or lead. However, in the case of our smallest slit collimators for creating submillimeter sized beams, we use Tungsten due its combined high attenuation coefficient and material strength to withstand daily, repeated use without risk of aperture deformation.

3.2.4 Geometric considerations

A variety of different SFRT and seamless broadbeam collimators are carefully designed to meet specific SFRT characteristics for each of our radiobiological studies. Such characteristics include peak dose, dose-rate, dose-profile, overall tumor coverage, peak-to-peak (P-P) distances, the peak width (full-width-at-half-maximum or FWHM) for the SFRT collimator peaks, and their valley widths and doses. Several physics and geometric factors play an important role in SFRT collimator design. One design element includes creating radiation beams with very high dose-gradients at the edge of the radiation beam field, called penumbra. Since the beam penumbra contributes to valley dose (dose located directly under the collimator) as well as the peak width (the FWHM of the beam), sharpening the beam penumbra is a very important. In an ideal point source (where the source-to-skin distance is significantly greater than the source width), the radiation beams would be nearly step-wise, with very narrow penumbra. However, given that the radiation source in the XRad irradiator is 8mm-wide and effectively not a point source, collimating the radiation field results in wide geometric penumbra.

Figure 8, on the left, shows a point source of radiation compared to a wide source and the resulting wide penumbra S_1 . The geometric penumbra width increases with distance between the collimator and the detector (or skin); therefore, we minimize this penumbra and sharpen the beam edges by decreasing the collimator-to-skin distance (CSD) and positioning the detector (or skin) as close to the collimator exit as possible (shown by position S_2). In addition, reducing the CSD in position S_2 of Figure 8 also increases the dose-rate of the beam, a side-effect of reducing the photons' geometric attenuation (by decreasing the overall source-to-detector distance) (see Footnote¹). However, the beam

¹Supposing we draw a straight line from the source through a slab of material with attenuation coefficient (μ) of thickness (t) to the radiation detector, the total number of photons that reach the detector without interaction make up the uncollided dose $D^o(r) = \frac{S_p R(E)}{4\pi r^2} \times e^{-\mu(E)t}$, where the total *material attenuation* is $e^{-\mu(E)t}$, the *geometric attenuation* of the photons radiating outward from the point source is $\frac{1}{4\pi r^2}$, and R is the dose air-to-tissue conversion coefficient for the detector [190].

penumbra width is also inversely proportional to the source-to-collimator distance (SCD); therefore, increasing the SCD as much as possible will decrease the geometric penumbra width as well as the dose-rate. As discussed previously, the number of photons that penetrate the attenuating medium (collimator in this case) is a function of the attenuator thickness. Figure 8, on the right, shows that photons that are not completely attenuated by the collimator, known as transmission penumbra, may also contribute to the beam penumbra and the valley dose. Increasing the collimator thickness reduces the number of photons directly underneath the collimator, both in the sharpened geometric penumbra and the reduced number of transmission photons and therefore minimizes the valley dose. As can also be seen in Figure 8, reducing the collimator separation as well as increasing the collimator width will also help minimize the number of photons that contribute to the valley dose. Although intended to reduce valley dose, this effect has a distinct disadvantage; both reducing the collimator separation and increasing the collimator thickness also lower the peak dose rate of the resulting beams.

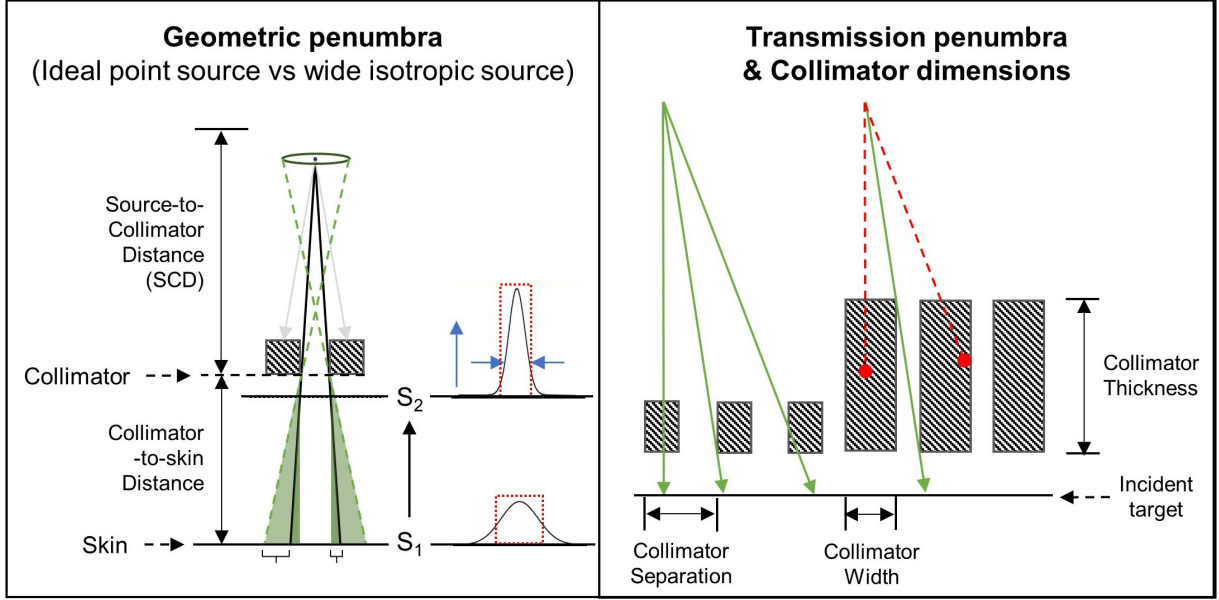


Figure 8: This schematic drawing illustrates the effects of SFRT collimator design on the resulting *geometric penumbra*, on the left, and the *transmission penumbra*, on the right, of the resulting SFRT beams. *Geometric penumbra* may be minimized by maximizing the source-to-skin distance while minimizing the collimator-to-skin distance, shown in the figure as positions S_1 and S_2 . The *transmission penumbra* may be minimized by increasing the collimator thickness as well as the collimator width.

To maintain peak dose rates and other SFRT-treatment requirements, other geometric design factors must be considered, including solid angle and source-to-collimator distance (SCD). Increasing the collimator thickness and decreasing collimator separation has the intended effect of attenuating photons that travel at an oblique angle from the source to the detector (or skin). The solid angle subtended by the span of the collimators from the source is dependent on the source-to-collimator distance (SCD). At large solid angles, this geometry may limit the span of the beams (the total number of beams) that may be generated. Since treatment areas may be as wide as 2cm in diameter, significantly larger than the x-ray source, it is very important to increase the span of the beams as much as possible to achieve complete target coverage. Increasing the distance between the source and collimator (SCD) is an effective way to decrease the solid angle subtended by the span of the collimators and therefore increase the overall span of the SFRT beams. However, this

has the unintended effect of also reducing the dose-rate of the SFRT beams via geometric attenuation (see Footnote1.) Therefore, SFRT collimators need to be positioned such that they are optimally situated between the radiation source (focal spot of the x-ray tube) and the target through a combination of careful collimator positioning, trial and error, and testing.

SFRT collimators are carefully designed in the hope of yielding specific treatment outcomes. To this effect, achieving specific SFRT characteristic dosimetric parameters requires a thoughtful balance of collimator aperture width, thickness, and separation, among other parameters. Figure 9 shows an example SFRT collimator configuration that was rigorously designed to achieve specific peak dose and width, valley dose and width, peak-to-valley dose ratio, percentage of tumor directly irradiated, and other parameters that are discussed in great detail in Chapter . This collimator was created by pouring heated liquid Cerrobend into a 20x20x1cm mold and then manually drilling aperture slits and a circular 1cm diameter cross-section hole to fit an endoscopic camera.

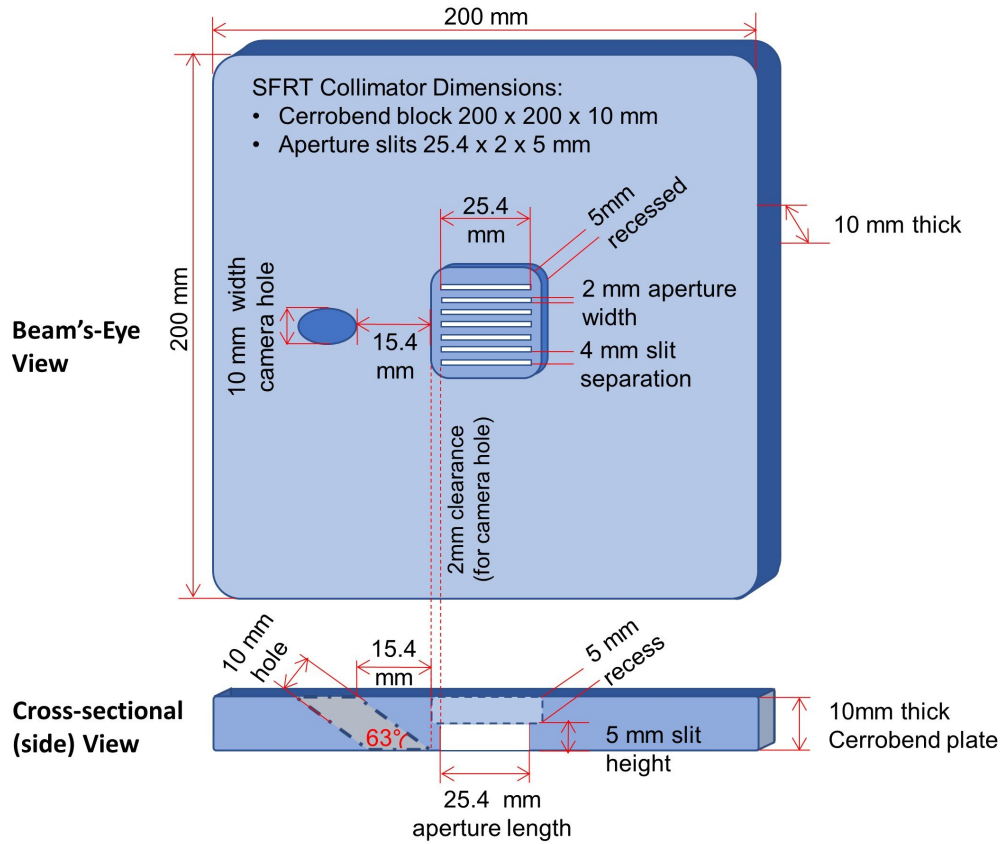


Figure 9: The schematic above illustrates an example of a SFRT-Minibeam style collimator that was carefully designed with all physics and geometric considerations mind. In addition, a 1cm bore hole was drilled into the collimator at a steep, 63-degree angle for insertion of a PC-linked camera. The steep, 63-degree camera viewing angle allows for collimator-to-target alignment, discussed in detail in Section 3.2.5.

3.2.5 Animal considerations

Animal welfare must be carefully considered as an essential part of any radiotherapy treatment design. Using live animals in radiobiological studies adds several additional requirements, both institutional and practical, that must be made before performing any radiotherapy treatments. As such, all protocols are approved by Institutional Animal Concerns and Use Committee (IACUC) and all recommended NIH guidelines are strictly followed to ensure that animal welfare remains a top priority in all studies.

The dose to surrounding non-targeted normal tissues should always be minimized

for any given radiotherapy treatment; however, preventing radiation toxicity-triggered euthanasia is especially vital in longitudinal studies where the long-term survival of the animal is critically important to completing the study. The sub-millimeter geometry of the SFRT beamlets not only makes them very difficult to align with the treatment target (usually a tumor), but it also makes minimizing the dose delivered to surrounding normal tissues in the region increasingly challenging. To overcome these positioning challenges, we created a treatment system that includes two cameras as well as an animal/target height- and angle-positioning platform, shown in Figure 10.

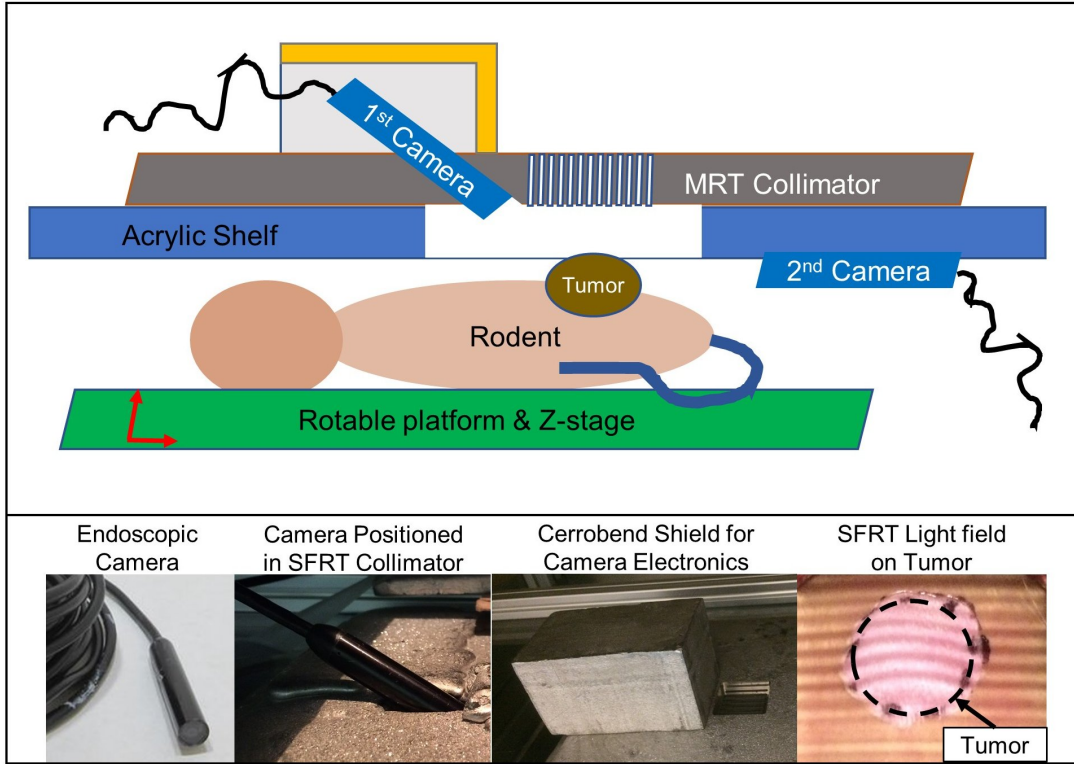


Figure 10: The SFRT delivery system includes two cameras, one for animal monitoring during treatment, and the other for beam-to-animal alignment aided by the rotatable, height-adjustable platform. Large cerrobend blocks shield the animal and electronics from unintended irradiation. The cerrobend shields, collimators, electronics, and other equipment are supported by a 1cm thick acrylic shelf that is cut to fit the length of the irradiator and that has a large square hole drilled through the center for photons to travel unimpeded from the collimator to the animal. In addition, the shelf is reinforced lengthwise with two anodized aluminum 80/20 T-slot bars [80/20 Inc, Columbia, IN, USA], a type of high strength(yield strength 35,000 psi), light-weight metal [191].

During animal treatments, the animal platform is positioned downstream from the stationary collimator and shielding blocks, and the position of the SFRT collimator with respect to the x-ray source is determined via the built-in light field of the XRad irradiator. A small hole through the Cerrobend shield near the collimator exit is fitted with a PC-linked endoscopic camera. The resulting live video feed provides a beams'-eye-view of the target during alignment with the radiation light-field. In addition, each animal is fixed to a height-adjustable rotatable platform and angled with the radiation light field in such a way that normal tissues lie beneath the Cerrobend shielding and are maximally spared.

The small beam widths of the SFRT collimators makes the resulting beams especially prone to beam spreading due to motion blur; therefore, animals are rendered immobile and fixed to the rotatable platform throughout treatments. To minimize stress to the animal during the procedure as well as to reduce animal motion, all irradiations are performed under anesthesia, typically continuously-delivered vaporized isoflurane. Delivering anesthesia safely requires continual animal monitoring as prolonged exposure to isoflurane anesthesia may result in respiratory and cardiac depression as well as hypothermia and hypoglycemia [192]. Shown in Figure 10, the SFRT treatment setup includes a second camera for post-alignment monitoring of the animal's respiration, since change in respiration may be an early indicator of potential problems during treatment. For example, animal respiratory rate and depth may be determined by observing chest wall motion, where 10-40 breaths per minute is the expected normal range when the animal is exposed to the recommended isoflurane anesthesia flow rate of 1.5 liters/min oxygen mixed with 1.5% isoflurane [193]. As the depth of anesthesia increases, the respiratory rate and volume will decrease; however, abnormally low respiratory rate ($< 8 - 10$ breaths per minute) may indicate that the anesthetic level is too high and needs to be reduced [193]. Conversely, an elevated respiratory rate is the first sign of animal arousal from anesthesia, which may impact radiotherapy treatment delivery due to motion.

The low dose-rates of the SFRT beams may result in relatively long radiation exposure

times which translate into long periods under anesthesia for the animals. For animal anesthesia exposures lasting longer than 10 minutes, animals are susceptible to body temperature depression. Temperature depression is mitigated via a heat source placed underneath the animal, such as an externally controlled, electronic heated platform. For any radiotherapy treatment involving the use of vaporized isoflurane, an anesthesia scavenger should be included in the anesthesia setup to remove the vented gas from the irradiation chamber. In addition, longer exposure times may result in exhaled anesthetic gas or anesthesia rodent nose cone leakage buildup in the irradiation chamber during course of treatment. For irradiations lasting longer than 20 minutes, an active (electric) scavenger is highly recommended as it is the most effective method for removal of anesthetic waste gas. Figure 11 shows the electronics components of an electronic heated platform that maintains the animal body temperature at a constant 38.2 degrees Celsius, as well as an active scavenging unit that suctions airflow from waste anesthetic gas and then passes it through an activated charcoal canister to adsorb the toxins before discharging the cleaned air back into the room. These precautions are especially important to maintain animal welfare during and after treatment, as well as ensure the effectiveness of said treatment.



Figure 11: The animal body temperature is maintained via an externally-controlled electric heating pad, external electrical component shown, and an anesthesia active scavenger is used to draw anesthetic waste gas from the irradiation chamber.

3.3 Machine Specific Dosimetry

3.3.1 Equipment for measurements of exposure

The radiation output and quality of x-rays in a given machine may be highly susceptible to minute changes in the x-ray tube. Ensuring the stability and reliability of the machine x-ray output under standard operating conditions are critical in our SFRT experiments to ensure that the treatment dose is delivered to the target as intended. Therefore, we perform a series of extensive machine output measurements for quality assurance testing as a standard practice and first step prior to adding an SFRT collimator for small animal dosimetry.

The radiation output of the machine may be measured in terms of *exposure*, or the amount of ionization the radiation produces in a volume of air. Under charged particle equilibrium conditions (see footnote1), an *ion* chamber may be used to measure radiation exposure, where a voltage potential, applied between two electrodes in the ion chamber

with an incremental volume of air, measures the total charge (C) generated by the ion pairs that are liberated and completed stopped in air, per unit mass of air (kg) (or $2.58 \times 10^{-4} C/kg$) [190]. These exposure measurements may also then be used to calculate absolute dose, discussed in Section 3.3.2.

We used several different ion chambers throughout our studies; however, the calibration for each may be traced to a national Accredited Dosimetry Calibration Laboratory (ADCL) traceable to the National Institutes of Standards and Technology (NIST), as recommended [194], [195]. Furthermore, each measurement was verified with a second, independent source whenever possible for enhanced measurement confidence. When measuring the XRad machine output, we used an ion chamber from Duke University's Radiation Dosimetry Laboratory and cross-calibrated it against an ion chamber in the Department of Radiation Oncology at UNC Chapel Hill. In addition, all measurements are corrected for differences between ion chamber calibration conditions at the ADCL and any changes in measurement conditions. The fully-corrected ion chamber reading, M , then is calculated as follows:

$$M = M_{raw} \times P_{TP} \times P_{ion} \times P_{pol} \times P_{elec}$$

, where M_{raw} corresponds to the Raw, uncorrected ion chamber reading, chamber corrections for temperature and pressure (P_{TP}), ion recombination (P_{ion}), polarity effects (P_{pol}), and electrometer accuracy (P_{elec}) [194].

Prior to measuring machine output, we take a measure of the ion chamber dark current (the residual current in the device without the presence of ionizing radiation), to ensure the ion chamber itself does not affect reading results. Shown in Figure 12, measurements of the ion chamber dark current are on the order of tens of milliRoentgen (mR), a negligible amount as the machine output readings expected are on the order of hundreds of R.

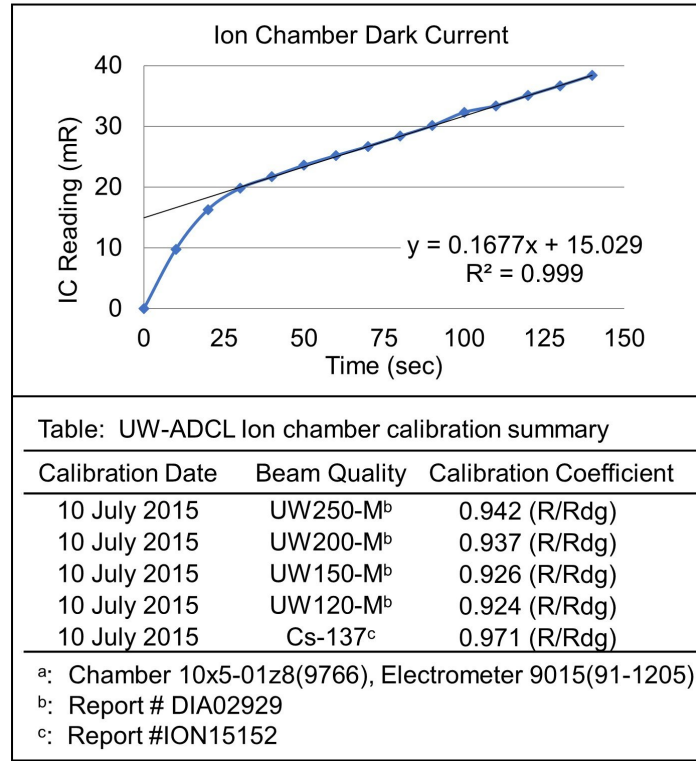


Figure 12: The ion chamber dark current, residual internal noise, may indicate potential measurement issues. For this ion chamber, the dark current is negligible. In addition, the ion chamber should be used for the dose ranges at which it was calibrated, shown in the table.

3.3.2 Dose calculation

While measurements of exposure are informative for determining how much radiation is present in air (air ionization), a more useful measure is how much energy that radiation deposits to a specific medium, called the absorbed dose, which is linked to how much radiation damage will occur in that medium. Absorbed dose is equal to the radiation exposure multiplied by the ionization energy of that radiation in the medium ionized in J/kg (and $1J/kg = 1Gy = 100rad$). For example, an exposure of 1 Roentgen ($2.58 \times 10^{-4}C/Kg$) yields a dose of $0.00876J/Kg$ in air (or $0.876Gy$ or $0.876rad$), where the ionization energy of dry air is $33.97J/C$ at normal temperature and pressure conditions.

For the radiotherapy and radiobiology study applications outlined in this dissertation,

the absorbed dose to tissue is of special interest. Therefore, we follow the American Association of Physicists in Medicine (AAPM) guidelines set by the Radiation Therapy Committee Task Group 61(TG – 61) for low (superficial) to medium (orthovoltage) energy x-rays, 40 – 300kV [194]. The protocols outlined in TG-61 yield absorbed dose in water and tissue at the point of measurement absent the ion chamber. For all of our small animal radiotherapy experiments, doses need only be calculated at depths $\leq 2\text{cm}$, and at points on or near the surface of the skin (with measurement reference depth $z_{ref} = 0$); therefore, the “in air” method described in TG-61 is the preferred method for calibration of our x-ray beams and dose calculation. The absorbed dose “in air” is calculated using the formula:

$$D_{w,d=0} = MM_k B_w P_{stem,air} \left[\left(\frac{\mu_{en}}{\rho} \right)^w \right]_{air}$$

,where M is the ion chamber reading at the reference measurement depth ($d_{ref} = 0$), $\left[\left(\frac{\mu_{en}}{\rho} \right)^w \right]_{air}$ is the mean mass energy-absorption coefficient ratio of water to air, N_k is the ion chamber correction factor for the x-ray beam quality used, $P_{stem,air}$ is the ion chamber correction factor that accounts for any changes in field size as compared to the initial calibration conditions that result in differences in measured charge in the ion chamber stem, and B_w is the photon backscatter correction factor.

3.3.3 Beam quality

For calculating dose to tissue, the mass energy-absorption coefficient ratio of water to air needs to be determined from the beam quality of the x-rays (320kV tube potential). The x-rays half-value layer (HVL) and the tube potential are both used to characterize the beam quality, where HVL is the thickness of material (usually Aluminum or Copper) required to attenuate the beam intensity down to half of its original value. Shown in Figure13, SpekCalc software is used to generate the x-ray emission spectra, on the left, and is used to calculate their corresponding mean and effective (equivalent monoenergetic

photon) energies and HVLs [196], [197]. In addition, Figure 13 shows the various photon interaction coefficients for Dry Air and Soft Tissue (ICRU-44), calculated using XMuDat software (*International Atomic Energy Agency – Nuclear Data Section, Vienna, Austria*) [189]. The table in Figure 14 summarizes the resulting dose calculation coefficients needed for determining absorbed dose in tissue, including calculations for HVL, mean and effective energy, and their corresponding mass-energy absorption coefficients [194].

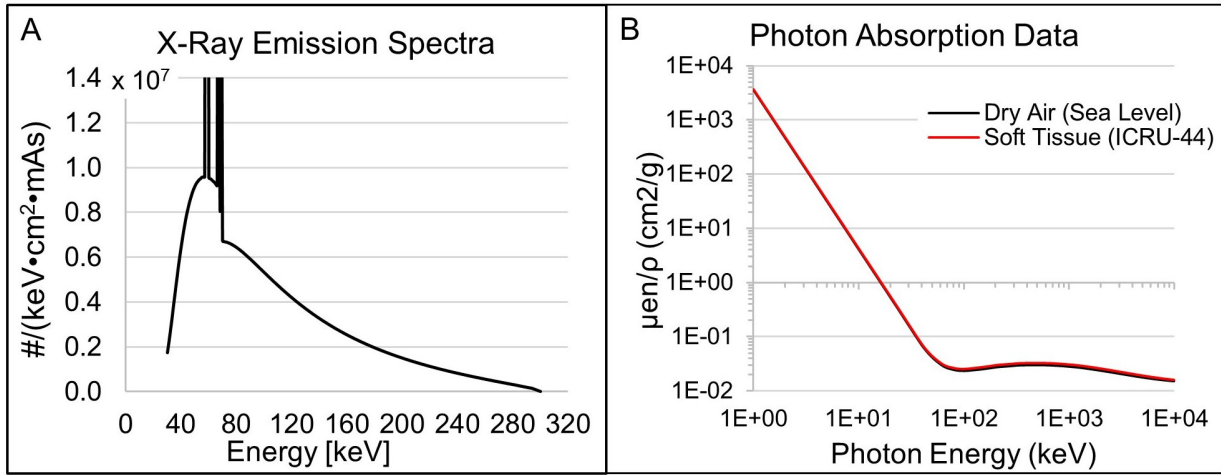


Figure 13: The f-factors in Figure 14 were calculated from energy spectra generated with Spekcalc, shown on the left [196], [197], which were used to determine the the mass-energy absorption coefficients in XMuDat, shown on the right [189]. The resulting f-factor calculations are used for converting converting the ion chamber in-air measurements of exposure to dose in water [194].

Dose calculation coefficients for 320kVp Tungsten anode 320kVp, 12.5mA x-ray photons using using Cu_{0.254mm} filtration

Energy (keV)		HVL ^a (mm)	$(\mu_{\text{en}}/\rho) _{\text{air}}^{\text{b}}$ (cm ² /g)	$(\mu_{\text{en}}/\rho) _{\text{tissue}}^{\text{b,c}}$ (cm ² /g)	Ratio ^d
Mean E	95.4	-	0.0234	0.0256	1.0931
Effective E (Al)	80.4	12.8	0.0243	0.0264	1.0859
Effective E (Cu)	87.8	1.26	0.0237	0.0259	1.0897

^a: The 1st half value layers are calculated for Al and Cu using SpekCalc [xxx].

^b: Mass-energy coefficients for air and tissue [available from Hubbel and Seltzer, NIST Database [xxx].]

^c: ICRU-44 Tissue type used for mass-energy coefficient calculation. [xxx]

^d: Ratio of tissue-to-air mass energy coefficients $(\mu_{\text{en}}/\rho)|_{\text{tissue}} / (\mu_{\text{en}}/\rho)|_{\text{air}}$.

Figure 14: Dose calculation coefficients for converting the ion chamber in-air measurements of exposure to dose in water. [188]. The f-factors were calculated from energy spectra generated with Spekcalc [196], [197], which were used to determine the the mass-energy absorption coefficients in XMuDat [189].

3.3.4 Irradiator linearity of current output

Absorbed dose is linearly related to the machine tube current; hence we perform linearity of output measurements to verify the linear relationship between machine output and current. Measurements were performed on the X-RAD 320 X-Ray Irradiator located in Marsico B121 and under normal operating conditions on November 16, 2016. For all the following measurements, the ion chamber was placed on 1cm of acrylic and measurements were taken at the approximate open field isocenter at 37cm from the source. The plots in Figure 15 show the machine output plotted as a function of the tube current at a constant 250kVp tube potential and 0.254mm Cu filtration. There is a linear relationship between the exposure rate and current ($R^2 = 0.9841$), where the exposure doubles as the current is doubled, as expected. This linearity response is confirmed with measurements from a second ion chamber (0.18cc farmer chamber). The small deviations in the linearity measurements may be accounted for by the end effect, the amount of time that is not accounted for by the internal machine timing mechanism during the exposures.

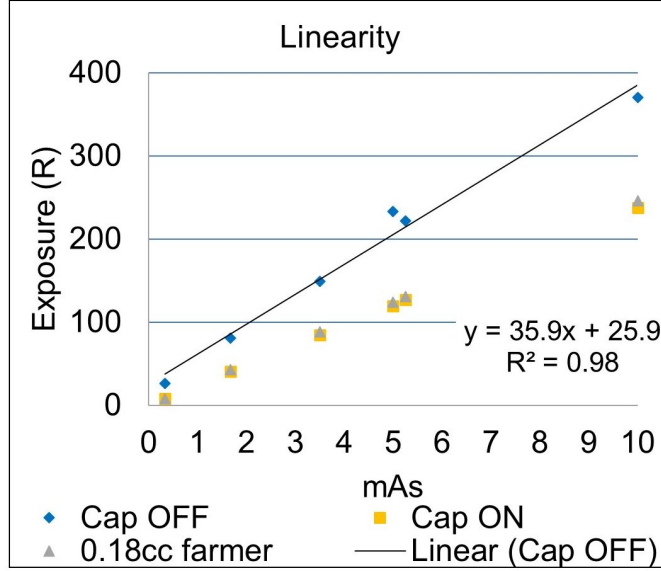


Figure 15: The current-time product, in milliAmpere-seconds (mAs), is varied for different time and current combinations and then plotted against the measured ion chamber, in-air exposures. The linearity of output R^2 value indicates the machine current output is relatively stable. Linearity of output measurement conditions included 250kVp, 0.254mmCu added filtration, at 38cm SSD.

3.3.5 Irradiator energy response and kVp check

Figure 16 details the energy response of the machine output. The top panel is a plot of the machine exposure as a function of peak tube voltage (kVp). In general, the energy response of the x-ray tube output is expected to be a quadratic function and approximately a square of the tube voltage, where, depending on the filtration used, doubling the energy will quadruple the measured output. For a copper filter 0.254mm thick, the measured machine response is consistent with a fitted quadratic curve ($R^2 = 0.9995$) and doubling the energy from 160kVp (60.4R) to 320kVp (234.55R) yields an output 3.89 times the initial output, just 2.9% short of the expected $4\times$ output. The bottom panel in Figure 16 is a table of the XRad-320 X-Ray Irradiator kVp accuracy test measurements for selected kVp tube potentials within a range of 50 to 150kVp and a fixed tube current of 1mA. All nine measurements were within the recommended accuracy limit $+/- 5\%$ for all selected tube potentials with a mean kVp accuracy of 2% [198].

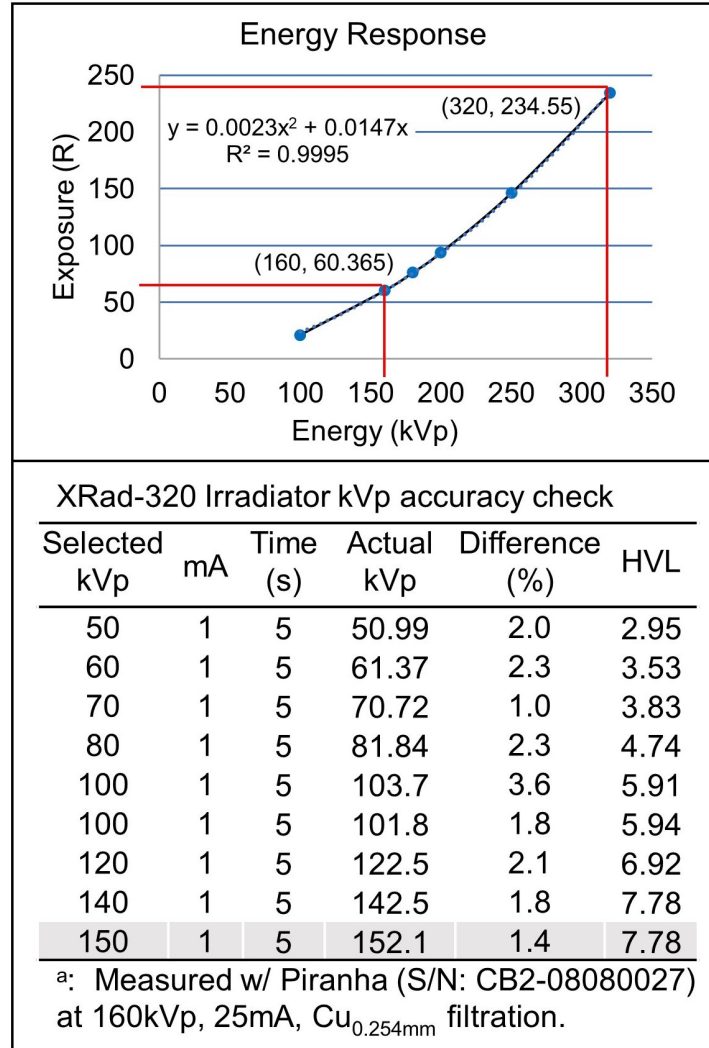


Figure 16: (Top) The machine energy exposure response was measured by varying the tube potential while maintaining the current constant. (Bottom) A kVp check of the XRad-320 Irradiator was performed to verify the accuracy of the selected kVp against actual kVp measurements.

3.3.6 Radiation field uniformity- flatness and symmetry

Looking at the wide field uniformity, namely via calculations of the field flatness and symmetry, will help determine the optimal SFRT collimator positions for achieving the most uniform beams possible. Point measurements along the x- and y-axis were made to determine the cross-beam profiles of the generated x-rays for an open, 18cm x 18cm field (with the large collimator in the fully open position) at 38cm axial distance from the

source. Shown in Figure 17, the ion chamber was positioned at several points within the irradiation chamber along the x- and y-axis, approximately 2cm apart.

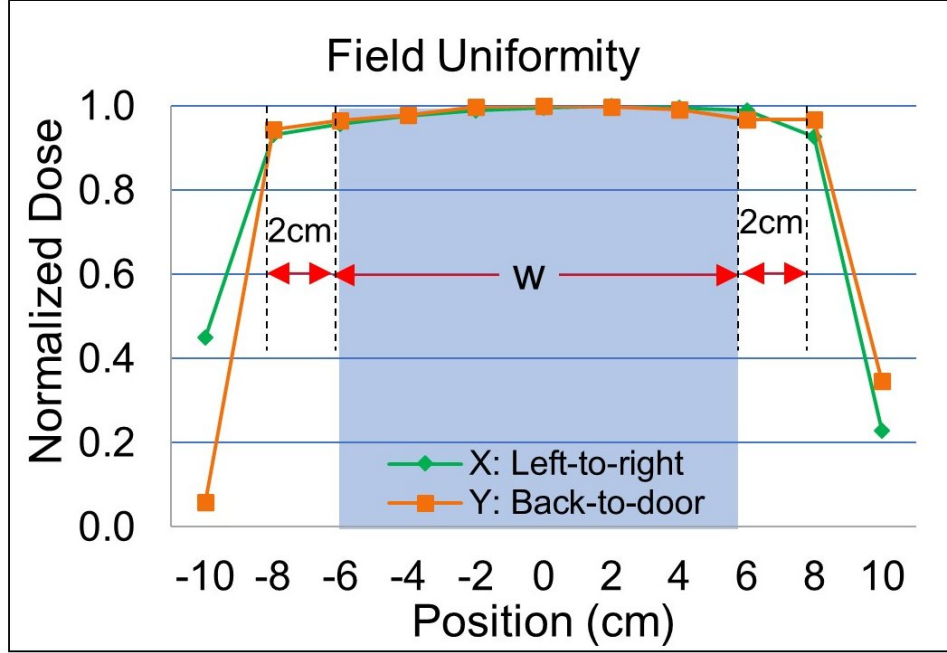


Figure 17: The large-field radiation beam profiles were measured through the central beam axis along the vertical, y-axis (back-to-front) and horizontal, x-axis (left-to-right) directions and subsequently plotted. Each ion chamber measurement lasted 20seconds and was completed under standard conditions (320kVp, 12.5mA, $Cu_{0.254m}$ added filtration).

For our study, the reference region of flatness is defined as the region extending from the central axis outward up to 2cm from the field edges to exclude penumbral effects of the outer beam [187]. In Figure 17, the reference region for calculating beam flatness is defined in light blue. Along the x-axis (as measured from left-to-right within the chamber) the flatness differed from measurements at the central axis of the field by as much as +3.76% (at -6cm from the central axis, 38cm from the source.) Similarly, along the y-axis (as measured from the back wall to the front chamber door) the flatness differed as much as 3.5% (at -6cm from the central axis, 38cm from source.) Though this is not perfect field flatness, the variation is significantly decreased nearer the central axis of the field, less than 0.7% difference within 2cm from the central axis in all directions. To determine field

symmetry, the x- and y-axis profiles are folded at the field center and the two halves are compared. The field symmetry varies from the central ray as much as 3.3% for the x-axis and 2.6% for the y-axis at the outer edges of the radiation field. Again, the field symmetry increases closer to the central axis, and at 2cm is only 1.1% different from the isocenter.

3.4 Relative Dosimetry

Measurements of absolute exposure (or dose) via ion chamber are the gold standard in radiation therapy due to their low energy dependence, real-time measurement capabilities, and reliability for use in repeated measurements. However, while extremely valuable tools for large field clinical dosimetry, when it comes to their use in preclinical SFRT dosimetry, ion chambers are severely limited in their ability to measure regions of high-gradient fields. Even the smallest ion chambers lack the high spatial resolution necessary to measure sub-millimeter beam widths of our preclinical SFRT collimators in real-time while maintaining charged particle equilibrium [187]. Among the many challenges impeding the widespread clinical translation of SFRT technology is the lack of a suitable radiation detector and overcoming this barrier is instrumental to advancing preclinical SFRT research. Other types of radiation detectors for performing relative dosimetry include semiconductors, thermoluminescent dosimeters (TLDs), radiographic film, and the novel NanoFOD fiber-optic detector; however, each come with their own limitations, including accuracy and precision, energy response, dose or dose-rate dependence, directional dependence, spatial resolution, and real-time (or timely) dose read-out, among others. In these next sections, I will describe these alternative measurement methods, and their benefits and flaws in relation to this body of work.

3.4.1 Relative dosimetry using film

Gafchromic film is one of only a select few radiation detector types that are readily available and meet some of the requirements for use in SFRT dosimetry. With a very

high spatial resolution ($25\mu\text{m}$ or less [199]) and low energy dependence of $< 5\%$ in the $100\text{keV} - 18\text{MeV}$ photon range [199], it is the most commonly used relative dosimeter type in preclinical SFRT research [181]. Gafchromic film dosimeters contain a layer of “photo-monomer molecules” in the form of a gel that undergoes self-polymerization chemical changes when exposed to high energy photons such as those in ionization radiation [199], [200]. Gafchromic EBT-3 film consists of a thin active layer of the polymerizable gel, $28\mu\text{m}$ thick that is sandwiched between two layers of a clear polyester base, $125\mu\text{m}$ thick [199]. In addition, the gel polymers are largely insensitive to low-energy radiation such as visible light and develop without post-exposure treatment since they do not require any special wet chemical processing. However, EBT-3 Gafchromic film requires a lengthy development time that may take anywhere between 4hrs – 48 hours [199]. This lack of timely dose readout makes it less than ideal for fast-paced, practical SFRT dosimetry and research. Nevertheless, the high spatial resolution capabilities of film dosimeters make using them a practical method for SFRT dosimetry.

3.4.2 EBT-3 film calibration

Accurate EBT-3 film dosimetry first requires the film to be calibrated against an ion chamber to establish a film-dose response curve. The film is cross-calibrated with the ion chamber in large-field conditions, without any SFRT collimators in place, and the irradiator is operated under identical conditions as those used during treatment, (at full power using 320kVp anode voltage, 12.5mA current, and with 0.254mm Cu copper added filtration). A sheet of film is cut into rectangular pieces, approximately 3cm x 2cm area, using a precision paper cutter to minimize damage to the outer edges of the film (since frayed film edges are known to result in erroneous measurements.) In addition, the film orientation is recorded and maintained (relative to the original uncut sheet) for all exposures, handling, and film readout as any changes in the film orientation may result in measurement error [199].

Film calibration setup is shown in Figure 18, a film piece is carefully placed on top of water-equivalent bolus material and directly beside the ion chamber, at a height matching the approximate center of the ion chamber’s sensitive volume such that ion chamber readings would very closely correspond to the film results. In addition, these are all placed onto a metal z-axis stage for adjusting the height of the detectors for specific source-to-detector-distances, with a 1cm-thick acrylic slab placed between the detectors and stage to minimize backscatter from the metal. The film is then irradiated for a pre-determined length of time, the ion chamber reading is recorded, and the film piece is removed and stored in the dark for readout later, taking care not to disturb the exposure setup. This procedure is identically repeated for each new piece of unirradiated film, varying only the exposure time, for accurate and reproducible film dosimetry. We limit film exposures to the optimal dynamic range of the EBT-3 film, between 0.2Gy – 10Gy [199], [200].

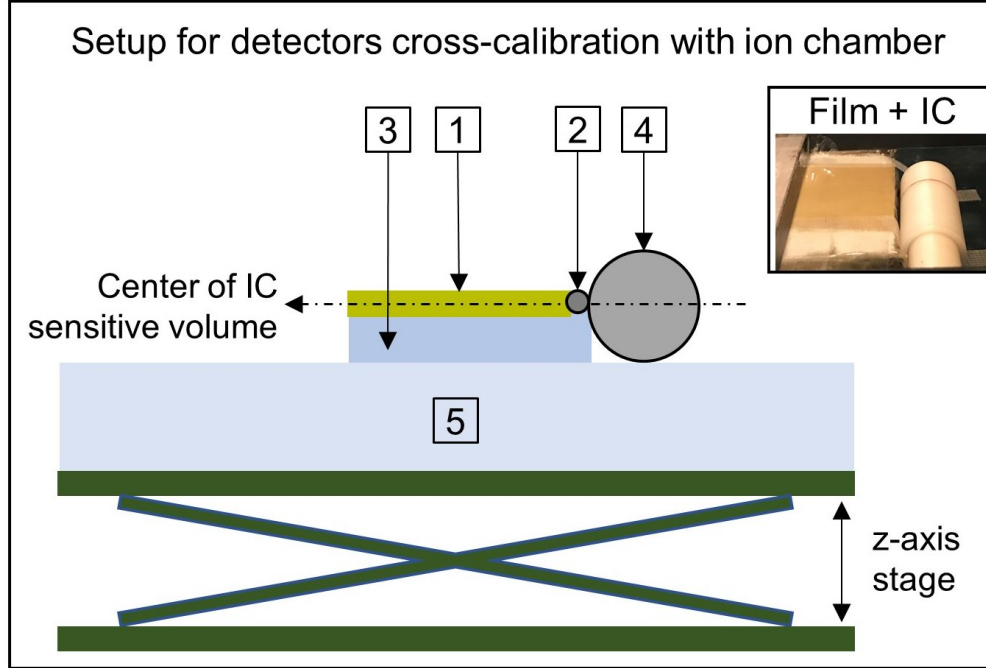


Figure 18: Different components of the EBT-3 film and nanoFOD detectors setup for cross-calibration with ion chamber (IC). The EBT-3 film (1) and nanoFOD scintillator tip (2) are both placed on top of water equivalent bolus material (3) and directly next to the ion chamber (cross-sections of each are visible) (4). In addition, these are all placed onto a metal z-axis stage for height adjustment with a 1cm-thick acrylic slab (5) placed in between for limiting the photon backscatter from the metal stage. The figure insert shows a piece of film (sitting above a piece of water-equivalent bolus) placed next to the ion chamber, as viewed from above.

For film readout we adhere to scanner and EBT-3 Gafchromic film manufacturer recommendations [199]. Film is read out using a 48-bit RGB flatbed photo scanner (such an Epson 10000XL or similar model with transparency adapter) and takes place approximately 24hrs post-exposure (exact time post-exposure is recorded). The film are handled with gloves and any smudges on the film are gently removed using alcohol wipes prior to scanning. After the scanner has been warmed up, according to manufacturer instructions, the film are placed in the center of the sensitive area of the scanner and then scanned with all image and color correction features turned off using 72dpi resolution and 48-bit color settings. The scanned film images are saved as TIFF files due to their lossless “deep color” formatting, retaining the 16-bit RGB color components need for triple channel

dosimetry.

Figure 19, bottom, shows a complete film calibration set. The calibration regions of interest are shown as blue dotted rectangles are shown below the calibration curve. Figure regions of interest are selected near the center of the film, with a 2mm margin from the edge of the film where the dose is most uniform. The digitized film transmission values for each 16-bit color channel (red, green, and blue) are averaged within the regions of interest using ImageJ (NIH public domain, MD, USA) and plotted against their respective ion-chamber-derived dose values to create the three separate film dose response curves, shown in Figure 19. The dose measurement points are fitted to an interpolating polynomial to create a continuous curve. A Matlab [103] script was written to perform automatic dose conversion calculations from film transmission value input. The film calibration is valid at a specific point in time and requires re-calibration at minimum every 6 months or sooner based on film storage conditions or machine changes. The red channel is used for dose calculations up to 10Gy due to its high sensitivity to changes in dose (This determination is based on the red channel's observable steep dose response curve).

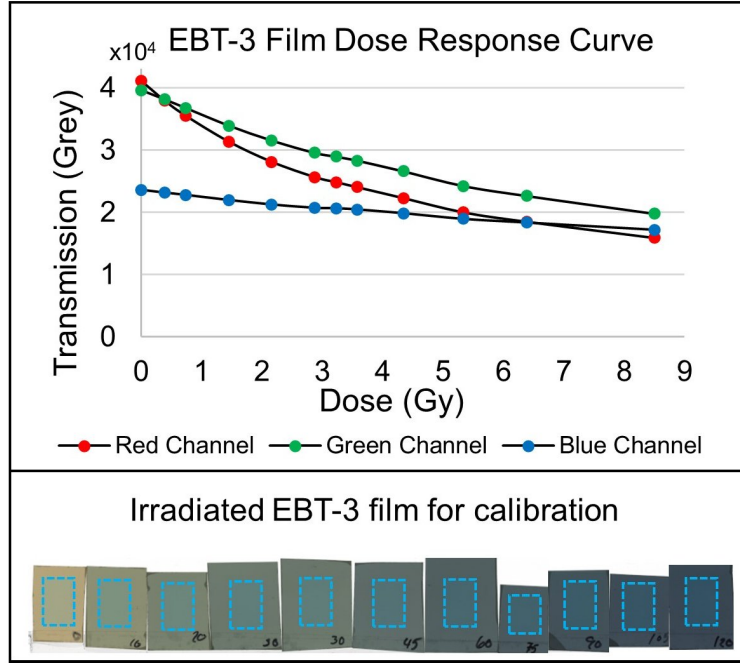


Figure 19: (Bottom) EBT-3 film pieces are calibrated against an ion chamber and scanned. The dotted blue lines indicate regions with 2mm margins in the center of each film that are used for computing the average film-response for a given energy. (Top) The resulting film dose-response curves are plotted and used for converting film readings to dose.

3.4.3 Film limitations

Given the limited dynamic range of the film, we are limited to exposures within $0.2Gy \leq x \leq 10Gy$. These values are simultaneously greater than the minimum/valley dose of some of our SFRT treatments (at the lower end of the film dynamic range) as well as less than the peak dose of the SFRT treatments (at the higher end of the dynamic range.) Therefore, overcoming this film limitation requires careful dose-rate calculation and extrapolation to determine the peak and valley doses of our SFRT treatments. To determine the valley dose in the $300\mu m$ SFRT collimator, film is intentionally over-exposed in the peak region so as to bring the valley dose film regions up to within the dynamic range of the film, ideally somewhere along the steepest portion of the calibration curve. After scanning the resulting film, the measured dose in the valley region is divided by the recorded total exposure time to determine the valley dose-rate. Similarly, to measure

the dose in the peak regions of the SFRT beams, the film is intentionally under-exposed in the peak region so as to lower the peak dose to within the dynamic range of the film. After scanning the resulting film, the measured dose in the peak region is divided by the recorded total exposure time to determine the peak dose-rate. These two measurements of peak- and valley- dose rate combined help determine the peak and valley doses for a treatment with a given exposure time.

3.4.4 Film dosimetry for SFRT

After positioning the SFRT collimators, $3\text{cm} \times 4\text{cm}$ rectangles of ETB-3 film are irradiated under the area defined by the collimated beams. Of specific interest are measurements of the SFRT beam profiles, the profile of irradiation perpendicular to the radiation beams, and their percentage dose distribution in depth, the profile of irradiation parallel to the radiation beams. Shown in Figure 20, this is achieved by tightly sandwiching a piece of film between two identical $3\text{cm} \times 3\text{cm} \times 4\text{cm}$ solid rectangular acrylic prisms that act as phantom for the percentage depth dose film measurement. For this depth dose measurement, the film is positioned edgewise, both parallel to the collimated rays and centered along the lateral profile of the beams. Additionally, a second piece of film is fixed to the top of the acrylic phantom (acrylic-film-sandwich), placed perpendicular to collimated rays and centered over the percentage depth dose film. In the figure, the approximate location of the percentage depth dose film underneath the beam profile film is indicated by the red line. The film setup is then aligned with the collimator and source, then irradiated. The process described above for measuring SFRT beam profiles and PDDs is repeated for all collimators as needed for beam profile or percentage depth dose measurement.

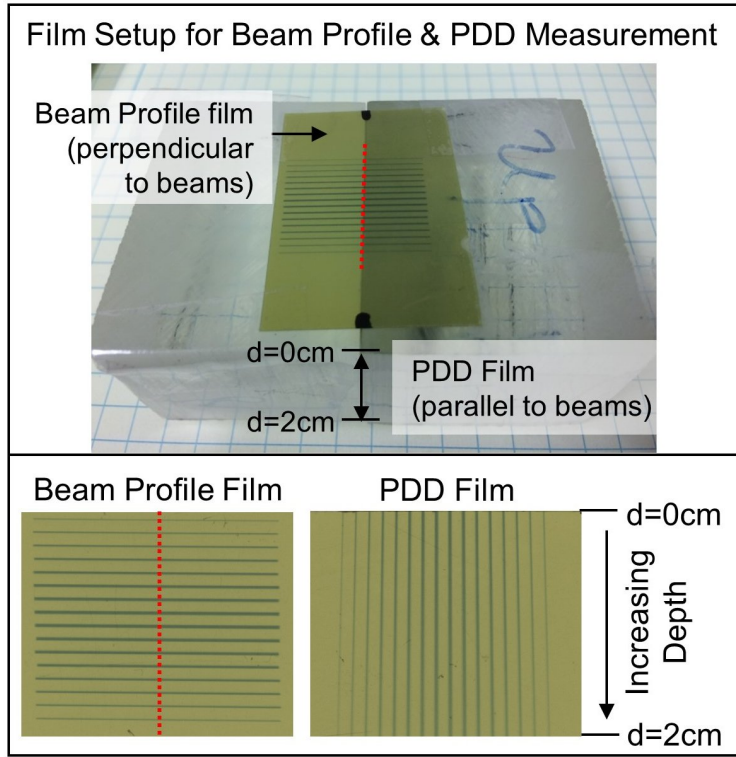


Figure 20: The SFRT beam profile is taken perpendicular to the lateral direction of the SFRT beams. The SFRT PDD measurements are calculated for up to 2cm depth along the direction of the beam. RED drawings on film indicate location of Beam Profile and PDD measurements. Similar measurement procedure is followed for all other SFRT beam patterns.

3.4.5 Relative dosimetry using the NanoFOD

In addition to using film, we use a second, efficient dose measurement technique for SFRT using a new technology based on nano-scintillator fiber-optic detector (nanoFOD), created in conjunction with Duke University Department of Medical Physics. The nanoFOD system successfully achieves real-time dosimetry measurements by simultaneously employing an integrated positioning stage and automatic dose-rate integration script. In addition, the nanoFOD is a portable, low-cost, real-time high-resolution dosimeter, which is particularly useful for research labs such as our own. In addition, the 20-um-sized detector tip makes it especially suitable for measurements of the peak dose of our smallest SFRT beams and the beam profile [201].

Shown in Figure 21, this device uses inorganic nano-crystalline ($Y_{1.9}O_3, Eu_{0.1}, Li_{0.16}$) powder that is compressed into an $20\mu\text{m}$ -sized pellet and attached to one terminal of a $60\mu\text{m}$ UV/Vis Optical Fiber (LEONI Fiber Optics, Inc) [202]. The scintillating pellet consists of highly sensitive photon absorbers in the x-ray range, with emission spectra that peak at 611nm, well within the visible light part of the electromagnetic spectrum. The emission photons travel down the fiberoptic cable, which is coupled to a S150C compact silicone photodiode power sensor, selected for fiber-based optical power measurements in the wavelength range 350-1100nm and optical power range 50nW-5mW, for photon detection [201], [202]. The output is then read out by a PM100USB Power and Energy Meter Interface which is operated and powered via PC [201], [202]. A standard laptop is used for all data collection and display. In addition, the optical fiber is coated with black paint to attenuate signals from ambient light.

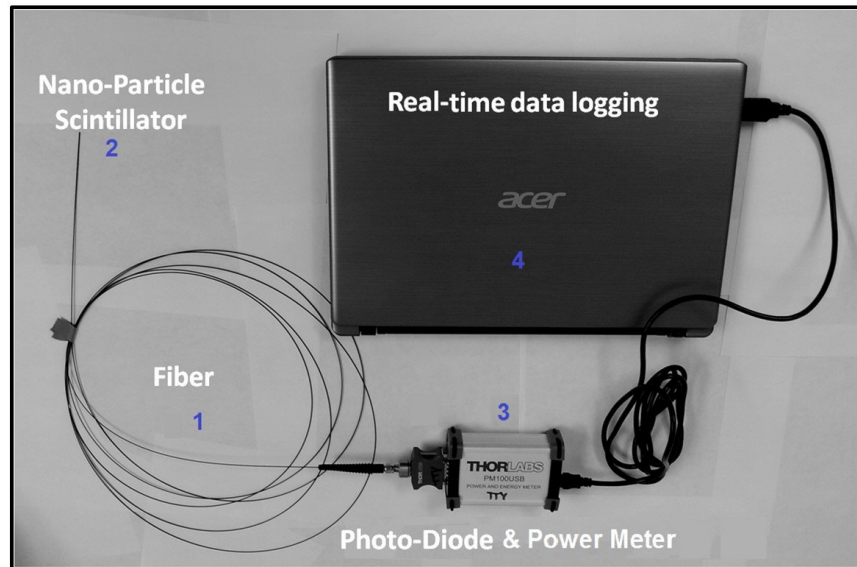


Figure 21: A (2) $20\mu\text{m}$ -wide, inorganic, nanocrystalline, scintillating pellet is attached to (1) the tip of an ultraviolet/visible wavelength optical fiber (Leoni Fiber Optics). The signal travels through the (1) fiber and is detected by a (3) S150C silicone photo-diode and PM100USB photo-diode laser power meter (Thorlabs) and then read out using a (4) standard laptop for data collection and display. Photo adapted from Belley et al. [201]

3.4.6 NanoFOD calibration

With proper calibration, the nanoFOD may be used to calculate the amount of radiation incident on the nanoparticle scintillator (measured in Gy) based on the scintillation energy of the photo-diode (measured in Joules). Both film and nanoFOD dosimeters are calibrated together using the ion chamber for large-field geometry as recommended by TG-61, using the setup shown previously in Figure 18. The nanoFOD scintillation tip is placed into a fixed position next to the ion chamber and irradiated for a predetermined length of time. Figure 22 shows resulting nanoFOD signal after a 30 second exposure, with background signal (from ambient light and internal component noise, shown in red) subtracted. The area under the signal-time curve (in green) is integrated to determine the Integral Net output value. This procedure is repeated for multiple different exposures and all resulting integrated output values are plotted against their respective ion chamber measurements to create the NanoFOD Response Curve, shown in Figure 22 in the panel on the right. The linear slope of this curve corresponds to the nanoFOD calibration factor ($CF(E)$), as a function of energy, and is used for converting the nanoFOD light output (L) to a measurement of Dose (D) at a given energy using equation,

$$D = L \times CF(E)$$

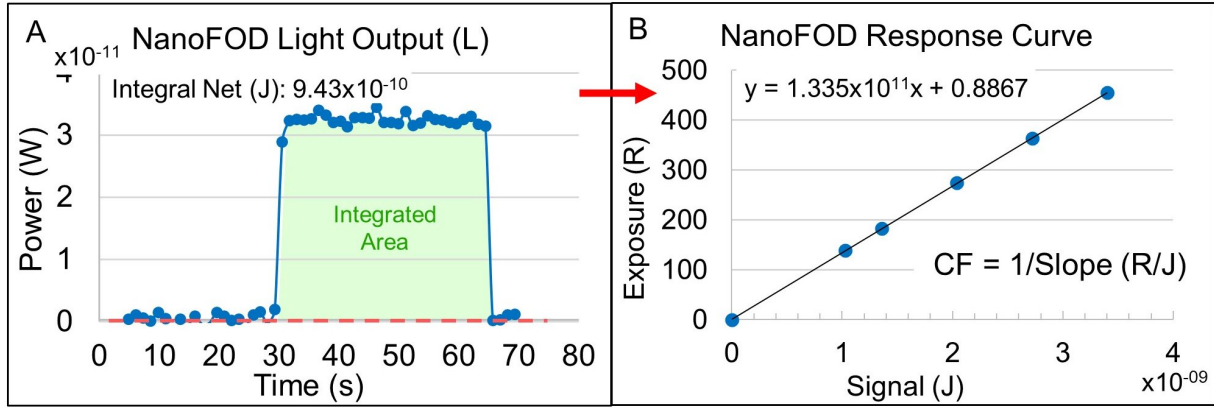


Figure 22: The nanoFOD calibration factor, CF, is used for converting the nanoFOD light output measurement under the radiation to Absorbed Dose in tissue (or Exposure). Once the scintillation tip is in a fixed position, ready for measurement, the light output (J/s) of the NanoFOD is linear with Dose (D) at a given energy. To calibrate the nanoFOD, background signal is collected and then the beam is turned on. After subtracting the background signal (red dotted line) the area under the signal-time curve (green shaded area) is integrated to determine the Integral Net output value. This value is plotted onto the NanoFOD Response Curve. The linear slope for several plotted values is calculated and dose conversion is performed by comparing the integrated signal from nano-FOD system (J) to cumulative exposure (R) 2% cumulative calibration uncertainty.

3.4.7 NanoFOD dosimetry for SFRT

For accurate nanoFOD positioning, especially for peak dose and lateral beam profile measurements under the SFRT micro-collimator, the nanoFOD is attached to a computer-controlled positioning stage, which positions the detector tip precisely under the micro-collimator beams. Figure 23 graphically displays the measurement setup and an example output graph is shown in the insert. Additionally, we developed a user-friendly automatic data collection script for easy use of the nanoFOD system, shown in Figure 23. The script controls both detector data collection, performing automatic dose conversion for real-time readings and background measurement subtractions, as well as the computer-controlled positioning stage, ensuring that the data and stage are synchronized. Data collection begins with background acquisition and is followed by dose measurement. The GUI displays dose, dose rate, position, and speed of the detector in real time, shown

in the graphical insert (bottom right) where we compare the performance of two different scintillator tips. Of these two tips, *one* displays a 910% increase in signal sensitivity compared to an older generation detector with small crystal (purple line).

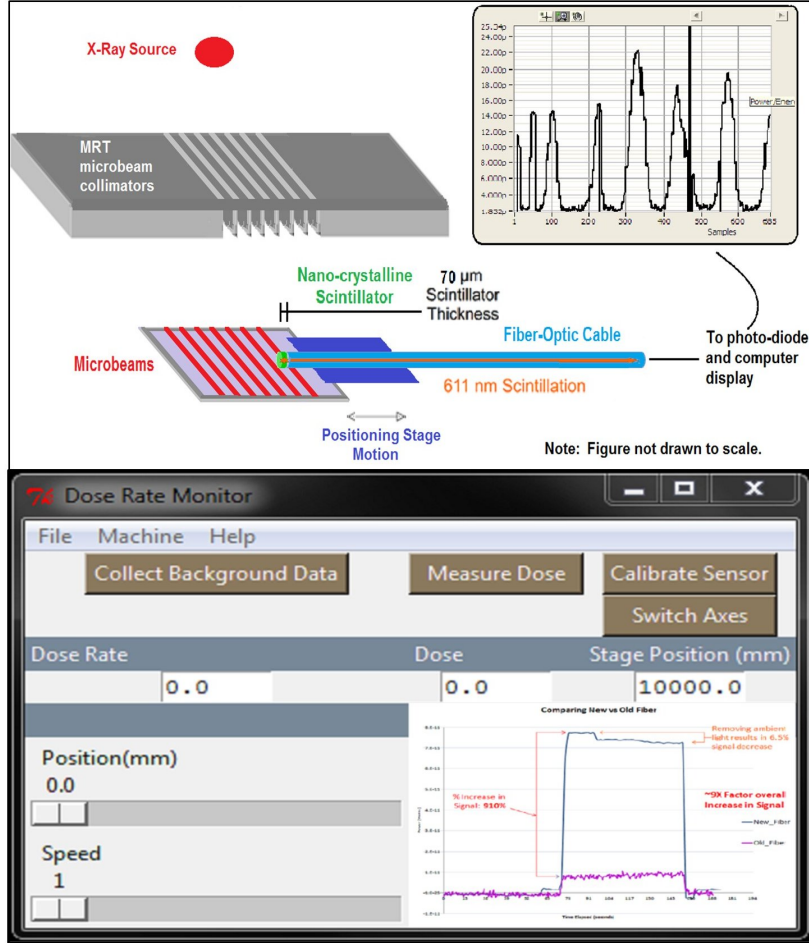


Figure 23: The nanoFOD scintillation tip is fixed to a x-y translation stage and is translated through the lateral direction of the SFRT beams profile. A in-house written script performs automatic data collection, background correction, data collection and synchronization with stage translation, signal-to-dose conversion, and displays the data in real time for quick readout.

3.4.8 NanoFOD limitations

Several limitations have been encountered with NanoFOD dosimetry that make SFRT dosimetry challenging.

1. The nanoFOD scintillator is strongly energy dependent; therefore, dose measurements in the valley region of the SFRT beams are unreliable, because scattered photons in the valley region may have vastly different energy spectra than those photons lying directly in the path of the beam.
2. NanoFOD measurements for SFRT are only valid when the entire scintillator tip (active volume) is illuminated; therefore, as the solid angle between the scintillator tip and the radiation source changes, the active volume of the scintillator becomes either only partially illuminated at the edge of the SFRT beams or completely blocked in the valley regions directly underneath the SFRT collimator.
3. At long exposure times nanoFOD measurements undergo upwards signal drift, and noise amplitude rises over time due to increases in natural temperature and resistance of the detector's internal components; therefore, a heat exchanger should be included in future detector setups to mitigate thermal noise and related measurement error .

3.5 SFRT Dosimetry for Small Animal Studies

3.5.1 SFRT beam profiles

Shown in Figure 24, the $300\mu\text{m}$ -sized SFRT collimator dose profile was measured using both the EBT-3 Gafchromic film and the nanoFOD detectors, and these results were compared. In the SFRT peak regions, the film and nanoFOD largely agreed, with less than 2% difference in measurements for the central 7 peaks. Unsurprisingly, measurements in the valley region did not agree. This is likely due to the nanoFOD limitations discussed earlier, namely the strong energy dependence of the nanoFOD detector as well as changes to the percentage area activated in the scintillator as a function of position.

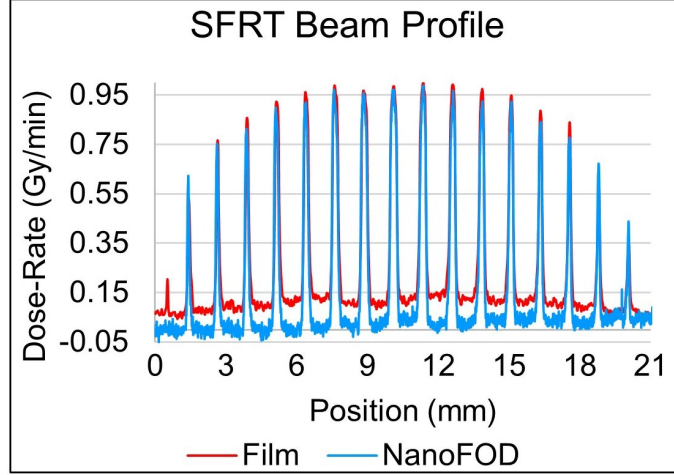


Figure 24: EBT-3 Gafchromic film and nanoFOD were both used to measure the SFRT beam profile for a multi-slit collimator with $300\mu\text{m}$ -wide peaks. The film and nanoFOD largely agreed in the peak with $< 2\%$ difference (after correcting for upwards signal drift due to noise). Measurements do not agree in the valley region largely due to strong nanoFOD detector energy dependence and variability in detector scintillated active area as a function of position. Setup conditions included a 320kVp tube potential, 12.5mA, and $\text{Cu}_{0.254\text{mm}}$ added filtration.

Additional film beam dose profile results are shown in Figure 25. A variety of different “broad beam” or large field collimators as well as SFRT collimator measurements are included to demonstrate the versatility of the radiotherapy treatment setup. While the primary focus of the treatment setup was to develop a system capable of delivering spatially fractionated radiotherapy beams, an important aspect of radiobiological studies involves comparing the SFRT treatments against their more conventional “seamless”, or uniform, radiotherapy counterparts. The radiotherapy beam dose profile measurements are largely taken at 320kVp; however, two plots notably contain an additional measurement at 160kVp (Figure 25-A and G). The “TBI- Large Field” and “SFRT-TBI” curves correspond to a total body irradiation study (TBI), where the entire mouse (with dimensions 3cm-width and approximately 8cm-length) undergoes radiotherapy treatment with SFRT. The corresponding large TBI collimators, $4 \times 10\text{cm}$, were dosimetrically tested at both 320kVp and 160kVp to determine at which treatment energy superior SFRT beams and

corresponding peak-to-valley dose ratios were produced for the given TBI treatment field size requirements.

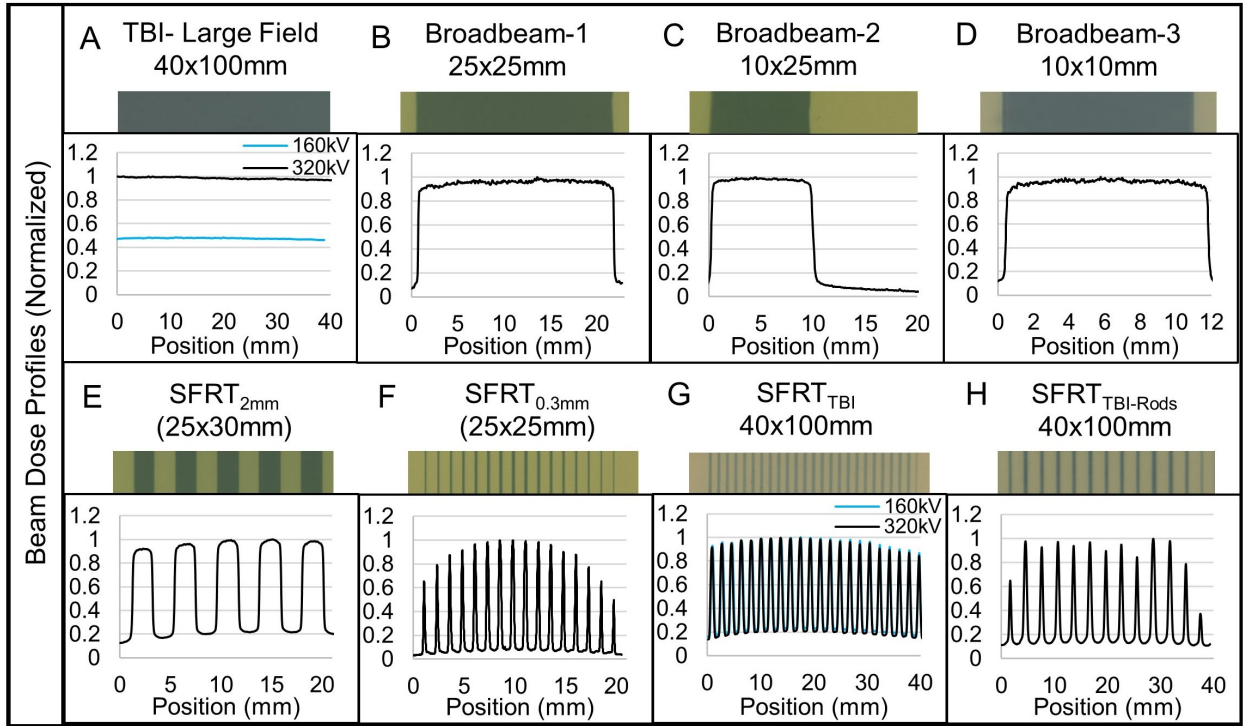


Figure 25: The measured relative beam profiles are shown for a variety of SFRT collimators. The large variation in fractionation scale demonstrates the flexibility of the SFRT treatment system for potentially delivering a wide range treatments for a number of disease sites. Calibrated EBT-3 film was used for measuring the dose profiles (largely at 320kVp, 12.5mA with 0.254mmCu added filtration.) Additional details for each collimator are shown in Figure 26.

Beam profile measurements are useful for determining a number of dosimetric parameters for radiotherapy treatments. Figure 26 summarizes several of the computed dosimetric parameters for the collimator dose beam profiles shown in Figure 25. The table in Figure 26 includes the overall field size (or span of the SFRT beams) for each of the collimators as well as their collimator factors, ratio of the maximum (or peak) dose to the open-field measurements under the same measurement conditions. In addition, the table includes several characteristic SFRT parameters such as peak-to-valley-dose-ratio (calculated as the average dose in the “peaks” divided by the average dose in the “valleys”

of the SFRT beams), the average SFRT peak beam width (calculated as the average full-width-at-half-maximum of the SFRT beams), the average width of the “valley” regions, and their corresponding peak-to-peak distances. It should be noted that not all studies used the same treatment conditions. For example, the TBI-Large Field and SFRT-TBI dose profile measurements are at depth $d = 10\text{mm}$, whereas all other dose profile measurements are at depth $d = 0\text{mm}$.

Summary of SFRT collimator dosimetric parameters^a

Collimator	Field Size (mm ²)	Collimator Factor ^b -	PVDR -	Valley Width (mm)	Peak Width (mm)	Peak-to-Peak Distance (mm)
TBI- Large Field	40x100	0.98	-	-	-	-
Broadbeam-1	25x25	0.96	-	-	-	-
Broadbeam-2	10x25	0.89	-	-	-	-
Broadbeam-3	10x10	0.87	-	-	-	-
SFRT _{2mm}	25x30	0.89	5.6	2	2.2	4.2
SFRT _{0.3mm}	25x25	0.72	13.3	0.9	0.31	20.3
SFRT _{TBI}	40x100	0.62	5.11	1.18	0.69	1.87
SFRT _{TBI-Rods}	40x100	0.84	7.31	2.44	0.59	3.03

^a: All measurements computed 320kVp, 12.5mA, with 0.254mm Cu added filtration, approximately 37cm SSD at the surface, depth $d=0\text{mm}$ depth, except for SFRT_{TBI} and SFRT_{TBI-Rods} collimators where parameters were computed at $d=10\text{mm}$ depth.

^b: Collimator factors are computed using the maximum (or peak) / open-field dose ratio except for the SFRT_{2mm} collimator, which is computed based on estimates from PDD.

Figure 26: Dosimetric results for a variety of SFRT collimators used in small animal studies. The first 4 are uniform, seamless radiotherapy collimators, intended distinguish the effects of SFRT treatments from more conventional therapies. The bottom 4 are all SFRT collimators varying in shape.

3.5.2 SFRT percentage depth dose

In our small animal experiments, the radiation target or region of interest may often be tissue, lying at or just below the surface of the skin, or a tumor up to 10mm deep. However, the dose deposited to tissue generally decreases with increasing depth, and for larger treatment targets the tissue exit dose deposition will differ significantly from

deposition at the tissue entrance. This depth-dependent variable dose distribution may be characterized as percentage depth dose (PDD), defined as the dose distribution in depth (D) normalized to 100% of the maximum dose (D_{max}) along the central axis of the beam, where

$$PDD = \frac{D}{D_{max}} \times 100$$

[187]. For beam energies below 400kVp such as our own, D_{max} corresponds to a depth of $d = 0$; however, at higher energies, the depth of D_{max} may be significantly greater, $d \gg 0$. Figure 27 shows the PDD film measurement results for some of the various collimators used in our radiobiological studies

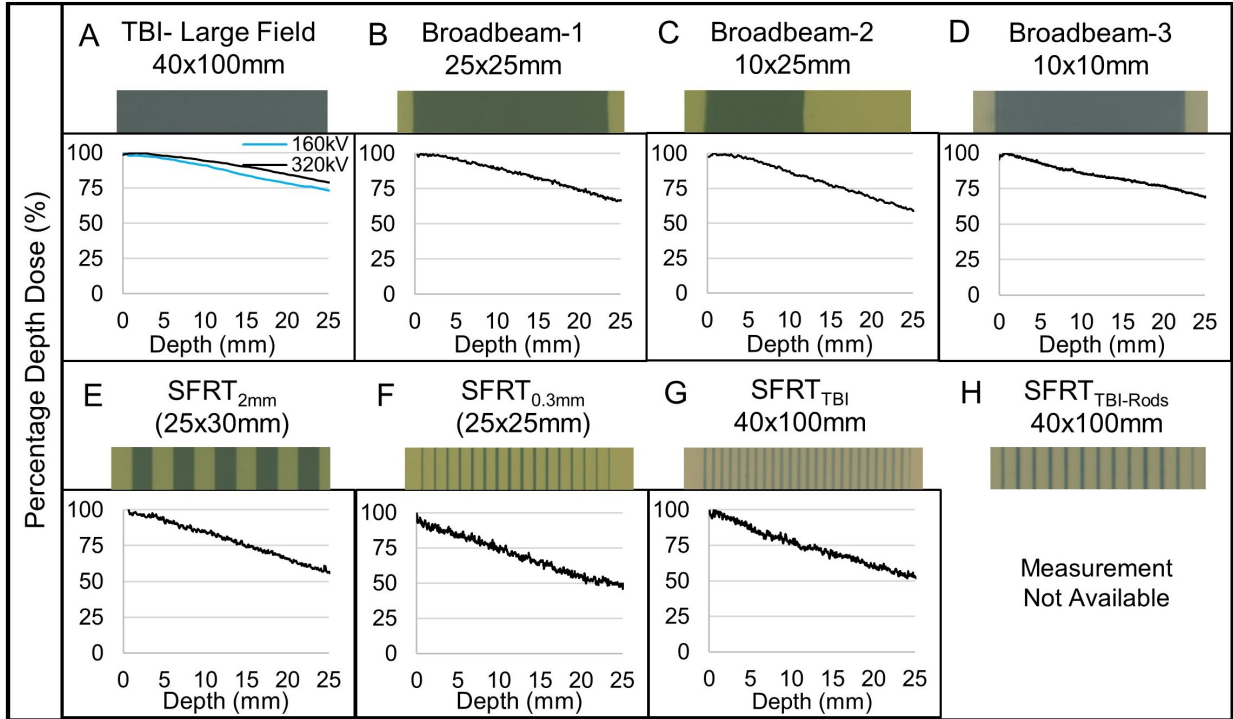


Figure 27: Some of the wide variety of SFRT collimators we used in our preclinical studies are shown. Panel 'A' corresponding to the "TBI-Large Field" collimator film measurement shows both 160kVp and 320kVp PDD calculations. The size and shape of the collimator, photon energies, and experimental setup conditions all play a role in dose depositions in depth. Hence, film irradiated at different energies were often examined to aid in the experimental design of a preclinical study. Percentage Depth Dose (PDD) results for a variety of SFRT collimators that we used in animal studies.

PDD measurements for the different collimators were largely taken at 320kVp; however, the TBI- Large Field plot also includes a PDD measurement at 160kVp. Note the steeper dose fall-off for the lower energy 160kVp beam. TBI treatments should ensure near-uniform (or as uniformly as possible) delivery of radiotherapy to the entire body. As the TBI radiotherapy beams enter the body they become attenuated by approximately 20% at the torso exit at 320kVp and by nearly 30% at 160kVp, which demonstrates that the 320kVp treatment energy delivers a more uniform dose. For this reason, among others, the 320kVp treatment energy was chosen for the TBI mouse study.

3.5.3 Integral dose calculation

Some studies require knowledge of the absorbed dose in tumor and normal tissues, integrated over their entire volumes. The volume-averaged doses are approximated by computing the film dose within an area of $1cm \times 1cm(depth)$ of the scanned PDD film. Similarly, to capture the effects of the radiation on nearby tissues that may have been exposed, the volume-averaged tissue dose is approximated by computing the film dose average within a $2cm \times 2cm(depth)$ of the PDD film, as shown in Figure 28. The Trapezoidal Riemann summation method is used to approximate the area under the definite integral along both dimensions of the 2D film-dose response surface shown, giving the volume-averaged tissue dose approximations.

$$\int_a^b f(x)dx \approx \sum_{n=0}^{N-1} \left(\frac{1}{2}\right) (f_n + f_{n+1})(\Delta x)_n$$

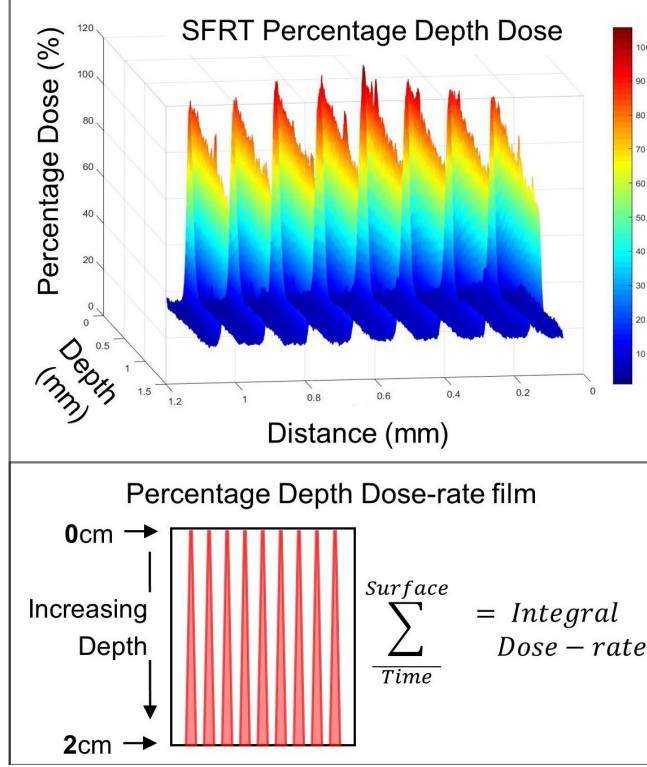


Figure 28: Integral dose was determined for specific depths in tissue from Percentage Depth Dose (*PDD*) film measurement results and were computed using an in-house generated Matlab script (Mathworks, Natick, MA) [103]. The top panel shows a 2Dimensional dose intensity map (with x-dimension in cm, z-dimension in cm, and y-dimension displaying the radiation intensity (*Gy*) of the 2D film PDD measurements for the $300\mu\text{m}$ peak width collimator. The integral dose is calculated in depth, shown in the middle panel, and the Riemman summation method is used to compute the definite integral for the area under the 2Dimensional curved dose surface of the PDD film.

3.6 SFRT Delivery System

SFRT radiobiological studies are ready to begin after completing dosimetry. Standardized protocols, located in the Appendix, were created for consistent, repeatable treatment system setup and animal alignment and to enable reliable radiotherapy delivery. Figure 29 shows the full SFRT treatment system setup. The external beam x-ray source (1) produces a large radiation field that is attenuated by one of the custom Cerrobend collimators (2). The position of the collimator with respect to the x-ray source is determined via a built-in light field in the XRad irradiator and the dosimetry

measurements. Once the optimal position is identified, the collimator is fixed onto the custom-made stationary shelf. The animal stage is positioned below the stationary collimator and shielding blocks. Both the animal and tumor (4) are aligned with the source-collimator setup using the beam's-eye-view PC-linked camera (3) as well as the rotatable platform and z-stage for angle and height adjustment (5). Live video feeds via a second PC-linked endoscopic camera will be used for animal tumor alignment as well as monitoring vitals throughout the procedure.

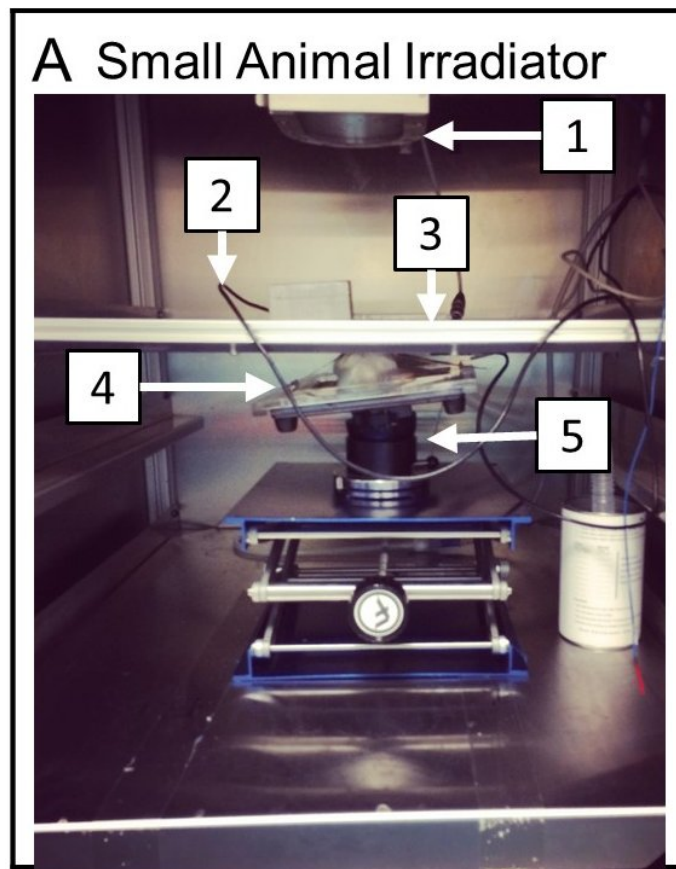


Figure 29: The SFRT treatment delivery system includes (1) the uncollimated treatment source, (2) a live-video feed endoscopic camera that is angled for target viewing and alignment, (3) a lead-alloy collimator and other shielding placed onto an aluminum-reinforced acrylic shelf, (4) a second PC-linked endoscopic camera placed close to the anesthetized animal for treatment monitoring, as well as (5) the height- and angle-adjustable platform for animal positioning under the collimated radiation field.

Prior to irradiating the animal, radiochromic film is placed over the tumor/radiation

target, directly on top of the skin. This is to verify tumor alignment with radiation field during treatment. This film is intended as a second method to verify post-treatment that the radiotherapy beams were aligned with and delivered to the target as intended, though the treatment-verification film has multiple other uses. If any target motion occurs, this may be indicated on the treatment-verification film. Treatment-verification film also ensures that there were no off-target or otherwise unintentional exposures during the course of treatment. These films serve as treatment documentation, for record-keeping purposes, and may be re-examined at a later date if necessary.

3.7 SFRT Delivery System Limitations

Despite the great care and consideration taken for several possible factors that may affect our radiation treatments and setup, there are still several important limitations. First, there is no on-board imaging available for this treatment machine or setup. Clinically, on-board imaging is used regularly and has proven incredibly beneficial for accurate treatment delivery. However, delivering accurate treatments to targets such as tumors or specific internal organs without on-board imaging is very difficult and subject to high incidences of off-target treatments, such as the one shown in Figure 30.

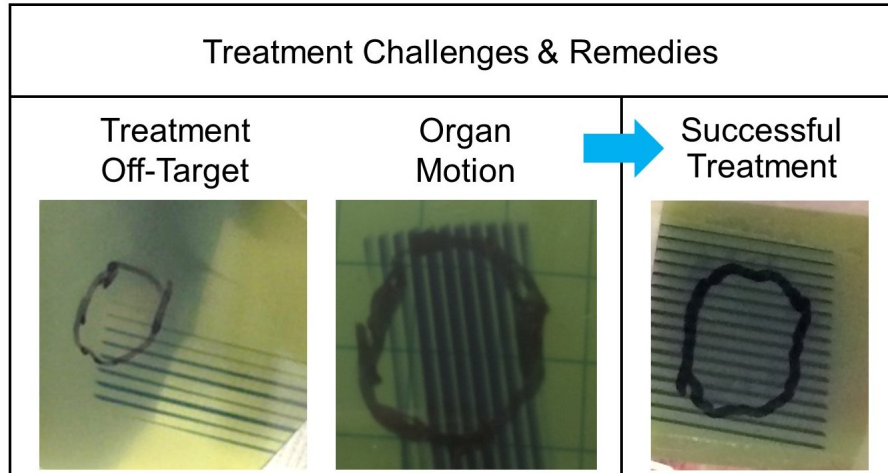


Figure 30: Several challenges were encountered during SFRT delivery system design. Examples of some of these challenges include off-target treatment failure due to a lack of pre-treatment imaging for precise targeting of the SFRT beams to the treatment site and beam smearing caused by animal cardiac or respiratory motion. These challenges were met with creative solutions for overcoming them, involving a combination of several techniques, including developing strategies to minimize their impact such as selectively choosing treatment sites that are distant from motion-causing organs, placing a PC-linked endoscopic camera near the target for target viewing and alignment, and trial and error, among others.

To overcome this limitation, we use several techniques to ensure that we have a high probability of hitting our target. We include a 5mm margin around all gross tumor (or other target) areas to account for variations in shape and position of the target during treatment and decrease the probability of treatment failure. While this inevitably may sub-optimally expose more normal tissues to high doses of radiation, we look to decades of preclinical data that have demonstrated the preferential normal tissue sparing effect and safety of high dose SFRT. Additionally, whenever possible, we use externally visible anatomic markers to identify regions of interest. For example, when targeting a mouse brain for a whole brain irradiation treatment (with rodent lying prone and viewed in the frontal/coronal plane), the mouse cerebellum within the skull very reliably lies inferior to ocular cavity and superior to the ear lobes, a section approximately 1cm long. Furthermore, when viewed in the sagittal plane, the brain reliably occupies half the cranial cavity, lying

inferior to the esophagus/oral cavity. For superficial solid tumor tissues we physically palpate the tumors to identify tumor/normal tissue boundaries and delineate them with permanent marker to visually define them for treatment. In addition to visual external markers, we use a PC-linked live video feed from a small endoscopic camera with a near beam's-eye-viewing angle help align the target with the radiation light field. Finally, the post-treatment verification film is used to verify that we delivered the intended dose to the target as described earlier. However, with no access to onboard imaging, or live video-rate CT, x-ray imaging of the treatment, or *in vivo* during treatment, we have no way of knowing what the animal organs look like or where they are at any given time, so it is nearly impossible to avoid them. Though on-board imaging would be ideal, our error is mitigated with visual and technological tools, and when error occurs, it is reliably identified with post-treatment verification radiochromic film.

A second limitation to our SFRT treatment setup is that all dosimetric calculations do not consider potential effects from cardiac or respiratory motion. Shown in Figure 30, motion blur has the unintended consequence of smearing the sub-millimeter treatment beams and reducing the peak dose while increasing the valley dose such that the delivered dose more closely resembles a conventional radiotherapy treatment, effectively eliminating the potential impact of SFRT. For this reason our radiobiological studies primarily focus on treatment targets that are distant from the source of organ motion, near the animal pelvis or head/neck area. In addition, animals are immobilized as much as is feasible during treatments without restricting breathing. However, even after immobilization and controlling for disease site, there may still be some organ motion effects beneath the skin to consider; therefore, the 5mm margin around the radiation target may also help account for any resulting variation in target shape or position in addition to limiting the target size to fit within this margin. Developing creative solutions to overcoming some of these design and implementation challenges or minimizing their impact is essential for successfully carrying out SFRT treatments.

A third limitation in our SFRT delivery system is the limited treatment planning techniques we have available. While we do have a treatment planning method that uses a combination of dosimetry, modeling on matlab, visual image alignment, etc. these methods do not allow for accurate dose delivery and do not provide dose volume histogram information. However, we do not expect this limitation to impact any of the final study results as these are limitations that affect all study arms throughout each of the studies and not on any specific study arm.

CHAPTER 4: CONVENTIONAL DOSE RATE SPATIALLY FRACTIONATED RADIATION THERAPY TREATMENT RESPONSE AND ITS ASSOCIATION WITH DOSIMETRIC PARAMETERS – A PRECLINICAL STUDY IN A FISHER 344 RAT MODEL

4.1 Overview

Previously, we demonstrated the feasibility of creating a compact and low-cost spatially fractionated radiation therapy (SFRT) delivery system for use in advancing preclinical SFRT research. Despite decades of research showing that SFRT has an enhanced therapeutic ratio over conventional radiotherapy, SFRT remains poorly understood, which hinders its broad clinical translation. One front to advance wide-spread clinical translation of this approach is to identify key SFRT dosimetric parameters that have close associations with treatment outcomes in the hopes of gaining a better understanding of SFRT.

This chapter has been submitted for publication in PLOS One and is in review at the time of this writing². I have included the study here in full and have additionally incorporated several additional figures (Figures 41, 45, 46, and 36) of statistical analysis results as well as their accompanying text throughout the Methods, Results, and Discussion sections. These are included only to elaborate on several ideas presented throughout the paper that was originally condensed for publication.

²This chapter has been submitted as an article in the Journal PLOS One. The original citation is as follows: Rivera JN, Kierski TM, Kasoji SK, Abrantes AS, Dayton PA, Chang SX, *Conventional dose rate spatially-fractionated radiation therapy (SFRT) treatment response and its association with dosimetric parameters – A preclinical study in a Fisher 344 rat model*. PlosONE. 2020 [Manuscript In Review]

4.2 Introduction

Spatially-fractionated radiation therapy (SFRT) is a nonconventional radiation therapy that is characterized by intentionally-created high dose inhomogeneities, ultra-high maximum doses, and single fraction treatments [70], [97]. The dose inhomogeneity consists of many small sub-regions with alternating high and low doses throughout the treatment volume. SFRT includes clinical GRID therapy [70], [77] and preclinical microbeam radiation therapy (MRT) [203], each of which has a decades-long history demonstrating its superior therapeutic ratio compared to conventional radiation therapy, especially in terms of normal organ sparing. Detailed summaries can be found in two recent reviews by Billena and Khan [204] for GRID therapy and by Eling et al. [203], [205] for MRT. Today, there are a number of modern treatment delivery technologies available for clinical SFRT including multi-leaf collimator generated GRID [96], LATTICE [88], [100], [206], Tomotherapy [204], and particle GRID therapy [207], [208]. For preclinical SFRT, newer technologies include “minibeams” with larger spatial fractionation scales (on the order of millimeter instead of the tens of microns used in classical MRT) [209], [210] and with conventional dose-rates [180], [186]. Most published MRT research utilized brilliant x-rays generated from synchrotron accelerator facilities with ultrahigh dose rates [203]. The conventional dose rate SFRT radiations, such as the ones used in this study, are highly relevant to translational research for LINAC-based SFRT clinical applications, where conventional dose rates are also used.

Despite the long history and well demonstrated therapeutic ratio advantage over conventional uniform dose radiation therapy, SFRT remains an experimental therapy. There are several reasons attributed to the sluggish clinical translation progress including a lack of understanding of SFRT working mechanisms and of the association between SFRT treatment response and dosimetry. While we have verified treatment dosimetry and tumor control outcome correlations for conventional radiation therapy (i.e., tumor

minimum dose and Equivalent Uniform Dose (EUD) are closely correlated with tumor control) [211]; however, we do not yet have such understanding for SFRT, which has significantly more complex dosimetry than that of conventional radiation therapy. Unique SFRT dosimetric parameters that describe the dosimetry include peak dose, valley dose, peak-to-valley-dose-ratio, peak width, valley width, and percentage tumor volume directly irradiated. It is reasonable to assume that not all these dosimetric parameters have the same clinical significance. To effectively advance SFRT clinical translation it is critically important to identify which parameters have strong/weak associations with a given treatment response.

The goal of this study is to identify key dosimetric parameters that are most closely associated with treatment response using a preclinical animal model. We hypothesize that while peak dose has always been used to prescribe SFRT treatment for both clinical and preclinical applications, peak dose may not be the dosimetric parameter most closely associated with SFRT tumor control or treatment toxicity. If it is not, which SFRT dosimetric parameters are? Further, we ask that, for a given pattern of SFRT treatment, what is its conventional radiation therapy equivalence for a given treatment response? The answers to these questions are crucial to advance clinical translation of SFRT. Unfortunately, decades of synchrotron-based MRT studies may not be able to answer these questions due to the use of ultrahigh dose rates (1000sGy/sec) [212]. Recent research on FLASH radiation has shown that radiation with dose-rates of 100Gy/s or higher selectively spares normal tissue not tumor [203], [213], [214]. This new finding revealed that the ultrahigh dose-rate alone is partially responsible for the observed high therapeutic-ratio demonstrated in the majority of SFRT research published so far [203]. This study will help discern the impact of radiation spatial fractionation at dose rates relevant to clinical SFRT treatments.

Today, SFRT is receiving much deserved renewed attention and enthusiasm in the field of radiation oncology. In 2018 National Cancer Institute and Radiosurgery Society jointly held the first workshop on Understanding High-Dose, Ultra-Dose-Rate and Spatially

Fractionated Radiotherapy and created three standing working groups (clinical, biology, and physics) aiming to provide guidelines on SFRT research and clinical application [215]. We hope this work will assist in this endeavor by shedding light on the clinical impact of SFRT dosimetry parameters.

4.3 Materials and Methods

4.3.1 Study design

The secret of SFRT lays in its radiation dose spatial fractionation. Although this work does not address the very much needed understanding of working mechanism it addresses another important matter for SFRT application - the association of SFRT dosimetric parameters with treatment response at conventional dose rates (dose rate ranges from 4.27 to 5.25Gy/min was used). Figure 31 shows a six-arm study design using a very large span of radiation spatial fractionation, constructed to explore the impact of radiation spatial fractionation. The table in Figure 32 summarizes the dosimetric parameters of each of the six arms. To study the effect of radiation spatial fractionation under the condition of equal volume-averaged dose we used the following four study arms: 20GyUniformRT (entire tumor directly irradiated), 20GyHalfRT (only one-half of tumor directly irradiated), 20Gy2mmSFRT (50% of tumor directly irradiated by 2mm-wide planar beam array), and 20GySFRT (20% of tumor directly irradiated with 0.3mm-wide planar beam array). Note that the doses are volume-averaged doses computed for the entire tumor volume. A 50GySFRT arm (50Gy volume-averaged dose, beam width 0.31mm) is added as it has a peak dose of 225Gy, which is within the known minibeam peak dose range showing tumor control. To account for unavoidable variations in tumor position under the 20Gy2mmSFRT treatment beams during animal irradiations, we computed the maximum and minimum beam coverage positions and calculated their corresponding dosimetric specifications. The 20Gy2mmSFRT treatment arm dosimetric values reported in Table 1 correspond to the

average at these positions for a 10mm diameter tumor. For example, a 10mm sized tumor is irradiated by at most three 2mm-peaks and at minimum two 2mm-peaks and the average dosimetric parameter at these two positions was calculated.

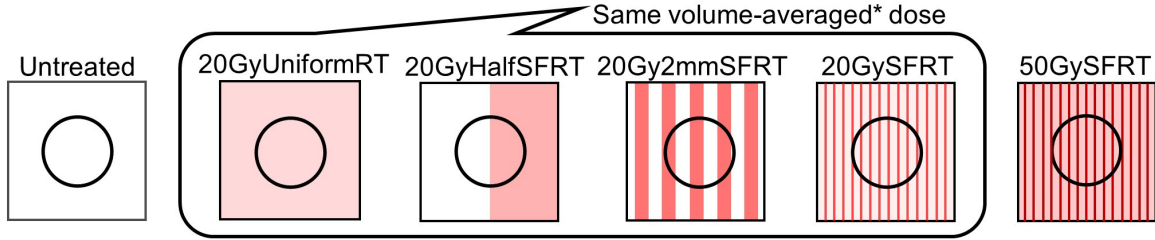


Figure 31: A very large range of radiation spatial fractionation scale was used to derive the impact of radiation spatial fractionation. Four arms share the same 20Gy volume-average dose. The high dose 50GySFRT arm is added because 20GySFRT is not known to have tumor control. The dosimetric parameters studied and number of animals per study arm are listed in 32.

Summary of nine SFRT Dosimetric parameter specifications in the six-arm study									
Treatment Arm	# of Animals	Vol-Avg Dose ^a (Gy)	Peak Surface Dose (Gy)	Valley Surface Dose (Gy)	EUD (T ^a /N ^e)	PVDR	Valley Width (mm)	Peak Width (mm)	% Volume Irradiated
Untreated	8	0	0	0	0	N/A	0	0	0
20GyUniformRT	8	20	20.8	20.8	19.9/20.1	1	20	20	100
20GyHalf-SFRT	5	20	39	3.1	2.9/30.5	12.6	10	10	47.8(±2.2) ^d
20Gy2mmSFRT ^c	6	17.6 ^b	34.5	6.2	5.2/25.1	5.6	2	2.2	51.5(±11.6)
20GySFRT	9	20	91	6.8	5.3/47.4	13.3	0.9	0.31	20.3
50GySFRT	6	50	225	16.8	13.1/117.3				

^a: Computed within 1cm depth (the tumor depth).

^b: 17.63Gy instead of the intended 20Gy was used.

^c: Dosimetric parameters for 20Gy2mmSFRT arm computed considering the maximum range of possible tumor positioning under the collimator.

^d: Percentage volume irradiated for the 20GyHalfSFRT arm was computed using treatment verification film analysis of the irradiated tumors.

^e: T/N denotes Tumor EUD and normal tissue EUD. Tumor EUD is computed using $a = -10$ for 1cm diameter tumor. Normal tissue EUD is computed using $a = 5$ and 2cm diameter normal tissue volume. Note tumor EUD is lower than valley surface dose because valley dose is measured at surface while EUDs are computed using volumetric dose.

Figure 32: Summary of nine SFRT dosimetric parameter specifications in the six-arm study.

Custom-made radiation blocks and collimators made of Cerrobend or tungsten were used to define the $2\text{cm} \times 2\text{cm}$ field for 20GyUniformRT arm treatment, the $2\text{cm} \times 1\text{cm}$ for 20GyHalfSFRT treatment, and the beamlet array $2\text{cm} \times 2\text{cm}$ fields for both the 20Gy2mmSFRT and 20Gy/50GySFRT treatments. The 2cm field size in the direction of the uniform dose within each of SFRT planar beams is made possible by the very large focal spot size (8mm^2) of the XRad irradiator (Precision X-ray Inc., North Branford, CT USA). All irradiations in this study used the same irradiator.

4.3.2 Animal tumor model

This study was carried out in strict accordance with the recommendations in the Guide for the Care and Use of Laboratory Animals of the National Institutes of Health (NIH). The University of North Carolina- Chapel Hill Institutional Animal Care and Use Committee (IACUC) reviewed and approved the animal protocol (IACUC ID: 15-366.0) in accordance with NIH standards. All animal surgical, radiation, and imaging procedures were performed under general anesthesia and all efforts were made to minimize suffering.

Forty-two eight-week-old female Fischer 344 rats from Charles River Labs and rat fibrosarcoma tumor allografts were used [216]. The rat fibrosarcoma (FSA) allograft model has been well characterized in several radiotherapy response studies by our and collaborator labs [216]–[218]. Rat FSA is characterized as a local, non-metastasizing tumor that is highly vascular and oxygen dependent [219], [220]. It is an appropriate tumor model for our long-term study goal that investigates the association of SFRT dosimetric parameters with treatment responses, which is reported here, and the association between SFRT treatment response and tumor vascular change post radiation using 3D acoustic angiography. The latter is ongoing research for future publication.

All surgical, radiation, and imaging procedures were performed under general anesthesia, induced in the animals initially using 5% vaporized isoflurane mixed with pure oxygen as the carrier gas and then maintained at 2.5% isoflurane mixed with pure oxygen throughout

each procedure. Depth of anesthesia was monitored by toe pinch reflex and breathing rate. Ophthalmic ointment was placed on the animal’s eyes during anesthesia to provide lubrication and body temperature under anesthesia was maintained via electronically controlled heating pad. Tumors were grown in each rat by implanting freshly resected tumor tissue ($1mm^3$) that was harvested from tumor-bearing donor rats into the subcutaneous space of the rodent flank using blunt dissection. Postoperative care included daily incision surveillance, body temperature monitoring, and a water bottle containing 6mg/mL cherry-flavored, dye-free children’s Tylenol diluted in water for a minimum of 24-hrs post-surgery to alleviate any associated pain from the implantation procedure. Animals were used for experiments 2-3 weeks post-implantation, when the tumors reached the target RT treatment size of approximately 5-10mm.

In preclinical studies the pre-treatment tumor volume is known to be strongly correlated with treatment tumor control [216]. We minimize this unwanted effect by controlling the pre-treatment tumor volume in a randomized, matched group study design. We binned animals according to their pre-treatment tumor volume and then randomly assigned these matched bins of animals such that at least one animal from each bin is assigned to each treatment group. This technique resulted in an average initial tumor volume across groups of $566 \pm 47mm^3$ on RT treatment day. Biological variability was minimized by ordering animals from the same vendor and of the same age (6 weeks old), implanting tumor on the same day and from the same donor animal, treating with radiation on the same day, and housing animals in the same Vivarium location with identical husbandry conditions. All animals (mixed caged) were provided identical standard laboratory rodent diets of (23% > crude protein) and water ad libitum throughout the study. In addition, all animal diets were supplemented with high-calorie, nutritionally fortified water-based gel cups to help mitigate any potential significant weight loss and dehydration post-radiation.

The animals body weight and tumor volumes are monitored prior to radiation and every third day thereafter for up to 30 days. Study endpoints are maximum tumor burden

(2.5cm or larger in any dimension), weight loss in excess of 15%, body condition scores [221] less than or equal to 2, or other signs of pain, discomfort, or moribundity as recommended by University of North Carolina- Chapel Hill Division of Comparative Medicine veterinary staff. Animals that met study end-point criteria will be ethically euthanized primarily via compressed carbon dioxide gas or vaporized isoflurane overdose followed by thoracotomy as a secondary means of physical euthanasia per the approved animal study protocol.

4.3.3 Animal radiation dosimetry

XRad Irradiator and 320kV x-rays were used in this study. Surface dose rates ranging from 4.27 to 5.25Gy/min were used for all study arms. Figure 33 shows the treatment setup, the radiation light field on animal seen by the camera, and treatment verification films. Dosimetry was measured via EBT-3 film calibrated by an ADCL-calibrated ion chamber under large field conditions.

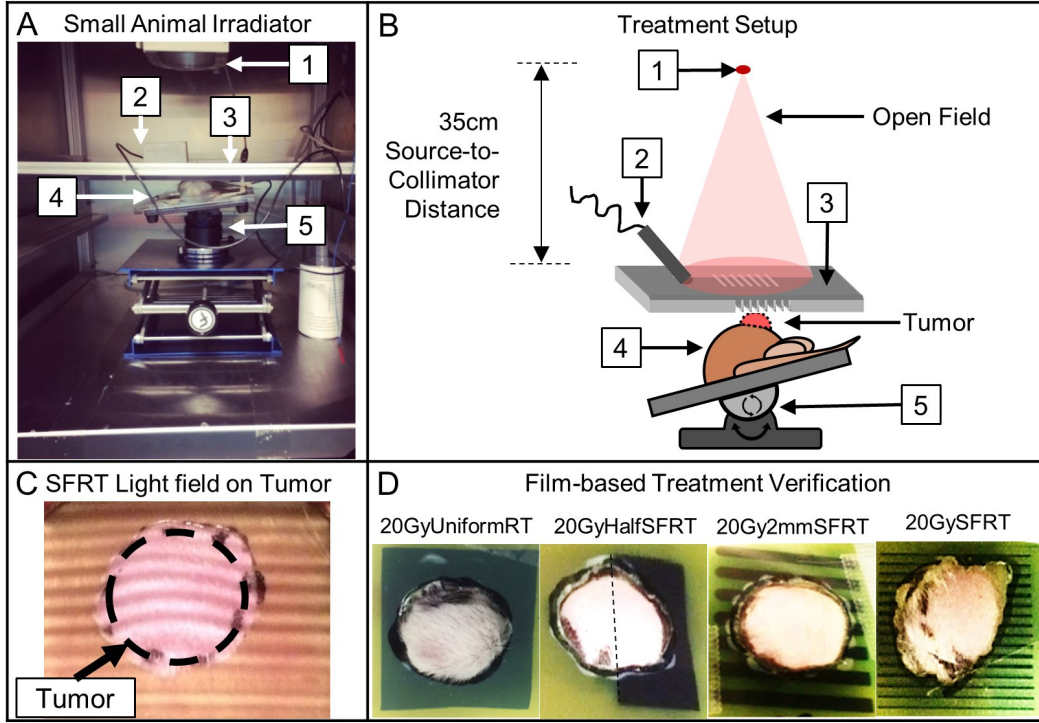


Figure 33: Animal irradiation setup and treatment alignment and verification. (*A – B*) The treatment setup components include (1) X-ray source, (2) endoscopic camera (lens shielded), (3) field shaping collimator for all treated arms (20GySFRT shown), (4) animal and tumor, and the (5) 3-axial heated animal positioning stage. (*C*) Photo of the built-in irradiator light shines through the 50GySFRT collimator and onto the outlined tumor as seen from the beams-eye view camera (live feed used to position tumor within the treatment fields.) (*D*) EBT-3 treatment verification films with a cutout in the tumor region. The films were reviewed for all treated animals for treatment targeting verification.

Acrylic phantom measurement setup and beam profile and percentage depth dose (PDD) dosimetry are shown in Figs 3 and 4. The volume-averaged tumor dose was approximated by computing the film average dose within an area of 1cm by 1cm (depth) of the PDD film. The differential dose volume histograms of the PDD films were used for tumor and normal tissue EUD calculations as described by Niemierko [222] using values of $a = -10$ for tumor and $a = 5$ for normal tissue and the resulting computed EUDs are shown in Figure 36.

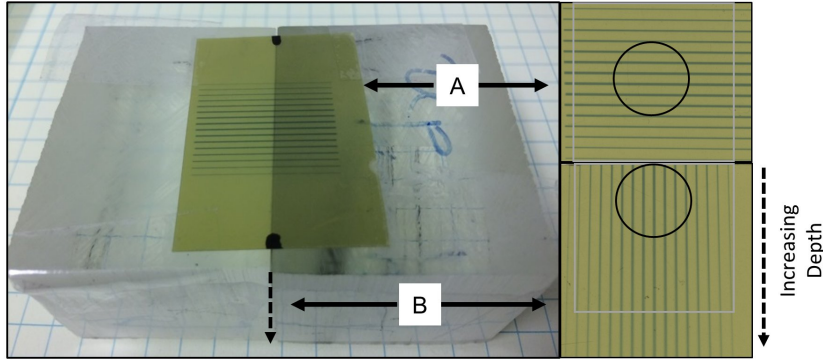


Figure 34: EBT-3 films were calibrated by ion chamber under large field conditions. All beam profiles and corresponding percentage depth dose were measured using two films as shown: one is on the surface perpendicular to radiation beam (A) and one sandwiched between two small phantom blocks parallel to radiation beam (B). The circles indicate the film areas used for volume-average dose calculation estimates. The following assumption was made for volume-averaged tumor dose and EUD calculations: dose value does not vary $+/- 1\text{cm}$ along the direction parallel to the same valleys/peaks.

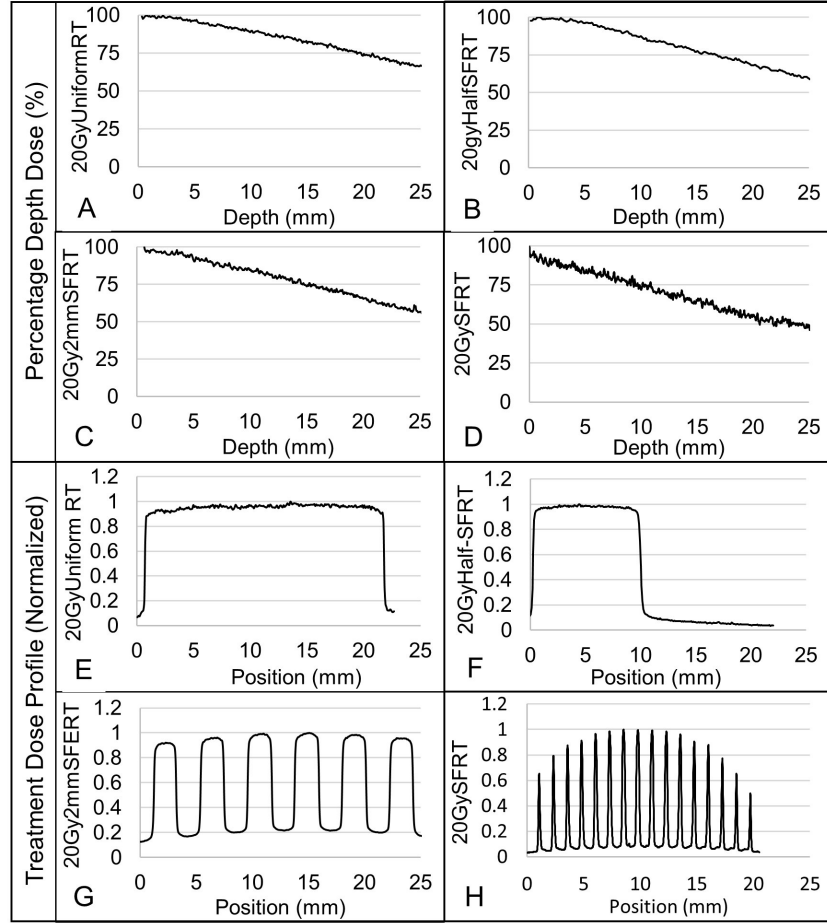


Figure 35: (A – D) Figures display the percentage depth doses for each of the 20Gy volume-averaged treatment arms. (E – H) Figures display the corresponding SFRT beam profiles for each of the 20Gy volume-averaged treatment arms. Note that the 20GySFRT and 50GySFRT arms share the same SFRT collimator and thus the same relative dosimetry. The large non-uniformity of the peak doses in the SFRT radiation is due to the finite x-ray target size and the nondivergence of the SFRT collimator. However, the actual peak dose non-uniformity in the treated tumor (diameter of 10mm) is within 10%.

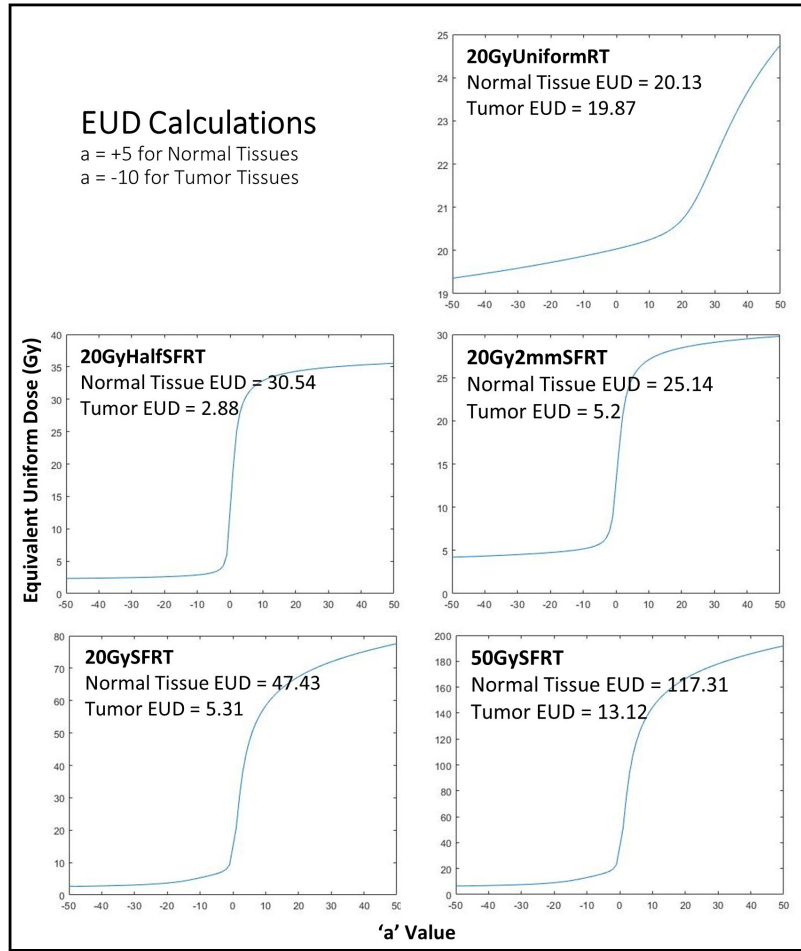


Figure 36: Tumor and normal tissue Equivalent Uniform Dose, EUD, calculations are shown for the different collimators used in each of the 5 radiotherapy treated arms. EUD dose calculation is a relatively new technique for summarizing inhomogenous dose distributions under the assumption that they are "equivalent" if the induce the same radiobiological effects. EUD was calculated using the differential dose volume histogram of the PDD film-based dose distribution and the expected number of surviving clonogens within the tumor as described by Niemierko [222].

EUD dose calculation is a relatively new technique for "summarizing and reporting inhomogeneous dose distributions" developed by Niemierko [222]. It assumes that any two non-uniform dose distributions are considered equivalent if they cause the same radiobiological effect. For calculating EUD, we estimate that the dose distribution within the tumor does not vary significantly along the 1cm length of the tissue in the direction of the valley or peak dose regions. This allows us to compute EUD using the differential dose

volume histogram of the PDD film (depth) as well as the expected number of surviving clonogens within the tumor as described by Niemierko [222].

4.3.4 Animal radiation delivery and verification

All of the RT collimators were aligned with x-ray target of the irradiator using film dosimetry. Animals were anesthetized with vaporized isoflurane mixed with oxygen carrier gas and positioned on an electronically controlled heating pad (Figure 33, panels A and B). For radiation tumor targeting we used the light field and a PC-linked camera before radiation and verified it with film dosimetry during each irradiation (Fig 2, panel C). Live video-feed from the camera was used for animal tumor-radiation alignment and for animal monitoring during treatment. Radiation targeting is achieved by (a) delineating the tumor boundary on animal skin using marker pre-treatment, (b) transferring the marking onto the verification EBT-3 film taped on skin and cutting out the tumor portion of the film, (c) taping the film back with the tumor inside the cutout, (d) placing the animal in the irradiator and align the tumor with the radiation, and (e) animal monitoring throughout irradiation. The treatment verification films were reviewed post-radiation for radiation targeting documentation (Figure 33, panel D).

4.3.5 Tumor volume imaging and body weight monitoring

Three-dimensional B-mode ultrasound imaging of the tumors was performed using a Vevo 770 preclinical ultrasound scanner (Vevo 770, VisualSonics, Toronto, ON, Canada) and the resulting images used to calculate tumor volume, as described in a previous publication [216]. Imaging was performed on the day before treatment as well as every third day post-treatment for approximately 30 days, or when maximal tumor burden was met, at which point the animals were humanely sacrificed per IACUC-approved animal protocol. 37 shows an illustration of the 3D ultrasound tumor imaging setup and acquisition. Three-dimensional imaging is performed by mechanically stepping the

ultrasound probe in the elevational dimension and acquired a two-dimensional image at each step (100 μ m step size, 2cm elevational scan length). The reconstructed 3D ultrasound images were used to calculate tumor volume. The longest orthogonal tumor dimensions in each 3D image were measured using the digital caliper feature on the Vevo 770 imaging software and tumor volume was approximated using the volume formula for an ellipsoid, $V = \frac{4}{3}\pi a \times b \times c$, where V is the calculated tumor volume, and a , b , and c are each the half lengths of the principal axes of the tumor [223]. A sample tumor volume change post radiation from a 20GyHalfSFRT arm animal shows no tumor control (Figure 37, panel D). Animal body weight was measured using the same schedule.

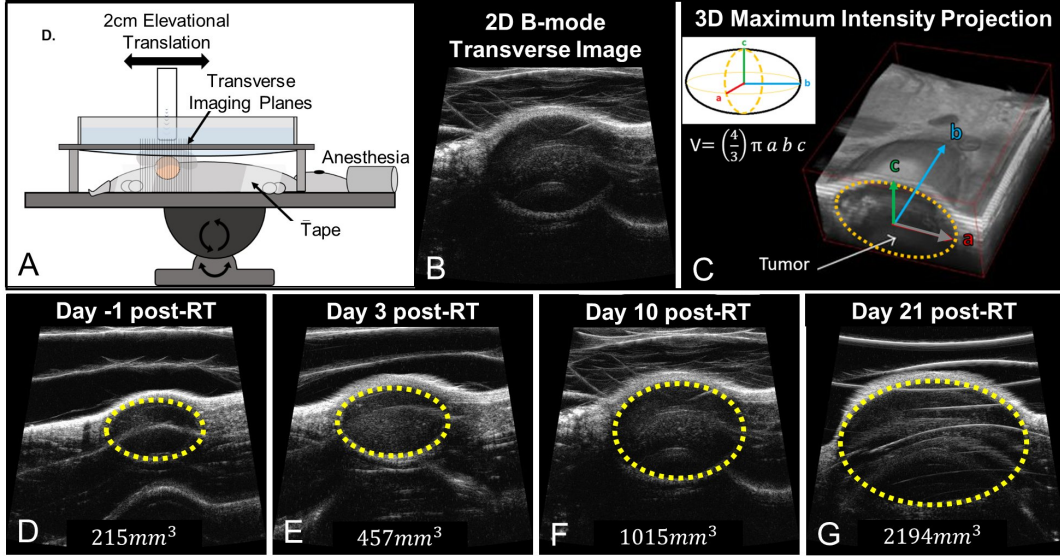


Figure 37: Figure (A) is an illustration of the 3D ultrasound imaging setup with anesthetized animal [216]. Two-dimensional transverse image slices (B) are acquired along the elevational direction and are then reconstructed into 3D images [224] (C). Tumors are visually identified on the ultrasound images. Resulting 3D images (C) are used to measure the tumor dimensions and calculate tumor volume. Imaging data is acquired pre-treatment (D) and every third day thereafter (E – G). In images D-G the tumor (yellow dotted line) and corresponding tumor volume grow over time following a 20GyHalfSFRT treatment.

4.3.6 Association between SFRT dosimetry and treatment response

We analyzed the associations between animal treatment responses and each of the nine dosimetric parameters, listed in the table in Figure 32. The treatment responses are time-to-euthanasia, proportion of animals surviving to Day 17, and change in animal body weight on Day 17. We deem animal survival is a better indicator of tumor treatment response than tumor size change in this study. When tumors reach the maximum tumor mass, defined by the IACUC-approved animal protocol, ethical euthanasia is performed. As a result, animal numbers in different study arms decrease at different rates, which can introduce biases due to unbalanced sample sizes in the study. Hence, Day 17 was chosen for the linear regression association studies because at this timepoint there is a good compromise between the number of animals available for statistical consideration and the magnitude of radiation effects (20GyUniformRT $n = 8$, 20GyHalfSFRT $n = 3$, 20Gy2mmSFRT $n = 4$, 20GySFRT $n = 4$, 50GySFRT $n = 5$, Untreated $n = 0$). We also fit a more robust Cox Proportional Hazards (CoxPH) model to the full data set that includes all animals. Animal body weight change on Day 17 is used as an indicator of treatment toxicity. Animal body weight change is a gross assessment on treatment toxicity, especially in this study where tumors were implanted in the rodent flank, near the lower gastro-intestinal tract (including the rodent anus, rectum, colon, and cecum) and parts of the upper gastro-intestinal tract (including portions of the small bowel). We speculate that some treatment arms may induce more GI toxicity than others. We subtracted the tumor weight from the measured body weight and regard this “net” animal body weight change as an indication, not confirmation, of treatment toxicity. To confirm any lower GI toxicity, additional tissue histological staining or organ function examination studies would be necessary, both of which are beyond the scope of this work.

4.3.7 Statistical methods

We computed Product-Limit (Kaplan-Meier) Estimator and Logrank (Mantel-Haenszel) test for statistical significance of survival difference between each pair of treatment arms [225]. Multiple simple linear regression models [226] were used to study the association between dosimetric parameters with animal body weight and percentage survival within treatment group on Day 17. R^2 (square of the Pearson correlation) coefficient is computed to estimate the proportion of variance explained in each of the linear regression models. In general, the greater the magnitude of the test statistic (t or F), the more closely associated the dosimetric parameter studied is with the treatment response (survival or body weight). In addition to linear regressions, we fit Cox Proportional Hazard (CoxPH) models with individual animal survival as the time-to-event outcome, which used data from all dates including Day 17. This allowed us to calculate the hazard ratio associated with the impact of dosimetric parameters on treatment response. We also used hierarchical linear regression analysis of predictors to show the association of dosimetric parameters to body weight change as well as a Pearson Correlation matrix to show the cross-correlation between each pair of the dosimetric parameters. All data collected were analyzed using R (version 3.5.3) statistical software available from R Core Team [227] .

4.4 Results

4.4.1 Overall treatment response

Figure 38 shows (A) animal survival, (B) normalized tumor volume, and (C) normalized body weight post treatment for all 6 study arms. Figure 39 also shows the non-normalized tumor volume in units of mm^3 . In this study no animal died of body condition deterioration. All endpoints were due to ethical animal euthanasia triggered by tumors exceeding the maximum allowable burden per IACUC-approved animal protocol limitations. Our data shows that the 20GyUniformRT arm has the best tumor control followed by the 50GySFRT

and 20Gy2mmSFRT arms. Note that among the four arms sharing similar volume-averaged dose (20Gy or 18Gy) survival varies greatly, from 33% to 100% on Day 17, which is a strong indication that volume-averaged dose is poorly associated with tumor treatment response. The tumor volume data indicate that although 50GySFRT arm and 20Gy2mmSFRT arm have similar survival the former has a better tumor volume reduction than the latter arm. Only the 20GyUniformRT arm experienced weight loss post-treatment and then recovered back to pre-treatment weight after week three. The 20GySFRT and 20Gy2mmSFRT arms experienced similar body weight gains as the untreated arm, indicating little treatment toxicity from the two SFRT treatments.

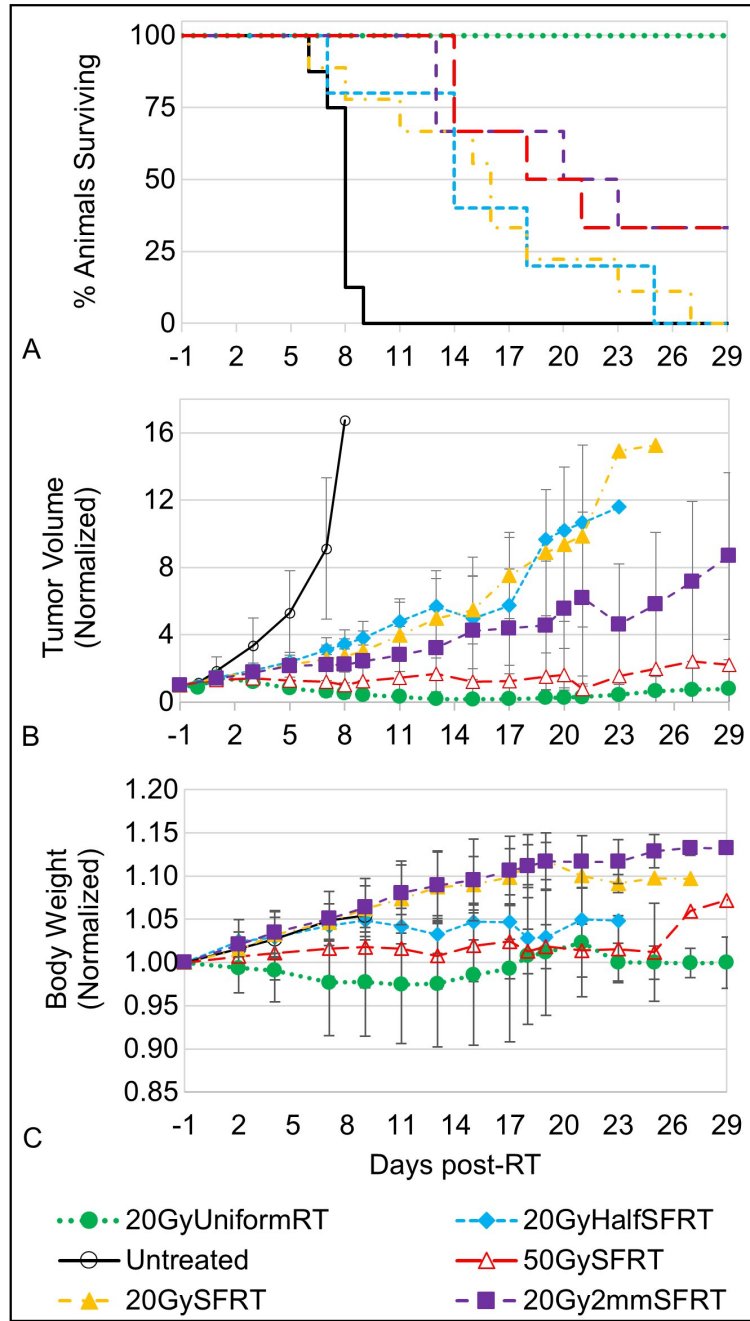


Figure 38: Animal survival (A), normalized tumor volume (B), and normalized body weight (C) are shown for all six study arms. The differences between survival curve pairs are significant ($p < 0.05$) for 20GyUniformRT-50GySFRT, 20GyUniformRT-20GyHalfSFRT, 20GyUniformRT-20Gy2mmSFRT, 20GyUniformRT-Untreated, Untreated-20GySFRT, Untreated-20Gy2mmSFRT, Untreated-50GySFRT, and Untreated-20GySFRT, and moderately significant ($0.1 > p > 0.05$) for 20GyHalfSFRT-50GySFRT, 20Gy2mmSFRT-50GySFRT, and 20GySFRT-50GySFRT.

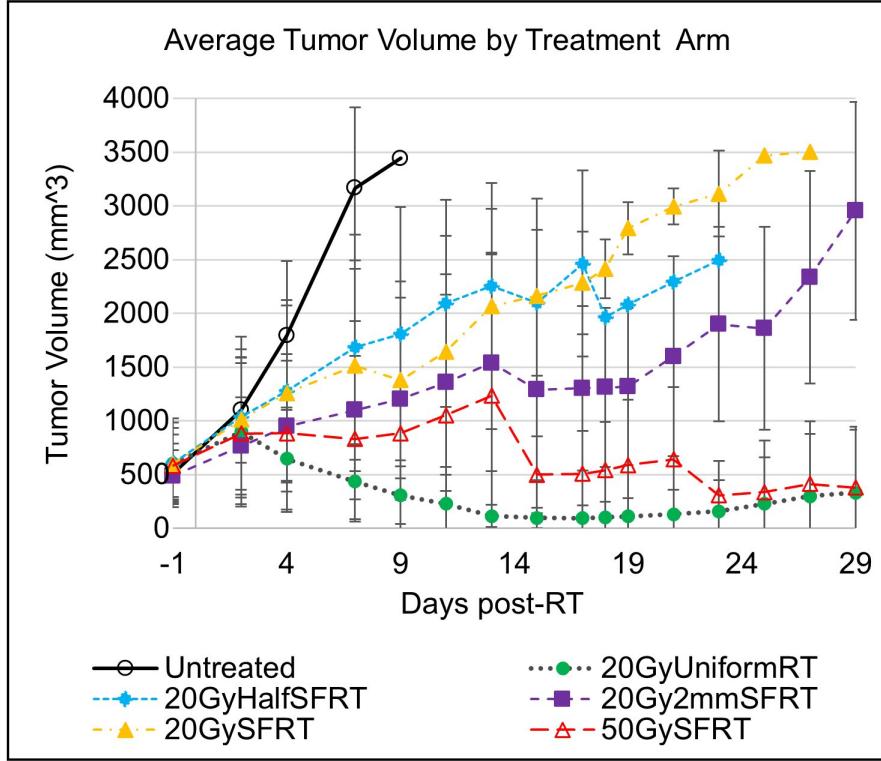


Figure 39: Tumor volumes for all animals within each treatment arm are averaged and then plotted over time in units of mm^3 . Error bars represent one standard deviation from the mean.

4.4.2 Association between tumor response and SFRT dosimetry

We associated eight dosimetric parameters with percentage of animals surviving to Day 17 and with the survival curves shown in Figure 38. Figure 40 shows scatter plots of eight tumor-related dosimetric parameters vs. percentage survival at Day 17, each fitted with a corresponding regression line, R^2 (Figure 40). In addition, Figure 41 is the table of coefficients for the corresponding linear regression models used in Figure 40. The table contains 8 models with single covariates, one for each dosimetric parameter and their corresponding statistics. Tumor EUD ($R^2 = 0.7923$, $F - stat = 15.26^*$), Valley dose ($R^2 = 0.7636$, $F - stat = 12.92^*$), and percentage volume directly irradiated ($R^2 = 0.7153$, $F - stat = 10.05^*$) are the top three most statistically significant dosimetric parameters in terms of association with the animal survival at Day 17 (see Figure 41). Peak

dose ($R^2 = 0.04472$, $F - stat = 0.6874$ (not sig.)) and AVG Dose ($R^2 = 0.2745$, $F - stat = 1.514$ (not sig.)) showed little association with survival.

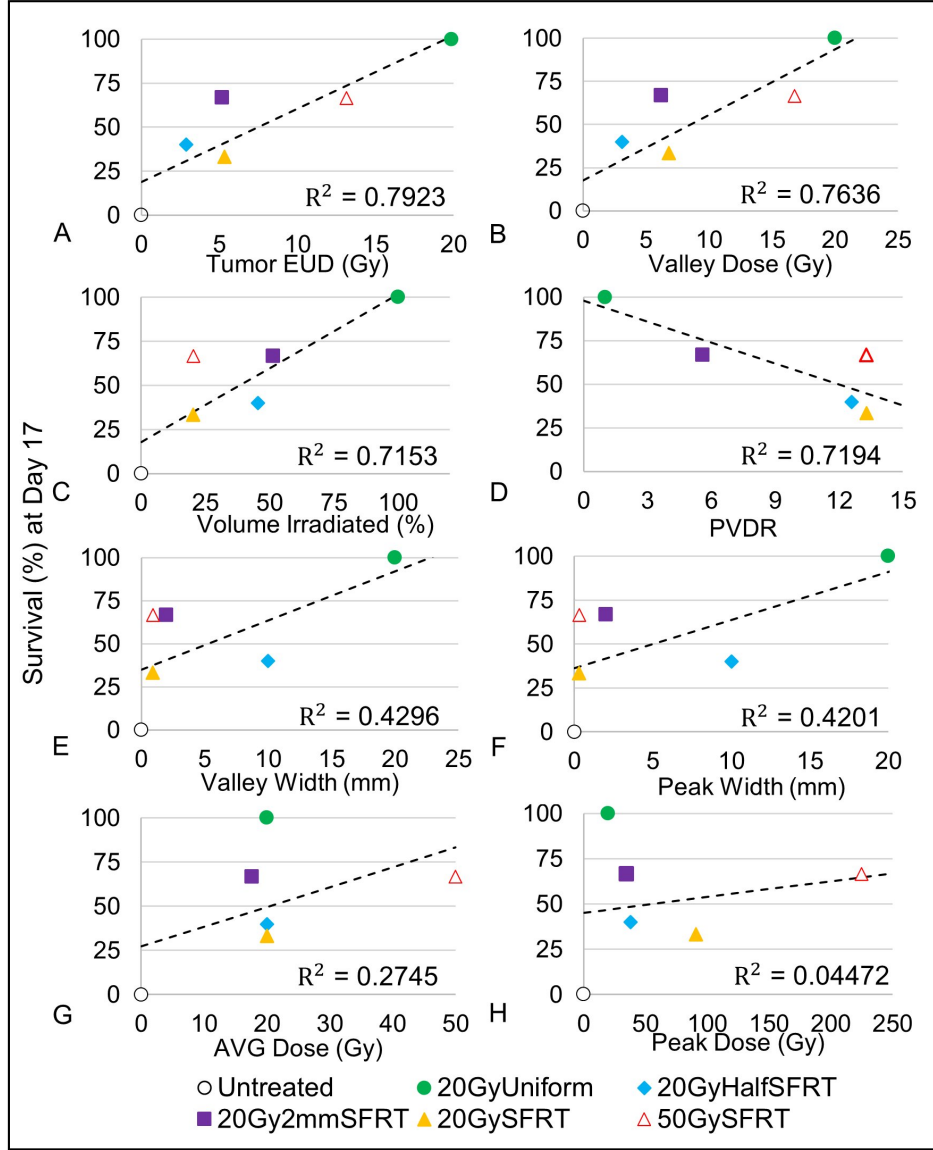


Figure 40: Tumor EUD (A), valley dose (B), percentage volume irradiated (C), valley width (D), peak width (E), volume-averaged dose (F), peak dose (G), and PVDR (H) vs survival (%) at Day 17 are presented as well as their corresponding regression lines and R^2 values. Eight linear regression models with single covariates, one for each dosimetric parameter, were used to calculate the R^2 value and corresponding statistics.

Univariate linear regression analysis of Survival Day 17				
Dosimetric Parameter	Estimate (StdErr)	R ²	t statistic	F-statistic
Tumor EUD	4.155 (1.064)*	0.7923	3.906*	15.26*
Valley Dose	3.711 (1.032)	0.7636	3.595*	12.92*
PVDR	-4.002 (1.443)	0.7194	-2.773	7.691
% Vol. Irr.	0.8289 (0.2615)	0.7153	3.170*	10.05*
Valley Width	2.842 (1.637)	0.4296	1.736	3.012
Peak Width	2.766 (1.625)	0.4201	1.702	2.898
AVG Dose	1.1205 (0.9107)	0.2745	1.230	1.514
Peak Dose	0.0883 (0.204)	0.04472	0.433	0.6874
<i>P values: *p<0.05, **p<0.01</i>				

Figure 41: Univariate linear regression analysis of Survival on Day 17.

Analyzing data for a single timepoint (Day17) is limited by animal losses at Day 17 (ie: missing data). To validate the above finding in Fig 7 we used data from the entire survival curves in Univariate Cox Proportional Hazards analysis, a more robust statistical model that utilizes all of the data, and the results are shown in Table 3. The results from the Univariate Cox Proportional Hazards analysis confirms the results from the linear regression analysis - among the eight dosimetric parameters analyzed tumor EUD ($z - stat = -4.07 **$), valley/min dose ($z - stat = -4.338 **$), and percentage tumor volume directly irradiated ($z - stat = -3.837 **$) have the closest associations with animal survival. Compared to the linear regression analysis (Fig 7) the improved p-values in the CoxPH model analysis is likely due to the increased sample size. The Hazard Ratio shows the impact of change in each of the dosimetric parameters to the hazard rate (risk of death). For instance, when valley/min dose parameter changes by 1 Gy, the hazard rate (risk of death) changes by 19% (95% CI, 26% – 11%) with p-value of 1.44×10^{-5} . For a 1Gy change in peak dose, the corresponding change in hazard rate is 0.2% (95% CI, 0.7% - 0.3%) with p-value of 0.432. Three additional statistical tests were used to validate the CoxPH z-test statistics results for each model (Likelihood Ratio Test, Wald Test, and

Logrank Test) and all three tests largely agree with the results presented in Figure 42.

Table of Coefficients for Univariate Cox Proportional Hazards analysis of Survival				
Dosimetric Parameter	Estimate (StdErr)	Hazard Ratio [95% CI]	Test Stat (z)	P value
Valley Dose	-0.20947(0.04828)	0.81 [0.74 0.89]	-4.338***	1.44x10 ⁻⁰⁵
Tumor EUD ^a	-0.2650 (0.06511)	0.77 [0.68 0.87]	-4.07***	4.7x10 ⁻⁰⁵
% Vol. Irradiated	-0.04089 (0.01066)	0.96 [0.94 0.98]	-3.837***	1.25x10 ⁻⁰⁴
PVDR	0.1835 (0.06016)	1.20 [1.07 1.35]	3.05**	2.29x10 ⁻⁰³
Peak Width	-0.1227 (0.0406)	0.88 [0.82 0.96]	-3.024**	2.5x10 ⁻⁰³
Valley Width	-0.1312 (0.04366)	0.88 [0.81 0.96]	-3.005**	2.65x10 ⁻⁰³
AVG Dose	-0.0687 (0.02444)	0.93 [0.89 0.98]	-2.811**	4.91x10 ⁻⁰³
Peak Dose	-2.150x10 ⁻⁰³ (2.74x10 ⁻⁰³)	0.998 [0.993 1.003]	-0.786	0.432

*P values: *p<0.05, **p<0.01*

^a: Tumor tissue equivalent uniform dose calculated using $a=-10$.

Figure 42: Table of coefficients for univariate Cox Proportional Hazards analysis of survival.

4.4.3 Association between body weight change and SFRT dosimetry

Eight dosimetric parameters are associated with the body weight change on Day-17. Note that the body weight is the measured body weight subtracted the measured tumor weight to remove the influence of tumor size on the analysis. Figure 43 is a scatter plot of the dosimetric parameters vs. the “net” body weight at Day 17. This time point was chosen for both the tumor and body weight study because it is a good compromise between data statistics and magnitude of treatment response. The table in Figure 44 is a table of coefficients for the corresponding linear regression models used in Figure 43. In general, the greater the magnitude of the t statistic, the greater the individual parameter association with Body Weight (Day 17). For the F-statistic, the greater the statistic value, the more closely associated the model is with Body Weight (Day 17). Based on the t statistics and F-statistics, among the eight dosimetric parameters studied the Valley Dose has the greatest, yet modest, association with Body Weight (Day 17). The order of decreasing association with the body weight change are: valley dose ($R^2 = 0.3814$, $F - stat = 13.45 * *$), valley

width ($R^2 = 0.2853$, $F - stat = 8.783*$), peak width ($R^2 = 0.2759$, $F - stat = 8.382*$), percentage volume irradiated ($R^2 = 0.1985$, $F - stat = 5.448*$), PVDR ($R^2 = 0.1203$, $F - stat = 3.009$ (not sig.)), volume-averaged dose ($R^2 = 0.03308$, $F - stat = 0.7526$ (not sig.)), normal tissue EUD ($R^2 = 1.022 \times 10^{-03}$, $F - stat = 0.882$ (not sig.)), and peak dose ($R^2 = 5.99 \times 10^{-06}$, $F - stat = 1.32 \times 10^{-04}$ (not sig.)). A strong similarity between the peak width and valley width association with body weight is expected (see discussion in section 4.5.3.5). Further, no significant association is observed between body weight change post radiation and PVDR, average dose, normal tissue EUD, and peak dose.

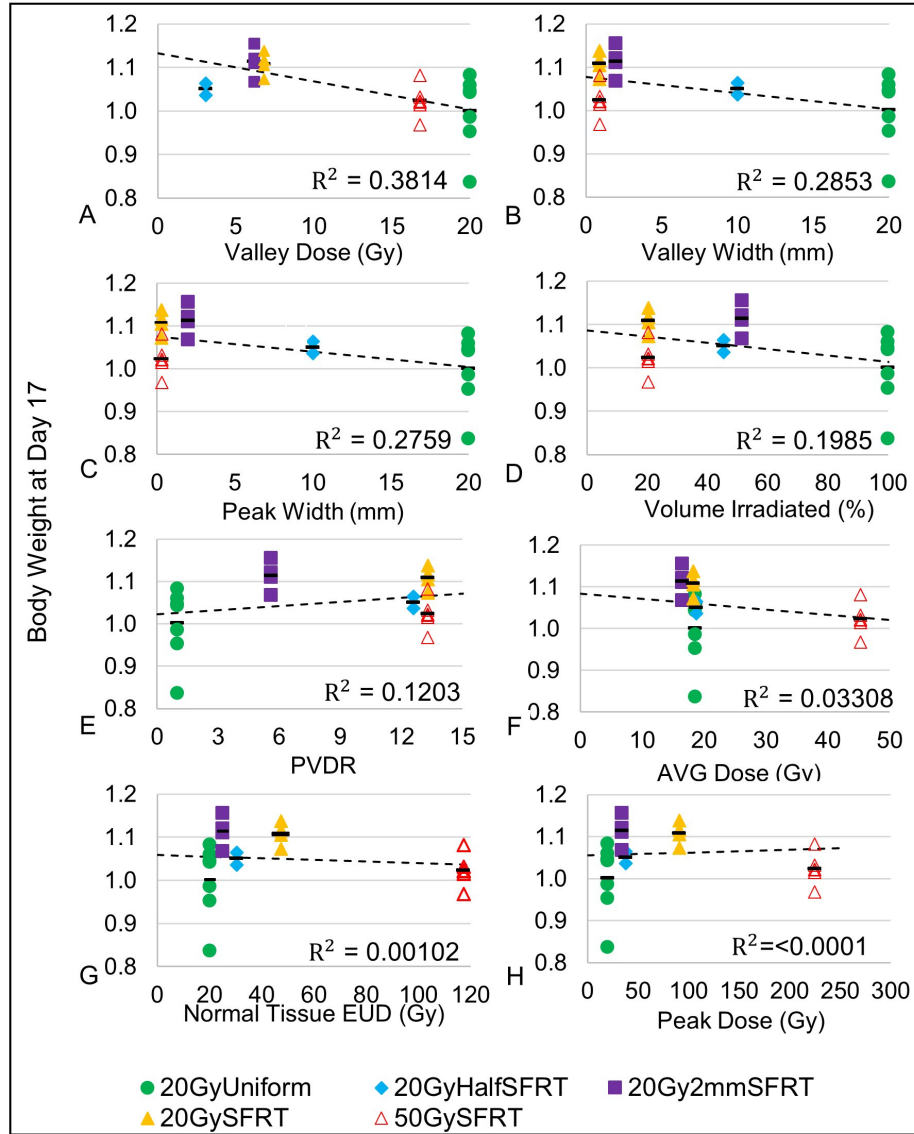


Figure 43: Scatter plots of each of the 8 treatment dosimetric parameters: valley dose (A), valley width (B), peak width (C), percentage volume irradiated (D), normal tissue EUD (E), PVDR (F), volume-averaged dose (G), and peak dose (H) vs % Body Weight at Day 17 and their corresponding regression lines and R^2 values are shown. Eight linear regression models with single covariates, one for each dosimetric parameter, were used to calculate the R^2 value and corresponding statistics.

Table of coefficients for univariate linear regression analysis of Body Weight (Day 17)				
Dosimetric Parameter	Estimate (StdErr)	R ²	t value	F-statistic
Valley Dose	-6.306x10 ⁻⁰³ (1.713x10 ⁻⁰³)	0.3814	-3.683**	13.56**
Valley Width	-4.498x10 ⁻⁰³ (1.518x10 ⁻⁰³)	0.2853	-2.964**	8.783**
Peak Width	-4.333x10 ⁻⁰³ (1.497x10 ⁻⁰³)	0.2759	-2.895**	8.382**
%Vol. Irradiated	-9.519x10 ⁻⁰⁴ (4.08x10 ⁻⁰⁴)	0.1985	-2.334*	5.448*
PVDR	4.525x10 ⁻⁰³ (2.609x10 ⁻⁰³)	0.1203	1.735	3.009
AVG Dose	-1.054x10 ⁻⁰³ (1.215x10 ⁻⁰³)	0.03308	-0.867	0.7526
Tissue EUD ^a	-6.184x10 ⁻⁰⁵ (4.123x10 ⁻⁰⁴)	1.022x10 ⁻⁰³	-0.15	0.882
Peak Dose	-2.252x10 ⁻⁰⁶ (1.961x10 ⁻⁰⁴)	5.99x10 ⁻⁰⁶	-0.011	1.32x10 ⁻⁰⁴

P values: *p<0.05 , **p<0.01

^a: Normal tissue equivalent uniform dose calculated using a=5.

Figure 44: Table of coefficients for univariate linear regression analysis of Body Weight (Day 17)

To determine the combined effects of multiple dosimetric parameters on treatment body weight outcomes, we tested several different multivariate models. Results for select variables are shown in the table in Figure 45, a coefficient table of a multivariable, hierarchical linear regression analysis of body weight on Day 17. The table contains 4 models with 2 or 3 covariates(dosimetric parameters) each and their corresponding statistics. Included in the table are the combinations of dosimetric parameters with highest F-statistic values from the table in Figure 44, namely valley/min dose (12.29**), valley width (5.69*), and peak width (5.45*). The results are that body weight change is associated with Valley Dose combined with Peak Width ($F - stat = 4.466$, $p < 0.01$) and that Valley Dose combined with Valley Width ($F - stat = 6.348$, $p < 0.01$). This indicates that Valley dose combined with either Peak Width or Valley Width have a significant effect on Body Weight (Day 17); however, since Peak Width and Valley Width are co-linear (see Discussion in section 4.5), then the combination of the 3 dosimetric parameters together results in an insignificant test statistic and the model lose is predictive capability.

Hierarchical regression analysis of predictors of Body Weight (Day 17).				
Dosimetric Parameters	Regression1	Regression2	Regression3	Regression4
Valley Dose	-4.830x10 ⁻⁰³ *		-4.751x10 ⁻⁰³ *	-3.944x10 ⁻⁰³
Peak Width	-1.975x10 ⁻⁰³	7.560x10 ⁻⁰²		2.9412x10 ⁻⁰²
Valley Width		-8.163x10 ⁻⁰²	-2.076x10 ⁻⁰³	-3.2496x10 ⁻⁰²
R ²	0.05871	0.06134	0.4189	0.05968
R ² -change	0.4178	0.3646	0.4189	0.427
F-statistic	7.534**	6.025**	7.569**	4.969**

P values: *p<0.05, **p<0.01, ***p<0.001

^a: Normal tissue equivalent uniform dose calculated using a=5.

Figure 45: Multivariate hierarchical regression analysis of predictors of Body Weight (Day 17)

Before completing the formal statistical analysis of the data, we analyze what role both the pre-treatment body weight and pre-treatment tumor volumes have on Survival outcomes when analyzed together with each of the other dosimetric parameters. These results are displayed in Figure 38, a multivariate, hierarchical CoxPH coefficient table for each of the eight dosimetric parameters studied as well as the pre-treatment tumor volume and the pre-treatment body weight used as controls. The table in Figure 46 shows that the Pre-TX tumor volume is associated with treatment outcome, where the row of pre-treatment tumor volume parameter p-values across 7 of the 8 models are statistically significant; however, the pre-TX tumor volume does not change the results shown in models from the tables in Figures 41, 42, and 44. The two models with highest Logrank Test values still support that Tumor EUD and Valley Dose are most significant for predicting individual survival outcomes, while pre-treatment body weight is not a significant predictor of survival outcomes.

<i>Hierarchical multivariate CoxPH analysis of predictors of Survival</i>								
Dosimetric Parameter	Model 1	Model 2	Model 3	Model 4	Model 5	Model 6	Model 7	Model 8
Pre-Tx Body Weight	0.0079	-0.027*	-0.024	-0.013	0.0052	0.0036	-0.046*	-0.120
Pre-Tx Tumor Volume	0.0018**	0.0011	0.0013*	0.0020**	0.0021**	0.0020**	0.0023**	0.0021**
Valley Dose	-0.23***							
Peak Dose		-0.0022						
AVG Dose			-0.076**					
Tumor EUD				-0.28***				
Valley Width					-0.163***			
Peak Width						-0.149***		
PVDR							0.191**	
% Vol. Irrad.								-0.048***
Logrank Test	39.7***	7.19	13.32**	39.9***	19.46***	18.77***	24.07***	27.16***
P-value	1x10 ⁻⁰⁸	0.07	0.004	1x10 ⁻⁰⁸	0.0002	0.0003	.00002	5x10 ⁻⁰⁶
P values: *p<0.05, **p<0.01, ***p<0.001								

Figure 46: Hierarchical multivariate CoxPH analysis of predictors of Survival

4.5 Discussion

4.5.1 Study limitations

There are several limitations in this study, many of which are discussed below. (i) There was no image-guidance used in the irradiation study. Our remedy for the lack of online imaging technology included the use of light field and video-based animal alignment, of treatment verification film, and lastly, removal of treatment-misaligned animals from the study. This was judged from reviewing the treatment verification film for each animal. Our remedy worked well, resulting in a 20GyHalfRT arm % volume irradiated of 47.8.8% (± 2.2) and which is near the target value of 50% and these results are shown in Figure 47. (ii) No CT-based treatment planning. Based on the anatomical location of the implanted tumor (rodent flank) we believe a portion of the rodent GI tract may have been irradiated but the actual volume irradiated is unknown. Because all animals were randomized across

study arms such that all arms have the same average pre-treatment tumor size and similar tumor location distribution, it is reasonable to assume that any variations in portions of GI track irradiated do not bias any particular study arm. (iii) Only a single tumor model used. The FSA rat tumor model does not represent tumors with low vascularity, which may have different treatment responses. The study should be repeated using different tumor and animal models. (iv) The dosimetric parameters have strong cross correlations in this study, which is discussed in more detail at the end of this section.

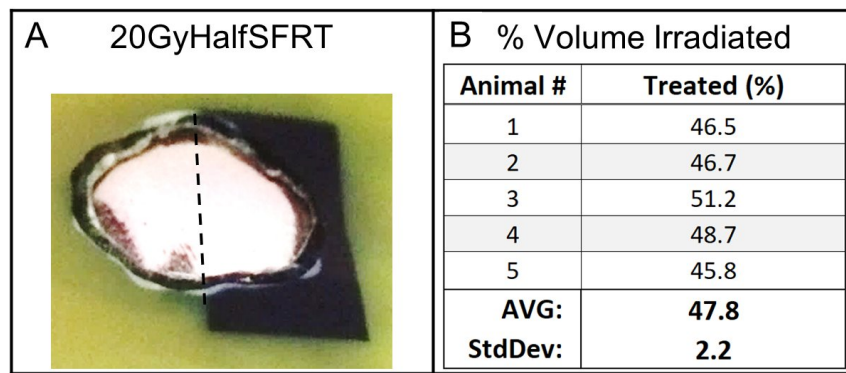


Figure 47: (A) The post-treatment verification film for a 20GyHalfSFRT treated tumor shows that only one-half the tumor was treated as intended. The black dashed line in the photograph was drawn to illustrate which half of the tumor was irradiated. (B) The verification films for all 5 animals included in the study arm were analyzed by calculating the percentage area of the tumor irradiated.

The potential impact of spatial fractionation pattern (lines vs. dots, for instance) on treatment response is beyond the scope of this work. However, it is a very important question that deserves methodical investigations as some spatial fractionation patterns are easier to achieve than others in practical application. Our data shows that valley/minimum dose has the closest association with treatment response for tumor and body weight. However, different spatial fractionation patterns with the same valley dose may not lead to the same treatment response when a different endpoint is used. In our study the 20Gy2mmSFRT arm and the 20GySFRT arm have similar valley doses but dissimilar survival fraction on Day 17. To investigate the impact of radiation spatial fractionation

pattern alone on given treatment responses, carefully designed new studies are needed.

The exciting noncytotoxic effects of SFRT, such as induction therapy to sensitize tumor to increase therapeutic ratio of the following therapy including anti-tumor immunotherapy, remain largely underexplored [228]; however, they are also beyond of the scope of this work. Our own and others' work have demonstrated that SFRT radiation impacts tumor microenvironment and modulates immune system very differently than uniform radiation therapy [150], [220], [229]. We intend to conduct similar studies to identify associations between dosimetric parameters and these indirect effects of SFRT in the future.

4.5.2 SFRT dosimetric association with treatment tumor response

4.5.2.1 Valley dose and tumor EUD

The importance of tumor minimum dose to tumor control has long been established in conventional radiation therapy [230]. Does the same association between tumor control and minimum/valley dose hold for SFRT? For some the answer is yes and sophisticated techniques have been developed to “fill up” the dose valleys in an MRT beam by interlacing the microbeams from MRT from different irradiation angles. As a result, a uniform dose distribution inside the tumor is reached [133] while the surrounding normal tissue out of the “cross-firing” range still receive largely MRT radiation pattern of peaks and valleys. In a synchrotron-MRT study Ibahim et al. [231] reported that valley dose is closely correlated with cell survival, but valley dose alone does not determine the observed radiobiological effects. Our study shows that the tumor EUD ($a = -10$) and minimum/valley tumor dose have the highest linear associations ($R^2 = 0.7923$, $F - stat = 15.26*$; $R^2 = 0.7636$, $F - stat = 12.92*$, respectively) with tumor treatment response (Figure 40, 41, and 42). This observed association between tumor treatment response with tumor valley/minimum dose and tumor EUD dose in this preclinical study is consistent with their known association in tumor treatment response seen in clinical conventional

uniform dose radiation therapy. Our data suggests that valley/minimum dose or Tumor EUD are more appropriate than peak dose for SFRT treatment prescription. When tumor control is the endpoint, we suggest that equal valley or minimum dose be used for comparative study between a uniform radiation and SFRT therapy or among different SFRT treatments.

4.5.2.2 Peak-to-valley dose ratio

Our data showed that PVDR has a consistent but not statistically significant association with tumor treatment response ($R^2 = 0.7194$, $F - stat = 7.691$) (Figure 40, 41). The linear regression analysis on day 17 was not statistically significant. The CoxPH analysis using the entire survival data set show a modest association with survival. Although not statistically significant, an inverse association is observed between PVDR value and survival fraction on Day 17 - the higher PVDR value the less survival fraction. The inverse association is largely determined by the uniform radiation arm where PVDR value is 1.0. If this data point is removed, the PVDR association with survival for all SFRT arms is inconclusive (Figure 40). We believe this result of inverse association is likely biased by the study design that has very limited PVDR values (4 values) and strong cross-correlations between PVDR and other SFRT parameters (see more discussion later in the section). A better understanding of PVDR's association with a given treatment response requires a carefully designed new study that focuses on the impact of PVDR value on treatment response.

4.5.2.3 Percentage volume irradiated, peak width, and valley width

It seems logical that tumor treatment response is closely associated with the tumor volume irradiated. However, this is not supported by a clinical GRID therapy study by Neuner et al. [97] where both MLC-based and collimator-based GRID treatments showed

similar response rates for pain, mass effect, other patient complaints, and have similar adverse reactions. The collimator-generated GRID had 50% of the radiation field open while the MLC-generated GRID had only 31% open. In our study the 20GyHalfSFRT and 20Gy2mmSFRT arms have similar percentage-volume-irradiated (as well as PDD curves) but there is a difference of 5 days in the 50% survival time (Figure 31 and Figurefig:Fig6). Nonetheless, our data shows that percentage-volume-irradiated has the 3rd highest linear association ($R^2 = 0.7153$, $F - stat = 10.05*$) with tumor treatment response (Figure 40 and figures 41 and 34). Since percentage-volume-irradiated is jointly determined by peak width and valley width it is understandable to see moderate associations between tumor treatment response and peak width ($R^2 = 0.4201$, $F - stat = 2.898$ (*not sig.*)) and valley width ($R^2 = 0.4296$, $F - stat = 3.012$ (*not sig.*)). In a synchrotron microbeam brain study using multiple beams Serduc et al. kept valley dose constant while varying peak width and peak dose. They concluded that the latter two parameters have strong influence therapeutic ratio [129].

4.5.2.4 *Volume-averaged dose and peak dose*

This study is designed to scrutinize the association of volume-averaged dose with tumor treatment response (Figure 31). The four study arms sharing very similar volume-averaged doses (20 or 18 Gy) exhibited very different tumor treatment responses (Figure 38 and 40) showing the survival rate at day 17 varied from 100% to 33%. Therefore, the association between volume-average dose and tumor treatment response is weak. We found that peak dose has little to no association with tumor treatment response ($R^2 = 0.04472$, $F - stat = 0.6874$ (*not sig.*)) (Fig 40, Figure 41, and Figure 42). This finding is significant because peak dose has been used for treatment prescription in practically all SFRT treatments [88], [96]. Although the linear regression analysis on day 17 showed a weak association between peak dose and survival that was not statistically significant, the CoxPH analysis

using the entire survival data set did show a modest association with survival.

4.5.3 SFRT dosimetric association with normal tissue toxicity

We did not study treatment induced normal tissue toxicity directly in this study. We used body weight change post radiation (targeted to the flank, lower abdominal region of the animal) as an indicator, not evidence of normal tissue toxicity. We did not see a strong association between animal body weight change and any of the eight dosimetric parameters studied, except a modest association with valley/minimum dose.

4.5.3.1 Valley dose

The strongest association we observed is a weak one between body weight change and valley/min dose ($R_2 = 0.3814$, $F - stat = 13.56^{**}$) (Figure 44). Note that valley/min dose is also strongly associated with tumor treatment response ($R^2 = 0.7636$, $F - stat = 12.92^{*}$). Our finding is consistent with a normal mouse brain MRT study Nakayma et al. reported that valley dose is one of the important factors to determine normal brain dose tolerance [232]. Our data suggests that valley dose may have a close correlation with both tumor control and toxicity, and thus is a crucial dosimetric parameter in SFRT treatment.

4.5.3.2 Valley width, peak width, percentage volume irradiated

The valley width, peak width, and percentage volume of the tumor that is irradiated parameters were only weakly associated with animal body weight change post radiation ($R^2 = 0.2853$, $F - stat = 8.783^{**}$; $R^2 = 0.2759$, $F - stat = 8.382^{**}$; and $R^2 = 0.1985$, $F - stat = 5.448^{*}$, respectively) (Figure 43 and Figure 44). Note that in this study peak width and valley width are closely correlated (more discussion on correlations, below). Percentage volume directly irradiated showed no statistically important association with body weight change. Neuner et al. reported that they observed similar treatment responses from

clinical GRID treatments of different percentages of volume directly irradiated [97].

4.5.3.3 Normal tissue EUD, peak width, percentage volume irradiated

The normal tissue EUD, PVDR, volume-averaged dose, and peak dose parameters showed little to no association with body weight change post radiation ($R^2 = 1.022 \times 10^{-03}$, $F - stat = 0.882$ (*not sig.*); $R^2 = 0.1203$, $F - stat = 3.009$ (*not sig.*); $R^2 = 0.03308$, $F - stat = .7526$ (*not sig.*); and $R^2 = 5.99 \times 10^{-06}$, $F - stat = 1.32 \times 10^{-04}$ (*not sig.*), respectively). Our finding is consistent with a rat normal brain minibeam study by Prezado et al. showing arms with similar volume-average-doses have drastic differences in survival (14) and inconsistent with a MRT study on normal mouse skin by Priyadarshika et al. concluded that integrated dose (i.e., volume-averaged dose) rather than peak or valley dose, may dictate the acute skin toxicity [233].

4.5.3.4 2mm wide beam array SFRT

Our data indicates that the 20Gy2mmSFRT arm is not only the most relevant to clinical application because of its millimeter scale, but it also has the potential for superior therapeutic ratio. The 20Gy2mmSFRT arm showed similar survival with the 50GySFRT arm but has significantly lower valley dose (6.2 Gy vs. 17 Gy). At the same time, it showed the least, if any, body weight change compared to the untreated arm while the 50GySFRT arm with 0.31mm beam width exhibited significant body weight growth deficit (Table 1 and Fig 6). The 20GyUniform arm has the best tumor treatment response and the worst body weight change. Our data indicated the 2mm wide beam array is a kV photon SFRT pattern that has the potential for high therapeutic ratio SFRT and deserves further investigation.

4.5.3.5 *Cross-correlation in the SFRT dosimetry parameters*

The dosimetric parameters studied in this work are not all independent variables and their cross-correlations are shown in the table of Pearson Correlation coefficients (Figure 48). The larger the magnitude of the coefficient, the more co-linear and correlated the pair of dosimetric parameters. In this study, peak width and valley width are perfectly co-linear (correlation of 1.0) by study design. Valley/min dose, a parameter used in tumor EUD calculation, is also highly correlated with tumor EUD (correlation of 0.99). These strong correlations explain the similar statistical associations of these parameters with treatment responses. These correlations also limited the study's ability to better exam the association between a given treatment response with each of the dosimetric parameters. For example, in Figure 48, the multi-variate analysis of predictors of Body Weight, when both Peak Width and Valley Width and Valley Dose are analyzed together in a three variable model, their combined effect on Body Weight Day 17 is no longer significant due to the co-linearity of Peak Width and Valley Width.

Pearson Correlation coefficient matrix for the eight SFRT dosimetric parameters relevant for tumor treatment response.

	Valley Dose	Peak Dose	AVG Dose	Tissue EUD	Tumor EUD	Peak Width	Valley Width	PVDR	% Vol. Irradiated
Valley Dose	1.00								
Peak Dose	0.38	1.00							
AVG Dose	0.63	0.91	1.00						
Tissue EUD	0.44	0.99	0.95	1.00					
Tumor EUD	0.99	0.26	0.53	0.32	1.00				
Peak Width	0.63	-0.36	0.00	-0.28	0.72	1.00			
Valley Width	0.65	-0.34	0.02	-0.25	0.74	1.00	1.00		
PVDR	-0.57	0.64	0.40	0.61	-0.67	-0.78	-0.77	1.00	
% Vol. Irradiated	0.70	-0.26	0.13	-0.17	0.78	0.93	0.93	-0.94	1.00

Figure 48: Pearson Correlation coefficient matrix for the eight SFRT dosimetric parameters relevant for tumor treatment response.

4.6 Summary

In this conventional dose rate small animal SFRT study we used a large range of radiation spatial fractionation scales to study the association of dosimetric parameters with treatment response. We concluded that valley/minimum dose, tumor EUD, and percentage tumor irradiated have strong and proportional associations with tumor treatment response while peak dose exhibited little association. Among the SFRT dosimetric parameters studied valley/min dose also showed the highest but modest association with body weight change post radiation

4.7 Acknowledgments

One of the authors (Chang) acknowledges Dr. Mark W. Dewhirst for his decade long unwavering encouragements and expert radiobiology advices, which are invaluable for this (and other) original work exploring the magic of radiation spatial fractionation. One of authors (Rivera) expresses her appreciation to Leith Rankine, MS for his kind help on EUD calculation.

CHAPTER 5: MINIBEAM RADIATION IS SUPERIOR TO UNIFORM RADIATION FOR ABSCOPAL EFFECT WITH COMBINED PD-L1 CHECKPOINT INHIBITOR IMMUNOTHERAPY

5.1 Overview

Previously, we demonstrated the feasibility of creating a compact, spatially fractionated radiation therapy (SFRT) delivery system for use in preclinical studies and then applied it in a dosimetric parameter study of SFRT. This chapter presents a different avenue for advancing our understanding of SFRT, using the SFRT delivery system for investigating the advantages of SFRT in multimodality therapy approaches such as anti-cancer immunotherapy.

Recent evidence suggests that SFRT may have different mechanisms of tumor cell killing than conventional radiotherapy, which may include bystander and systemic immune activating effects such as the abscopal effect, wherein the control or elimination of distant tumors occurs subsequent to irradiation of the primary tumor. Such effects are thought to be immune mediated and have been shown to be enhanced by immune therapy, specifically immune checkpoint inhibition. This chapter explores the combination of SFRT with PD-L1 checkpoint inhibition in a duo-synchronous tumor model of murine mammary carcinoma. This chapter has been submitted for publication³ in the journal Radiation Research and is in review at the time of this writing. I have included the study here in full, with minor changes such as including using full-color versions for all figures.

³This chapter has been submitted as an article in the journal Radiation Research. The original citation is as follows: Rivera JN, Laemont K, Tovmasyan A, Stryker S, Young K, Chang SX, Palmer GM. *Minibeam Radiation is Superior to Uniform Radiation for Abscopal Effect when Combined with PD-L1 Checkpoint Inhibitor Immunotherapy*. Radiation Research. 2020 [Manuscript In Review]

5.2 Introduction

Spatially fractionated radiation therapy (SFRT) includes clinical GRID and Lattice therapy and preclinical microbeam and minibeam radiation therapy. All forms of SFRT can be characterized by many alternating sub-volumes receiving very high dose separated by and volumes receiving no direct radiation in a single or a few fraction treatment [69], [204]. Impressive treatment outcomes have been reported in GRID clinical studies demonstrating the absence of increased treatment toxicity and benefits of palliation and local control for patients with bulky and treatment-resistant tumors, especially when SFRT was followed by a conventional course of chemoradiation [52], [73], [97], [206], [234]. The preclinical research also produced fascinating results on both the lack of radiation toxicity and tumor control [70], [120], [160], [210]. Although SFRT research and clinical use have decades of history, it remains an unconventional treatment and with limited application. One key reason for it is the lack of understanding of its working mechanism, which not only impacts its wide acceptance in the field but also hinders the optimization of SFRT treatment techniques. In 2018, partnered with the Radiosurgery Society, the National Cancer Institute created a new international working group dedicated to investigating SFRT and the related Flash radiotherapy [215]. The working group is tasked to develop strategies to guide the field to advance our understanding of SFRT in biology, physics, and clinical translation of this promising radiation therapy approach. One area of special interest that deserves more research is abscopal effect, a systemic anti-cancer effect of localized radiation, which may be enhanced using anti-cancer immunotherapy.

We hypothesize that compared to the uniform dose radiation therapy we use today SFRT may have advantages in enhancing anti-cancer immunotherapy. SFRT may results in unique effects on the tumor microenvironment that in turn may result in different mechanisms of cell killing such as bystander effects [137], [140] and effects on stromal cells including the tumor vasculature [128], [143], [146], [150], [235]. Of interest are

radiation-induced immunological effects which can lead to abscopal or distant tumor responses. These have been reported in a variety of contexts involving SFRT both with and without immune therapies [49], [123], [173], [220], [228]. For instance, Kanagavelu et al. reported a significant growth inhibition in distant unirradiated Lewis lung carcinoma tumors following partial volume radiation of a primary tumor, which was correlated with a T-cell mediated immune response [173]. Clinical data also supports the efficacy of partial volume irradiation targeting the hypoxic tumor regions specifically to elicit an immune mediated abscopal response [136]. The leading theory is that SFRT induces a systemic immune response that can target distant (unirradiated) tumor sites. The combination of SFRT with immunotherapies has also been shown to have potential synergy and may have unique effects relative to broad beam radiation therapy [45], [49], [123], [173], [220]. The high spatial dose variability in the tumor may induce unique effects by sparing some fraction of the resident immune population while still delivering high dose [49], to elicit the in-situ vaccine effect that has been reported for uniform radiotherapy [236]. Several clinical studies have indicated that “the tumor can serve as an autologous vaccine through RT-induced immunogenic cancer cell death” [237]. That is, that the radiation itself may act to activate or enhance the host-immune response against future metastatic tumor cells, which may lead to better long-term prognoses in patients [237]–[243]. Despite the tremendous promise of this treatment combination, the specific immune responses elicited are relatively poorly understood. Therefore, the goal of this study is to characterize the efficacy of combination radiation (SFRT or uniform radiation) with anti-PD-L1 therapy, as well as to use flow cytometry to characterize the immune cells present in the primary irradiated tumor, distant unirradiated tumor, and also systemically.

5.3 Methods

5.3.1 Study design

In this study we aim to investigate potential advantage of minibeam radiation therapy (MinibeamRT) over uniform radiation therapy (UniformRT) in synergistic effect with immune checkpoint inhibitor therapy. We hypothesize that Minibeam is more effective in activating the host systemic immune response and thus more effectively potentiating this immunotherapeutic effect. Hence, we compare a single fraction 50Gy (peak/max dose) MinibeamRT treatment against a 10Gy (uniform dose) conventional seamless UniformRT treatment (both with and without immunomodulator, anti-PD-L1 antibody) delivered to one of two tumors in a dual tumor mouse model of adenocarcinoma. The primary endpoint for this study is tumor growth inhibition on both the irradiated and unirradiated tumor sites.

A 50Gy peak dose was chosen for the MinibeamRT group based on our initial dose-determination pilot study comparing single fraction 50Gy peak dose and 100Gy peak dose MinibeamRT against a 10Gy UniformRT treatments for abscopal tumor control in a distant, unirradiated tumor. Results from this pilot study indicated that a the 50Gy MinibeamRT was more effective than the 100Gy MinibeamRT at inhibiting tumor growth in the unirradiated tumor and hence potentially enabling a more robust immune response. The table in Figure 49 shows the 5 treatment groups designed for this study, where both MinibeamRT and UniformRT with and without immunotherapy are tested against Control (untreated) group. Pre-treatment tumor volumes in both flanks are also reported in Figure 49. Initial tumor size at the time of treatment is strongly correlated with treatment outcome. Care was taken minimize this unwanted effect using a randomized, matched study design with respect to the pre-treatment tumor volume. This was achieved by organizing the animals into groups of similarly sized right flank tumor volumes and then randomly assigning animals to each treatment arm within this ordered category.

This results in similar average pre-treatment tumor volumes and size ranges in the right flank tumors among different treatment groups; however, we have no control over the volumes in the left flank tumors per group. To minimize the variance among the left flank pre-treatment tumor volumes, we set minimum and maximum acceptable pre-treatment volume limits and excluded any tumor volumes outside of this range from consideration in the study. The randomized, matched study design technique described above resulted in an average pre-treatment tumor volume for all right flank tumors of approximately 124mm^3 ($\pm 7\%$ *standard – error*) as well as an average pre-treatment tumor volume for all left flank tumors of 132mm^3 ($\pm 8\%$ *standard – error*).

Experimental design of seamless (UniformRT) vs spatially fractionated (MinibeamRT) radiation therapy study of the systemic immune response of mice.

Treatment Groups	Animal Numbers ^b (n=59)	Dose ^a (Gy)	Pre-treatment Tumor Volumes ^d	
			Right (Irradiated)	Left (Unirradiated)
Controls+isotype ^c	15	0	140.7($\pm 25\%$)	146.8($\pm 19\%$)
UniformRT+isotype	11	10	124.3($\pm 12\%$)	141.0($\pm 13\%$)
UniformRT+ α -PD-L1	12	10	118.3($\pm 14\%$)	115.9($\pm 17\%$)
MinibeamRT+isotype	11	50 ^b	121.2($\pm 13\%$)	122.0($\pm 15\%$)
MinibeamRT+ α -PD-L1	10	50 ^b	117.0($\pm 13\%$)	133.0($\pm 23\%$)

^a: Dose is calculated using EBT-3 film at the skin surface. For MinibeamRT treatments the dose in the peak regions is used.

^b: Approximately n=5 animals for each treatment group were harvested for flow cytometry immune profiling.

^c: Controls+isotype treatment arm animals received no radiation to either tumor.

^d: Average tumor volume ($\pm\%$ standard-error) reported for each treatment group.

Figure 49: Experimental design of seamless (UniformRT) vs spatially fractionated (MinibeamRT) radiation therapy study of the systemic immune response of mice.

5.4 Animal Model Description and Cell Culture

This study was carried out in strict accordance with the recommendations in the Guide for the Care and Use of Laboratory Animals of the National Institutes of Health

(NIH). The University of North Carolina- Chapel Hill Institutional Animal Care and Use Committee (IACUC) reviewed and approved the animal protocol (IACUC ID: 19-041.0) in accordance with NIH standards. All animal radiation procedures were performed under general anesthesia and all efforts were made to minimize suffering.

A dual-tumor model of 6-week-old female C57BL/6 mice with murine mammary adenocarcinoma (EO771) were used in all in vivo experiments. EO771 cells were derived from a metastatic mammary gland adenocarcinoma in a C57BL/6 mouse [244]–[246]. This model was chosen as it is an immune competent, clinically relevant model whose radiotherapy-induced tumor microenvironment modulation effects have previously been extensively studied by our group [247]. This mammary gland adenocarcinoma is characterized as a poorly metastatic, triple negative model of breast cancer.

Tumor cells were cultured in DMEM with 10% FBS (Gibco 16140071) and 1% antibiotic-antimycotic (Gibco 15240062). Cells were injected into the subcutaneous space of both mouse flanks such that the right flank received 250,000 cells, and the left flank received 100,000 cells. Figure 50 shows a graphical timeline of the experiment. Following cell injections, tumors on both flanks are grown naturally for approximately 2 weeks, until the primary tumor reach the target radiotherapy treatment size of approximately 120mm^3 . Tumors on the right flank served as the “primary” tumor and target for radiation therapy, while tumors on the left flank served as a “secondary” tumor outside the radiation field for the purpose of evaluating the abscopal (unirradiated tumor growth control) response. Immediately following radiotherapy treatments, animals are injected with anti-PD-L1 monoclonal antibody (BioXCell clone 10F) or Isotype control antibody (isotype control, IgG2a). The antibody drug dose is based on our previous studies on mice, i.e. $250\text{ }\mu\text{g}$ for a single injection. Antibodies are administered via intraperitoneal injection every 3 days beginning on the day of radiation treatment for a total of 4 injections. At 14 days post-radiotherapy, approximately $n=5$ animals from each treatment group are ethically euthanized for immunophenotyping of spleen and the irradiated and unirradiated tumors,

per IACUC-approved animal protocol. The spleens were homogenized using a syringe plunger and filtered through the cell strainer (40 mm, Corning, *cat*#431750). The red blood cells were lysed with the lysis buffer (15.5 mM NH_4Cl , 1.2 mM $NaHCO_3$, 0.01 M EDTA). Tumor lymphocytes were isolated using the GentleMACS dissociator, Miltenyi Biotec, in a solution of 0.2mg/ml DNase I, 1 mg/ml collagenase IV and 0.1 mg/ml hyaluronidase from, Sigma. This was incubated at 37 degrees Celsius for 1 hour and then passed through a 40 μ M strainer, Falcon, to get single cell suspensions. Next, the cells were stained with anti-CD16/32 Ab (BioLegend) to block non-specific binding and LIVE/DEAD Fixable Violet Dead Cell Stain Kit (Thermo Fisher), which enables exclusion of dead cells. The cells were stained with antibodies against CD45, CD3, CD4, CD8, CD19, CD335, CD11b, F4/80, Gr1 and PD-1 (BioLegend) and analyzed by multiparameter flow cytometry (FACSCanto, BD Bioscience). Analysis of data was performed using FlowJo (Tree Star).

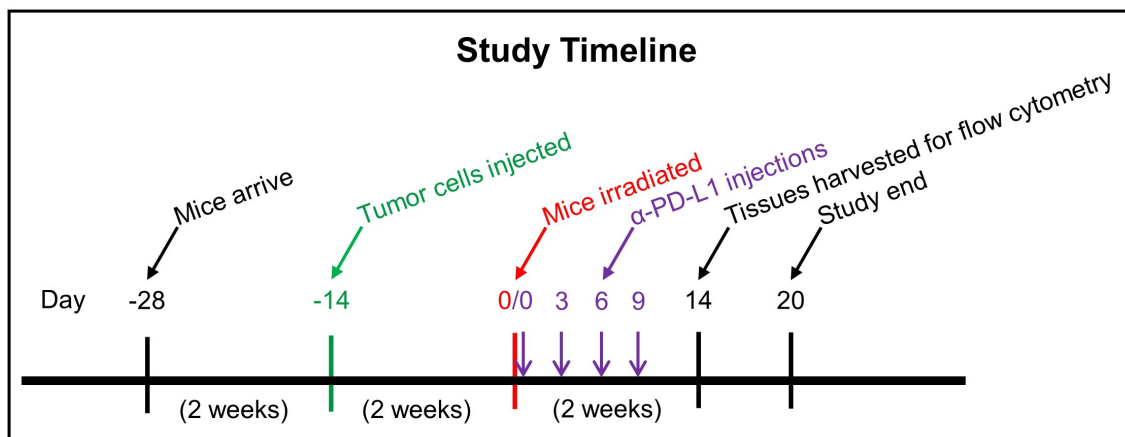


Figure 50: The timeline of the study is shown. A single fraction radiation is given two weeks after tumor cell implantation. Anti-PD-L1 immune drug was given in 4 fractions starting on day 0. On day 14 tissues are harvested from n=5 animals per treatment group for flow cytometry immunophenotypic analysis. The remaining animals are monitored for tumor growth and the study ends on day 20.

5.4.1 Animal monitoring and husbandry

Animals were monitored before irradiation as well as every third day thereafter until study end-point criteria were met. Study endpoints included a maximum combined tumor

burden of 3000mm^3 (or greater than 2cm in any dimension for a single tumor), weight loss in excess of 15%, body condition scores of ≤ 2 , as well as any other signs of pain, discomfort, or moribundity as recommended by DCM veterinary staff. Animals that met study end-point criteria were ethically euthanized via compressed carbon dioxide gas followed by a secondary means of physical euthanasia (thoracotomy) per the approved animal study protocol. Animal body weights and tumor volumes were recorded prior to radiotherapy treatments as well as every third day thereafter for up to 30 days. Tumor dimensions were measured via digital caliper and tumor volumes were calculated using the approximate volume for an oblate spheroid, $V = \left(\frac{1}{2}\right) L \times W \times W$, as recommended by Faustino-Rocha et al [223]. To minimize biological variability between animals and experimental rounds, all animals were of similar age and supplied by same vendor [Charles River Laboratories, Inc., Wilmington, MA], had a full 2 weeks to acclimate to their environments before the start of any treatments, were injected with cells on the same day, and were provided identical (mixed caged) housing and husbandry in a UNC Division of Comparative Medicine (DCM) operated vivarium facility. Further, all animals were provided with identical standard laboratory rodent diets consisting of 23% > crude protein and water ad libitum throughout the study. To help mitigate any potential significant weight loss or dehydration post-radiation, all animal diets were supplemented with high-calorie, nutritionally fortified water-based gel and hydration cups.

5.4.2 Radiotherapy dosimetry and treatments

Radiotherapy treatments were delivered using a commercially available small animal research irradiator, XRad-320 [Precision XRay, Inc., North Branford, CT], at 320kVp and 12.5mA. Different inhouse made collimators were used to deliver both collimated MinibeamRT and UniformRT radiation patterns to solid tumors. Figure 51 shows (A) the results for the beam profile and percentage depth dosimetry measurements for both the MinibeamRT and UniformRT treatments, (B) the small animal radiotherapy treatment

system setup, and (C) an image of an 10Gy UniformRT-treated mouse example.

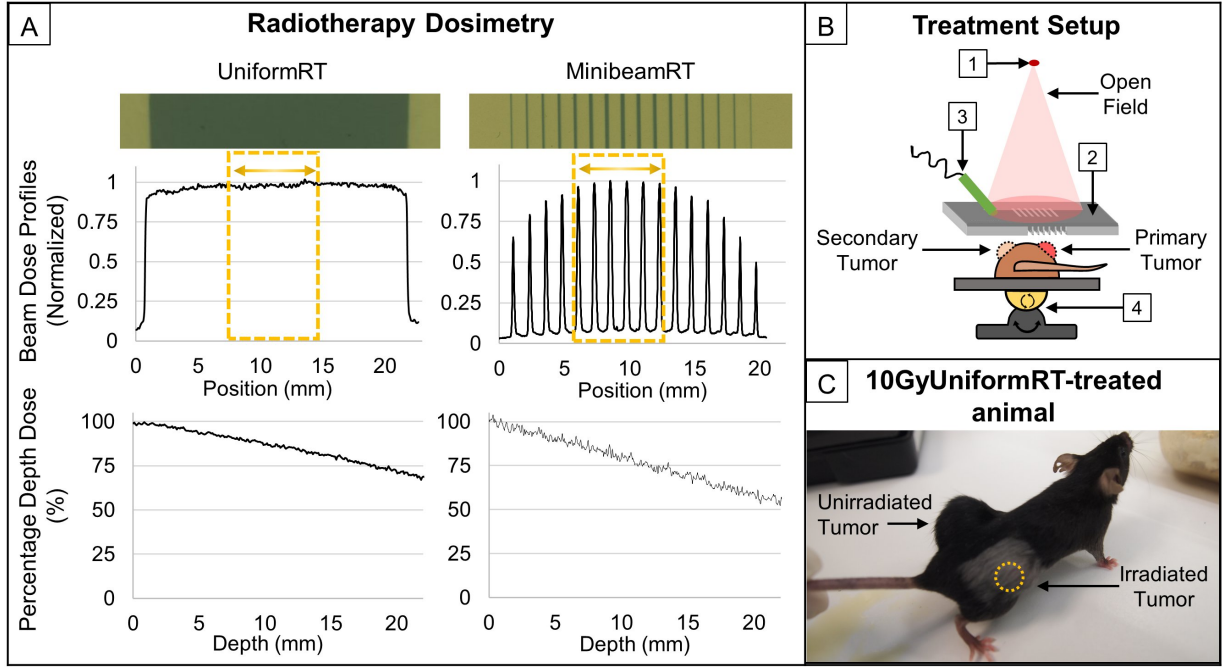


Figure 51: (A) Dosimetry beam profiles and percentage depth dose (PDD) for the UniformRT and MinibeamRT treatments by EBT-3 film. The yellow dotted rectangle represents the approximate size of a typical tumor at the time of irradiation and the position in the treatment field. (B) The radiation treatment setup, includes [1] an external beam x-ray source, [2] an in-house Cerrobend MinibeamRT or UniformRT collimator, [3] a PC-linked camera provides beam's-eye-view of the light field on animal skin, and [4] a 6-degree freedom platform for angle and height adjustment. (C) image of an animal treated with 10Gy UniformRT, photographed approximately 3 weeks post-radiation. A demarcated square patch of white fur is visible, corresponding to the radiation field, indicating a localized radiation-induced epidermal and fur depigmentation disorder (vitiligo). No abscopal effect is observed in this animal.

Radiotherapy dosimetry was measured via EBT-3 Gafchromic film [Ashland Inc., Covington, KY] calibrated against an ADCL-calibrated ion chamber in large-field geometry. The table in Figure 52 shows the relevant dosimetric parameters for the UniformRT and MinibeamRT treatment arms calculated from the dosimetry film (Figure 51, panel A). To determine the surface peak dose and valley dose for the MinibeamRT treatments the individual peak/valley doses are first calculated and then averaged over the peaks that span 10mm around the center of the overall MinibeamRT field. Surface

dose-rates are 4.27Gy/min for MinibeamRT and 5.25Gy/min for UniformRT treatments. The volume-Averaged dose for both radiotherapy treatment types are approximated by computing the average dose on the 10mm (width) \times 10mm (depth) area of the percentage depth dose (PDD) dosimetry film.

Dosimetric parameters used in both treatment types used the study						
Radiation treatment type	Peak ^a dose (Gy)	Min ^a dose (Gy)	Avg ^b dose (Gy)	Peak width (mm)	Valley width (mm)	PVDR
UniformRT	10	10	9.2	-	-	-
MinibeamRT	50	3.7	11	0.31	0.9	13.5

^a: Peak and minimum dose are calculated at 0mm (surface) depth. For MinibeamRT, the average of the peak/valley regions across a \sim 10mm span of beams is used.

^b: Volume-averaged dose is calculated through a 10mm depth.

Figure 52: Dosimetric parameters for both radiotherapy treatment types used in the study

Both the uniform and minibeam radiation were formed by inhouse-made collimators. A single radiation treatment is targeted to the tumors with a 5mm margin for each radiotherapy treatment type. Radiation targeting is achieved by (a) depilating animal flanks to locate tumors and delineating target tumor boundaries on skin using marker, (b) transferring the markings onto a $3cm \times 3cm$ square of Gafchromic film placed over the tumor (for treatment verification) as viewed from the beams-eye-view frame of reference, (c) cutting out the tumor portion of the film and placing the film back over the tumor with the tumor inside the cutout, (d) fixing the film in place with tape and placing the animal in the irradiator, (e) aligning the tumor with the radiation field using the built-in light field inside the irradiator together with a PC-linked endoscopic camera live video feed, (f) performing tumor/animal height adjustments via a manual Z- stage and angle adjustments via rotatable heated animal platform, and (e) monitoring animal throughout irradiation via a second PC-linked endoscopic camera. All animals are anesthetized with isoflurane mixed with 2% oxygen carrier gas as described above throughout the tumor-to-radiotherapy beam

alignment and irradiation procedures to minimize both stress to the animal and off-target error due to tumor motion during radiotherapy treatment. The treatment verification film records the targeting accuracy of the treatment and allows for post-radiation film reviewal and documentation.

5.4.3 Flow cytometry studies and analysis methods

At 14 days post-radiation approximately n=5 animals from each treatment group were ethically euthanized and animal spleens and both the irradiated and unirradiated tumors were harvested for immune profile analysis, per IACUC-approved protocol. Flow cytometry was used to characterize the prevalence of different immune cell subtypes within these tissues. Different cell surface markers were identified using fluorescent labeled antibodies and cells expressing defined combinations of markers could be then categorized into their respective types. CD45 has been shown to be an essential regulator of T-cell and B-cell antigen receptor signaling. As such, this makes it a useful selection marker for leukocytes. Thresholding is used to identify (count) cells high in this marker. To further categorize the leukocyte population into the primary subtypes, three additional markers were used. CD3 is a protein that is expressed by a high percentage of circulating peripheral T cells which makes it a highly effective T cell marker and is useful in further categorizing the CD45+ leukocytes. CD4 is a glycoprotein commonly found on the surface of immune cells such as the T helper cell (*Th*); hence, we use it in our study as a marker for T-helper cell presentation. Finally, we use the CD8 co-receptor as a marker in our study as it is predominantly expressed on the surface of cytotoxic T cells (*Tc*) as well as natural killer cells (*NKcells*). Thus cells high for both CD3 and CD4 markers were counted as helper T cells, and cells high in both CD3 and CD8 were counted as cytotoxic T cells.

5.5 Results

5.5.1 Irradiated tumor response

Figure 53, on the left side, shows results for normalized tumor volume growth curves for the irradiated “primary” tumors. Ethical euthanasia was largely triggered by tumors exceeding the maximum combined tumor burden for both tumors per IACUC- approved protocol limitations. Our data shows that conventional UniformRT groups (10Gy surface peak dose and 9.2Gy average dose to tumor), with or without anti-PD-L1 drug, have better tumor growth control than the corresponding MinibeamRT arms (50Gy surface peak dose and 11Gy average dose to tumor.) The impact of anti-PD-L1 on the radiation tumor growth control, however, are different: it suppressed tumor growth in the MinibeamRT arms but enhanced tumor growth in the UniformRT arms.

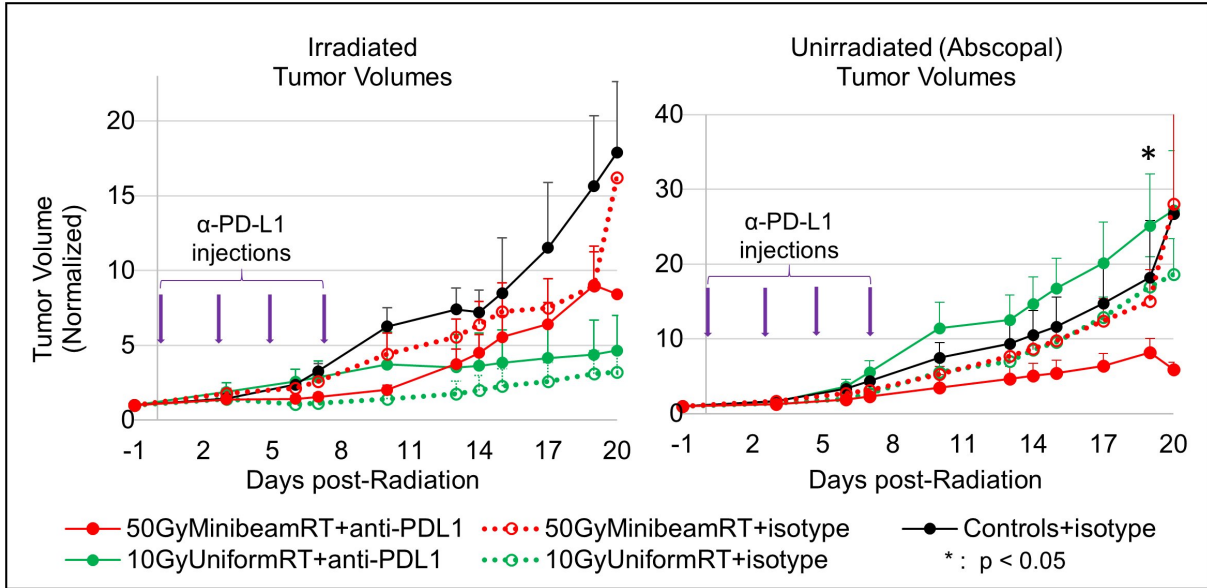


Figure 53: Normalized tumor volume change post radiation is shown for both the irradiated tumor (left) and the unirradiated tumor (right) in the dual tumor animal model study. For the unirradiated tumor, the difference between the 10GyUniformRT+anti-PD-L1 and the 50GyMinibeamRT+anti-PD-L1 treatment groups at the end of study is statistically significant ($p=0.04948$). Differences between any other two groups are not statistically significant.

5.5.2 Unirradiated tumor response

Figure 53, on the right side of the page(B)), shows results for normalized tumor volume growth curves for the unirradiated tumor. In the absence of anti-PD-L1 drug the UniformRT and MinibeamRT radiation treatment to the primary tumor have practically no impact on the secondary, unirradiated tumor, whose growth curves are similar to those of the control arm animals. When anti-PD-L1 is combined with radiation, MinibeamRT radiation exhibits the strongest abscopal effect, where the growth of the unirradiated tumor is significantly reduced, especially when compared to the UniformRT+anti-PD-L1 arm ($p=0.04948$). Further, the combination of anti-PD-L1 with UniformRT radiation appears to generate a negative abscopal effect, where the tumor growth is enhanced compared to uniform radiation alone; however, differences between these and any other two groups are not statistically significant.

5.5.3 Spleen lymphocyte profile

Figure 4 shows the flow cytometry immune profiling data from spleen. We analyzed CD45+, CD3+, CD4+, CD8+, B cells, and NK cells. A few clear differences are seen. First, the CD4+ cell population is similarly elevated for both the MinibeamRT+isotype and UniformRT+isotype arms ($p=0.01322$) compared to Controls, and similarly lowered for the anti-PD-L1 with RT-treated animals, which are very similar and not statistically significantly different from the Control arm. A similar but inverse trend is seen for the CD8+ cells, where the control and RT+anti-PD-L1 drug combination treated animals retained their CD8+ cell population percentages compared to Controls (and so were not statistically significant from Controls); however, the RT-alone (without anti-PD-L1 drug) treated animals showed statistically significantly lowered levels compared to Controls ($p=0.02685$ for Uniform+isotype arm; $p=0.0256$ for the MinibeamRT+isotype arm.) B and NK cells may also be slightly elevated for all the treatment groups relative to the controls,

but no statistically significant trend is seen among the MinibeamRT and UniformRT groups.

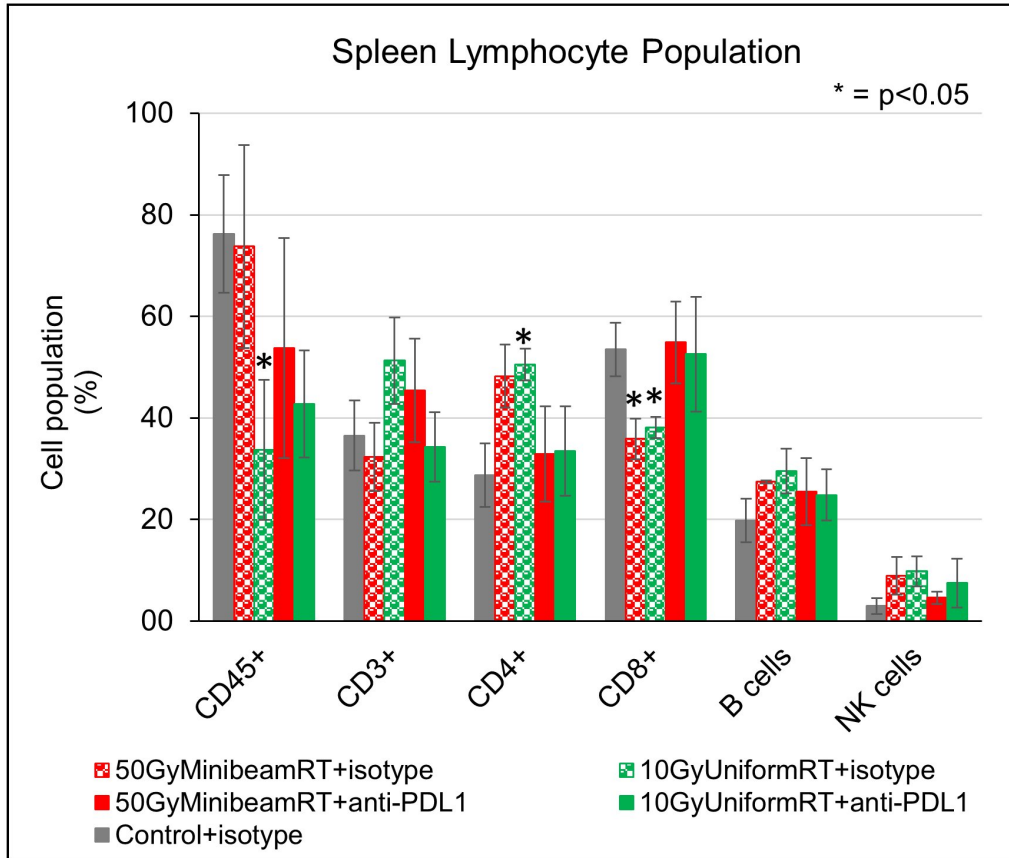


Figure 54: Flow cytometry immunophenotypic analysis of spleen cells that are harvested at 14 days post-radiotherapy. Approximately five animals per study group are harvested. When statistically compared against the Control+isotype arm, the 10GyUniformRT+isotope arm is significantly different for CD45+ ($p=0.04378$), CD4+ ($p=0.01322$), and CD8 ($p=0.02685$). In addition, for CD8 cells the 50GyMinibeamRT+isotope arm is significantly different from Control+isotype ($p=0.0256$). Differences between all other arms are not statistically significant.

5.5.4 Tumor lymphocyte profiles

Figure 55 shows the flow cytometry immune profiling data from both the irradiated and unirradiated tumors. where CD3+, CD8+, and CD4+ cell population percentages are analyzed. For the irradiated tumor, UniformRT alone (without anti-PD-L1) appears to cause greatest depletion of the overall T-cell population (CD3+), while the MinibeamRT

alone arm CD3+ population remained nearly same as for the Control arm. This may indicate that MRT is able to spare some fraction of the resident lymphocyte population. However, anti-PD-L1 drug enhanced the resident T-cell population in both radiation groups, especially for the UniformRT group.

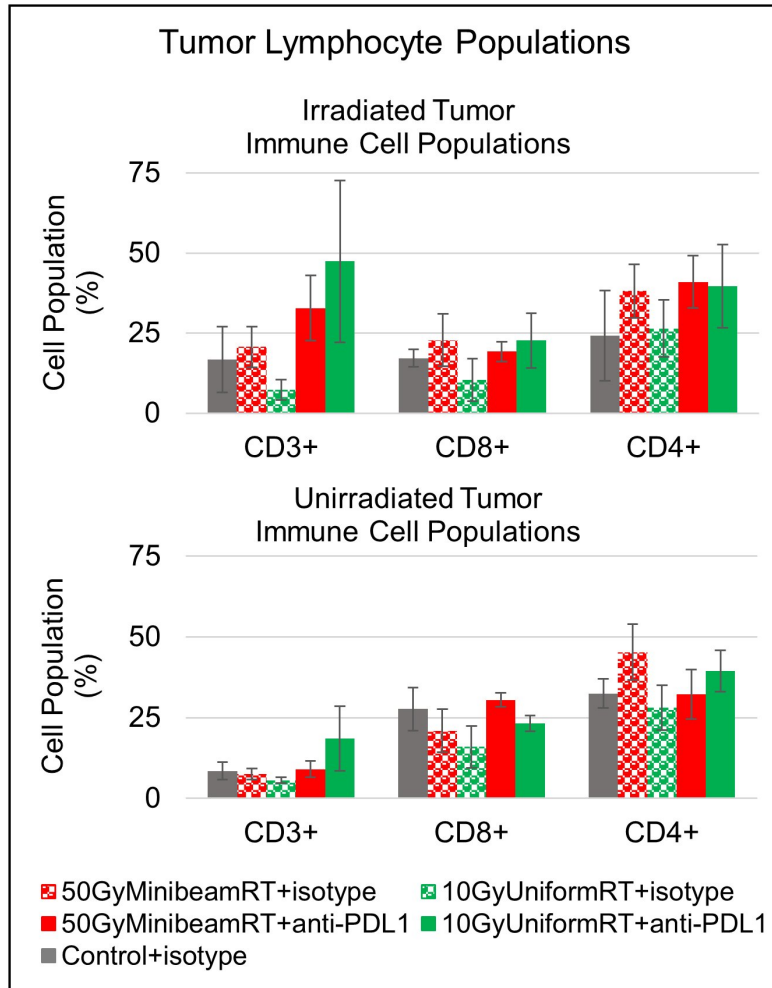


Figure 55: Flow cytometry immunophenotypic analysis of tumor cells harvested from the irradiated tumor (left) and unirradiated tumors (right) of a dual tumor mouse model of adenocarcinoma. Tumors were harvested from approximately n=5 animals per treatment group at 14 days. Differences between all arms are not statistically significant.

For the distant unirradiated tumor, there is not a clear difference among the immune cell populations as a whole. However, there does appear to be a trend towards higher CD8+ cytotoxic T cells in the MRT+anti-PD-L1 group, which would indicate greater

anti-tumor immune activity. This is also consistent with the spleen data, where the MRT+anti-PD-L1 had the highest CD8+ T cell population among the irradiated animals. This would indicate a greater systemic CD8+ T cell response, which has been shown to be a critical determinant of response in several models. These observed trends are consistent with our hypothesis that MRT induces and enhances systemic immune response. However, the relatively large within group variance and exploratory nature of this study does not allow us to establish statistical significance between the groups.

5.6 Discussion and Conclusions

Our study demonstrates that when combined with anti-PD-L1 therapy minibeam radiation is superior to uniform radiation in eliciting abscopal effect. This is indicated primarily by the tumor growth data, in which a distant tumor showed the significant growth inhibition in response to Minibeam radiation to a primary tumor site when combined with anti-PD-L1 therapy. This effect was notably different than a comparable UniformRT radiation, where a possible negative abscopal effect is observed. Note that we did not observed negative abscopal effect from *UniformRT + anti - PD - L1* in a previous pilot study, however it also showed that *MinibeamRT + anti - PD - L1* had stronger abscopal effect than *UniformRT + anti - PD - L1*. This is consistent with other studies [47], [248] showing that a single dose of seamless, uniform radiotherapy does not induce an abscopal tumor response. However, many more studies need to be conducted to make the case for any specific dose and fractionation schedule.

Our study indicates the potentially advantageous role of SFRT and MinibeamRT in eliciting a systemic anti-tumor immune response. These results are supported by trends seen in the flow cytometry characterization of immune cell infiltrates. Notably, elevated CD8+ T cells were seen in the distant (unirradiated) tumor site, as well as the spleen, indicating greater systemic cytotoxic immune response. In addition, the overall T cell populations were elevated in MinibeamRT+ anti-PD-L1 treated groups which may indicate

greater retention of resident T cell populations, in line with our hypothesis. This is consistent with previous reports on the immune response following more conventional radiation, where CD8+ T cell response has been reported to be elevated following combined radiation and PD-1/PD-L1 blockade in mouse models of glioblastoma multiform [249]. Deng et al. also showed that CD8+ T cells play a critical role in the response to UniformRT + immune checkpoint inhibition in a breast cancer mouse model [250]. Elevated CD8+ T cells is also a positive prognostic factor clinically [251], and immune checkpoint inhibition in combination with radiation has been demonstrated to increase the prevalence and activation of CD8+ T cell populations as an important mechanism of response [252]. Thus, the fact that MinibeamRT appears to further enhance this response, may be an important indication of this treatment's potential role in enhancing the immune response following combination therapy as discussed previously [49], [123], [173], [220], [228]. In this work, we have chosen to use anti-PD-L1 as an immune therapy because it has been shown to synergize with radiation therapy in a wide range of tumor models and is also being studied clinically. However, there are a wide range of other potential immune therapies that have also been shown to be synergistic in combination with radiation therapy.

One challenge in any SFRT scheme is the large parameter space over which to select and optimize the therapeutic regimen. The spatial dose distribution clearly has a significant role in how the immune response develops, and this dependence is likely to be dependent on the specific microenvironmental properties of the tumor. Thus, future work is needed to better understand how the spatial dose distribution affects immune response, and how this can be optimally implemented clinically. Our data shows that while Minibeam radiation is superior at initiating abscopal effect the conventional uniform radiation is better at local irradiated tumor control. If our finding is validated, there may be a treatment strategy that can best harvest the benefits of both SFRT and uniform radiation therapy. The treatment strategy can be first, SFRT+anti-PD-L1 to enhance systemic anti-cancer immunotherapy and second, conventional radiation therapy for local irradiated tumor control. Research is

needed to determine the best timing of the conventional treatment course.

5.7 Conflicts

None.

5.8 Acknowledgements

The authors acknowledge Mr. Anthony S. Abrantes for his kind help on statistical methods consulting.

The authors did not receive funding support for this research

CHAPTER 6: MICROBEAM RADIATION THERAPY ENHANCED TUMOR DELIVERY OF PEGYLATED LIPOSOMAL DOXORUBICIN IN A TRIPLE NEGATIVE BREAST CANCER MOUSE MODEL

6.1 Overview

Previously, we showed the potential for spatially fractionated radiation therapy (SFRT) to enhance the systemic immune response in mice when used in combination with immunomodulatory anti-cancer drugs. In a similar vein, this chapter presents an investigation into the potential advantages of SFRT over conventional radiotherapy in enhancing novel anti-cancer, chemotherapeutic drug delivery.

Carrier-Mediated Agents (CMAs) are a new class of chemotherapy drugs that have demonstrated to be much safer than typical chemotherapy drugs with significantly less cardiotoxicity, longer circulation time, and greater tumor exposure than seen with conventional, free doxorubicin. However, the lack of drug uptake into the tumor hinders the clinical translation of this promising treatment approach. The purpose of this study is to investigate the use of SFRT, a safe, experimental radiotherapy approach that preferentially eradicates tumors while sparing normal tissues, as a potential method for enhancing CMA anti-cancer drug delivery into tumors as compared to conventional, seamless radiotherapy methods in a GEMM of aggressive claudin-low triple-negative breast cancer.

This chapter has been submitted for publication⁴ in the journal *Therapeutic Advances in Medical Oncology* and is in review at the time of this writing. I have included the study

⁴This chapter has been submitted as an article in the journal *Therapeutic Advances in Medical Oncology*. The original citation is as follows: Price LSL, Rivera JN, Madden AJ, Herity LB, Piscitelli JA, Mageau S, Santos CM, Roques JR, Midkiff B, Feinberg N, Darr D, Chang SX, Zamboni WC. *Microbeam radiation therapy enhanced tumor delivery of PEGylated liposomal doxorubicin in a triple negative breast cancer mouse model*. *Therapeutic Advances in Medical Oncology*, 2020 [Manuscript In Review]. Authors Price and Rivera contributed equally to this work and should be considered co-first authors. Senior coauthors, Zamboni and Chang, contributed equally to this work.

here in full, with minor changes, including full-color versions for all figures and changes to formatting and terminology for consistency with previous chapters in this dissertation.

6.2 Introduction

The theoretical advantages of carrier mediated agents (CMAs) in cancer treatment include increased solubility, prolonged duration of exposure, selective delivery of entrapped drug to the tumor, and an improved therapeutic index [253], [254]. The primary types of anticancer CMAs are liposomes, nanoparticles (NPs) and conjugated agents. PEGylated liposomal doxorubicin (Doxil®; PLD), liposomal daunorubicin (DaunoXome®) and paclitaxel albumin-bound particles (Abraxane®) are members of this relatively new class of drugs that are approved by the U.S. FDA for the treatment of solid tumors [255]. However, the promise of these drugs is currently unfulfilled due to an overall low tumor uptake [256], [257]. In theory, enhancing permeability of the tumor vasculature allows CMAs to enter the tumor interstitial space, while suppressed lymphatic filtration allows them to stay there. This phenomenon, termed the Enhanced Permeability and Retention (EPR) effect, may be exploited by CMAs to deliver drugs to tumors [256], [257]. However, progress in developing effective CMAs using this approach has been hampered by heterogeneity of EPR effect in different tumors and the lack of information on factors that influence EPR [256]–[259]. In addition, cancer cells in tumors are surrounded by a complex microenvironment comprised of endothelial cells of the blood and lymphatic circulation, stromal fibroblasts, collagen, cells of the mononuclear phagocyte system (MPS) and other immune cells that may be associated with the variability in EPR and are potential barriers to tumor delivery of CMAs [256], [258]–[264]. Moreover, it appears that the ability of CMAs to enter tumors by EPR or other factors is highly variable across tumor types and thus all solid tumors may not be conducive for CMA delivery and treatment [256], [264]–[271]. It also is unclear how these factors affect CMAs of different sizes and shapes [267], [272], [273]. Thus, it is important to develop new methods to overcome barriers and increase the tumor delivery of several different types of CMAs in solid tumors with different degrees of EPR effect.

The pharmacokinetics (PK) of CMAs is dependent upon the carrier and not the encapsulated drug it carries [263]–[266]. Drug that remains encapsulated within the carrier has a completely different clearance and distribution compared to small molecule (SM) drugs. In theory, the EPR effect exists in tumors and may be exploited for selective delivery of drugs to tumor by CMAs. However, PK studies show that in reality the tumor delivery of CMAs is low and inefficient due to tumor heterogeneity and associated barriers [259], [263], [264], [266]. Recent publications have highlighted the relatively lower efficiency of tumor delivery seen with CMAs compared with SMs. In addition, a workshop by the Alliance for Nanotechnology in Cancer concluded that there are major gaps in the understanding of factors that affect and inhibit CMA and NP tumor delivery and new fundamental preclinical and clinical studies in this area are needed to effectively advance CMA and NP drug delivery and efficacy in solid tumors [256], [274]. So far, the advancement of CMA and NP treatment of cancer has been focused primarily on modifying formulations to overcome PK, efficacy and toxicity issues. However, this approach alone may not be adequate as biologic issues, such as barriers within the tumor microenvironment appear to play important roles in low and inefficient tumor delivery of CMAs.

Maximizing tumor control while minimizing treatment toxicity is the holy grail of all cancer treatments including chemotherapy, radiation therapy, and surgery, the three standard modalities for cancer treatment. Treatment associated toxicities directly limit the treatment “dosage” and thus hinder cancer control. Treatment toxicity is becoming more of an issue, as more cancer patients today live longer due to better cancer treatments and live to experience cancer reoccurrence years later.

Radiation therapy has been used as cytotoxic therapy for cancer local control since the discovery of x-rays by Wilhelm Conrad Röntgen in 1895. Therapeutic radiation is targeted at the tumor and causes tumor cell DNA double strand breaks, which lead to cell death and then tumor control. Although non-direct radiation effects such as bystander effect, abscopal effect, and radiation-induced anti-cancer immune responses

have received increasing attention from research communities today these effects remain poorly understood [128], [150], [212]. Microbeam radiation therapy (MRT) is a preclinical radiotherapy with promising clinical potential. In animal studies high dose MRT has shown an extremely high tissue-type selectivity where it eradicates tumors without damaging or inhibiting the function of normal tissues that are exposed to the same high dose radiation [150], [212]. The extraordinary MRT effect may be stemmed from its unique spatial, temporal, and dosimetric characteristics, which are radically different than those of the conventional broadbeam radiation therapy (BRT). MRT consists of many parallel microplanar beams at peak dose levels that are 10-100 times greater than BRT [212]. Remarkably, in animal studies the ultrahigh cytotoxic MRT dose is well tolerated by normal tissue while producing tumor control and survival comparable to conventional BRT. The MRT normal tissue sparing effect are well accepted and include two major hypotheses: (1) surviving stem cells in the low dose MRT, termed “valley” regions repopulate and repair tissue damage and (2) its mature microvasculature is resistant to MRT damage. Further, the mechanism behind MRT tumor control is still poorly understood; however, there are two major hypotheses under active investigation: (1) cellular bystander effects, wherein unirradiated or less-irradiated cells in the beam low-dose, “valley”, regions are exposed to the cytotoxic factors released by nearby dying cells from the beam “peak” regions that received massive radiation dose; and (2) immature tumor microvasculature damage effects, where tumor microvasculature is more susceptible to damage by the high dose MRT compared to normal tissue. In addition to these direct impacts on tumor control, MRT may also alter the tumor microenvironment factors important to the delivery of CMAs. Griffin et al. reported that MRT induced a transient but drastic reduction in tumor hypoxia which might open up vessels for better drug delivery [128]. The combination of direct anti-tumor activity and improved tumor delivery of CMAs with low off-target toxicity makes MRT an attractive therapy for multi-modal cancer treatment.

6.3 Methods

Animal Model All animal studies were completed under a protocol approved by the University of North Carolina at Chapel Hill Institutional Animal Care and Use Committee and in accordance with all relevant animal welfare regulations. Mice were maintained in a barrier facility on a 12-hour light/dark cycle and were provided with folate-free chow and water *ad libitum*. Tumors derived from BALB/c TP53 -/- orthotopic mammary gland transplant line (T11) were transplanted into the inguinal mammary fat pad of 12-week-old wild-type BALB/c mice (The Jackson Laboratory; strain 000651 [271]). Mice were housed in the UNC Lineberger Comprehensive Cancer Center’s Mouse Phase I Unit and observed for tumors as per the standard practice [275]. Mice were randomized to treatment cohorts, and therapy began once a tumor reached approximately 300-500 mm^3 .

6.3.1 Treatments

An XRAD-320 Research Irradiator (Precision X-Rays, Inc.) with customized collimators was used to produce the BRT and MRT radiation. For both, a $2cm \times 2cm$ irradiation treatment area was centered over the tumor. Radiation dosimetry of the BRT and MRT radiation was achieved via EBT3 Gafchromic film calibrated against an ion chamber under large field conditions [194], [199]. The in-house developed MRT collimator generated microbeams with an average beam width of $307\mu m$ and a peak-to-peak separation of $1260\mu m$. PLD was purchased from FormuMax Scientific and diluted with 5% dextrose in water to 1.2 mg/mL before injection.

6.3.2 Pharmacokinetic studies

Mice (n=3 per treatment per time point) were anesthetized using isoflurane and treated with either BRT 7Gy, MRT 28Gy, or MRT 100Gy. Following completion of radiation, mice were returned to the vivarium and monitored for signs of toxicity. Either 16 hours

(for MRT 28Gy) or 24 hours (for BRT 7Gy and MRT 100Gy) after radiation, mice were administered 6 mg/kg PLD IV $\times 1$ via a tail vein. An additional group of mice with no radiation exposure were also administered an identical dose of PLD. At predefined time points following PLD administration (5 minutes, 24 hours, and 96 hours), mice were anesthetized using 100 mg/kg ketamine IP $\times 1$ and 1 mg/kg dexmedetomidine IP $\times 1$ then ethically euthanized via cardiac puncture for collection of blood. Tumors were excised post-mortem and snap frozen in liquid nitrogen and stored at -80 degrees Celsius until processing. Additional animals received a second treatment of MRT 28Gy + PLD 16 hours post-MRT one week after the initial treatment. Mice (n=3 per timepoint) were sacrificed 5 minutes and 24 hours following the second dose of PLD and blood and tissues collected as above.

6.3.3 PLD quantification

The complete methods for sample collection, preparation and analysis of encapsulated doxorubicin in plasma and sum total (encapsulated + released) doxorubicin in tumor after administration of PLD have been previously described [271], [276]–[280]. Briefly, blood samples were collected in sodium heparin tubes at 0.083, 3, 6, 24, 48, and 96 hours after the administration of PLD. Blood was centrifuged at 1,500xg for 5 minutes to obtain plasma. Encapsulated and released doxorubicin in plasma were separated using solid phase separation. Upon processing, tumors were thawed, weighed, and diluted in a 1:3 ratio with phosphate buffered saline prior to homogenizing with a Precellys 24 bead mill homogenizer (Omni International Inc, Kennesaw, GA). Samples were further processed by addition of 800 μ L extraction solution (acetonitrile with 100 ng/mL Daunorubicin internal standard) to 200 μ L of plasma or tumor homogenate. The samples were vortexed for 10 minutes and centrifuged at 10,000xg for 10 minutes at 4 degrees Celsius. The supernatant was removed to a clean tube, evaporated to dryness under nitrogen, and reconstituted in 150 μ L of 15% acetonitrile in water plus 0.1% formic acid. The samples were then vortexed,

transferred to autosampler vials, and analyzed by high-performance liquid chromatography with fluorescence detection (HPLC-FL) set to excitation wavelength 490nm/emission wavelength 590nm. The HPLC-FL technique had a quantitative range of 10 – 3,000 ng/mL for sum total doxorubicin in tumor and 300 – 30,000 ng/mL for encapsulated doxorubicin in plasma. Samples that returned a concentration above the quantitative limit were diluted to fall within the quantitative range and reinjected.

6.3.4 Pharmacokinetics analysis

The PK of PLD plasma and tumor was analyzed by noncompartmental analysis using Phoenix WinNonlin Professional Edition version 8.0 (Pharsight Corp., Cary, NC, USA). The area under the doxorubicin concentration versus time curve (AUC) was calculated using the linear up/log down rule for plasma and tumor from T_0 to T_{last} (24 or 96 hours, depending on treatment group).

6.3.5 Tumor Staining and Immunohistochemistry

A separate group of T11 mice were randomized to either no radiation, BRT 7Gy, MRT 28Gy, or MRT 100Gy and irradiated as above. Twenty-four hours after radiation mice were anesthetized with ketamine and dexmedetomidine and sacrificed by cervical dislocation. Tumors were excised post-mortem and placed into 10% formaldehyde for paraffin embedding. Tumors were then sliced and mounted on slides for staining. Samples were stained using Masson’s Trichrome Stain (MTS), anti-Collagen IV monoclonal antibody, anti-F4/80 monoclonal antibody, and anti-CD31 monoclonal antibody as previously described. Stained slides were scanned using ScanScope XT (Leica Biosystems Inc.) an Automated High-Throughput Scanner. A quantifying algorithm employing a modified membrane analysis was utilized to automatically quantify the stained area of viable tumor [271]. Collagen IV, MTS, and macrophages (F4/80) in the viable tumor tissue were quantified by standard H-score [271], [281] and microvessels (CD31) were quantified by

microvessel density analysis ($1/mm^2$) [271], [281].

6.4 Results and Discussion

In order to assess the impact of MRT on the tumor delivery enhancement of CMAs we evaluated the pharmacokinetics (PK) of PEGylated liposomal doxorubicin (PLD) in a genetically engineered mouse model of triple negative breast cancer (T11) following either MRT or conventional BRT. Radiation-enhanced accumulation of nanoparticles and macromolecules in tumors has been reported in several previous studies [282], [283]. However, this is the first publication comparing the impact of conventional BRT and the novel MRT on the tumor microenvironment and the tumor accumulation of a drug-loaded nanoparticle. We also evaluated the impact of MRT on the tumor microenvironment through histological examination of tumor in irradiated animals.

6.4.1 Single dose pharmacokinetics

We first evaluated the PK of PLD in tumor-bearing T11 mice following a single dose of either PLD alone, BRT 7Gy + PLD, MRT 28Gy + PLD, or MRT 100Gy + PLD. For the MRT 28Gy + PLD arm, radiation was administered 16h prior to PLD. In the remaining two combination therapy arms (BRT7 Gy + PLD and MRT100 Gy + PLD), radiation was administered 24 h prior to PLD. The encapsulated plasma and sum total tumor doxorubicin concentration vs time profiles for all single dose treatments are presented in Figure 56. The encapsulated plasma and sum total tumor doxorubicin AUC_{0-96h} and ratio of tumor to plasma AUC_{0-96h} are presented in the table in Figure 57.

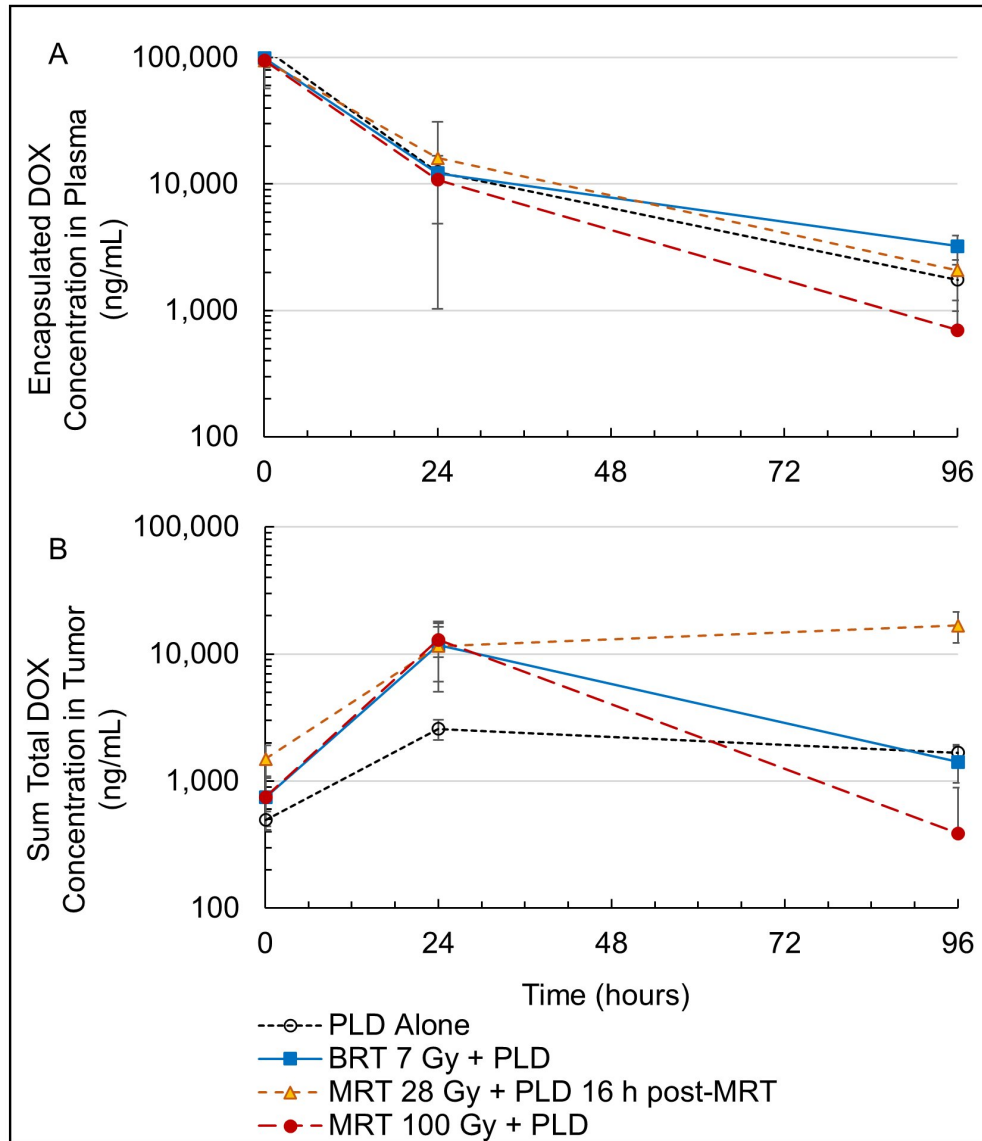


Figure 56: Mean encapsulated doxorubicin concentration in plasma (A) and sum total doxorubicin concentration in tumor (B) vs time profiles in female T11 mice after administration of: 1) PLD 6 mg/kg alone, 2) BRT 7Gy + PLD, 3) MRT 28Gy + PLD 16hours post-MRT, or 4) MRT 100Gy + PLD. The encapsulated doxorubicin exposure in plasma is similar among all groups, consistent with a lack of effect of irradiation on plasma clearance of PLD. The tumor exposure of sum total doxorubicin is significantly enhanced at 24 hours post-PLD for all radiation therapy groups compared to PLD alone, with the greatest increase in tumor exposure of sum total doxorubicin after treatment with MRT 28Gy + PLD 6 mg/kg 16 hours post-MRT.

Summary of PLD Pharmacokinetics After a Single Dose of PLD Alone, BRT + PLD, or MRT + PLD

PK Parameter	PLD Alone	BRT 7Gy + PLD	MRT 28Gy + PLD (16h post-MRT)	MRT 100Gy + PLD
Encapsulated Plasma AUC_{0-96h} (h*ng/mL)	1,521,581	1,483,098	1,347,050	1,197,501
Sum Total Tumor AUC_{0-96h} (h*ng/g)	187,548	501,635	1,176,656	420,780
Ratio of Tumor:Plasma AUC_{0-96h} (%)	12.33	33.82	87.35	35.14

Figure 57: Summary of PLD Pharmacokinetics After a Single Dose of PLD Alone, BRT + PLD, or MRT + PLD

The encapsulated plasma concentration vs time profiles and AUC_{0-96h} did not significantly differ between treatments. Because the irradiated area in this study was limited to a relatively small area centered on the tumor mass, little impact was anticipated on the primary clearance pathway of nanoparticles – the MPS. Consistent with this hypothesis, the plasma exposure of PLD was similar across all groups ($< 25\%$ difference in AUC_{0-96h}), regardless of radiation type or dose, suggesting that a single dose of BRT or MRT minimally alters the plasma clearance and disposition of PLD.

In contrast, all BRT and MRT treatment groups had significantly higher sum total tumor doxorubicin exposure compared to PLD alone. The sum total tumor doxorubicin AUC_{0-96h} was 2.7-fold and 2.2-fold higher following BRT 7Gy and MRT 100Gy, respectively, compared to PLD alone. MRT 28Gy yielded the highest PLD tumor delivery enhancement with a tumor AUC_{0-96h} 6.3-fold higher compared to PLD alone.

The tumor:plasma doxorubicin AUC ratio represents the relative delivery of nanoparticles to tumor compared to the plasma. Tumor delivery results following radiation therapy mirrored the tumor exposure due to the limited impact of radiation on

the plasma exposure. The ratio of tumor to plasma AUC_{0-96h} were 2.7-fold, 7.1-fold, and 2.8-fold higher following BRT 7Gy, MRT 28Gy, and MRT 100Gy, respectively, compared to PLD alone. These results show that MRT provides comparable enhancement of tumor nanoparticle accumulation to BRT when given at 14 times the peak dose (i.e., MRT 100Gy was similar to BRT 7Gy). Despite increased peak doses, MRT typically has significantly lower normal tissue toxicity when compared to BRT while maintaining anti-tumor efficacy [72], [174], [212]. The combination of independent anti-tumor activity, low normal tissue adverse effects, and comparable tumor delivery enhancement makes MRT an attractive modality for combination therapy in this manner.

Intriguingly, the lower peak radiation dose (MRT 28Gy) provided the most significant enhancement of tumor delivery following a single dose, suggesting that the relationship between radiation dose and tumor delivery enhancement may not be direct. While the administration of BRT 7Gy + PLD enhanced the relative delivery of PLD to the tumor 2.7-fold compared to PLD alone, MRT 28Gy + PLD 16 hours post-MRT enhanced the relative delivery of PLD a further 2.6-fold compared to BRT 7Gy + PLD. Similarly, MRT 28Gy + PLD 16 hours post-MRT enhanced relative delivery of PLD to tumor 2.5-fold compared to MRT 100Gy + PLD, which itself provided 2.8-fold enhancement relative to PLD alone.

Additionally, we explored the efficacy of MRT to enhance the tumor delivery of PLD at varying levels of systemic exposure. Using the treatment with the greatest tumor delivery enhancement after a single dose (MRT 28Gy + PLD 16 hours post-MRT), we compared a group of animals (n=3) with higher plasma doxorubicin exposure 96 hours after PLD administration to a group of animals (n=3) with lower plasma doxorubicin exposure. The tumor size, encapsulated plasma doxorubicin concentration, sum total tumor concentration, and tumor to plasma concentration ratio for these animals is presented in the table in Figure 58.

Comparison of MRT-Induced Delivery Enhancement at Low and High Plasma Exposures After a Single Dose of MRT 28Gy + PLD 16 h post-MRT		
PK Parameter	PLD Alone	BRT 7Gy + PLD
Tumor Size (mm^3)	75.3 ± 0.6	210.3 ± 52.8
Encapsulated Plasma Concentration (ng/mL)	$9,311 \pm 2,174$	$2,079 \pm 1,090$
Sum Total Tumor Concentration (ng/g)	$110,416 \pm 29,753$	$16,780 \pm 4,539$
Ratio of Tumor:Plasma Concentration	11.80 ± 0.60	10.13 ± 5.88

Figure 58: Comparison of MRT-Induced Delivery Enhancement at Low and High Plasma Exposures After a Single Dose of MRT 28Gy + PLD 16h post-MRT

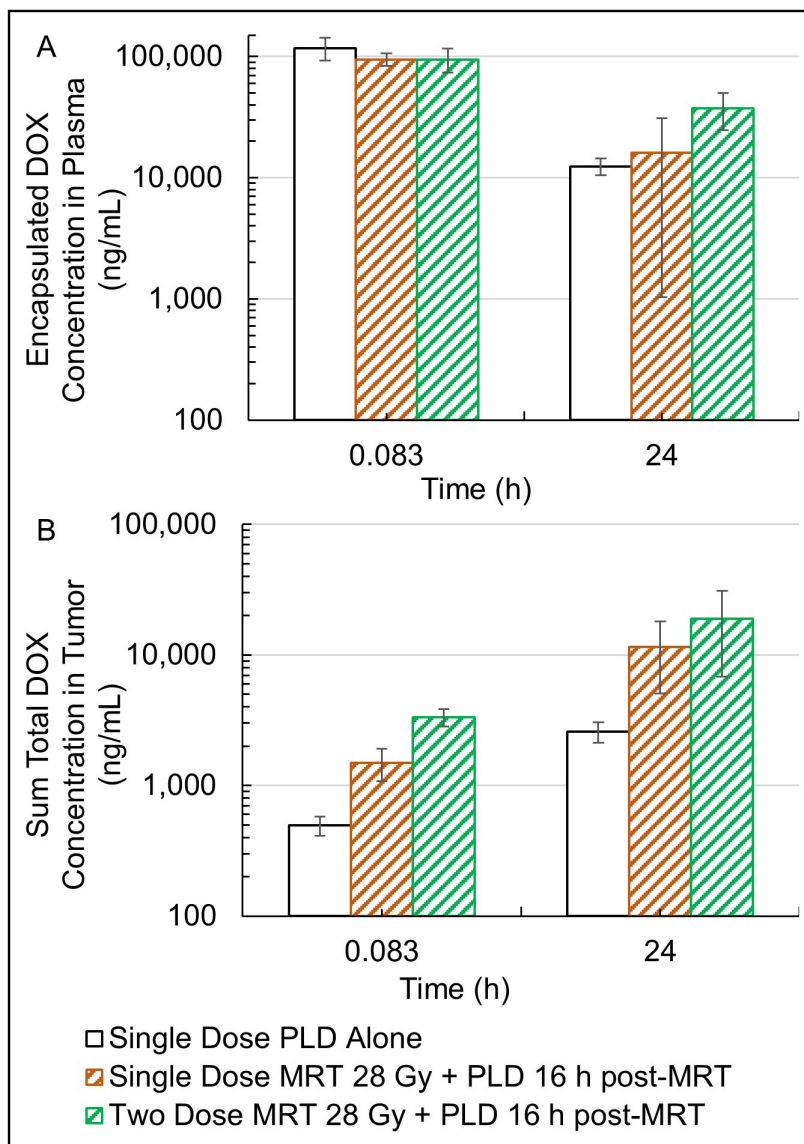
The animals with higher plasma doxorubicin exposure had smaller tumors ($75.3 \pm 0.6 \text{ mm}^3$) while those with lower plasma doxorubicin exposure had larger tumors ($210.3 \pm 52.8 \text{ mm}^3$). Higher plasma exposure led to higher sum total tumor doxorubicin concentration ($110,416 \pm 29,753$ vs $16,780 \pm 4,539$ ng/g) but the ratio of tumor to plasma doxorubicin concentration did not differ between the groups (11.80 ± 0.60 vs 10.13 ± 5.88). This suggests that the tumor delivery enhancement provided by MRT is not limited by nanoparticle dose across an approximately 4-fold range of plasma concentrations.

6.4.2 Multiple dose pharmacokinetics

After identifying enhanced tumor delivery following a single dose of MRT 28Gy + PLD 16 hours post-MRT, the efficacy of repeated dosing was investigated. The encapsulated plasma and sum total tumor doxorubicin concentration vs time profiles for 24 hours following PLD administration for single dose PLD alone, single dose MRT 28Gy + PLD 16 hours post-MRT, and two dose MRT 28Gy + PLD 16 hours post-MRT weekly are presented in Figure 59. The encapsulated plasma and sum total tumor doxorubicin AUC_{0-24h} and ratio of tumor to plasma AUC_{0-24h} for these treatments are presented in

the table in Figure 60.

Figure2



Summary of PLD Pharmacokinetics After a Single Dose of PLD Alone or One or Two Treatments of MRT 28 Gy + PLD Weekly			
PK Parameter	Single Dose PLD Alone	Single Treatment MRT 28Gy + PLD (16h post-MRT)	Two Treatments MRT 28Gy + PLD (16h post-MRT)
Encapsulated Plasma AUC_{0-24h} (h*ng/mL)	1,129,373	854,637	1,480,638
Sum Total Tumor AUC_{0-24h} (h*ng/g)	36,710	156,244	267,275
Ratio of Tumor:Plasma AUC_{0-24h} (%)	3.25	18.28	18.05

Figure 60: Summary of PLD Pharmacokinetics After a Single Dose of PLD Alone or One or Two Treatments of MRT 28Gy + PLD Weekly.

There are slight differences in the encapsulated plasma doxorubicin exposures with single dose MRT 28Gy + PLD 16 hours post-MRT giving an AUC_{0-24h} approximately 24% lower relative to PLD alone and two dose MRT 28Gy + PLD, which is 31% higher relative to PLD alone. The tumor accumulation of sum total doxorubicin is significantly enhanced following one or two doses of MRT 28Gy + PLD 16 hours post-MRT compared to PLD alone. The sum total tumor doxorubicin AUC_{0-24h} are 36,710, 156,244, and 267,275 $\frac{hng}{g}$ following a single dose of PLD alone, a single dose of MRT 28Gy + PLD 16 hours post-MRT, and two doses of MRT 28Gy + PLD 16 hours post-MRT weekly, respectively. In addition, tumor sum total doxorubicin exposure is increased following a second dose of MRT 28Gy + PLD 16 hours post-MRT relative to a single dose, consistent with increased plasma encapsulated doxorubicin exposure. The relative tumor delivery (given by the ratio of tumor to plasma AUC_{0-24h}) is similar following one (18.28%) or two (18.05%) doses of MRT 28Gy + PLD 16 hours post-MRT and higher than following a single dose of PLD alone (3.25%). The relative tumor delivery (ratio of tumor to plasma AUC_{0-24h}) was approximately 5.6-fold higher following either one or two doses of MRT 28Gy + PLD 16 hours post-MRT compared to PLD alone. The relative tumor delivery

enhancement of PLD following MRT is conserved following a second dose.

6.4.3 Tumor microenvironment profiling

The tumor microenvironment plays a pivotal role in the delivery and accumulation of nanoparticle drugs. In particular, alterations in macrophages and vasculature have been associated with changes in nanodrug delivery to tumors [257], [260], [263], [268]. A separate group of T11 mice were randomized to either no radiation, BRT 7Gy, MRT 28Gy, or MRT 100Gy and tumors were profiled via immunohistochemistry. H-scores for F4/80, Collagen IV, and MTS and microvessel density (CD31) in viable tumor are presented in Figure 61.

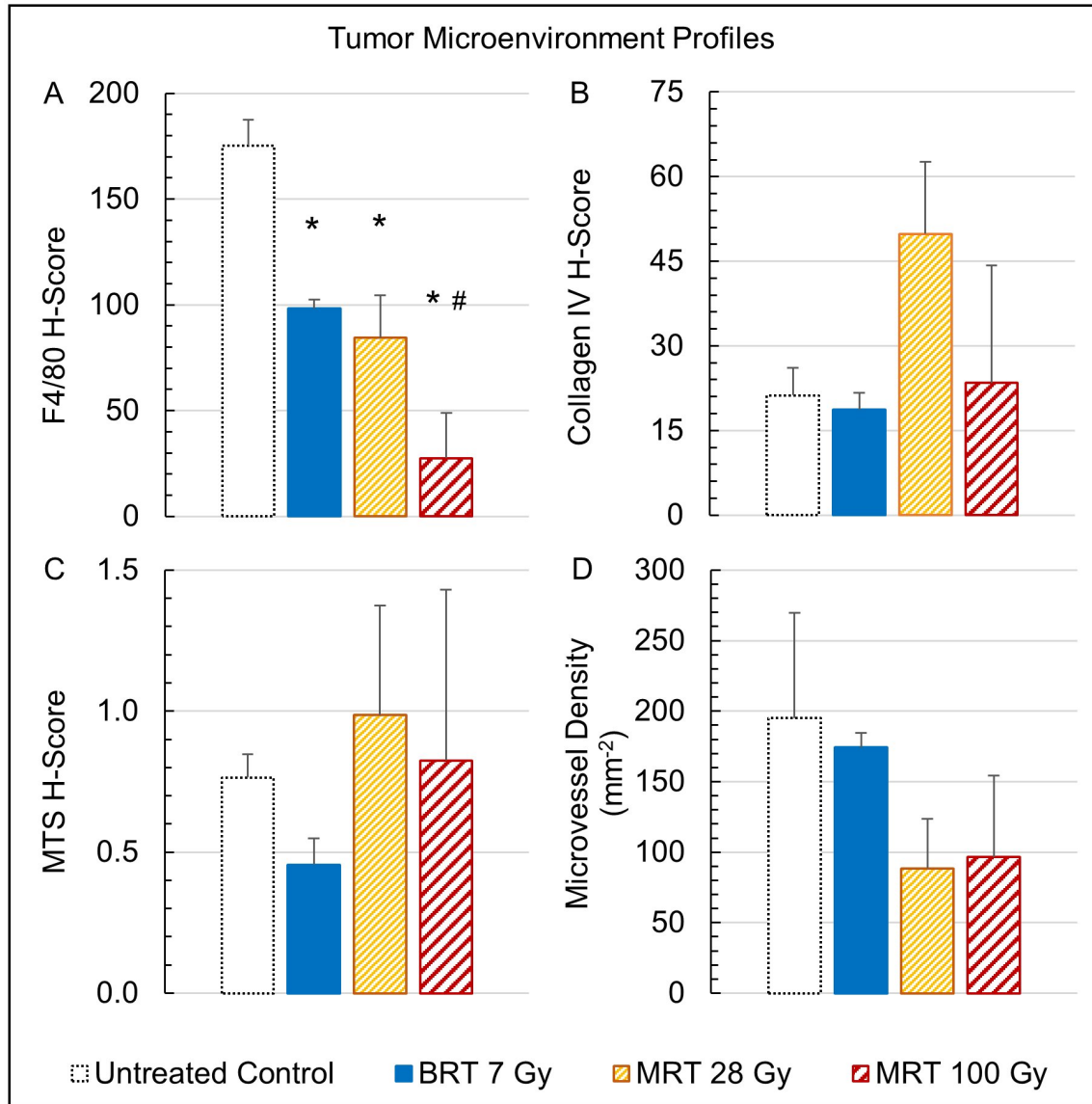


Figure 61: Tumor microenvironment profiles 24 h after 1) no radiation, 2) BRT 7 Gy, 3) MRT 28 Gy, or 4) MRT 100 Gy, in female T11 mice. A) F4/80 H-Scores, B) Collagen IV H-Scores, C) MTS H-Scores, D) CD31 Microvessel Density. * $p < 0.01$ vs Untreated Control, # $p < 0.01$ vs BRT 7 Gy. Both BRT and MRT decrease macrophages with MRT 100 Gy yielding a larger decrease in F4/80 H-Scores in viable tumor. There are no statistically significant ($p < 0.01$) changes in collagen as assessed by either Collagen IV or MTS or microvessel density (CD31) between untreated control and any radiation therapy group.

There is a significant, dose-dependent reduction in macrophages in viable tumor, as evidenced by decreases in F4/80 H-Scores, 24 hours after both BRT and MRT. The highest F4/80 H-score was observed in the Untreated Control group (175.3 ± 12.1) followed by the

lower radiation doses, BRT 7Gy (98.2 ± 4.3) and MRT 28Gy (84.4 ± 20.2). The higher peak radiation dose, MRT 100Gy, resulted in the lowest F4/80 H-score (27.5 ± 21.4). In this study, radiation led to depletion of macrophages in viable tumor tissue 24 hours after either BRT or MRT. Lower radiation doses, BRT 7Gy and MRT 28Gy, resulted in 44% and 52% reductions in macrophages, respectively, while the higher peak radiation dose of MRT 100Gy resulted in 84% reduction in macrophages. A previous BRT study associated a relative increase in macrophages following radiation with an increase in nanodrug delivery [284]. However, the relative timing of radiotherapy and nanodrug administration differed between the two studies. Miller et al. administered a therapeutic polymeric cisplatin prodrug NP (TNP) 72 hours post-irradiation and assessed macrophage presence 24 hours post-TNP administration (96 hours post-irradiation). Macrophage assessment and PLD administration in our study was performed 24 h post-irradiation. Furthermore, analytical techniques differed as macrophages were assessed relative to tumor cells in a flow cytometry assay by Miller et al. A potential explanation for these seemingly opposite findings would be a rapid radiation-induced nadir of macrophages (within 24 hours post-irradiation) followed by later macrophage infiltration resulting in the increased PLD tumor exposure 24-96 hours post-PLD (48-120 hours post-irradiation).

Collagen, assessed by both Collagen IV IHC and MTS, showed no significant changes between untreated control and irradiated tumors. In addition, microvessel density, assessed by CD31, also did not differ between untreated control and irradiated tumors. This suggests that, at least for the first 24 hours following radiation, there is not a change in collagen content or microvessel number driving the enhancement of nanoparticle delivery to tumors.

In this study we evaluated the impact of conventional BRT in comparison to novel MRT on the tumor microenvironment and ability to enhance tumor delivery of a drug loaded nanoparticle. In a GEMM of triple negative breast cancer, both BRT and MRT altered the microenvironment through depletion of macrophages and significantly enhanced

the tumor delivery of PLD. Notably, High dose MRT (100Gy peak dose and valley dose of approximately 8Gy) provided comparable PLD tumor delivery enhancement to BRT (7Gy). But the most significant enhancement of tumor delivery occurred when a lower peak radiation dose MRT of 28Gy was used (and valley dose of 2.26Gy). In addition, the tumor delivery enhancement provided by pretreatment with MRT 28Gy is maintained at both high and low plasma exposure and following repeated dosing. Further studies are warranted to assess the efficacy of radiation-induced tumor delivery enhancement in other tumor models and with other nanoparticles as well as the mechanism of radiation-induced tumor delivery enhancement.

6.5 Acknowledgements

The authors thank Nana Nikolaishvili-Feinberg and Bentley R. Midkiff in the UNC Translational Pathology Laboratory (TPL) for expert technical assistance. The UNC TPL is supported in part by grants from the NCI (2-P30-CA016086-40), NIEHS (2-P30ES010126-15A1), UCRF, and NCBT (2015-IDG-1007). Animal histopathology was performed by the Animal Histopathology & Laboratory Medicine Core at UNC, which is supported in part by an NCI Center Core Support Grant (5P30CA016086-41) to the UNC Lineberger Comprehensive Cancer Center. The authors wish to acknowledge Certara for providing academic access to Phoenix WinNonlin through the Center of Excellence program.

6.6 Funding

This investigation was funded, in part, by the UNC Eshelman Institute for Innovation (1U54CA198999-01) Carolina Center of Cancer Nanotechnology Excellence- Pilot Grant Program.

CHAPTER 7: DISCUSSION AND FINAL CONCLUSIONS

7.1 The Potential Global Impact of SFRT

There are nearly 20 million new cancer cases a year, with over 70% of them arising in the developing world [54], [285], [286]. From a public health perspective, the most rational and cost-effective method to address this crisis is through prevention and education, but cancer deaths are already on the rise, with nearly 10 million deaths worldwide in 2018, and deaths are expected to increase up to 12 million this year, doubled compared to a decade ago [285], [287].

Radiation therapy is one of the most cost-effective methods for treating cancer and has the potential for alleviating the global cancer burden [15], [288]; however, severe inequities exist in access to radiation therapy around the world [15], [288]. Numerous countries have access to only a limited number of radiotherapy treatment facilities, with most countries in Asia having only one unit available for every 1-2 million people [286], though often less, and 29 out of 52 countries in Africa have no radiotherapy facilities at all [289]. When a radiotherapy treatment facility is available, the barriers to implementation of radiation therapy are numerous and diverse; high up-front costs for facilities and equipment [15], [67], [290], the lack of training and personnel for the specialized team of healthcare professionals needed to use and maintain the equipment [67], [291], and widespread systemic barriers such as governmental policies or practices (or lack thereof) make implementation exceedingly difficult [67], [68], [291].

Even after mitigating some of these barriers, increasing access to radiotherapy facilities is just one small step towards helping meet the pressing clinical needs to effectively implement radiotherapy treatments. Studies have shown that developing countries also

have higher incidences of advanced disease presentation, up to 70% presenting with late stage illness according to the World Health Organization (WHO) [292]. Advanced disease presentation is correlated with poor prognostic outcomes, and treatments to minimize suffering, including palliative radiation, are often the only options left available [293]–[296]. With the high number of new cancer cases yearly, and the low number of facilities in high-need regions, the global cancer burden continues to rise. Alleviating this serious global cancer burden is critically important and requires new strategies for improving healthcare outcomes.

Accessible, low-cost radiotherapy and alternatives to conventional radiotherapy may play a part in utilizing available radiotherapy facilities to reducing cancer burden. Spatially fractionated radiation therapy is a strong candidate for helping meet some of the most pressing clinical needs in cancer therapy. As both a therapeutically- and cost-effective approach, SFRT may have an important role to play in improving patient outcomes in both the definitive and palliative settings for patients in underserved communities [297]. For example, SFRT treatment has been shown to be beneficial for those patients with very advanced, or bulky disease and for very aggressive tumors types [73], [204]. Hence, for those 70% of patients presenting with very advanced, late stage disease, palliative SFRT may offer a safe treatment option and dramatic pain symptom relief, especially for those that would otherwise suffer [73]. For the five most common cancers in developing countries, stomach, lung, liver, breast, and cervix [286], SFRT studies have reported good oncological outcomes in each of these disease sites [49], [52], [73], [82], [84]–[87], [90], [91]. From an economic perspective, definitive SFRT may be offered as a boost to conventional courses of radiotherapy without significantly added time or cost, while palliative SFRT may be offered as a single, cost-effective treatment, something that would be extremely beneficial for patients that have to travel long distances to an radiotherapy-equipped facility [287]. SFRT may also be easily implemented in existing radiotherapy units with very low added costs, since SFRT utilizing a relatively inexpensive, reusable GRID compensator (see

Chapter 2.4.1 on GRID Therapy) does not require use of the highly advanced, state-of-the-art radiation therapy treatment technologies, which are largely limited to highly developed industrialized nations.

7.2 New Horizons in SFRT

Despite its very high therapeutic ratio and long history, SFRT remains largely an experimental treatment and there are still many unanswered questions behind the promising radiotherapy approach. In the past decade, SFRT has recently gained traction, becoming a very active area of investigation, and its application in combination treatment strategies has made studying SFRT an interesting and valuable research endeavor. In fact, in 2018 the National Cancer Institute together with the Radiosurgery Society created a new, international working group dedicated to investigating SFRT, and the related Flash radiotherapy, with the goal of advancing our understanding of SFRT biology, physics, and clinical translation. The new working group consists of a researchers from around the country and the world, including many leaders in the field of SFRT and MRT technology research and development, as well as physicians and other stakeholders that have a special interest in the clinical translation of this promising treatment modality. In just the last two years, several clinical trials using SFRT have been developed specifically for targeting patients with massive, bulky tumors, patients with radioresistant tumors such as squamous cell carcinomas of the head and neck, as well as patients with pediatric osteosarcomas of the extremities [298]. Current, active clinical trials using SFRT include, but are not limited to:

1. GRID Therapy as Palliative Radiation for Patients with Advanced and Symptomatic Tumors (NCT02333110)
2. Phase I Clinical Trial of GRID Therapy in Pediatric Osteosarcoma of the Extremity (NCT03139318)

3. Understanding GRID Radiation Therapy Effects on Human Tumor Oxygenation and Interstitial Pressure to Increase Translation of Solid Tumor Therapy (NCT01967927)
4. Lattice Stereotactic Body Radiation Therapy (LATTICE SBRT) for Localized Unresectable or Metastatic Conventional Type Chondrosarcoma (NCT04098887)
5. Palliative Lattice Stereotactic Body Radiotherapy (SBRT) (NCT041333415)
6. MRI-Guided Lattice Extreme Ablative Dose Radiotherapy for Prostate Cancer (NCT01411319)
7. Randomized MRI-Guided Prostate Boosts via Initial Lattice Stereotactic vs Daily Moderately Hypofractionated Radiotherapy (BLaStM) (NCT02307058) [299]
8. Neoadjuvant Durvalumab and Tremelimumab Plus Radiation for High Risk Soft-Tissue Sarcoma (NEXIS) (NCT03116529)

Additionally, moves have been made at the European Synchrotron Facility (ESRF) in Grenoble, France to establish a modern SFRT, micro-collimated beamline for use in clinical patient trials [203]. The marked, growing interest in this promising treatment approach is readily apparent and is very encouraging for the future of the field of SFRT research as well as the future of cancer therapy.

In addition to the new clinical trials, it is very important to continue improving our understanding of the working mechanisms behind SFRT through preclinical studies. One avenue for potential SFRT advancement is by using larger animals as pre-clinical models [174]. Nolan et al noted the remarkable similarities in pet dog cancer outcomes and radiobiology when compared to humans and that modern veterinary radiation oncology utilizes the same treatment technologies as those used for human patients [300], including:

- MV energy LINACs capable of stereotactic radiosurgery [301]–[303] (see Section 1.4.3 SBRT in Chapter 1), as well as IMRT [304] (see Chapter 1.4.2 on IMRT),

- Modern dosimetry technology and protocols [301], [302], and
- Advanced treatment planning techniques [302].
- In addition, in one of our own studies, we implemented veterinary SFRT on a pet canine model of spontaneous soft-tissue sarcomas [305] while other studies have also applied SFRT on weanling pigs [115].

These advances in veterinary medicine may enable the use of large animals in pre-clinical SFRT studies as large animals have the potential for serving as acceptable surrogates for human clinical trials with similar clinical endpoints, but without the exceedingly high cost-barriers.

7.3 Conclusions

Clearly, a tremendous amount of work still needs to be completed to expand our knowledge of SFRT, its radiobiological effects, and what advantages it has to offer. This body of work attempts to shed light on some of the unanswered questions in SFRT in the hopes of advancing the broad clinical translation of this promising treatment technology, especially for those currently underserved patients that may benefit most. In particular, the fascinating observation that SFRT may modify the tumor microenvironment differently than conventional radiation has inspired us to formulate creative, innovative research ideas, aimed to not only understand this unique form of radiation, but also to develop its relevant technology and dosimetry and identify new applications for it. One such interesting application explored in this dissertation involves using SFRT multi-modality approaches for potentially enhancing the therapeutic ratio of anti-cancer drug therapies. Chapter 5 investigated the potential for SFRT to enhance the systemic immune response in mice when used in combination with anti-cancer immunomodulatory drugs. Results indicated that SFRT with immunomodulatory drugs significantly enhanced the abscopal effect, where distant unirradiated tumors exhibited control response, and results also showed

greater immune cell infiltration as compared to the corresponding conventional, uniform radiotherapy treatment. In addition, Chapter 6 investigated the potential for SFRT to enhance the delivery of novel, nanoparticle anticancer agents to tumors. Pharmacokinetic results indicated that low dose SFRT safely and effectively enhanced tumor delivery of the nanoparticle drugs compared to conventional radiotherapy and drug alone. These studies together help provide a deeper understanding of how the unique radiobiological effects induced by SFRT may be exploited for potentially enhancing treatment outcomes in combination therapy treatments.

One additional front for advancing the clinical translation of SFRT is a better understanding of the correlation between dosimetric parameters and treatment outcomes. In Chapter 4, we identified key SFRT dosimetric parameters and their association with treatment outcomes using a range of spatial-fractionation patterns at conventional dose-rates in a preclinical model. Results indicated that although peak dose is often used to prescribe clinical and pre-clinical SFRT treatments, among the various dosimetric parameters studied, peak dose was most weakly associated with treatment response, while the valley dose and tumor EUD were most closely associated with treatment response. This indicates that clinicians and researchers may need to more carefully consider the valley dose and tumor EUD, in addition the peak dose, when prescribing SFRT treatments and that more research examining the effects of dosimetric treatment parameters on treatment outcomes is warranted. Finally, Chapter 3 discusses the development of a novel, non-synchrotron-based, low-cost preclinical SFRT delivery system for use in small animal research, a system that may allow other SFRT researchers to more readily expand upon these findings and also explore uncharted horizons in our understanding of SFRT and its uses.

These studies may provide a deeper understanding of the underlying radiobiology of SFRT and may also reveal new additional pathways for increasing the therapeutic ratio in patients via combination therapy approaches. Most importantly, these studies may

allow us to proceed one step closer to the eventual clinical translation of these promising alternative treatments, with the hope that these cancer therapies may one day become a “saving grace” to those patients for whom conventional treatments are not an option.

REFERENCES

- [1] Y. A. Fouad and C. Aanei, “Revisiting the hallmarks of cancer,” *American Journal of Cancer Research*, vol. 7, no. 5, pp. 1016–1036, May 2017, ISSN: 2156-6976.
- [2] D. Hanahan and R. A. Weinberg, “The Hallmarks of Cancer,” English, *Cell*, vol. 100, no. 1, pp. 57–70, Jan. 2000, ISSN: 0092-8674, 1097-4172. DOI: 10.1016/S0092-8674(00)81683-9.
- [3] J. Welte, S. Loges, S. Dimmeler, and P. Carmeliet, “Recent molecular discoveries in angiogenesis and antiangiogenic therapies in cancer,” en, *The Journal of Clinical Investigation*, vol. 123, no. 8, pp. 3190–3200, Aug. 2013, ISSN: 0021-9738. DOI: 10.1172/JCI70212.
- [4] K. Harrington, P. Jankowska, and M. Hingorani, “Molecular Biology for the Radiation Oncologist: The 5Rs of Radiobiology meet the Hallmarks of Cancer,” en, *Clinical Oncology*, vol. 19, no. 8, pp. 561–571, Oct. 2007, ISSN: 0936-6555. DOI: 10.1016/j.clon.2007.04.009.
- [5] J. S. Good and K. J. Harrington, “The Hallmarks of Cancer and the Radiation Oncologist: Updating the 5Rs of Radiobiology,” English, *Clinical Oncology*, Advances in Clinical Radiobiology, vol. 25, no. 10, pp. 569–577, Oct. 2013, ISSN: 0936-6555, 1433-2981. DOI: 10.1016/j.clon.2013.06.009.
- [6] V. Law, C. Knox, Y. Djoumbou, T. Jewison, A. C. Guo, Y. Liu, A. Maciejewski, D. Arndt, M. Wilson, V. Neveu, A. Tang, G. Gabriel, C. Ly, S. Adamjee, Z. T. Dame, B. Han, Y. Zhou, and D. S. Wishart, “DrugBank 4.0: Shedding new light on drug metabolism,” en, *Nucleic Acids Research*, vol. 42, no. D1, pp. D1091–D1097, Jan. 2014, ISSN: 0305-1048. DOI: 10.1093/nar/gkt1068.
- [7] D. Hanahan and R. A. Weinberg, “Hallmarks of Cancer: The Next Generation,” en, *Cell*, vol. 144, no. 5, pp. 646–674, Mar. 2011, ISSN: 0092-8674. DOI: 10.1016/j.cell.2011.02.013.
- [8] K. C. Valkenburg, A. E. de Groot, and K. C. Pienta, “Targeting the tumour stroma to improve cancer therapy,” *Nature reviews. Clinical oncology*, vol. 15, no. 6, pp. 366–381, Jun. 2018, ISSN: 1759-4774. DOI: 10.1038/s41571-018-0007-1.
- [9] J. Plava, M. Cihova, M. Burikova, M. Matuskova, L. Kucerova, and S. Miklikova, “Recent advances in understanding tumor stroma-mediated chemoresistance in breast cancer,” *Molecular Cancer*, vol. 18, no. 1, p. 67, Mar. 2019, ISSN: 1476-4598. DOI: 10.1186/s12943-019-0960-z.
- [10] R. R. Langley and I. J. Fidler, “The seed and soil hypothesis revisited—The role of tumor-stroma interactions in metastasis to different organs,” en, *International Journal of Cancer*, vol. 128, no. 11, pp. 2527–2535, 2011, eprint: <https://onlinelibrary.wiley.com/doi/pdf/10.1002/ijc.26031>, ISSN: 1097-0215. DOI: 10.1002/ijc.26031.

- [11] G. Lorusso and C. Rüegg, “New insights into the mechanisms of organ-specific breast cancer metastasis,” en, *Seminars in Cancer Biology*, Novel Concepts in Cancer Metastasis, vol. 22, no. 3, pp. 226–233, Jun. 2012, ISSN: 1044-579X. DOI: 10.1016/j.semcancer.2012.03.007.
- [12] M. E. Hardee, A. E. Marciscano, C. M. Medina-Ramirez, D. Zagzag, A. Narayana, S. M. Lonning, and M. H. Barcellos-Hoff, “Resistance of Glioblastoma-Initiating Cells to Radiation Mediated by the Tumor Microenvironment Can Be Abolished by Inhibiting Transforming Growth Factor- β ,” en, *Cancer Research*, vol. 72, no. 16, pp. 4119–4129, Aug. 2012, ISSN: 0008-5472, 1538-7445. DOI: 10.1158/0008-5472.CAN-12-0546.
- [13] H. J. Park, R. J. Griffin, S. Hui, S. H. Levitt, and C. W. Song, “Radiation-Induced Vascular Damage in Tumors: Implications of Vascular Damage in Ablative Hypofractionated Radiotherapy (SBRT and SRS),” *Radiation Research*, vol. 177, no. 3, pp. 311–327, Jan. 2012, ISSN: 0033-7587. DOI: 10.1667/RR2773.1.
- [14] R. Baskar, K. A. Lee, R. Yeo, and K.-W. Yeoh, “Cancer and Radiation Therapy: Current Advances and Future Directions,” *International Journal of Medical Sciences*, vol. 9, no. 3, pp. 193–199, Feb. 2012, ISSN: 1449-1907. DOI: 10.7150/ijms.3635.
- [15] D. A. Jaffray and M. K. Gospodarowicz, “Radiation Therapy for Cancer,” eng, in *Cancer: Disease Control Priorities, Third Edition (Volume 3)*, H. Gelband, P. Jha, R. Sankaranarayanan, and S. Horton, Eds., Washington (DC): The International Bank for Reconstruction and Development / The World Bank, 2015, ISBN: 978-1-4648-0349-9 978-1-4648-0369-7.
- [16] J. Thoms and R. G. Bristow, “DNA Repair Targeting and Radiotherapy: A Focus on the Therapeutic Ratio,” en, *Seminars in Radiation Oncology*, Harnessing DNA Repair to Improve Radiotherapy Outcome, vol. 20, no. 4, pp. 217–222, Oct. 2010, ISSN: 1053-4296. DOI: 10.1016/j.semradonc.2010.06.003.
- [17] A. Yokoya, N. Shikazono, K. Fujii, A. Urushibara, K. Akamatsu, and R. Watanabe, “DNA damage induced by the direct effect of radiation,” en, *Radiation Physics and Chemistry*, The International Symposium on Charged Particle and Photon Interaction with Matter - ASR 2007, vol. 77, no. 10, pp. 1280–1285, Oct. 2008, ISSN: 0969-806X. DOI: 10.1016/j.radphyschem.2008.05.021.
- [18] A. C. Begg, F. A. Stewart, and C. Vens, “Strategies to improve radiotherapy with targeted drugs,” en, *Nature Reviews Cancer*, vol. 11, no. 4, pp. 239–253, Apr. 2011, ISSN: 1474-1768. DOI: 10.1038/nrc3007.
- [19] P. N. Martins, “A brief history about radiotherapy,” en, vol. 04, no. 02, p. 5, 2018.

- [20] R. F. Mould, *A Century of X-Rays and Radioactivity in Medicine: With Emphasis on Photographic Records of the Early Years*, en. CRC Press, Jan. 1993, ISBN: 978-0-7503-0224-1.
- [21] R. A. Sharma, R. Plummer, J. K. Stock, T. A. Greenhalgh, O. Ataman, S. Kelly, R. Clay, R. A. Adams, R. D. Baird, L. Billingham, S. R. Brown, S. Buckland, H. Bulbeck, A. J. Chalmers, G. Clack, A. N. Cranston, L. Damstrup, R. Ferraldeschi, M. D. Forster, J. Golec, R. M. Hagan, E. Hall, A.-R. Hanauske, K. J. Harrington, T. Haswell, M. A. Hawkins, T. Illidge, H. Jones, A. S. Kennedy, F. McDonald, T. Melcher, J. P. B. O'Connor, J. R. Pollard, M. P. Saunders, D. Sebag-Montefiore, M. Smitt, J. Staffurth, I. J. Stratford, and S. R. Wedge, "Clinical development of new drug-radiotherapy combinations," en, *Nature Reviews Clinical Oncology*, vol. 13, no. 10, pp. 627–642, Oct. 2016, ISSN: 1759-4782. DOI: 10.1038/nrclinonc.2016.79.
- [22] P. Montay-Gruel, L. Meziani, C. Yakkala, and M.-C. Vozenin, "Expanding the therapeutic index of radiation therapy by normal tissue protection," *The British Journal of Radiology*, vol. 92, no. 1093, Jan. 2019, ISSN: 0007-1285. DOI: 10.1259/bjr.20180008.
- [23] S. Webb, *The Physics of Three Dimensional Radiation Therapy: Conformal Radiotherapy, Radiosurgery and Treatment Planning*, en. CRC Press, Jan. 1993, ISBN: 978-1-4200-5036-3.
- [24] W. Schlegel and A. Mahr, *3D Conformal Radiation Therapy: Multimedia Introduction to Methods and Techniques*, Second. Springer Publishing Company, Incorporated, 2007, ISBN: 978-3-540-71550-4.
- [25] J. ur Rehman, Zahra, N. Ahmad, M. Khalid, H. M. N. u. H. K. Asghar, Z. A. Gilani, I. Ullah, G. Nasar, M. M. Akhtar, and M. N. Usmani, "Intensity modulated radiation therapy: A review of current practice and future outlooks," *Journal of Radiation Research and Applied Sciences*, vol. 11, no. 4, pp. 361–367, Oct. 2018, _eprint: <https://doi.org/10.1016/j.jrras.2018.07.006>, ISSN: null. DOI: 10.1016/j.jrras.2018.07.006.
- [26] N. Y. Lee and S. A. Terezakis, "Intensity-modulated radiation therapy," en, *Journal of Surgical Oncology*, vol. 97, no. 8, pp. 691–696, 2008, _eprint: <https://onlinelibrary.wiley.com/doi/pdf/10.1002/jso.21014>, ISSN: 1096-9098. DOI: 10.1002/jso.21014.
- [27] J. A. Purdy, "DOSE TO NORMAL TISSUES OUTSIDE THE RADIATION THERAPY PATIENT'S TREATED VOLUME: A REVIEW OF DIFFERENT RADIATION THERAPY TECHNIQUES," en-US, *Health Physics*, vol. 95, no. 5, pp. 666–676, Nov. 2008, ISSN: 0017-9078. DOI: 10.1097/01.HP.0000326342.47348.06.

- [28] M. R. Young and J. B. Yu, “Intensity Modulated Radiotherapy and Image Guidance,” en, in *Prostate Cancer*, Elsevier, 2016, pp. 413–426, ISBN: 978-0-12-800077-9. DOI: 10.1016/B978-0-12-800077-9.00045-1.
- [29] H. Paganetti, B. S. Athar, M. Moteabbed, J. A. Adams, U. Schneider, and T. I. Yock, “Assessment of radiation-induced second cancer risks in proton therapy and IMRT for organs inside the primary radiation field,” en, *Physics in Medicine & Biology*, vol. 57, no. 19, p. 6047, 2012, ISSN: 0031-9155. DOI: 10.1088/0031-9155/57/19/6047.
- [30] A. C. Tree, V. S. Khoo, R. A. Eeles, M. Ahmed, D. P. Dearnaley, M. A. Hawkins, R. A. Huddart, C. M. Nutting, P. J. Ostler, and N. J. van As, “Stereotactic body radiotherapy for oligometastases,” en, *The Lancet Oncology*, vol. 14, no. 1, e28–e37, Jan. 2013, ISSN: 1470-2045. DOI: 10.1016/S1470-2045(12)70510-7.
- [31] L. Potters, B. Kavanagh, J. M. Galvin, J. M. Hevezi, N. A. Janjan, D. A. Larson, M. P. Mehta, S. Ryu, M. Steinberg, R. Timmerman, J. S. Welsh, and S. A. Rosenthal, “American Society for Therapeutic Radiology and Oncology (ASTRO) and American College of Radiology (ACR) Practice Guideline for the Performance of Stereotactic Body Radiation Therapy,” English, *International Journal of Radiation Oncology • Biology • Physics*, vol. 76, no. 2, pp. 326–332, Feb. 2010, ISSN: 0360-3016. DOI: 10.1016/j.ijrobp.2009.09.042.
- [32] N. T. Sebastian, M. Xu-Welliver, and T. M. Williams, “Stereotactic body radiation therapy (SBRT) for early stage non-small cell lung cancer (NSCLC): Contemporary insights and advances,” *Journal of Thoracic Disease*, vol. 10, no. Suppl 21, S2451–S2464, Aug. 2018, ISSN: 2072-1439. DOI: 10.21037/jtd.2018.04.52.
- [33] R. Mohan and D. Grosshans, “Proton therapy – Present and future,” en, *Advanced Drug Delivery Reviews*, Radiotherapy for Cancer: Present and Future, vol. 109, pp. 26–44, Jan. 2017, ISSN: 0169-409X. DOI: 10.1016/j.addr.2016.11.006.
- [34] H. Paganetti, “Relative biological effectiveness (RBE) values for proton beam therapy. Variations as a function of biological endpoint, dose, and linear energy transfer,” en, *Physics in Medicine and Biology*, vol. 59, no. 22, R419–R472, Oct. 2014, ISSN: 0031-9155. DOI: 10.1088/0031-9155/59/22/R419.
- [35] D. De Ruysscher, M. Mark Lodge, B. Jones, M. Brada, A. Munro, T. Jefferson, and M. Pijls-Johannesma, “Charged particles in radiotherapy: A 5-year update of a systematic review,” en, *Radiotherapy and Oncology*, vol. 103, no. 1, pp. 5–7, Apr. 2012, ISSN: 01678140. DOI: 10.1016/j.radonc.2012.01.003.
- [36] A. Peeters, J. P. C. Grutters, M. Pijls-Johannesma, S. Reimoser, D. D. Ruysscher, J. L. Severens, M. A. Joore, and P. Lambin, “How costly is particle therapy? Cost analysis of external beam radiotherapy with carbon-ions, protons and photons,” English, *Radiotherapy and Oncology*, vol. 95, no. 1, pp. 45–53, Apr. 2010, ISSN: 0167-8140, 1879-0887. DOI: 10.1016/j.radonc.2009.12.002.

- [37] M. Brada, M. Pijls-Johannesma, and D. De Ruyscher, “Proton Therapy in Clinical Practice: Current Clinical Evidence,” en, *Journal of Clinical Oncology*, vol. 25, no. 8, pp. 965–970, Mar. 2007, ISSN: 0732-183X, 1527-7755. DOI: 10.1200/JCO.2006.10.0131.
- [38] Y. Lievens and K. Nagels, “Economic data for particle therapy: Dealing with different needs in a heterogeneous landscape,” en, *Radiotherapy and Oncology*, vol. 128, no. 1, pp. 19–25, Jul. 2018, ISSN: 0167-8140. DOI: 10.1016/j.radonc.2018.03.016.
- [39] T. S. Lawrence, B. G. Haffty, and J. R. Harris, “Milestones in the Use of Combined-Modality Radiation Therapy and Chemotherapy,” EN, *Journal of Clinical Oncology*, vol. 32, no. 12, pp. 1173–1179, Mar. 2014, ISSN: 0732-183X. DOI: 10.1200/JCO.2014.55.2281.
- [40] C. N. Coleman, T. S. Lawrence, and D. G. Kirsch, “Enhancing the Efficacy of Radiation Therapy: Premises, Promises, and Practicality,” *Journal of Clinical Oncology*, vol. 32, no. 26, pp. 2832–2835, Sep. 2014, ISSN: 0732-183X. DOI: 10.1200/JCO.2014.57.3865.
- [41] A. R. Kwilas, R. N. Donahue, M. B. Bernstein, and J. W. Hodge, “In the field: Exploiting the untapped potential of immunogenic modulation by radiation in combination with immunotherapy for the treatment of cancer,” *Frontiers in Oncology*, vol. 2, Sep. 2012, ISSN: 2234-943X. DOI: 10.3389/fonc.2012.00104.
- [42] J. A. Bonner, P. M. Harari, J. Giralt, N. Azarnia, D. M. Shin, R. B. Cohen, C. U. Jones, R. Sur, D. Raben, J. Jassem, R. Ove, M. S. Kies, J. Baselga, H. Youssoufian, N. Amellal, E. K. Rowinsky, and K. K. Ang, “Radiotherapy plus Cetuximab for Squamous-Cell Carcinoma of the Head and Neck,” *New England Journal of Medicine*, vol. 354, no. 6, pp. 567–578, Feb. 2006, eprint: <https://doi.org/10.1056/NEJMoa053422>, ISSN: 0028-4793. DOI: 10.1056/NEJMoa053422.
- [43] G. C. Barnett, C. M. L. West, A. M. Dunning, R. M. Elliott, C. E. Coles, P. D. P. Pharoah, and N. G. Burnet, “Normal tissue reactions to radiotherapy: Towards tailoring treatment dose by genotype,” en, *Nature Reviews Cancer*, vol. 9, no. 2, pp. 134–142, Feb. 2009, ISSN: 1474-1768. DOI: 10.1038/nrc2587.
- [44] C. M. West and G. C. Barnett, “Genetics and genomics of radiotherapy toxicity: Towards prediction,” en, *Genome Medicine*, vol. 3, no. 8, p. 52, 2011, ISSN: 1756-994X. DOI: 10.1186/gm268.
- [45] A. Bouchet, B. Lemasson, T. Christen, M. Potez, C. Rome, N. Coquery, C. Le Clec’h, A. Moisan, E. Bräuer-Krisch, G. Leduc, C. Rémy, J. A. Laissue, E. L. Barbier, E. Brun, and R. Serduc, “Synchrotron microbeam radiation therapy induces hypoxia in intracerebral gliosarcoma but not in the normal brain,” en,

Radiotherapy and Oncology, vol. 108, no. 1, pp. 143–148, Jul. 2013, ISSN: 01678140. DOI: 10.1016/j.radonc.2013.05.013.

- [46] B. Burnette and R. R. Weichselbaum, “Radiation as an Immune Modulator,” en, *Seminars in Radiation Oncology*, The Tumor as an Organ, vol. 23, no. 4, pp. 273–280, Oct. 2013, ISSN: 1053-4296. DOI: 10.1016/j.semradonc.2013.05.009.
- [47] S. J. Gandhi, A. J. Minn, R. H. Vonderheide, E. J. Wherry, S. M. Hahn, and A. Maity, “Awakening the immune system with radiation: Optimal dose and fractionation,” English (US), *Cancer Letters*, SI:Radiation and Immunity, vol. 368, no. 2, pp. 185–190, Nov. 2015, ISSN: 0304-3835. DOI: 10.1016/j.canlet.2015.03.024.
- [48] T. Kodaira, “SY17-4 - Radiation therapy with immune checkpoint inhibitor, future perspective,” en, *Annals of Oncology*, 2019 the Japanese Society of Medical Oncology Annual Meeting 18–20 July 2019, Kyoto, Japan, vol. 30, p. vi41, Oct. 2019, ISSN: 0923-7534. DOI: 10.1093/annonc/mdz347.
- [49] M. Mohiuddin, H. Park, S. Hallmeyer, and J. Richards, “High-Dose Radiation as a Dramatic, Immunological Primer in Locally Advanced Melanoma,” en, *Cureus*, Dec. 2015, ISSN: 2168-8184. DOI: 10.7759/cureus.417.
- [50] M. Brada and T. Bortfeld, “Proton Therapy: The Present and the Future,” English, *Seminars in Radiation Oncology*, vol. 23, no. 2, pp. 75–76, Apr. 2013, ISSN: 1053-4296, 1532-9461. DOI: 10.1016/j.semradonc.2012.11.001.
- [51] Y. Lievens, J. M. Borras, and C. Grau, “Cost calculation: A necessary step towards widespread adoption of advanced radiotherapy technology,” *Acta Oncologica*, vol. 54, no. 9, pp. 1275–1281, Oct. 2015, ISSN: 0284-186X. DOI: 10.3109/0284186X.2015.1066932.
- [52] J. L. Huhn, W. F. Regine, J. P. Valentino, A. S. Meigooni, M. Kudrimoti, and M. Mohiuddin, “Spatially fractionated GRID radiation treatment of advanced neck disease associated with head and neck cancer,” *Technology in cancer research & treatment*, vol. 5, no. 6, pp. 607–612, 2006.
- [53] N. Defourny, P. Dunscombe, L. Perrier, C. Grau, and Y. Lievens, “Cost evaluations of radiotherapy: What do we know? An ESTRO-HERO analysis,” en, *Radiotherapy and Oncology*, vol. 121, no. 3, pp. 468–474, Dec. 2016, ISSN: 0167-8140. DOI: 10.1016/j.radonc.2016.12.002.
- [54] J. Ferlay, I. Soerjomataram, R. Dikshit, S. Eser, C. Mathers, M. Rebelo, D. M. Parkin, D. Forman, and F. Bray, “Cancer incidence and mortality worldwide: Sources, methods and major patterns in GLOBOCAN 2012,” en, *International Journal of Cancer*, vol. 136, no. 5, E359–E386, 2015, eprint: <https://onlinelibrary.wiley.com/doi/pdf/10.1002/ijc.29210>, ISSN: 1097-0215. DOI: 10.1002/ijc.29210.

- [55] A. Poudel, S. Sinha, and A. Gajra, “Navigating the Challenges of Adjuvant Chemotherapy in Older Patients with Early-Stage Non-Small-Cell Lung Cancer,” English, *Drugs & Aging; Auckland*, vol. 33, no. 4, pp. 223–232, Apr. 2016, ISSN: 1170229X. DOI: <http://dx.doi.org.libproxy.lib.unc.edu/10.1007/s40266-016-0350-9>.
- [56] K. D. Miller, R. L. Siegel, C. C. Lin, A. B. Mariotto, J. L. Kramer, J. H. Rowland, K. D. Stein, R. Alteri, and A. Jemal, “Cancer treatment and survivorship statistics, 2016,” en, *CA: A Cancer Journal for Clinicians*, vol. 66, no. 4, pp. 271–289, Jul. 2016, ISSN: 1542-4863. DOI: 10.3322/caac.21349.
- [57] P. M. Medin and T. P. Boike, “Spinal Cord Tolerance in the Age of Spinal Radiosurgery: Lessons From Preclinical Studies,” *International Journal of Radiation Oncology*Biophysics*, vol. 79, no. 5, pp. 1302–1309, Apr. 2011, ISSN: 0360-3016. DOI: 10.1016/j.ijrobp.2010.10.052.
- [58] A. Ginot, J. Doyen, J. .-M. Hannoun-Lévi, and A. Courdi, “Dose de tolérance des tissus sains : La peau et les phanères,” *Cancer/Radiothérapie*, Dose de Tolérance à l’irradiation Des Tissus Sains, vol. 14, no. 4, pp. 379–385, Jul. 2010, ISSN: 1278-3218. DOI: 10.1016/j.canrad.2010.03.015.
- [59] A. R. Kirtane, S. M. Kalscheuer, and J. Panyam, “Exploiting nanotechnology to overcome tumor drug resistance: Challenges and opportunities,” *Advanced Drug Delivery Reviews*, Nanotechnology and Drug Resistance, vol. 65, no. 13, pp. 1731–1747, Nov. 2013, ISSN: 0169-409X. DOI: 10.1016/j.addr.2013.09.001.
- [60] G. Szakács, J. K. Paterson, J. A. Ludwig, C. Booth-Genthe, and M. M. Gottesman, “Targeting multidrug resistance in cancer,” English, *Nature Reviews. Drug Discovery; London*, vol. 5, no. 3, pp. 219–34, Mar. 2006, ISSN: 14741776. DOI: <http://dx.doi.org.libproxy.lib.unc.edu/10.1038/nrd1984>.
- [61] I. Skvortsova, P. Debbage, V. Kumar, and S. Skvortsov, “Radiation resistance: Cancer stem cells (CSCs) and their enigmatic pro-survival signaling,” *Seminars in Cancer Biology*, Complexity in Cancer Biology, vol. 35, no. Supplement C, pp. 39–44, Dec. 2015, ISSN: 1044-579X. DOI: 10.1016/j.semcancer.2015.09.009.
- [62] I. J. Fidler, “The Biology of Brain Metastasis: Challenges for Therapy,” en, *The Cancer Journal*, vol. 21, no. 4, pp. 284–293, 2015, ISSN: 1528-9117. DOI: 10.1097/PPO.0000000000000126.
- [63] R. L. Siegel, K. D. Miller, and A. Jemal, “Cancer statistics, 2020,” en, *CA: A Cancer Journal for Clinicians*, vol. 70, no. 1, pp. 7–30, 2020, eprint: <https://acsjournals.onlinelibrary.wiley.com/doi/pdf/10.3322/caac.21590>, ISSN: 1542-4863. DOI: 10.3322/caac.21590.

- [64] *2020Cancer Facts & Figures — American Cancer Society*, en, <https://www.cancer.org/research/cancer-facts-statistics/all-cancer-facts-figures/cancer-facts-figures-2020.html>.
- [65] C. N. Coleman and M. M. Ahmed, “Implementation of New Biology-Based Radiation Therapy Technology: When Is It Ready So “Perfect Makes Practice?”” en, *International Journal of Radiation Oncology*Biology*Physics*, vol. 105, no. 5, pp. 934–937, Dec. 2019, ISSN: 03603016. DOI: 10.1016/j.ijrobp.2019.08.013.
- [66] D. Rodin, D. Jaffray, R. Atun, F. M. Knaul, and M. Gospodarowicz, “The need to expand global access to radiotherapy,” *The Lancet Oncology*, vol. 15, no. 4, pp. 378–380, Apr. 2014, ISSN: 1470-2045. DOI: 10.1016/S1470-2045(14)70121-4.
- [67] R. Atun, D. A. Jaffray, M. B. Barton, F. Bray, M. Baumann, B. Vikram, T. P. Hanna, F. M. Knaul, Y. Lievens, T. Y. M. Lui, M. Milosevic, B. O’Sullivan, D. L. Rodin, E. Rosenblatt, J. V. Dyk, M. L. Yap, E. Zubizarreta, and M. Gospodarowicz, “Expanding global access to radiotherapy,” English, *The Lancet Oncology*, vol. 16, no. 10, pp. 1153–1186, Sep. 2015, ISSN: 1470-2045, 1474-5488. DOI: 10.1016/S1470-2045(15)00222-3.
- [68] M. Abdel-Wahab, E. Zubizarreta, A. Polo, and A. Meghzifene, “Improving Quality and Access to Radiation Therapy—An IAEA Perspective,” *Seminars in Radiation Oncology*, Global Health Disparities, vol. 27, no. 2, pp. 109–117, Apr. 2017, ISSN: 1053-4296. DOI: 10.1016/j.semradonc.2016.11.001.
- [69] W. Yan, M. K. Khan, X. Wu, C. B. Simone, J. Fan, E. Gressen, X. Zhang, C. L. Limoli, H. Bahig, S. Tubin, and W. F. Mourad, “Spatially fractionated radiation therapy: History, present and the future,” *Clinical and Translational Radiation Oncology*, vol. 20, pp. 30–38, Oct. 2019, ISSN: 2405-6308. DOI: 10.1016/j.ctro.2019.10.004.
- [70] E. Schültke, J. Balosso, T. Breslin, G. Cavaletti, V. Djonov, F. Esteve, M. Grotzer, G. Hildebrandt, A. Valdman, and J. Laissue, “Microbeam radiation therapy — grid therapy and beyond: A clinical perspective,” en, *The British Journal of Radiology*, vol. 90, no. 1078, p. 20170073, Oct. 2017, ISSN: 0007-1285, 1748-880X. DOI: 10.1259/bjr.20170073.
- [71] W. Yan and E. Gressen, “History: Evolution Of Spatially Fractionated Radiation Therapy,” en, p. 2,
- [72] M. Ghita, C. Fernandez-Palomo, H. Fukunaga, P. M. Fredericia, G. Schettino, E. Bräuer-Krisch, K. T. Butterworth, S. J. McMahon, and K. M. Prise, “Microbeam evolution: From single cell irradiation to pre-clinical studies,” en, *International Journal of Radiation Biology*, vol. 94, no. 8, pp. 708–718, Jul. 2018, ISSN: 0955-3002, 1362-3095. DOI: 10.1080/09553002.2018.1425807.

- [73] M. Mohiuddin, M. Fujita, W. F. Regine, A. S. Meigooni, G. S. Ibbott, and M. M. Ahmed, “High-Dose Spatially Fractionated Radiation GRID: A new paradigm in the management of advanced cancers,” English (US), *International Journal of Radiation Oncology* Biology* Physics*, vol. 45, no. 3, pp. 721–727, Apr. 1999.
- [74] J. E. Reiff, M. S. Huq, M. Mohiuddin, and N. Suntharalingam, “Dosimetric properties of megavoltage grid therapy,” *International Journal of Radiation Oncology* Biology* Physics*, vol. 33, no. 4, pp. 937–942, 1995.
- [75] A. S. Meigooni, K. Dou, N. J. Meigooni, M. Gnaster, S. Awan, S. Dini, and E. L. Johnson, “Dosimetric characteristics of a newly designed grid block for megavoltage photon radiation and its therapeutic advantage using a linear quadratic model: Dosimetric characteristics of a newly designed grid block,” en, *Medical Physics*, vol. 33, no. 9, pp. 3165–3173, Aug. 2006, eprint: <https://aapm.onlinelibrary.wiley.com/doi/pdf/10.1118/1.2241998>, ISSN: 2473-4209. DOI: 10.1118/1.2241998.
- [76] *DotDecimal.com*, <https://dotdecimal.com/>.
- [77] J. A. Laissue, H. Blattmann, and D. N. Slatkin, “Alban Köhler (1874-1947): Erfinder der Gittertherapie,” de, *Zeitschrift für Medizinische Physik*, vol. 22, no. 2, pp. 90–99, Jun. 2012, ISSN: 0939-3889. DOI: 10.1016/j.zemedi.2011.07.002.
- [78] E. Claridge Mackonis, N. Suchowerska, M. Zhang, M. Ebert, D. R. McKenzie, and M. Jackson, “Cellular response to modulated radiation fields,” en, *Physics in Medicine and Biology*, vol. 52, no. 18, pp. 5469–5482, Sep. 2007, ISSN: 0031-9155, 1361-6560. DOI: 10.1088/0031-9155/52/18/001.
- [79] S. J. McMahon, K. T. Butterworth, C. K. McGarry, C. Trainor, J. M. O’Sullivan, A. R. Hounsell, and K. M. Prise, “A Computational Model of Cellular Response to Modulated Radiation Fields,” en, *International Journal of Radiation Oncology*Biology*Physics*, vol. 84, no. 1, pp. 250–256, Sep. 2012, ISSN: 03603016. DOI: 10.1016/j.ijrobp.2011.10.058.
- [80] *Kohler: Zur röntgentiefentherapie mit massendosen - Google Scholar*, https://scholar.google.com/scholar_lookup?journal=Fortschr+Med&title=Zur+roentiefentherapie+mit+massendosen+MMW&author=H.+Kohler&volume=56&publication_year=1909&pages=2314-2316&.
- [81] H. Marks, “Clinical Experience with Irradiation Through a Grid,” *Radiology*, vol. 58, no. 3, pp. 338–342, Mar. 1952, ISSN: 0033-8419. DOI: 10.1148/58.3.338.
- [82] M. Mohiuddin, D. L. Curtis, W. T. Grizos, and L. Komarnicky, “Palliative treatment of advanced cancer using multiple nonconfluent pencil beam radiation: A pilot study,” en, *Cancer*, vol. 66, no. 1, pp. 114–118, Jul. 1990, ISSN: 1097-0142. DOI: 10.1002/1097-0142(19900701)66:1<114::AID-CNCR2820660121>3.0.CO;2-L.

- [83] G Mitev and N. Suntharalingham, “Semi-empirical calculation of dose distributions for high energy photon beam Grid therapy,” *Medical Physics*, vol. 13, 1986.
- [84] M. Mohiuddin, J. H. Stevens, J. E. Reiff, M. S. Huq, and N. Suntharalingam, “Spatially fractionated GRID radiation for palliative treatment of advanced cancer,” en, *Radiation Oncology Investigations*, vol. 4, no. 1, pp. 41–47, 1996, ISSN: 1520-6823. DOI: 10.1002/(SICI)1520-6823(1996)4:1<41::AID-ROI7>3.0.CO;2-M.
- [85] N. Somaiah, J. Warrington, H. Taylor, R. Ahmad, D. Tait, and J. Glees, “High Dose Spatially Fractionated Radiotherapy SFRT using a Megavoltage GRID in Advanced Lung Tumors: Preliminary Experience in UK,” English, *International Journal of Radiation Oncology • Biology • Physics*, vol. 72, no. 1, S490, Sep. 2008, ISSN: 0360-3016. DOI: 10.1016/j.ijrobp.2008.06.1439.
- [86] B. E. Amendola, N. C. Perez, X. Wu, J. M. Blanco Suarez, J. J. Lu, and M. Amendola, “Improved outcome of treating locally advanced lung cancer with the use of Lattice Radiotherapy (LRT): A case report,” en, *Clinical and Translational Radiation Oncology*, vol. 9, pp. 68–71, Feb. 2018, ISSN: 2405-6308. DOI: 10.1016/j.ctro.2018.01.003.
- [87] B. E. Amendola, N. C. Perez, X. Wu, M. A. Amendola, and I. Z. Qureshi, “Safety and Efficacy of Lattice Radiotherapy in Voluminous Non-small Cell Lung Cancer,” *Cureus*, vol. 11, no. 3, Mar. 2019, ISSN: 2168-8184. DOI: 10.7759/cureus.4263.
- [88] J. M. Blanco Suarez, B. E. Amendola, N. Perez, M. Amendola, and X. Wu, “The Use of Lattice Radiation Therapy (LRT) in the Treatment of Bulky Tumors: A Case Report of a Large Metastatic Mixed Mullerian Ovarian Tumor,” *Cureus*, vol. 7, no. 11, ISSN: 2168-8184. DOI: 10.7759/cureus.389.
- [89] A. Prasanna, M. M. Ahmed, M. Mohiuddin, and C. N. Coleman, “Exploiting sensitization windows of opportunity in hyper and hypo-fractionated radiation therapy,” *Journal of Thoracic Disease*, vol. 6, no. 4, pp. 287–302, Apr. 2014, ISSN: 2072-1439. DOI: 10.3978/j.issn.2072-1439.2014.01.14.
- [90] J. A. Peñagaricano, E. G. Moros, V. Ratanatharathorn, Y. Yan, and P. Corry, “Evaluation of Spatially Fractionated Radiotherapy GRID and Definitive Chemoradiotherapy With Curative Intent for Locally Advanced Squamous Cell Carcinoma of the Head and Neck: Initial Response Rates and Toxicity,” en, *International Journal of Radiation Oncology*Biology*Physics*, vol. 76, no. 5, pp. 1369–1375, Apr. 2010, ISSN: 03603016. DOI: 10.1016/j.ijrobp.2009.03.030.
- [91] J. Edwards, P. Shah, J. Huhn, W. St. Clair, W. Regine, M. Mohiuddin, and M. Kudrimoti, “Definitive GRID and Fractionated Radiation in Bulky Head and Neck Cancer Associated With Low Rates of Distant Metastasis,” en, *International Journal of Radiation Oncology*Biology*Physics*, vol. 93, no. 3, E334, Nov. 2015, ISSN: 03603016. DOI: 10.1016/j.ijrobp.2015.07.1399.

- [92] E. Alsahafi, K. Begg, I. Amelio, N. Raulf, P. Lucarelli, T. Sauter, and M. Tavassoli, "Clinical update on head and neck cancer: Molecular biology and ongoing challenges," en, *Cell Death & Disease*, vol. 10, no. 8, pp. 1–17, Jul. 2019, ISSN: 2041-4889. DOI: 10.1038/s41419-019-1769-9.
- [93] A. S. Grewal, J. Jones, and A. Lin, "Palliative Radiation Therapy for Head and Neck Cancers," en, *International Journal of Radiation Oncology*Biology*Physics*, vol. 105, no. 2, pp. 254–266, Oct. 2019, ISSN: 03603016. DOI: 10.1016/j.ijrobp.2019.05.024.
- [94] J.-C. M. Rwigema, D. E. Heron, R. L. Ferris, R. S. Andrade, M. K. Gibson, Y. Yang, C. Ozhasoglu, A. E. Argiris, J. R. Grandis, and S. A. Burton, "The Impact of Tumor Volume and Radiotherapy Dose on Outcome in Previously Irradiated Recurrent Squamous Cell Carcinoma of the Head and Neck Treated With Stereotactic Body Radiation Therapy," *American journal of clinical oncology*, vol. 34, no. 4, pp. 372–379, Aug. 2011, ISSN: 0277-3732. DOI: 10.1097/COC.0b013e3181e84dc0.
- [95] *Radiation Products Design - Radiation Products Design, Inc.*
<https://www.rpdinc.com/>.
- [96] J. K. Ha, G. Zhang, S. A. Naqvi, W. F. Regine, and C. X. Yu, "Feasibility of delivering grid therapy using a multileaf collimator: MLC grids," en, *Medical Physics*, vol. 33, no. 1, pp. 76–82, Dec. 2005, ISSN: 00942405. DOI: 10.1118/1.2140116.
- [97] G. Neuner, M. M. Mohiuddin, N. Vander Walde, O. Goloubeva, J. Ha, C. X. Yu, and W. F. Regine, "High-Dose Spatially Fractionated GRID Radiation Therapy SFGRT: A Comparison of Treatment Outcomes With Cerrobend vs. MLC SFGRT," en, *International Journal of Radiation Oncology*Biology*Physics*, vol. 82, no. 5, pp. 1642–1649, Apr. 2012, ISSN: 03603016. DOI: 10.1016/j.ijrobp.2011.01.065.
- [98] S. Gholami, H. A. Nedaie, F. Longo, M. R. Ay, S. Wright, and A. S. Meigooni, "Is grid therapy useful for all tumors and every grid block design?" *Journal of Applied Clinical Medical Physics*, vol. 17, no. 2, pp. 206–219, Mar. 2016, ISSN: 1526-9914. DOI: 10.1120/jacmp.v17i2.6015.
- [99] C. Buckey, S. Stathakis, K. Cashon, A. Gutierrez, C. Esquivel, C. Shi, and N. Papanikolaou, "Evaluation of a commercially-available block for spatially fractionated radiation therapy," *Journal of Applied Clinical Medical Physics*, vol. 11, no. 3, 2010.
- [100] X. Zhang, J. Penagaricano, Y. Yan, S. Sharma, R. J. Griffin, M. Hardee, E. Y. Han, and V. Ratanatharathom, "Application of Spatially Fractionated Radiation (GRID) to Helical Tomotherapy using a Novel TOMOGRID Template," eng, *Technology in Cancer Research & Treatment*, vol. 15, no. 1, pp. 91–100, Feb. 2016, ISSN: 1533-0346, 1533-0338. DOI: 10.7785/tcrtexpress.2013.600261.

- [101] M. Sammer, K. Teiluf, S. Girst, C. Greubel, J. Reindl, K. Ilicic, D. W. M. Walsh, M. Aichler, A. Walch, S. E. Combs, J. J. Wilkens, G. Dollinger, and T. E. Schmid, “Beam size limit for pencil minibeam radiotherapy determined from side effects in an in-vivo mouse ear model,” en, *PLOS ONE*, vol. 14, no. 9, e0221454, Sep. 2019, ISSN: 1932-6203. DOI: 10.1371/journal.pone.0221454.
- [102] W. X, A. M. M, W. J, G. S, and P. A, “On Modern Technical Approaches of Three-Dimensional High-Dose Lattice Radiotherapy (LRT),” *Cureus Journal of Medical Science*, vol. 2, no. 3, Mar. 2010. DOI: 10.7759/cureus.9.
- [103] *MATLAB - MathWorks*, en, <https://www.mathworks.com/products/matlab.html>.
- [104] E. Bräuer-Krisch, J.-F. Adam, E. Alagoz, S. Bartzsch, J. Crosbie, C. DeWagter, A. Dipuglia, M. Donzelli, S. Doran, P. Fournier, J. Kalef-Ezra, A. Kock, M. Lerch, C. McErlean, U. Oelfke, P. Olko, M. Petasecca, M. Povoli, A. Rosenfeld, E. A. Siegbahn, D. Sporea, and B. Stugu, “Medical physics aspects of the synchrotron radiation therapies: Microbeam radiation therapy (MRT) and synchrotron stereotactic radiotherapy (SSRT),” en, *Physica Medica, Radiation Therapy with Synchrotron Radiation: Achievements and Challenges*, vol. 31, no. 6, pp. 568–583, Sep. 2015, ISSN: 1120-1797. DOI: 10.1016/j.ejmp.2015.04.016.
- [105] *ESRF- Microbeam Radiation Therapy (MRT)*, en, <https://www.esrf.eu/home/UsersAndScience/Experiments/CBS/ID17/mrt-1.html>, Last Modified: Thu, 27 Sep 2018 14:39:31 GMT.
- [106] E. Bräuer-Krisch, H. Requardt, P. Régnard, S. Corde, E. Siegbahn, G. LeDuc, H. Blattmann, J. Laissue, and A. Bravin, “Exploiting geometrical irradiation possibilities in MRT application,” en, *Nuclear Instruments and Methods in Physics Research Section A: Accelerators, Spectrometers, Detectors and Associated Equipment*, vol. 548, no. 1-2, pp. 69–71, Aug. 2005, ISSN: 01689002. DOI: 10.1016/j.nima.2005.03.068.
- [107] E. Bräuer-Krisch, H. Requardt, T. Brochard, G. Berruyer, M. Renier, J. A. Laissue, and A. Bravin, “New technology enables high precision multislit collimators for microbeam radiation therapy,” en, *Review of Scientific Instruments*, vol. 80, no. 7, p. 074301, Jul. 2009, ISSN: 0034-6748, 1089-7623. DOI: 10.1063/1.3170035.
- [108] E. Siegbahn, E. Bräuer-Krisch, J. Stepanek, H. Blattmann, J. Laissue, and A. Bravin, “Dosimetric studies of microbeam radiation therapy (MRT) with Monte Carlo simulations,” en, *Nuclear Instruments and Methods in Physics Research Section A: Accelerators, Spectrometers, Detectors and Associated Equipment*, Proceedings of He 4th International Workshop on Medical Applications of Synchrotron Radiation, vol. 548, no. 1-2, pp. 54–58, Aug. 2005, ISSN: 0168-9002. DOI: 10.1016/j.nima.2005.03.065.

- [109] D. N. Slatkin, P. Spanne, F. A. Dilmanian, J. O. Gebbers, and J. A. Laissue, "Subacute neuropathological effects of microplanar beams of x-rays from a synchrotron wiggler," en, *Proceedings of the National Academy of Sciences*, vol. 92, no. 19, pp. 8783–8787, Sep. 1995, ISSN: 0027-8424, 1091-6490. DOI: 10.1073/pnas.92.19.8783.
- [110] C. P. Baker, H. J. Curtis, W. Zeman, and R. G. Woodley, "The Design and Calibration of a Deuteron Microbeam for Biological Studies," *Radiation Research*, vol. 15, no. 4, pp. 489–495, Oct. 1961, ISSN: 0033-7587. DOI: 10.2307/3571292.
- [111] W. Zeman, H. J. Curtis, and C. P. Baker, "Histopathologic Effect of High-Energy-Particle Microbeams on the Visual Cortex of the Mouse Brain," *Radiation Research*, vol. 15, no. 4, pp. 496–514, Oct. 1961, ISSN: 0033-7587. DOI: 10.2307/3571293.
- [112] J. A. Laissue, G. Geiser, P. O. Spanne, F. A. Dilmanian, J.-O. Gebbers, M. Geiser, X.-Y. Wu, M. S. Makar, P. L. Micca, M. M. Nawrocky, D. D. Joel, and D. N. Slatkin, "Neuropathology of ablation of rat gliosarcomas and contiguous brain tissues using a microplanar beam of synchrotron-wiggler-generated X rays," en, *International Journal of Cancer*, vol. 78, no. 5, pp. 654–660, Nov. 1998, ISSN: 1097-0215. DOI: 10.1002/(SICI)1097-0215(19981123)78:5<654::AID-IJC21>3.0.CO;2-L.
- [113] A. Dilmanian, G. Morris, G. Le Duc, X. Huang, B. Ren, T. Bacarian, J. Allen, J. KALEF-EZRa, I. Orion, E. Rosen, T. Sandhu, P. Sathé, X. Wu, Z. Zhong, and H. Shivaprasad, "Response of avian embryonic brain to spatially segmented X-ray microbeams," *Cellular and molecular biology (Noisy-le-Grand, France)*, vol. 47, pp. 485–93, Jun. 2001.
- [114] J. A. Laissue, H. Blattmann, H. P. Wagner, M. A. Grotzer, and D. N. Slatkin, "Prospects for microbeam radiation therapy of brain tumours in children to reduce neurological sequelae," eng, *Developmental Medicine & Child Neurology*, vol. 49, no. 8, pp. 577–581, Aug. 2007, ISSN: 0012-1622. DOI: 10.1111/j.1469-8749.2007.00577.x.
- [115] J. A. Laissue, H. Blattmann, M. D. Michiel, D. N. S. M.d, N. Lyubimova, R. Guzman, W. Zimmermann, S. Birrer, T. Bley, P. Kircher, R. Stettler, R. Fatzer, A. Jaggy, H. Smilowitz, E. Brauer, A. Bravin, G. L. Duc, C. Nemoz, M. Renier, W. C. Thomlinson, J. Stepanek, and H.-P. Wagner, "Weanling piglet cerebellum: A surrogate for tolerance to MRT (microbeam radiation therapy) in pediatric neuro-oncology," in *Penetrating Radiation Systems and Applications III*, vol. 4508, International Society for Optics and Photonics, Dec. 2001, pp. 65–73. DOI: 10.1117/12.450774.
- [116] J. A. Laissue, S. Bartzsch, H. Blattmann, E. Bräuer-Krisch, A. Bravin, D. Dalléry, V. Djonov, A. L. Hanson, J. W. Hopewell, B. Kaser-Hotz, J. Keyriläinen, P. P. Laissue, M. Miura, R. Serduc, A. E. Siegbahn, and D. N. Slatkin, "Response of

- the rat spinal cord to X-ray microbeams,” English, *Radiotherapy and Oncology: Journal of the European Society for Therapeutic Radiology and Oncology*, vol. 106, no. 1, pp. 106–111, Jan. 2013, ISSN: 0167-8140, 1879-0887. DOI: 10.1016/j.radonc.2012.12.007.
- [117] H. Fukunaga, K. Kaminaga, T. Sato, K. T. Butterworth, R. Watanabe, N. Usami, T. Ogawa, A. Yokoya, and K. M. Prise, “High-precision microbeam radiotherapy reveals testicular tissue-sparing effects for male fertility preservation,” en, *Scientific Reports*, vol. 9, no. 1, pp. 1–10, Oct. 2019, ISSN: 2045-2322. DOI: 10.1038/s41598-019-48772-3.
 - [118] A. Yokoya and N. Usami, “Targeting Specific Sites in Biological Systems with Synchrotron X-Ray Microbeams for Radiobiological Studies at the Photon Factory,” en, *Quantum Beam Science*, vol. 4, no. 1, p. 2, Jan. 2020, ISSN: 2412-382X. DOI: 10.3390/qubs4010002.
 - [119] C. Fernandez-Palomo, J. Fazzari, V. Trappetti, L. Smyth, H. Janka, J. Laissue, and V. Djonov, “Animal Models in Microbeam Radiation Therapy: A Scoping Review,” en, *Cancers*, vol. 12, no. 3, p. 527, Feb. 2020, ISSN: 2072-6694. DOI: 10.3390/cancers12030527.
 - [120] F. A. Dilmanian, T. M. Button, G. Le Duc, N. Zhong, L. A. Peña, J. A. L. Smith, S. R. Martinez, T. Bacarian, J. Tammam, B. Ren, P. M. Farmer, J. Kalef-Ezra, P. L. Micca, M. M. Nawrocky, J. A. Niederer, F. P. Recksiek, A. Fuchs, and E. M. Rosen, “Response of rat intracranial 9L gliosarcoma to microbeam radiation therapy,” *Neuro-Oncology*, vol. 4, no. 1, pp. 26–38, Jan. 2002, ISSN: 1522-8517.
 - [121] P. Régnard, E. Bräuer-Krisch, I. Troprès, J. Keyriläinen, A. Bravin, and G. Le Duc, “Enhancement of survival of 9L gliosarcoma bearing rats following intracerebral delivery of drugs in combination with microbeam radiation therapy,” en, *European Journal of Radiology*, Proceedings of the 5th Medical Application of Synchrotron Radiation 2007, vol. 68, no. 3, Supplement, S151–S155, Dec. 2008, ISSN: 0720-048X. DOI: 10.1016/j.ejrad.2008.04.049.
 - [122] P. Regnard, G. L. Duc, E. Bräuer-Krisch, I. Troprès, E. A. Siegbahn, A. Kusak, C. Clair, H. Bernard, D. Dallery, J. A. Laissue, and A. Bravin, “Irradiation of intracerebral 9L gliosarcoma by a single array of microplanar x-ray beams from a synchrotron: Balance between curing and sparing,” en, *Physics in Medicine and Biology*, vol. 53, no. 4, pp. 861–878, Feb. 2008, ISSN: 0031-9155, 1361-6560. DOI: 10.1088/0031-9155/53/4/003.
 - [123] H. M. Smilowitz, H. Blattmann, E. Bräuer-Krisch, A. Bravin, M. D. Michiel, J.-O. Gebbers, A. L. Hanson, N. Lyubimova, D. N. Slatkin, J. Stepanek, and J. A. Laissue, “Synergy of gene-mediated immunoprophylaxis and microbeam radiation therapy for advanced intracerebral rat 9L gliosarcomas,” en, *Journal of Neuro-Oncology*, vol. 78, no. 2, pp. 135–143, Jun. 2006, ISSN: 0167-594X, 1573-7373. DOI: 10.1007/s11060-005-9094-9.

- [124] A. Bouchet, M. Bidart, I. Miladi, C. Le Clec'h, R. Serduc, C. Coutton, P. Regnard, E. Khalil, S. Dufort, B. Lemasson, J. Laissue, L. Pelletier, and G. Le Duc, "Characterization of the 9L gliosarcoma implanted in the Fischer rat: An orthotopic model for a grade IV brain tumor," en, *Tumor Biology*, vol. 35, no. 7, pp. 6221–6233, Jul. 2014, ISSN: 1423-0380. DOI: 10.1007/s13277-014-1783-6.
- [125] A. Bouchet, E. Bräuer-Krisch, Y. Prezado, M. El Atifi, L. Rogalev, C. Le Clec'h, J. A. Laissue, L. Pelletier, and G. Le Duc, "Better Efficacy of Synchrotron Spatially Microfractionated Radiation Therapy Than Uniform Radiation Therapy on Glioma," en, *International Journal of Radiation Oncology*Biology*Physics*, vol. 95, no. 5, pp. 1485–1494, Aug. 2016, ISSN: 0360-3016. DOI: 10.1016/j.ijrobp.2016.03.040.
- [126] F. A. Dilmanian, G. M. Morris, N. Zhong, T. Bacarian, J. F. Hainfeld, J. Kalef-Ezra, L. J. Brewington, J. Tammam, and E. M. Rosen, "Murine EMT-6 Carcinoma: High Therapeutic Efficacy of Microbeam Radiation Therapy," en, *Radiation Research*, vol. 159, no. 5, pp. 632–641, May 2003, ISSN: 0033-7587, 1938-5404. DOI: 10.1667/0033-7587(2003)159[0632:MECHTE]2.0.CO;2.
- [127] A. Uyama, T. Kondoh, N. Nariyama, K. Umetani, M. Fukumoto, K. Shinohara, and E. Kohmura, "A narrow microbeam is more effective for tumor growth suppression than a wide microbeam: An in vivo study using implanted human glioma cells," en, *Journal of Synchrotron Radiation*, vol. 18, no. 4, pp. 671–678, Jul. 2011, ISSN: 0909-0495. DOI: 10.1107/S090904951101185X.
- [128] R. J. Griffin, N. A. Koonce, R. P. M. Dings, E. Siegel, E. G. Moros, E. Bräuer-Krisch, and P. M. Corry, "Microbeam Radiation Therapy Alters Vascular Architecture and Tumor Oxygenation and is Enhanced by a Galectin-1 Targeted Anti-Angiogenic Peptide," eng, *Radiation Research*, vol. 177, no. 6, pp. 804–812, May 2012, ISSN: 0033-7587. DOI: 10.1667/RR2784.1.
- [129] R. Serduc, A. Bouchet, E. Bräuer-Krisch, J. A. Laissue, J. Spiga, S. Sarun, A. Bravin, C. Fonta, L. Renaud, J. Boutonnat, E. A. Siegbahn, F. Estève, and G. Le Duc, "Synchrotron microbeam radiation therapy for rat brain tumor palliation—influence of the microbeam width at constant valley dose," *Physics in Medicine and Biology*, vol. 54, no. 21, pp. 6711–6724, Nov. 2009, ISSN: 0031-9155, 1361-6560. DOI: 10.1088/0031-9155/54/21/017.
- [130] M. Potez, C. Fernandez-Palomo, A. Bouchet, V. Trappetti, M. Donzelli, M. Krisch, J. Laissue, V. Volarevic, and V. Djonov, "Synchrotron Microbeam Radiation Therapy as a New Approach for the Treatment of Radioresistant Melanoma: Potential Underlying Mechanisms," en, *International Journal of Radiation Oncology*Biology*Physics*, vol. 105, no. 5, pp. 1126–1136, Dec. 2019, ISSN: 0360-3016. DOI: 10.1016/j.ijrobp.2019.08.027.
- [131] S. Girst, C. Marx, E. Bräuer-Krisch, A. Bravin, S. Bartzsch, U. Oelfke, C. Greubel, J. Reindl, C. Siebenwirth, O. Zlobinskaya, G. Multhoff, G. Dollinger, T. E. Schmid,

- and J. J. Wilkens, “Improved normal tissue protection by proton and X-ray microchannels compared to homogeneous field irradiation,” en, *Physica Medica, Radiation Therapy with Synchrotron Radiation: Achievements and Challenges*, vol. 31, no. 6, pp. 615–620, Sep. 2015, ISSN: 1120-1797. DOI: 10.1016/j.ejmp.2015.04.004.
- [132] E. Schültke, B. H. Juurlink, K. Ataelmannan, J. Laissue, H. Blattmann, E. Bräuer-Krisch, A. Bravin, J. Minczewska, J. Crosbie, H. Taherian, E. Frangou, T. Wysokinsky, L. D. Chapman, R. Griebel, and D. Fourney, “Memory and survival after microbeam radiation therapy,” en, *European Journal of Radiology*, Proceedings of the 5th Medical Application of Synchrotron Radiation 2007, vol. 68, no. 3, Supplement, S142–S146, Dec. 2008, ISSN: 0720-048X. DOI: 10.1016/j.ejrad.2008.04.051.
- [133] R. Serduc, E. Bräuer-Krisch, E. A. Siegbahn, A. Bouchet, B. Pouyatos, R. Carron, N. Pannetier, L. Renaud, G. Berruyer, C. Nemoz, T. Brochard, C. Rémy, E. L. Barbier, A. Bravin, G. Le Duc, A. Depaulis, F. Estève, and J. A. Laissue, “High-Precision Radiosurgical Dose Delivery by Interlaced Microbeam Arrays of High-Flux Low-Energy Synchrotron X-Rays,” en, *PLoS ONE*, vol. 5, no. 2, M. Lesniak, Ed., e9028, Feb. 2010, ISSN: 1932-6203. DOI: 10.1371/journal.pone.0009028.
- [134] P. Romanelli, E. Fardone, G. Battaglia, E. Bräuer-Krisch, Y. Prezado, H. Requardt, G. L. Duc, C. Nemoz, D. J. Anschel, J. Spiga, and A. Bravin, “Synchrotron-Generated Microbeam Sensorimotor Cortex Transections Induce Seizure Control without Disruption of Neurological Functions,” *PLOS ONE*, vol. 8, no. 1, e53549, Jan. 2013, ISSN: 1932-6203. DOI: 10.1371/journal.pone.0053549.
- [135] F. Studer, R. Serduc, B. Pouyatos, T. Chabrol, E. Bräuer-Krisch, M. Donzelli, C. Nemoz, J. A. Laissue, F. Estève, and A. Depaulis, “Synchrotron X-ray microbeams: A promising tool for drug-resistant epilepsy treatment,” en, *Physica Medica, Radiation Therapy with Synchrotron Radiation: Achievements and Challenges*, vol. 31, no. 6, pp. 607–614, Sep. 2015, ISSN: 1120-1797. DOI: 10.1016/j.ejmp.2015.04.005.
- [136] S. Tubin, H. H. Popper, and L. Brcic, “Novel stereotactic body radiation therapy (SBRT)-based partial tumor irradiation targeting hypoxic segment of bulky tumors (SBRT-PATHY): Improvement of the radiotherapy outcome by exploiting the bystander and abscopal effects,” *Radiation Oncology*, vol. 14, no. 1, p. 21, Jan. 2019, ISSN: 1748-717X. DOI: 10.1186/s13014-019-1227-y.
- [137] C. Fernandez-Palomo, E. Schültke, R. Smith, E. Bräuer-Krisch, J. Laissue, C. Schroll, J. Fazzari, C. Seymour, and C. Mothersill, “Bystander effects in tumor-free and tumor-bearing rat brains following irradiation by synchrotron X-rays,” *International*

Journal of Radiation Biology, vol. 89, no. 6, pp. 445–453, Jun. 2013, ISSN: 0955-3002. DOI: 10.3109/09553002.2013.766770.

- [138] C. Fernandez-Palomo, E. Schültke, E. Bräuer-Krisch, J. A. Laissue, H. Blattmann, C. Seymour, and C. Mothersill, “Investigation of Abscopal and Bystander Effects in Immunocompromised Mice After Exposure to Pencilbeam and Microbeam Synchrotron Radiation,” eng, *Health Physics*, vol. 111, no. 2, pp. 149–159, Aug. 2016, ISSN: 1538-5159. DOI: 10.1097/HP.0000000000000525.
- [139] R. S. Asur, S. Sharma, C.-W. Chang, J. Penagaricano, I. M. Kommuru, E. G. Moros, P. M. Corry, and R. J. Griffin, “Spatially fractionated radiation induces cytotoxicity and changes in gene expression in bystander and radiation adjacent murine carcinoma cells,” *Radiation research*, vol. 177, no. 6, pp. 751–765, 2012.
- [140] R. Asur, K. T. Butterworth, J. A. Penagaricano, K. M. Prise, and R. J. Griffin, “High dose bystander effects in spatially fractionated radiation therapy,” en, *Cancer Letters*, vol. 356, no. 1, pp. 52–57, Jan. 2015, ISSN: 03043835. DOI: 10.1016/j.canlet.2013.10.032.
- [141] H. Yuan, M. W. Gaber, K. Boyd, C. M. Wilson, M. F. Kiani, and T. E. Merchant, “Effects of fractionated radiation on the brain vasculature in a murine model: Blood–brain barrier permeability, astrocyte proliferation, and ultrastructural changes,” en, *International Journal of Radiation Oncology*Biophysics*, vol. 66, no. 3, pp. 860–866, Nov. 2006, ISSN: 03603016. DOI: 10.1016/j.ijrobp.2006.06.043.
- [142] R. Serduc, T. Christen, J. Laissue, R. Farion, A. Bouchet, B. van der Sanden, C. Segebarth, E. Bräuer-Krisch, G. Le Duc, A. Bravin, C. Rémy, and E. L. Barbier, “Brain tumor vessel response to synchrotron microbeam radiation therapy: A short-term *in vivo* study,” *Physics in Medicine and Biology*, vol. 53, no. 13, pp. 3609–3622, Jul. 2008, ISSN: 0031-9155, 1361-6560. DOI: 10.1088/0031-9155/53/13/015.
- [143] A. Bouchet, R. Serduc, J. A. Laissue, and V. Djonov, “Effects of microbeam radiation therapy on normal and tumoral blood vessels,” en, *Physica medica: PM: an international journal devoted to the applications of physics to medicine and biology: official journal of the Italian Association of Biomedical Physics (AIFB)*, Radiation Therapy with Synchrotron Radiation: Achievements and Challenges, vol. 31, no. 6, pp. 634–641, Sep. 2015, ISSN: 1120-1797. DOI: 10.1016/j.ejmp.2015.04.014.
- [144] M. M. Shareef, N. Cui, R. Burikhanov, S. Gupta, S. Satishkumar, S. Shajahan, M. Mohiuddin, V. M. Rangnekar, and M. M. Ahmed, “Role of Tumor Necrosis Factor-alpha and TRAIL in High-Dose Radiation-Induced Bystander Signaling in Lung Adenocarcinoma,” en, *Cancer Research*, vol. 67, no. 24, pp. 11 811–11 820, Dec. 2007, ISSN: 0008-5472, 1538-7445. DOI: 10.1158/0008-5472.CAN-07-0722.

- [145] S. Sathishkumar, S. Dey, A. S. Meigooni, W. F. Regine, M. Kudrimoti, M. M. Ahmed, and M. Mohiuddin, "The impact of TNF-alpha induction on therapeutic efficacy following high dose spatially fractionated GRID radiation," *Technology in cancer research & treatment*, vol. 1, no. 2, pp. 141–147, 2002.
- [146] S. Sathishkumar, B. Boyanovski, A. Karakashian, K. A. Rozenova, N. V. Giltaiy, M. Kudrimoti, M. Mohiuddin, M. M. Ahmed, and M. Nikolova-Karakashian, "Elevated sphingomyelinase activity and ceramide concentration in serum of patients undergoing high dose spatially fractionated radiation treatment: Implications for endothelial apoptosis," *Cancer biology & therapy*, vol. 4, no. 9, pp. 979–986, 2005.
- [147] N. Dubois, E. Rio, N. Ripoche, V. Ferchaud-Roucher, M.-H. Gaugler, L. Champion, M. Krempf, C. Carrie, M. Mahé, X. Mirabel, and F. Paris, "Plasma ceramide, a real-time predictive marker of pulmonary and hepatic metastases response to stereotactic body radiation therapy combined with irinotecan," en, *Radiotherapy and Oncology*, vol. 119, no. 2, pp. 229–235, May 2016, ISSN: 0167-8140. DOI: 10.1016/j.radonc.2016.03.014.
- [148] S. Tubin, M. Valeriani, G. Salerno, S. Bracci, A. Stoppacciaro, P. Cardelli, M. F. Osti, V. D. Sanctis, G. Minniti, and R. M. Enrici, "Manipulation of radiation-induced bystander effect in prostate adenocarcinoma by dose and tumor differentiation grade: In vitro study," *International Journal of Radiation Biology*, vol. 91, no. 2, pp. 166–171, Feb. 2015, eprint: <https://doi.org/10.3109/09553002.2015.959667>, ISSN: 0955-3002. DOI: 10.3109/09553002.2015.959667.
- [149] S. Tubin, M. M. Ahmed, and S. Gupta, "Radiation and hypoxia-induced non-targeted effects in normoxic and hypoxic conditions in human lung cancer cells," eng, *International Journal of Radiation Biology*, vol. 94, no. 3, pp. 199–211, Mar. 2018, ISSN: 1362-3095. DOI: 10.1080/09553002.2018.1422085.
- [150] A. N. Fontanella, M.-K. Boss, M. Hadsell, J. Zhang, T. Schroeder, K. G. Berman, M. W. Dewhirst, S. Chang, and G. M. Palmer, "Effects of High-Dose Microbeam Irradiation on Tumor Microvascular Function and Angiogenesis," en, *Radiation Research*, vol. 183, no. 2, pp. 147–158, Feb. 2015, ISSN: 0033-7587, 1938-5404. DOI: 10.1667/RR13712.1.
- [151] S. Sabatasso, J. A. Laissue, R. Hlushchuk, W. Graber, A. Bravin, E. Bräuer-Krisch, S. Corde, H. Blattmann, G. Gruber, and V. Djonov, "Microbeam Radiation-Induced Tissue Damage Depends on the Stage of Vascular Maturation," en, *International Journal of Radiation Oncology*Biology*Physics*, vol. 80, no. 5, pp. 1522–1532, Aug. 2011, ISSN: 03603016. DOI: 10.1016/j.ijrobp.2011.03.018.
- [152] M. Garcia-Barros, "Tumor Response to Radiotherapy Regulated by Endothelial Cell Apoptosis," *Science*, vol. 300, no. 5622, pp. 1155–1159, May 2003, ISSN: 00368075, 10959203. DOI: 10.1126/science.1082504.

- [153] G. L. Semenza, “Targeting HIF-1 for cancer therapy,” en, *Nature Reviews Cancer*, vol. 3, no. 10, pp. 721–732, Dec. 2003, ISSN: 1474-1768. DOI: 10.1038/nrc1187.
- [154] D. H. Gorski, M. A. Beckett, N. T. Jaskowiak, D. P. Calvin, H. J. Mauceri, R. M. Salloum, S. Seetharam, A. Koons, D. M. Hari, D. W. Kufe, and R. R. Weichselbaum, “Blockade of the Vascular Endothelial Growth Factor Stress Response Increases the Antitumor Effects of Ionizing Radiation,” en, *Cancer Research*, vol. 59, no. 14, pp. 3374–3378, Jul. 1999, ISSN: 0008-5472, 1538-7445.
- [155] A. M. Duffy, D. J. Bouchier-Hayes, and J. H. Harmey, *Vascular Endothelial Growth Factor (VEGF) and Its Role in Non-Endothelial Cells: Autocrine Signalling by VEGF*, en. Landes Bioscience, 2013.
- [156] B. J. Moeller and M. W. Dewhirst, “Raising the Bar: How HIF-1 Helps Determine Tumor Radiosensitivity,” *Cell Cycle*, vol. 3, no. 9, pp. 1105–1108, Sep. 2004, eprint: <https://doi.org/10.4161/cc.3.9.1099>, ISSN: 1538-4101. DOI: 10.4161/cc.3.9.1099.
- [157] L. S. Ziemer, C. J. Koch, A. Maity, D. P. Magarelli, A. M. Horan, and S. M. Evans, “Hypoxia and VEGF mRNA Expression in Human Tumors,” en, *Neoplasia*, vol. 3, no. 6, pp. 500–508, Jan. 2001, ISSN: 1476-5586. DOI: 10.1038/sj.neo.7900195.
- [158] J.-W. Lee, S.-H. Bae, J.-W. Jeong, S.-H. Kim, and K.-W. Kim, “Hypoxia-inducible factor (HIF-1)alpha: Its protein stability and biological functions,” eng, *Experimental & Molecular Medicine*, vol. 36, no. 1, pp. 1–12, Feb. 2004, ISSN: 1226-3613. DOI: 10.1038/emm.2004.1.
- [159] I. S. Moreira, P. A. Fernandes, and M. J. Ramos, “Vascular endothelial growth factor (VEGF) inhibition—a critical review,” eng, *Anti-Cancer Agents in Medicinal Chemistry*, vol. 7, no. 2, pp. 223–245, Mar. 2007, ISSN: 1871-5206. DOI: 10.2174/187152007780058687.
- [160] A. Bouchet, B. Lemasson, G. Le Duc, C. Maisin, E. Bräuer-Krisch, E. A. Siegbahn, L. Renaud, E. Khalil, C. Rémy, C. Poillot, A. Bravin, J. A. Laissue, E. L. Barbier, and R. Serduc, “Preferential Effect of Synchrotron Microbeam Radiation Therapy on Intracerebral 9L Gliosarcoma Vascular Networks,” en, *International Journal of Radiation Oncology*Biology*Physics*, vol. 78, no. 5, pp. 1503–1512, Dec. 2010, ISSN: 03603016. DOI: 10.1016/j.ijrobp.2010.06.021.
- [161] C. Boudou, M.-C. Biston, S. Corde, J.-F. Adam, A. Joubert, A.-M. Charvet, C. Nemoz, C. Ferrero, F. Estève, and H. Elleaume, “Dosimetry for synchrotron stereotactic radiotherapy: Fricke gel and Monte Carlo calculations,” en, *Nuclear Instruments and Methods in Physics Research Section A: Accelerators, Spectrometers, Detectors and Associated Equipment*, vol. 548, no. 1-2, pp. 65–68, Aug. 2005, ISSN: 01689002. DOI: 10.1016/j.nima.2005.03.067.

- [162] P. Deman, M. Vautrin, V. Stupar, E. L. Barbier, H. Elleaume, F. Esteve, and J. F. Adam, "Monochromatic minibeam radiotherapy: Theoretical and experimental dosimetry for preclinical treatment plans," *Physics in Medicine and Biology*, vol. 56, no. 14, pp. 4465–4480, Jul. 2011, ISSN: 0031-9155, 1361-6560. DOI: 10.1088/0031-9155/56/14/015.
- [163] M. Ghasemi, M. Shamsaei, M. Ghannadi, and G. Raisali, "Dosimetric studies of micropencil X-ray beam interacting with labelled tissues by Au and Gd agents using Geant4," en, *Radiation Protection Dosimetry*, vol. 133, no. 2, pp. 97–104, Feb. 2009, ISSN: 0144-8420, 1742-3406. DOI: 10.1093/rpd/ncp017.
- [164] M. Ptaszekiewicz, E. Braurer-Kirsch, M. Klosowski, L. Czopyk, and P. Olko, "TLD dosimetry for microbeam radiation therapy at the European Synchrotron Radiation Facility," en, *Radiation Measurements*, vol. 43, no. 2-6, pp. 990–993, Feb. 2008, ISSN: 13504487. DOI: 10.1016/j.radmeas.2007.12.050.
- [165] D. A. Bradley, R. P. Hugtenburg, A. Nisbet, A. T. Abdul Rahman, F. Issa, N. Mohd Noor, and A. Alalawi, "Review of doped silica glass optical fibre: Their TL properties and potential applications in radiation therapy dosimetry," en, *Applied Radiation and Isotopes*, XII International Symposium on Solid State Dosimetry, vol. 71, pp. 2–11, Dec. 2012, ISSN: 0969-8043. DOI: 10.1016/j.apradiso.2012.02.001.
- [166] E. Bräuer-Krisch, A. Bravin, M. Lerch, A. Rosenfeld, J. Stepanek, M. D. Michiel, and J. A. Laissue, "MOSFET dosimetry for microbeam radiation therapy at the European Synchrotron Radiation Facility," en, *Medical Physics*, vol. 30, no. 4, pp. 583–589, 2003, eprint: <https://aapm.onlinelibrary.wiley.com/doi/pdf/10.1118/1.1562169>, ISSN: 2473-4209. DOI: 10.1118/1.1562169.
- [167] J. Crosbie, "Synchrotron microbeam radiation therapy," eng, Thesis, Monash University. Faculty of Science. School of Physics, 2008.
- [168] S. Bartzsch, J. Lott, K. Welsch, E. Bräuer-Krisch, and U. Oelfke, "Micrometer-resolved film dosimetry using a microscope in microbeam radiation therapy," en, *Medical Physics*, vol. 42, no. 7, pp. 4069–4079, Jul. 2015, ISSN: 2473-4209. DOI: 10.1118/1.4922001.
- [169] G. Le Duc, I. Miladi, C. Alric, P. Mowat, E. Bräuer-Krisch, A. Bouchet, E. Khalil, C. Billotey, M. Janier, F. Lux, T. Epicier, P. Perriat, S. Roux, and O. Tillement, "Toward an Image-Guided Microbeam Radiation Therapy Using Gadolinium-Based Nanoparticles," *ACS Nano*, vol. 5, no. 12, pp. 9566–9574, Dec. 2011, ISSN: 1936-0851. DOI: 10.1021/nn202797h.
- [170] S. J. Doran, T. Brochard, J. Adamovics, N. Krstajic, and E. Bräuer-Krisch, "An investigation of the potential of optical computed tomography for imaging of synchrotron-generated x-rays at high spatial resolution," en, *Physics in Medicine*

- and Biology*, vol. 55, no. 5, pp. 1531–1547, Feb. 2010, ISSN: 0031-9155. DOI: 10.1088/0031-9155/55/5/018.
- [171] C. M. McErlean, E. Bräuer-Krisch, J. Adamovics, and S. J. Doran, “Assessment of optical CT as a future QA tool for synchrotron x-ray microbeam therapy,” en, *Physics in Medicine and Biology*, vol. 61, no. 1, pp. 320–337, Dec. 2015, ISSN: 0031-9155. DOI: 10.1088/0031-9155/61/1/320.
 - [172] C. Fernandez-Palomo, C. Mothersill, E. Bräuer-Krisch, J. Laissue, C. Seymour, and E. Schültke, “GH2AX as a Marker for Dose Deposition in the Brain of Wistar Rats after Synchrotron Microbeam Radiation,” *PLoS ONE*, vol. 10, no. 3, Mar. 2015, ISSN: 1932-6203. DOI: 10.1371/journal.pone.0119924.
 - [173] S. Kanagavelu, S. Gupta, X. Wu, S. Philip, M. M. Wattenberg, J. W. Hodge, M. D. Couto, K. D. Chung, and M. M. Ahmed, “In Vivo Effects of Lattice Radiation Therapy on Local and Distant Lung Cancer: Potential Role of Immunomodulation,” *Radiation Research*, vol. 182, no. 2, pp. 149–162, Jul. 2014, ISSN: 0033-7587. DOI: 10.1667/RR3819.1.
 - [174] S. Bartzsch, S. Corde, J. C. Crosbie, L. Day, M. Donzelli, M. Krisch, M. Lerch, P. Pellicoli, L. M. L. Smyth, and M. Tehei, “Technical advances in x-ray microbeam radiation therapy,” en, *Physics in Medicine & Biology*, vol. 65, no. 2, 02TR01, Jan. 2020, ISSN: 1361-6560. DOI: 10.1088/1361-6560/ab5507.
 - [175] V. Raj, “Role of synchrotron radiation in cancer: A review on techniques and applications,” English, *Journal of Analytical & Pharmaceutical Research*, vol. Volume 7, no. Issue 2, Apr. 2018, ISSN: 2473-0831. DOI: 10.15406/japlr.2018.07.00221.
 - [176] L. Zhang, H. Yuan, C. Inscoe, P. Chtcheprov, M. Hadsell, Y. Lee, J. Lu, S. Chang, and O. Zhou, “Nanotube x-ray for cancer therapy: A compact microbeam radiation therapy system for brain tumor treatment,” en, *Expert Review of Anticancer Therapy*, vol. 14, no. 12, pp. 1411–1418, Dec. 2014, ISSN: 1473-7140, 1744-8328. DOI: 10.1586/14737140.2014.978293.
 - [177] H. Blattmann, J.-O. Gebbers, E. Bräuer-Krisch, A. Bravin, G. Le Duc, W. Burkard, M. Di Michiel, V. Djonov, D. Slatkin, J. Stepanek, and J. Laissue, “Applications of synchrotron X-rays to radiotherapy,” en, *Nuclear Instruments and Methods in Physics Research Section A: Accelerators, Spectrometers, Detectors and Associated Equipment*, vol. 548, no. 1-2, pp. 17–22, Aug. 2005, ISSN: 01689002. DOI: 10.1016/j.nima.2005.03.060.
 - [178] H. Schmied, “The European synchrotron radiation story - phase ii,” en, *Synchrotron Radiation News*, vol. 3, no. 6, pp. 22–26, Nov. 1990, ISSN: 0894-0886, 1931-7344. DOI: 10.1080/08940889008602591.

- [179] M. Hadsell, J. Zhang, P. Laganis, F. Sprenger, J. Shan, L. Zhang, L. Burk, H. Yuan, S. Chang, J. Lu, and O. Zhou, "A first generation compact microbeam radiation therapy system based on carbon nanotube X-ray technology," *Applied Physics Letters*, vol. 103, no. 18, p. 183 505, Oct. 2013, ISSN: 0003-6951. DOI: 10.1063/1.4826587.
- [180] S. Bazyar, Y. Lee, O. Zhou, C. R. Inscoe, and E. Timothy O'Brien, "Minibeam radiotherapy with small animal irradiators; in-vitro and in-vivo feasibility studies," *Physics in Medicine and Biology*, Oct. 2017. DOI: 10.1088/1361-6560/aa926b.
- [181] S. Bartzsch, C. Cummings, S. Eismann, and U. Oelfke, "A preclinical microbeam facility with a conventional x-ray tube," eng, *Medical Physics*, vol. 43, no. 12, pp. 6301–6308, Dec. 2016, ISSN: 2473-4209. DOI: 10.1118/1.4966032.
- [182] P. Chtcheprov, L. Burk, H. Yuan, C. Inscoe, R. Ger, M. Hadsell, J. Lu, L. Zhang, S. Chang, and O. Zhou, "Physiologically gated microbeam radiation using a field emission x-ray source array," *Medical physics*, vol. 41, no. 8, p. 081 705, 2014.
- [183] L. Zhang, H. Yuan, L. M. Burk, C. R. Inscoe, M. J. Hadsell, P. Chtcheprov, Y. Z. Lee, J. Lu, S. Chang, and O. Zhou, "Image-guided microbeam irradiation to brain tumour bearing mice using a carbon nanotube x-ray source array," *Physics in Medicine and Biology*, vol. 59, no. 5, pp. 1283–1303, Mar. 2014, ISSN: 0031-9155, 1361-6560. DOI: 10.1088/0031-9155/59/5/1283.
- [184] H. Yuan, L. Zhang, J. E. Frank, C. R. Inscoe, L. M. Burk, M. Hadsell, Y. Z. Lee, J. Lu, S. Chang, and O. Zhou, "Treating Brain Tumor with Microbeam Radiation Generated by a Compact Carbon-Nanotube-Based Irradiator: Initial Radiation Efficacy Study," en, *Radiation Research*, vol. 184, no. 3, pp. 322–333, Sep. 2015, ISSN: 0033-7587, 1938-5404. DOI: 10.1667/RR13919.1.
- [185] S. Bazyar, C. R. Inscoe, T. Benefield, L. Zhang, J. Lu, O. Zhou, and Y. Z. Lee, "Neurocognitive sparing of desktop microbeam irradiation," *Radiation Oncology*, vol. 12, p. 127, Aug. 2017, ISSN: 1748-717X. DOI: 10.1186/s13014-017-0864-2.
- [186] Y. Prezado, M. Dos Santos, W. Gonzalez, G. Jouvion, C. Guardiola, S. Heinrich, D. Labiod, M. Juchaux, L. Jourdain, C. Sebrerie, and F. Pouzoulet, "Transfer of Minibeam Radiation Therapy into a cost-effective equipment for radiobiological studies: A proof of concept," *Scientific Reports*, vol. 7, Dec. 2017, ISSN: 2045-2322. DOI: 10.1038/s41598-017-17543-3.
- [187] F. M. Khan and J. P. Gibbons (Jr.), *Khan's The Physics of Radiation Therapy*, en. Lippincott Williams & Wilkins, 2014, ISBN: 978-1-4511-8245-3.
- [188] *NIST: X-Ray Mass Attenuation Coefficients - Section 2*, <https://physics.nist.gov/PhysRefData/XrayMassCoef/chap2.html>.

- [189] *Report* IAEA-NDS-195, *XMudat*,
<https://www-nds.iaea.org/publications/iaea-nds/iaea-nds-0195.htm>.
- [190] J. Shultis and R. Faw, *Radiation Shielding*. American Nuclear Society, 2000, ISBN: 978-0-89448-456-8.
- [191] *80/20 T-slot Aluminum Building System*, <https://8020.net/>.
- [192] K. Hohlbaum, B. Bert, S. Dietze, R. Palme, H. Fink, and C. Thöne-Reineke, “Severity classification of repeated isoflurane anesthesia in C57BL/6JRj mice—Assessing the degree of distress,” *PLoS ONE*, vol. 12, no. 6, Jun. 2017, ISSN: 1932-6203. DOI: 10.1371/journal.pone.0179588.
- [193] *Anesthesia Induction and Maintenance — Protocol*,
<https://www.jove.com/science-education/10263/anesthesia-induction-and-maintenance>.
- [194] C.-M. Ma, C. W. Coffey, L. A. DeWerd, C. Liu, R. Nath, S. M. Seltzer, and J. P. Seuntjens, “AAPM protocol for 40-300 kV x-ray beam dosimetry in radiotherapy and radiobiology,” en, *Medical Physics*, vol. 28, no. 6, pp. 868–893, Jun. 2001, ISSN: 00942405. DOI: 10.1118/1.1374247.
- [195] J. E. Reiff, “Accredited Dosimetry Calibration Laboratory (ADCL),” en, in *Encyclopedia of Radiation Oncology*, L. W. Brady and T. E. Yaeger, Eds., Berlin, Heidelberg: Springer, 2013, pp. 2–2, ISBN: 978-3-540-85516-3. DOI: 10.1007/978-3-540-85516-3_765.
- [196] G. G. Poludniowski and P. M. Evans, “I Calculation of x-ray spectra emerging from an x-ray tube. Part I. Electron penetration characteristics in x-ray targets,” en, *Medical Physics*, vol. 34, no. 6Part1, pp. 2164–2174, 2007, eprint: <https://aapm.onlinelibrary.wiley.com/doi/pdf/10.1118/1.2734725>, ISSN: 2473-4209. DOI: 10.1118/1.2734725.
- [197] G. G. Poludniowski, “II Calculation of x-ray spectra emerging from an x-ray tube. Part II. X-ray production and filtration in x-ray targets,” en, *Medical Physics*, vol. 34, no. 6Part1, pp. 2175–2186, 2007, eprint: <https://aapm.onlinelibrary.wiley.com/doi/pdf/10.1118/1.2734726>, ISSN: 2473-4209. DOI: 10.1118/1.2734726.
- [198] Akpochafor, *Assessment of peak kilovoltage accuracy in ten selected X-ray centers in Lagos metropolis, South-Western Nigeria: A quality control test to determine energy output accuracy of an X-ray generator*, <http://www.jhrr.org/article.asp?issn=2394-2010;year=2016;volume=3;issue=2;spage=60;epage=65;aulast=Akpochafor>.
- [199] *Garchromic EBT Films - GAFchromic™*,
<http://www.gafchromic.com/gafchromic-film/radiotherapy-films/EBT/index.asp>.

- [200] A. Niroomand-Rad, C. R. Blackwell, B. M. Coursey, K. P. Gall, J. M. Galvin, W. L. McLaughlin, A. S. Meigooni, R. Nath, J. E. Rodgers, and C. G. Soares, “Radiochromic film dosimetry: Recommendations of AAPM Radiation Therapy Committee Task Group 55,” en, *Medical Physics*, vol. 25, no. 11, pp. 2093–2115, 1998, eprint: <https://aapm.onlinelibrary.wiley.com/doi/pdf/10.1118/1.598407>, ISSN: 2473-4209. DOI: 10.1118/1.598407.
- [201] M. D. Belley, I. N. Stanton, M. Hadsell, R. Ger, B. W. Langloss, J. Lu, O. Zhou, S. X. Chang, M. J. Therien, and T. T. Yoshizumi, “Fiber-optic detector for real time dosimetry of a micro-planar x-ray beam,” *Medical Physics*, vol. 42, no. 4, pp. 1966–1972, Apr. 2015, ISSN: 0094-2405. DOI: 10.1118/1.4915078.
- [202] *Fiber Optics – LEONI*, <https://www.leoni-fiber-optics.com/en/>.
- [203] L. Eling, A. Bouchet, C. Nemoz, V. Djonov, J. Balosso, J. Laissue, E. Bräuer-Krisch, J. F. Adam, and R. Serduc, “Ultra high dose rate Synchrotron Microbeam Radiation Therapy. Preclinical evidence in view of a clinical transfer,” English, *Radiotherapy and Oncology*, FLASH Radiotherapy International Workshop, vol. 139, pp. 56–61, Oct. 2019, ISSN: 0167-8140, 1879-0887. DOI: 10.1016/j.radonc.2019.06.030.
- [204] C. Billena and A. J. Khan, “A Current Review of Spatial Fractionation: Back to the Future?” en, *International Journal of Radiation Oncology*Biology*Physics*, vol. 104, no. 1, pp. 177–187, May 2019, ISSN: 03603016. DOI: 10.1016/j.ijrobp.2019.01.073.
- [205] A. Bravin, P. Olko, E. Schültke, and J. J. Wilkens, “SYRA3 COST Action – Microbeam radiation therapy: Roots and prospects,” *Physica Medica*, Radiation Therapy with Synchrotron Radiation: Achievements and Challenges, vol. 31, no. 6, pp. 561–563, Sep. 2015, ISSN: 1120-1797. DOI: 10.1016/j.ejmp.2015.06.002.
- [206] G. Narayanasamy, X. Zhang, A. Meigooni, N. Paudel, S. Morrill, S. Maraboyina, L. Peacock, and J. Penagaricano, “Therapeutic benefits in grid irradiation on Tomotherapy for bulky, radiation-resistant tumors,” en, *Acta Oncologica*, vol. 56, no. 8, pp. 1043–1047, Aug. 2017, ISSN: 0284-186X, 1651-226X. DOI: 10.1080/0284186X.2017.1299219.
- [207] F. A. Dilmanian, J. G. Eley, A. Rusek, and S. Krishnan, “Charged Particle Therapy with Mini-Segmented Beams,” *Frontiers in Oncology*, vol. 5, Dec. 2015, ISSN: 2234-943X. DOI: 10.3389/fonc.2015.00269.
- [208] I. Martínez-Rovira, W. González, S. Brons, and Y. Prezado, “Carbon and oxygen minibeam radiation therapy: An experimental dosimetric evaluation,” eng, *Medical Physics*, vol. 44, no. 8, pp. 4223–4229, Aug. 2017, ISSN: 2473-4209. DOI: 10.1002/mp.12383.
- [209] Y. Prezado, P. Deman, P. Varlet, G. Jouvion, S. Gil, C. Le Clec’H, H. Bernard, G. Le Duc, and S. Sarun, “Tolerance to Dose Escalation in Minibeam Radiation

Therapy Applied to Normal Rat Brain: Long-Term Clinical, Radiological and Histopathological Analysis,” eng, *Radiation Research*, vol. 184, no. 3, pp. 314–321, Sep. 2015, ISSN: 0033-7587, 1938-5404. DOI: 10.1667/RR14018.1.

- [210] Y. Prezado, S. Sarun, S. Gil, P. Deman, A. Bouchet, and G. Le Duc, “Increase of lifespan for glioma-bearing rats by using minibeam radiation therapy,” *Journal of Synchrotron Radiation*, vol. 19, no. 1, pp. 60–65, Jan. 2012, ISSN: 0909-0495. DOI: 10.1107/S0909049511047042.
- [211] A. Terahara, A. Niemierko, M. Goitein, D. Finkelstein, E. Hug, N. Liebsch, D. O’Farrell, S. Lyons, and J. Munzenrider, “Analysis of the relationship between tumor dose inhomogeneity and local control in patients with skull base chordoma,” eng, *International Journal of Radiation Oncology, Biology, Physics*, vol. 45, no. 2, pp. 351–358, Sep. 1999, ISSN: 0360-3016. DOI: 10.1016/s0360-3016(99)00146-7.
- [212] E. Bräuer-Krisch, R. Serduc, E. Siegbahn, G. Le Duc, Y. Prezado, A. Bravin, H. Blattmann, and J. Laissue, “Effects of pulsed, spatially fractionated, microscopic synchrotron X-ray beams on normal and tumoral brain tissue,” eng, *Mutation Research/Reviews in Mutation Research*, vol. 704, no. 1-3, pp. 160–166, 2010 Apr-Jun, ISSN: 0027-5107. DOI: 10.1016/j.mrrev.2009.12.003.
- [213] V. Favaudon, C. Fouillade, and M.-C. Vozenin, “[Ultrahigh dose-rate, ”flash” irradiation minimizes the side-effects of radiotherapy],” fre, *Cancer Radiotherapie: Journal De La Societe Francaise De Radiotherapie Oncologique*, vol. 19, no. 6-7, pp. 526–531, Oct. 2015, ISSN: 1769-6658. DOI: 10.1016/j.canrad.2015.04.006.
- [214] P. Montay-Gruel, A. Bouchet, M. Jaccard, D. Patin, R. Serduc, W. Aim, K. Petersson, B. Petit, C. Bailat, J. Bourhis, E. Bräuer-Krisch, and M.-C. Vozenin, “X-rays can trigger the FLASH effect: Ultra-high dose-rate synchrotron light source prevents normal brain injury after whole brain irradiation in mice,” eng, *Radiotherapy and Oncology: Journal of the European Society for Therapeutic Radiology and Oncology*, vol. 129, no. 3, pp. 582–588, Dec. 2018, ISSN: 1879-0887. DOI: 10.1016/j.radonc.2018.08.016.
- [215] *The Radiosurgery Society® to Co-Host a Workshop on High-Dose, Ultra-Dose-Rate and Spatially Fractionated Radiotherapy*, <https://www.prweb.com/releases/2018/07/prweb15605284.htm>.
- [216] S. K. Kasoji, J. N. Rivera, R. C. Gessner, S. X. Chang, and P. A. Dayton, “Early Assessment of Tumor Response to Radiation Therapy using High-Resolution Quantitative Microvascular Ultrasound Imaging,” en, *Theranostics*, vol. 8, no. 1, pp. 156–168, 2018, ISSN: 1838-7640. DOI: 10.7150/thno.19703.
- [217] T. Schroeder, H. Yuan, B. L. Viglianti, C. Peltz, S. Asopa, Z. Vujaskovic, and M. W. Dewhirst, “Spatial Heterogeneity and Oxygen Dependence of Glucose Consumption in R3230Ac and Fibrosarcomas of the Fischer 344 Rat,” en, *Cancer*

- Research*, vol. 65, no. 12, pp. 5163–5171, Jun. 2005, ISSN: 0008-5472, 1538-7445. DOI: 10.1158/0008-5472.CAN-04-3900.
- [218] S. M. Fix, V. Papadopoulou, H. Velds, S. K. Kasoji, J. N. Rivera, M. A. Borden, S. Chang, and P. A. Dayton, “Oxygen microbubbles improve radiotherapy tumor control in a rat fibrosarcoma model - A preliminary study,” eng, *PloS One*, vol. 13, no. 4, e0195667, 2018, ISSN: 1932-6203. DOI: 10.1371/journal.pone.0195667.
 - [219] S. X. Chang, J. N. Rivera, L. B. Herity, L. S. Price, A. J. Madden, J. R. Roques, C. Santos, D. Darr, and W. C. Zamboni, “Abstract 5051: Comparison of microbeam versus conventional broadbeam radiation therapy on tumor delivery enhancement of PEGylated liposomal doxorubicin in a triple negative breast cancer mouse model,” in *Experimental and Molecular Therapeutics*, American Association for Cancer Research, Jul. 2017, pp. 5051–5051. DOI: 10.1158/1538-7445.AM2017-5051.
 - [220] Y. Yang, A. Swierczak, M. Ibahim, P. Paiva, L. Cann, A. W. Stevenson, J. C. Crosbie, R. L. Anderson, and P. A. W. Rogers, “Synchrotron microbeam radiotherapy evokes a different early tumor immunomodulatory response to conventional radiotherapy in EMT6.5 mammary tumors,” English, *Radiotherapy and Oncology: Journal of the European Society for Therapeutic Radiology and Oncology*, vol. 133, pp. 93–99, Apr. 2019, ISSN: 0167-8140, 1879-0887. DOI: 10.1016/j.radonc.2019.01.006.
 - [221] D. L. Hickman and M. Swan, “Use of a Body Condition Score Technique to Assess Health Status in a Rat Model of Polycystic Kidney Disease,” eng, *Journal of the American Association for Laboratory Animal Science: JAALAS*, vol. 49, no. 2, pp. 155–159, Mar. 2010, ISSN: 1559-6109.
 - [222] A. Niemierko, “Reporting and analyzing dose distributions: A concept of equivalent uniform dose,” en, *Medical Physics*, vol. 24, no. 1, pp. 103–110, 1997, eprint: <https://aapm.onlinelibrary.wiley.com/doi/pdf/10.1118/1.598063>, ISSN: 2473-4209. DOI: 10.1118/1.598063.
 - [223] A. Faustino-Rocha, P. A. Oliveira, J. Pinho-Oliveira, C. Teixeira-Guedes, R. Soares-Maia, R. G. da Costa, B. Colaço, M. J. Pires, J. Colaço, R. Ferreira, and M. Ginja, “Estimation of rat mammary tumor volume using caliper and ultrasonography measurements,” en, *Lab Animal*, vol. 42, no. 6, pp. 217–224, Jun. 2013, ISSN: 0093-7355, 1548-4475. DOI: 10.1038/labon.254.
 - [224] R. C. Gessner, C. B. Frederick, F. S. Foster, and P. A. Dayton, “Acoustic Angiography: A New Imaging Modality for Assessing Microvasculature Architecture,” en, *International Journal of Biomedical Imaging*, vol. 2013, e936593, Jul. 2013, ISSN: 1687-4188. DOI: 10.1155/2013/936593.
 - [225] P. D. Allison, *Survival Analysis Using SAS: A Practical Guide, Second Edition*, en. SAS Institute, Mar. 2010, ISBN: 978-1-59994-884-3.

- [226] M. Kutner, *Applied Linear Statistical Models*, en, ser. McGraw-Hill International Edition. McGraw-Hill Irwin, 2005, ISBN: 978-0-07-112221-4.
- [227] *R: The R Project for Statistical Computing*, <https://www.r-project.org/>.
- [228] A. Bouchet, N. Sakakini, M. El Atifi, C. Le Clec'h, E. Brauer, A. Moisan, P. Deman, P. Rihet, G. Le Duc, and L. Pelletier, "Early gene expression analysis in 9L orthotopic tumor-bearing rats identifies immune modulation in molecular response to synchrotron microbeam radiation therapy," eng, *PloS One*, vol. 8, no. 12, e81874, 2013, ISSN: 1932-6203. DOI: 10.1371/journal.pone.0081874.
- [229] *Abstract 5051: Comparison of microbeam versus conventional broadbeam radiation therapy on tumor delivery enhancement of PEGylated liposomal doxorubicin in a triple negative breast cancer mouse model — Cancer Research*, https://cancerres.aacrjournals.org/content/77/13_Supplement/5051.
- [230] P. Mavroidis, B. K. Lind, and A. Brahme, "Biologically effective uniform dose (D) for specification, report and comparison of dose response relations and treatment plans," eng, *Physics in Medicine and Biology*, vol. 46, no. 10, pp. 2607–2630, Oct. 2001, ISSN: 0031-9155. DOI: 10.1088/0031-9155/46/10/307.
- [231] M. J. Ibahim, J. C. Crosbie, Y. Yang, M. Zaitseva, A. W. Stevenson, P. A. W. Rogers, and P. Paiva, "An Evaluation of Dose Equivalence between Synchrotron Microbeam Radiation Therapy and Conventional Broadbeam Radiation Using Clonogenic and Cell Impedance Assays," *PLoS ONE*, vol. 9, no. 6, Jun. 2014, ISSN: 1932-6203. DOI: 10.1371/journal.pone.0100547.
- [232] M. Nakayama, N. Mukumoto, H. Akasaka, D. Miyawaki, H. Nishimura, K. Umetani, N. Nariyama, T. Kondoh, K. Shinohara, and R. Sasaki, "Dose Estimation of Normal Brain Tissue Tolerance for Microbeam Radiation Therapy," English, *International Journal of Radiation Oncology • Biology • Physics*, vol. 90, no. 1, S804, Sep. 2014, ISSN: 0360-3016. DOI: 10.1016/j.ijrobp.2014.05.2321.
- [233] R. C. U. Priyadarshika, J. C. Crosbie, B. Kumar, and P. A. W. Rogers, "Biodosimetric quantification of short-term synchrotron microbeam versus broad-beam radiation damage to mouse skin using a dermatopathological scoring system," *The British Journal of Radiology*, vol. 84, no. 1005, pp. 833–842, Sep. 2011, ISSN: 0007-1285. DOI: 10.1259/bjr/58503354.
- [234] J. I. Choi, J. Daniels, D. Cohen, Y. Li, C. S. Ha, and T. Y. Eng, "Clinical Outcomes of Spatially Fractionated GRID Radiotherapy in the Treatment of Bulky Tumors of the Head and Neck," en, *Cureus*, May 2019, ISSN: 2168-8184. DOI: 10.7759/cureus.4637.
- [235] F. A. Dilmanian, Y. Qu, L. E. Feinendegen, L. A. Peña, T. Bacarian, F. A. Henn, J. Kalef-Ezra, S. Liu, Z. Zhong, and J. W. McDonald, "Tissue-sparing effect of

- x-ray microplanar beams particularly in the CNS: Is a bystander effect involved?” en, *Experimental Hematology*, vol. 35, no. 4, pp. 69–77, Apr. 2007, ISSN: 0301472X. DOI: 10.1016/j.exphem.2007.01.014.
- [236] M. E. Rodríguez-Ruiz, C. Vanpouille-Box, I. Melero, S. C. Formenti, and S. Demaria, “Immunological Mechanisms Responsible for Radiation-Induced Abscopal Effect,” en, *Trends in Immunology*, vol. 39, no. 8, pp. 644–655, Aug. 2018, ISSN: 14714906. DOI: 10.1016/j.it.2018.06.001.
- [237] S. J. Chmura, P. P. Connell, and R. R. Weichselbaum, “Retuning the Radio in Radiobiology,” en, *JNCI: Journal of the National Cancer Institute*, Nov. 2017, ISSN: 0027-8874, 1460-2105. DOI: 10.1093/jnci/djx234.
- [238] D. G. Kirsch, M. Diehn, A. H. Kesarwala, A. Maity, M. A. Morgan, J. K. Schwarz, R. Bristow, S. Demaria, I. Eke, R. J. Griffin, D. Haas-Kogan, G. S. Higgins, A. C. Kimmelman, R. J. Kimple, I. M. Lombaert, L. Ma, B. Marples, F. Pajonk, C. C. Park, D. Schaeue, and E. J. Bernhard, “The Future of Radiobiology,” eng, *Journal of the National Cancer Institute*, Nov. 2017, ISSN: 1460-2105. DOI: 10.1093/jnci/djx231.
- [239] S. C. Formenti and S. Demaria, “Radiation Therapy to Convert the Tumor Into an In Situ Vaccine,” *International journal of radiation oncology, biology, physics*, vol. 84, no. 4, pp. 879–880, Nov. 2012, ISSN: 0360-3016. DOI: 10.1016/j.ijrobp.2012.06.020.
- [240] ———, “Combining Radiotherapy and Cancer Immunotherapy: A Paradigm Shift,” en, *JNCI: Journal of the National Cancer Institute*, vol. 105, no. 4, pp. 256–265, Feb. 2013, ISSN: 0027-8874, 1460-2105. DOI: 10.1093/jnci/djs629.
- [241] E. B. Golden, A. Chhabra, A. Chachoua, S. Adams, M. Donach, M. Fenton-Kerimian, K. Friedman, F. Ponzio, J. S. Babb, J. Goldberg, S. Demaria, and S. C. Formenti, “Local radiotherapy and granulocyte-macrophage colony-stimulating factor to generate abscopal responses in patients with metastatic solid tumours: A proof-of-principle trial,” *The Lancet Oncology*, vol. 16, no. 7, pp. 795–803, Jul. 2015, ISSN: 1470-2045. DOI: 10.1016/S1470-2045(15)00054-6.
- [242] C. Vanpouille-Box, K. A. Pilonis, E. Wennerberg, S. C. Formenti, and S. Demaria, “In situ vaccination by radiotherapy to improve responses to anti-CTLA-4 treatment,” English, *Vaccine; Kidlington*, vol. 33, no. 51, pp. 7415–7422, Dec. 2015, ISSN: 0264410X. DOI: <http://dx.doi.org.libproxy.lib.unc.edu/10.1016/j.vaccine.2015.05.105>.
- [243] P. M. Dimberu and R. M. Leonhardt, “Cancer Immunotherapy Takes a Multi-Faceted Approach to Kick the Immune System into Gear,” *The Yale Journal of Biology and Medicine*, vol. 84, no. 4, pp. 371–380, Dec. 2011, ISSN: 0044-0086.

- [244] A. E. Casey, G. L. Ross, and R. R. Langston, “Selective XYZ Factor in C57 Black Mammary Carcinoma Eo771,” en, *Experimental Biology and Medicine*, vol. 72, no. 1, pp. 83–89, Oct. 1949, ISSN: 1535-3702, 1535-3699. DOI: 10.3181/00379727-72-17339.
- [245] L. J. Dunham and H. L. Stewart, “A survey of transplantable and transmissible animal tumors,” eng, *Journal of the National Cancer Institute*, vol. 13, no. 5, pp. 1299–1377, Apr. 1953, ISSN: 0027-8874.
- [246] C. N. Johnstone, Y. E. Smith, Y. Cao, A. D. Burrows, R. S. N. Cross, X. Ling, R. P. Redvers, J. P. Doherty, B. L. Eckhardt, A. L. Natoli, C. M. Restall, E. Lucas, H. B. Pearson, S. Deb, K. L. Britt, A. Rizzitelli, J. Li, J. H. Harmey, N. Pouliot, and R. L. Anderson, “Functional and molecular characterisation of EO771.LMB tumours, a new C57BL/6-mouse-derived model of spontaneously metastatic mammary cancer,” en, *Disease Models & Mechanisms*, vol. 8, no. 3, pp. 237–251, Mar. 2015, ISSN: 1754-8403, 1754-8411. DOI: 10.1242/dmm.017830.
- [247] A. S. Betof, C. D. Lascola, D. Weitzel, C. Landon, P. M. Scarbrough, G. R. Devi, G. Palmer, L. W. Jones, and M. W. Dewhirst, “Modulation of Murine Breast Tumor Vascularity, Hypoxia, and Chemotherapeutic Response by Exercise,” en, *JNCI: Journal of the National Cancer Institute*, vol. 107, no. 5, May 2015, ISSN: 1460-2105, 0027-8874. DOI: 10.1093/jnci/djv040.
- [248] M. Z. Dewan, A. E. Galloway, N. Kawashima, J. K. Dewyngaert, J. S. Babb, S. C. Formenti, and S. Demaria, “Fractionated but not single dose radiotherapy induces an immune-mediated abscopal effect when combined with anti-CTLA-4 antibody,” *Clinical cancer research : an official journal of the American Association for Cancer Research*, vol. 15, no. 17, pp. 5379–5388, Sep. 2009, ISSN: 1078-0432. DOI: 10.1158/1078-0432.CCR-09-0265.
- [249] J. Zeng, A. P. See, J. Phallen, C. M. Jackson, Z. Belcaid, J. Ruzevick, N. Durham, C. Meyer, T. J. Harris, E. Albesiano, G. Pradilla, E. Ford, J. Wong, H.-J. Hammers, D. Mathios, B. Tyler, H. Brem, P. T. Tran, D. Pardoll, C. G. Drake, and M. Lim, “Anti-PD-1 Blockade and Stereotactic Radiation Produce Long-Term Survival in Mice With Intracranial Gliomas,” eng, *International Journal of Radiation Oncology, Biology, Physics*, vol. 86, no. 2, pp. 343–349, Jun. 2013, ISSN: 1879-355X. DOI: 10.1016/j.ijrobp.2012.12.025.
- [250] L. Deng, H. Liang, B. Burnette, M. Beckett, T. Darga, R. R. Weichselbaum, and Y.-X. Fu, “Irradiation and anti-PD-L1 treatment synergistically promote antitumor immunity in mice,” English, *The Journal of Clinical Investigation*, vol. 124, no. 2, pp. 687–695, Jan. 2014, ISSN: 0021-9738, 1558-8238. DOI: 10.1172/JCI67313.
- [251] I. H. Park, S.-Y. Kong, J. Y. Ro, Y. Kwon, J. H. Kang, H. J. Mo, S.-Y. Jung, S. Lee, K. S. Lee, H.-S. Kang, E. Lee, J. Joo, and J. Ro, “Prognostic Implications of Tumor-Infiltrating Lymphocytes in Association With Programmed Death Ligand

- 1 Expression in Early-Stage Breast Cancer,” eng, *Clinical Breast Cancer*, vol. 16, no. 1, pp. 51–58, Feb. 2016, ISSN: 1938-0666. DOI: 10.1016/j.clbc.2015.07.006.
- [252] C. T.-S. Victor, A. J. Rech, A. Maity, R. Rengan, K. E. Pauken, E. Stelekati, J. L. Benci, B. Xu, H. Dada, P. M. Odorizzi, R. S. Herati, K. D. Mansfield, D. Patsch, R. K. Amaravadi, L. M. Schuchter, H. Ishwaran, R. Mick, D. A. Pryma, X. Xu, M. D. Feldman, T. C. Gangadhar, S. M. Hahn, E. J. Wherry, R. H. Vonderheide, and A. J. Minn, “Radiation and Dual Checkpoint Blockade Activates Non-Redundant Immune Mechanisms in Cancer,” *Nature*, vol. 520, no. 7547, pp. 373–377, Apr. 2015, ISSN: 0028-0836. DOI: 10.1038/nature14292.
- [253] S. E. McNeil, “Unique Benefits of Nanotechnology to Drug Delivery and Diagnostics,” in *Characterization of Nanoparticles Intended for Drug Delivery*, S. E. McNeil, Ed., vol. 697, Totowa, NJ: Humana Press, 2011, pp. 3–8, ISBN: 978-1-60327-197-4 978-1-60327-198-1. DOI: 10.1007/978-1-60327-198-1_1.
- [254] ———, “Challenges for nanoparticle characterization,” eng, *Methods in Molecular Biology (Clifton, N.J.)*, vol. 697, pp. 9–15, 2011, ISSN: 1940-6029. DOI: 10.1007/978-1-60327-198-1_2.
- [255] W. P. Caron, G. Song, P. Kumar, S. Rawal, and W. C. Zamboni, “Interpatient Pharmacokinetic and Pharmacodynamic Variability of Carrier-Mediated Anticancer Agents,” eng, *Clinical Pharmacology & Therapeutics*, vol. 91, no. 5, pp. 802–812, May 2012, ISSN: 0009-9236, 1532-6535. DOI: 10.1038/clpt.2012.12.
- [256] U. Prabhakar, H. Maeda, R. K. Jain, E. M. Sevik-Muraca, W. Zamboni, O. C. Farokhzad, S. T. Barry, A. Gabizon, P. Grodzinski, and D. C. Blakey, “Challenges and Key Considerations of the Enhanced Permeability and Retention Effect for Nanomedicine Drug Delivery in Oncology,” eng, *Cancer Research*, vol. 73, no. 8, pp. 2412–2417, Apr. 2013, ISSN: 0008-5472, 1538-7445. DOI: 10.1158/0008-5472.CAN-12-4561.
- [257] W. C. Zamboni, V. Torchilin, A. K. Patri, J. Hrkach, S. Stern, R. Lee, A. Nel, N. J. Panaro, and P. Grodzinski, “Best Practices in Cancer Nanotechnology: Perspective from NCI Nanotechnology Alliance,” eng, *Clinical Cancer Research: An Official Journal of the American Association for Cancer Research*, vol. 18, no. 12, pp. 3229–3241, Jun. 2012, ISSN: 1078-0432, 1557-3265. DOI: 10.1158/1078-0432.CCR-11-2938.
- [258] V. P. Chauhan, T. Stylianopoulos, Y. Boucher, and R. K. Jain, “Delivery of Molecular and Nanoscale Medicine to Tumors: Transport Barriers and Strategies,” eng, *Annual Review of Chemical and Biomolecular Engineering*, vol. 2, no. 1, pp. 281–298, Jul. 2011, ISSN: 1947-5438, 1947-5446. DOI: 10.1146/annurev-chembio-eng-061010-114300.

- [259] R. K. Jain and T. Stylianopoulos, “Delivering nanomedicine to solid tumors,” en, *Nature Reviews Clinical Oncology*, vol. 7, no. 11, pp. 653–664, Nov. 2010, ISSN: 1759-4774, 1759-4782. DOI: 10.1038/nrclinonc.2010.139.
- [260] H. Maeda, H. Nakamura, and J. Fang, “The EPR effect for macromolecular drug delivery to solid tumors: Improvement of tumor uptake, lowering of systemic toxicity, and distinct tumor imaging in vivo,” eng, *Advanced Drug Delivery Reviews*, vol. 65, no. 1, pp. 71–79, Jan. 2013, ISSN: 1872-8294. DOI: 10.1016/j.addr.2012.10.002.
- [261] R. K. Jain, “Normalizing Tumor Microenvironment to Treat Cancer: Bench to Bedside to Biomarkers,” eng, *Journal of Clinical Oncology: Official Journal of the American Society of Clinical Oncology*, vol. 31, no. 17, pp. 2205–2218, Jun. 2013, ISSN: 0732-183X, 1527-7755. DOI: 10.1200/JCO.2012.46.3653.
- [262] C. P. Raut, Y. Boucher, D. G. Duda, J. A. Morgan, R. Quek, M. Ancukiewicz, J. Lahdenranta, J. P. Eder, G. D. Demetri, and R. K. Jain, “Effects of Sorafenib on Intra-Tumoral Interstitial Fluid Pressure and Circulating Biomarkers in Patients with Refractory Sarcomas (NCI Protocol 6948),” eng, *PLoS ONE*, vol. 7, no. 2, S. Basu, Ed., e26331, Feb. 2012, ISSN: 1932-6203. DOI: 10.1371/journal.pone.0026331.
- [263] J. Liu, S. Liao, B. Diop-Frimpong, W. Chen, S. Goel, K. Naxerova, M. Ancukiewicz, Y. Boucher, R. K. Jain, and L. Xu, “TGF- β blockade improves the distribution and efficacy of therapeutics in breast carcinoma by normalizing the tumor stroma,” eng, *Proceedings of the National Academy of Sciences of the United States of America*, vol. 109, no. 41, pp. 16 618–16 623, Oct. 2012, ISSN: 0027-8424, 1091-6490. DOI: 10.1073/pnas.1117610109.
- [264] B. Diop-Frimpong, V. P. Chauhan, S. Krane, Y. Boucher, and R. K. Jain, “Losartan inhibits collagen I synthesis and improves the distribution and efficacy of nanotherapeutics in tumors,” eng, *Proceedings of the National Academy of Sciences of the United States of America*, vol. 108, no. 7, pp. 2909–2914, Feb. 2011, ISSN: 0027-8424, 1091-6490. DOI: 10.1073/pnas.1018892108.
- [265] R. K. Jain, L. L. Munn, and D. Fukumura, “Measuring Vascular Permeability in Mice,” eng, *Cold Spring Harbor Protocols*, vol. 2013, no. 5, pp. 444–446, May 2013, ISSN: 1559-6095. DOI: 10.1101/pdb.prot074344.
- [266] T. Stylianopoulos, J. D. Martin, M. Snuderl, F. Mpekris, S. R. Jain, and R. K. Jain, “Coevolution of Solid Stress and Interstitial Fluid Pressure in Tumors During Progression: Implications for Vascular Collapse,” eng, *Cancer Research*, vol. 73, no. 13, pp. 3833–3841, Jul. 2013, ISSN: 0008-5472, 1538-7445. DOI: 10.1158/0008-5472.CAN-12-4521.
- [267] K. S. Chu, W. Hasan, S. Rawal, M. D. Walsh, E. M. Enlow, J. C. Luft, A. S. Bridges, J. L. Kuijper, M. E. Napier, W. C. Zamboni, and J. M. DeSimone, “Plasma, tumor and tissue pharmacokinetics of Docetaxel delivered via nanoparticles of different

- sizes and shapes in mice bearing SKOV-3 human ovarian carcinoma xenograft,” eng, *Nanomedicine: Nanotechnology, Biology, and Medicine*, vol. 9, no. 5, pp. 686–693, Jul. 2013, ISSN: 1549-9642. DOI: 10.1016/j.nano.2012.11.008.
- [268] W. C. Zamboni, J. L. Eiseman, S. Strychor, P. M. Rice, E. Joseph, B. A. Zamboni, M. K. Donnelly, J. Shurer, R. A. Parise, M. E. Tonda, N. Y. Yu, and P. H. Basse, “Tumor disposition of pegylated liposomal CKD-602 and the reticuloendothelial system in preclinical tumor models,” eng, *Journal of Liposome Research*, vol. 21, no. 1, pp. 70–80, Mar. 2011, ISSN: 0898-2104, 1532-2394. DOI: 10.3109/08982101003754385.
- [269] M. D. Walsh, S. K. Hanna, J. Sen, S. Rawal, C. B. Cabral, A. V. Yurkovetskiy, R. J. Fram, T. B. Lowinger, and W. C. Zamboni, “Pharmacokinetics and Antitumor Efficacy of XMT-1001, a Novel, Polymeric Topoisomerase I Inhibitor, in Mice Bearing HT-29 Human Colon Carcinoma Xenografts,” eng, *Clinical Cancer Research: An Official Journal of the American Association for Cancer Research*, vol. 18, no. 9, pp. 2591–2602, May 2012, ISSN: 1078-0432, 1557-3265. DOI: 10.1158/1078-0432.CCR-11-1554.
- [270] A. J. Madden, S. Rawal, K. Sandison, R. Schell, A. Schorzman, A. Deal, L. Feng, P. Ma, R. Mumper, J. DeSimone, and W. C. Zamboni, “Evaluation of the efficiency of tumor and tissue delivery of carrier-mediated agents (CMA) and small molecule (SM) agents in mice using a novel pharmacokinetic (PK) metric: Relative distribution index over time (RDI-OT),” *Journal of nanoparticle research : an interdisciplinary forum for nanoscale science and technology*, vol. 16, no. 11, Nov. 2014, ISSN: 1388-0764. DOI: 10.1007/s11051-014-2662-1.
- [271] G. Song, D. B. Darr, C. M. Santos, M. Ross, A. Valdivia, J. L. Jordan, B. R. Midkiff, S. Cohen, N. Nikolaishvili-Feinberg, C. R. Miller, T. K. Tarrant, A. B. Rogers, A. C. Dudley, C. M. Perou, and W. C. Zamboni, “Effects of Tumor Microenvironment Heterogeneity on Nanoparticle Disposition and Efficacy in Breast Cancer Tumor Models,” eng, *Clinical Cancer Research: An Official Journal of the American Association for Cancer Research*, vol. 20, no. 23, pp. 6083–6095, Dec. 2014, ISSN: 1078-0432, 1557-3265. DOI: 10.1158/1078-0432.CCR-14-0493.
- [272] J. P. Rolland, B. W. Maynor, L. E. Euliss, A. E. Exner, G. M. Denison, and J. M. DeSimone, “Direct Fabrication and Harvesting of Monodisperse, Shape-Specific Nanobiomaterials,” eng, *Journal of the American Chemical Society*, vol. 127, no. 28, pp. 10 096–10 100, Jul. 2005, ISSN: 0002-7863, 1520-5126. DOI: 10.1021/ja051977c.
- [273] M. C. Parrott, J. C. Luft, J. D. Byrne, J. H. Fain, M. E. Napier, and J. M. Desimone, “Tunable Bifunctional Silyl Ether Cross-Linkers for the Design of Acid-Sensitive Biomaterials,” eng, *Journal of the American Chemical Society*, vol. 132, no. 50, pp. 17 928–17 932, Dec. 2010, ISSN: 0002-7863, 1520-5126. DOI: 10.1021/ja108568g.

- [274] A. Gabizon, M. Bradbury, U. Prabhakar, W. Zamboni, S. Libutti, and P. Grodzinski, "Cancer nanomedicines: Closing the translational gap," eng, *Lancet (London, England)*, vol. 384, no. 9961, pp. 2175–2176, Dec. 2014, ISSN: 01406736. DOI: 10.1016/S0140-6736(14)61457-4.
- [275] J. I. Herschkowitz, W. Zhao, M. Zhang, J. Usary, G. Murrow, D. Edwards, J. Knezevic, S. B. Greene, D. Darr, M. A. Troester, S. G. Hilsenbeck, D. Medina, C. M. Perou, and J. M. Rosen, "Comparative oncogenomics identifies breast tumors enriched in functional tumor-initiating cells," eng, *Proceedings of the National Academy of Sciences of the United States of America*, vol. 109, no. 8, pp. 2778–2783, Feb. 2012, ISSN: 1091-6490. DOI: 10.1073/pnas.1018862108.
- [276] A. Gabizon, R. Shiota, and D. Papahadjopoulos, "Pharmacokinetics and tissue distribution of doxorubicin encapsulated in stable liposomes with long circulation times," eng, *Journal of the National Cancer Institute*, vol. 81, no. 19, pp. 1484–1488, Oct. 1989, ISSN: 0027-8874. DOI: 10.1093/jnci/81.19.1484.
- [277] S. Amselem, A. Gabizon, and Y. Barenholz, "Optimization and upscaling of doxorubicin-containing liposomes for clinical use," eng, *Journal of Pharmaceutical Sciences*, vol. 79, no. 12, pp. 1045–1052, Dec. 1990, ISSN: 0022-3549. DOI: 10.1002/jps.2600791202.
- [278] J. S. Petschauer, A. J. Madden, W. P. Kirschbrown, G. Song, and W. C. Zamboni, "The effects of nanoparticle drug loading on the pharmacokinetics of anticancer agents," *Nanomedicine (London, England)*, vol. 10, no. 3, pp. 447–463, Feb. 2015, ISSN: 1743-5889, 1748-6963. DOI: 10.2217/nnm.14.179.
- [279] W. C. Zamboni, S. Strychor, E. Joseph, D. R. Walsh, B. A. Zamboni, R. A. Parise, M. E. Tonda, N. Y. Yu, C. Engbers, and J. L. Eiseman, "Plasma, tumor, and tissue disposition of STEALTH liposomal CKD-602 (S-CKD602) and nonliposomal CKD-602 in mice bearing A375 human melanoma xenografts," eng, *Clinical Cancer Research: An Official Journal of the American Association for Cancer Research*, vol. 13, no. 23, pp. 7217–7223, Dec. 2007, ISSN: 1078-0432. DOI: 10.1158/1078-0432.CCR-07-1035.
- [280] C. K. Anders, B. Adamo, O. Karginova, A. M. Deal, S. Rawal, D. Darr, A. Schorzman, C. Santos, R. Bash, T. Kafri, L. Carey, C. R. Miller, C. M. Perou, N. Sharpless, and W. C. Zamboni, "Pharmacokinetics and Efficacy of PEGylated Liposomal Doxorubicin in an Intracranial Model of Breast Cancer," en, *PLoS ONE*, vol. 8, no. 5, A. Ahmad, Ed., e61359, May 2013, ISSN: 1932-6203. DOI: 10.1371/journal.pone.0061359.
- [281] D. A. Budwit-Novotny, K. S. McCarty, E. B. Cox, J. T. Soper, D. G. Mutch, W. T. Creasman, J. L. Flowers, and K. S. McCarty, "Immunohistochemical Analyses of Estrogen Receptor in Endometrial Adenocarcinoma Using a Monoclonal Antibody,"

- eng, *Cancer Research*, vol. 46, no. 10, pp. 5419–5425, Oct. 1986, ISSN: 0008-5472, 1538-7445.
- [282] C. d. L. Davies, L. M. Lundstrøm, J. Frengen, L. Eikenes, Ø. S. Bruland S, O. Kaalhus, M. H. B. Hjelstuen, and C. Brekken, “Radiation improves the distribution and uptake of liposomal doxorubicin (caelyx) in human osteosarcoma xenografts,” eng, *Cancer Research*, vol. 64, no. 2, pp. 547–553, Jan. 2004, ISSN: 0008-5472. DOI: 10.1158/0008-5472.can-03-0576.
 - [283] T. Lammers, V. Subr, P. Peschke, R. Kühnlein, W. E. Hennink, K. Ulbrich, F. Kiessling, M. Heilmann, J. Debus, P. E. Huber, and G. Storm, “Image-guided and passively tumour-targeted polymeric nanomedicines for radiochemotherapy,” en, *British Journal of Cancer*, vol. 99, no. 6, pp. 900–910, Sep. 2008, ISSN: 0007-0920, 1532-1827. DOI: 10.1038/sj.bjc.6604561.
 - [284] M. A. Miller, R. Chandra, M. F. Cuccarese, C. Pfirschke, C. Engblom, S. Stapleton, U. Adhikary, R. H. Kohler, J. F. Mohan, M. J. Pittet, and R. Weissleder, “Radiation therapy primes tumors for nanotherapeutic delivery via macrophage-mediated vascular bursts,” en, *Science Translational Medicine*, vol. 9, no. 392, eaal0225, May 2017, ISSN: 1946-6234, 1946-6242. DOI: 10.1126/scitranslmed.aal0225.
 - [285] J. Ferlay, M. Colombet, I. Soerjomataram, C. Mathers, D. M. Parkin, M. Piñeros, A. Znaor, and F. Bray, “Estimating the global cancer incidence and mortality in 2018: GLOBOCAN sources and methods,” en, *International Journal of Cancer*, vol. 144, no. 8, pp. 1941–1953, 2019, eprint: <https://onlinelibrary.wiley.com/doi/pdf/10.1002/ijc.31937>, ISSN: 1097-0215. DOI: 10.1002/ijc.31937.
 - [286] S. B. Jones, “Cancer in the developing world: A call to action,” *BMJ : British Medical Journal*, vol. 319, no. 7208, pp. 505–508, Aug. 1999, ISSN: 0959-8138.
 - [287] M. B. Barton, M. Frommer, and J. Shafiq, “Role of radiotherapy in cancer control in low-income and middle-income countries,” en, *The Lancet Oncology*, vol. 7, no. 7, pp. 584–595, Jul. 2006, ISSN: 1470-2045. DOI: 10.1016/S1470-2045(06)70759-8.
 - [288] R. Baskar and K. Itahana, “Radiation therapy and cancer control in developing countries: Can we save more lives?” *International Journal of Medical Sciences*, vol. 14, no. 1, pp. 13–17, Jan. 2017, ISSN: 1449-1907. DOI: 10.7150/ijms.17288.
 - [289] E. H. Zubizarreta, E. Fidarova, B. Healy, and E. Rosenblatt, “Need for radiotherapy in low and middle income countries – the silent crisis continues,” eng, *Clinical Oncology (Royal College of Radiologists (Great Britain))*, vol. 27, no. 2, pp. 107–114, Feb. 2015, ISSN: 1433-2981. DOI: 10.1016/j.clon.2014.10.006.

- [290] E. Van de Werf, J. Verstraete, and Y. Lievens, “The cost of radiotherapy in a decade of technology evolution,” en, *Radiotherapy and Oncology*, vol. 102, no. 1, pp. 148–153, Jan. 2012, ISSN: 0167-8140. DOI: 10.1016/j.radonc.2011.07.033.
- [291] M. Abdel-Wahab, J.-M. Bourque, Y. Pynda, J. Izewska, D. Van der Merwe, E. Zubizarreta, and E. Rosenblatt, “Status of radiotherapy resources in Africa: An International Atomic Energy Agency analysis,” English, *The Lancet Oncology*, vol. 14, no. 4, e168–e175, Apr. 2013, ISSN: 1470-2045, 1474-5488. DOI: 10.1016/S1470-2045(12)70532-6.
- [292] WHO — *Cancer in developing countries: Facing the challenge*, https://www.who.int/dg/speeches/2010/iaea_forum_20100921/en/. DOI: [/entity/dg/speeches/2010/iaea_forum_20100921/en/index.html](https://www.who.int/dg/speeches/2010/iaea_forum_20100921/en/index.html).
- [293] J. D. Schiffman, P. G. Fisher, and P. Gibbs, “Early detection of cancer: Past, present, and future,” eng, *American Society of Clinical Oncology Educational Book. American Society of Clinical Oncology. Annual Meeting*, pp. 57–65, 2015, ISSN: 1548-8756. DOI: 10.14694/EdBook_AM.2015.35.57.
- [294] S. C. Hiom, “Diagnosing cancer earlier: Reviewing the evidence for improving cancer survival,” *British Journal of Cancer*, vol. 112, no. Suppl 1, S1–S5, Mar. 2015, ISSN: 0007-0920. DOI: 10.1038/bjc.2015.23.
- [295] B. A. Virnig, N. N. Baxter, E. Habermann, R. D. Feldman, and C. J. Bradley, “A Matter Of Race: Early- Versus Late-Stage Cancer Diagnosis,” *Health affairs (Project Hope)*, vol. 28, no. 1, pp. 160–168, 2009, ISSN: 0278-2715. DOI: 10.1377/hlt.haff.28.1.160.
- [296] T. A. Farley and J. T. Flannery, “Late-stage diagnosis of breast cancer in women of lower socioeconomic status: Public health implications,” *American Journal of Public Health*, vol. 79, no. 11, pp. 1508–1512, Nov. 1989, ISSN: 0090-0036. DOI: 10.2105/AJPH.79.11.1508.
- [297] S. S. Poh, M. L. K. Chua, and J. T. S. Wee, “Why we should give spatially fractionated radiation therapy (GRID) a second look—especially in nasopharyngeal carcinoma,” en, *Annals of Nasopharynx Cancer*, vol. 1, pp. 1–1, 2018, ISSN: 26164191. DOI: 10.21037/anpc.2018.04.01.
- [298] *Search of: Lattice therapy - List Results - ClinicalTrials.gov*, en, <https://clinicaltrials.gov/ct2/results?cond=&term=lattice+therapy&cntry=&state=&city=&dist=&Search=Search>.
- [299] A. Pollack, F. M. Chinae, E. Bossart, D. Kwon, M. C. Abramowitz, C. Lynne, M. Jorda, B. Marples, V. N. Patel, X. Wu, I. Reis, M. T. Studenski, J. Casillas, and R. Stoyanova, “Phase I Trial of MRI-Guided Prostate Cancer Lattice Extreme Ablative Dose (LEAD) Boost Radiation Therapy,” en, *International Journal of*

*Radiation Oncology*Biology*Physics*, Feb. 2020, ISSN: 0360-3016. DOI: 10.1016/j.ijrobp.2020.01.052.

- [300] M. W. Nolan, M. S. Kent, and M.-K. Boss, “Emerging Translational Opportunities in Comparative Oncology With Companion Canine Cancers: Radiation Oncology,” English, *Frontiers in Oncology*, vol. 9, 2019, ISSN: 2234-943X. DOI: 10.3389/fonc.2019.01291.
- [301] T. L. Gieger and M. W. Nolan, “Linac-based stereotactic radiation therapy for canine non-lymphomatous nasal tumours: 29 cases (2013-2016),” en, *Veterinary and Comparative Oncology*, vol. 16, no. 1, E68–E75, 2018, eprint: <https://onlinelibrary.wiley.com/doi/pdf/10.1111/vco.12334>, ISSN: 1476-5829. DOI: 10.1111/vco.12334.
- [302] J. Walters, S. Ryan, and J. F. Harmon, “Characterization of differences in calculated and actual measured skin doses to canine limbs during stereotactic radiosurgery using Gafchromic film,” en, *Medical Dosimetry*, vol. 37, no. 2, pp. 201–207, Jun. 2012, ISSN: 0958-3947. DOI: 10.1016/j.meddos.2011.07.003.
- [303] R. Bloomfield, “Stereotactic radiation therapy in veterinary medicine,” *The Canadian Veterinary Journal*, vol. 56, no. 1, pp. 95–97, Jan. 2015, ISSN: 0008-5286.
- [304] J. Z. Walz, N. Desai, N. Van Asselt, V. J. Poirier, K. Hansen, and L. Selmic, “Definitive-intent intensity-modulated radiation therapy for treatment of canine prostatic carcinoma: A multi-institutional retrospective study,” eng, *Veterinary and Comparative Oncology*, Dec. 2019, ISSN: 1476-5829. DOI: 10.1111/vco.12561.
- [305] M. W. Nolan, T. L. Gieger, A. A. Karakashian, M. N. Nikolova-Karakashian, L. P. Posner, D. M. Roback, J. N. Rivera, and S. Chang, “Outcomes of Spatially Fractionated Radiotherapy GRID for Bulky Soft Tissue Sarcomas in a Large Animal Model,” en, *Technology in Cancer Research & Treatment*, vol. 16, no. 3, pp. 357–365, Feb. 2017, ISSN: 1533-0346. DOI: 10.1177/1533034617690980.